Absorption and Spatial Dispersion in Electromagnetic Susceptibility Models

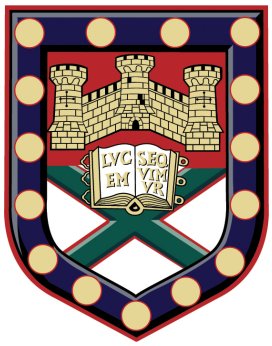

Robin Jeffrey Churchill
School of Physics
University of Exeter

A thesis submitted for the degree of
Doctor of Philosophy in Physics
August 2017

Absorption and Spatial Dispersion in Electromagnetic Susceptibility Models

Submitted by Robin Jeffrey Churchill, to the University of Exeter as a thesis for the degree of Doctor of Philosophy in Physics.
August 2017

I certify that all material in this thesis which is not my own work has been identified and that no material has previously been submitted and approved for the award of a degree by this or any other University.

Robin Jeffrey Churchill

Date

Acknowledgments

Firstly, I would like to thank my main supervisor Dr Tom Philbin for all the discussions, advice and guidance he has provided over the course of my research.

Next, a big thank you to my second supervisor Dr Simon Horsley, Dr Janet Anders and the rest of the PhD students who made up our little theory group. My thanks also go out to Charles Downing and Tom Sturges of the QSN group.

Finally, I would like to thank my family, both for their constant support and their willingness to listen to me ramble on about my work over the past four years.

Abstract

This thesis focuses on two key aspects of light-matter interactions: absorption and spatial dispersion, both of which are described on a macroscopic scale by the electromagnetic susceptibility.

The first part of this thesis contains an investigation into the microscopic origin of absorption in dielectric models, providing a detailed calculation for a long-held assumption of the Hopfield model that has formed the basis of many key works on the subject. While previous work has either focused on the quantum regime or used phenomenological methods which lack a clear relationship to the underlying physics, the microscopic model and calculations presented here are purely classical in nature, matching Hopfields initial proposal. A discrete model of a dielectric is developed, containing nonlinear interaction terms between polarizable dipoles and lattice vibrations. The lattice vibrations are found to act as a pseudo-reservoir, leading to broadband absorption of electromagnetic radiation that naturally emerges from the model, without the need to add damping terms to the dynamics. The effective linear susceptibility is calculated using a perturbative iteration method and is found to match the form of a model that is widely used for real dielectrics.

The second half of the thesis presents a series of modifications to the Halevi-Fuchs susceptibility model, which is used to calculate the electromagnetic reflection and transmission coefficients of a spatially-dispersive half-infinite medium. The initial model, valid only for an idealized single-resonance scalar susceptibility with a specific wave vector dependence, is extended to include many more of the susceptibility features found in real materials, including unequal transverse and longitudinal components, multiple resonances, anisotropy and alternate wave vector dependences. In each case, the effect of the boundary is characterized by a set of phenomenological reflection coefficients for the polarization waves in the medium, with specific values corresponding to various additional boundary conditions for Maxwell's equations. The exact expressions derived for the electromagnetic reflection and transmission coefficients can be used in the calculation of a range of physical phenomena near the boundary of the medium. This thesis considers the spectral energy density of thermal and zero-point radiation outside the medium, with the key result that the inclusion of spatial dispersion naturally removes an unphysical divergence associated with the use of a spatially local susceptibility model.

Contents

Publications

Absorption in dipole-lattice models of dielectrics
R. J. Churchill and T. G. Philbin, Phys. Rev. A, **93**, 053809 (2016).

Electromagnetic reflection, transmission, and energy density at boundaries of nonlocal media
R. J. Churchill and T. G. Philbin, Phys. Rev. B, **94**, 235422 (2016).

Reflection and transmission in nonlocal susceptibility models with multiple resonances
R. J. Churchill and T. G. Philbin, Phys. Rev. B, **95**, 205406 (2017).

List of Symbols

Chapter 3: Absorption in Dielectrics

Notation	Definition
$A(z,t)$	Scalar field acting as projection of electromagnetic vector potential
$A_h(q,\omega)$	Homogeneous solution of the A field in the absence of coupling
a	Lattice spacing
c	Speed of light in vacuum
$F(q,\omega)$	Sum over all possible intermediate steps for iteration processes that start and end with $p(q,\omega)$, under certain restrictions
$F_n(q,\omega)$	Sum of all terms in $F(q,\omega)$ with a factor of σ^n
F_{2p}, F_{2u}, F_{4p}	Terms of F_n corresponding to specific iteration processes
$f_{1/2}(q,q')$	L_{ppu} nonlinear coupling function
$G_A(k,\omega)$	Retarded Green function of A field in the absence of coupling
$G_p(q,\omega)$	Retarded Green function of p field in the absence of coupling
$G_p^d(q,\omega)$	Retarded Green function of p field dressed with A by linear interactions in the ML model
$G_p'(q,\omega)$	Effective Green function of p field dressed with u by nonlinear interactions in the MN model
$G_u(q,\omega)$	Retarded Green function of u field in the absence of coupling
H	Collection of homogeneous solutions
k	Wave vector
L_A, L_p, L_u	"Free" Lagrangians
L_{pA}, L_{ppu}	Interaction Lagrangians
M	Particle mass
$\mathbb{P}$	Principal-valued term
$p_h(q,\omega)$	Homogeneous solution of the p field in the absence of coupling
$p_n(t)$	Electric dipole moment of n^{th} particle in 1D model
$Q(\omega)$	Inverse of $\nu(q)$
q	Wave vector (limited to first Brillouin zone)
t	Time

Notation	Definition
$U(q)$	Choice of function for u_h
U_0	Amplitude of $U(q)$
$u_h(q,\omega)$	Homogeneous solution of the u field in the absence of coupling
$u_n(t)$	Displacement of n^{th} particle in 1D model
V_0	Dipole-dipole interaction strength
$Z_{\mathrm{L}}[A]$	Collection of linear A terms resulting from iteration process
$Z_{\mathrm{NL}}[A]$	Collection of nonlinear A terms resulting from iteration process
z	Position
z_n	Lattice position of n^{th} particle in 1D model
$\alpha(z)$	Function describing finite size of particles in 1D model
β	L_{pA} linear coupling parameter
γ	Damping coefficient of the Lorentz model
$\delta(z)$, $\delta(q)$	Dirac delta function
κ_n	n^{th}-nearest-neighbor displacement strength
λ	Wavelength
ν_0	Resonant frequency of single displacement u_n
$\nu_0(q)$	Resonant frequency of u field
$\rho(\omega)$	Density of states
σ	L_{ppu} nonlinear coupling parameter (rescaled)
τ_n	n^{th}-nearest-neighbor dipole-dipole interaction strength (rescaled)
ω	Angular frequency
ω_0	Resonant frequency of single electric dipole p_n
$\omega_0(q)$	Resonant frequency of p field
ω_p	Resonance strength of the Lorentz model
ω_T	Resonant frequency of the Lorentz model
$\chi(q,\omega)$	Linear susceptibility of the ML model
$\chi_{\mathrm{eff}}(q,\omega)$	Effective linear susceptibility of the MN model
ML model	Microscopic linear model
MN model	Microscopic nonlinear model
QFT	Quantum field theory

Chapters 4-7: Assumptions in ABC models & Extending the Halevi-Fuchs model

Notation	Definition
$\boldsymbol{A}$	Electromagnetic vector potential
a	Lattice spacing of discrete 1D model
$\boldsymbol{B}$	Magnetic induction
c	Speed of light in vacuum
$\boldsymbol{c}$	Crystal axis in uniaxial medium
$\boldsymbol{D}$	Displacement Field
D, D_h, D_l,	
D_m, $D_\perp$, $D_\parallel$	Nonlocal k^2 parameter of susceptibility models
D_{eff}, D^*	Nonlocal k^2 parameter in single-resonance approximation susceptibility models
$\boldsymbol{E}$	Electric field
$\boldsymbol{E}_0$	Incident electric field wave
$\boldsymbol{E}_r$	Reflected electric field wave
$\boldsymbol{E}^{(n)}$	n^{th} transmitted electric field wave
$g(\omega)$	Arbitrary function used in discrete 1D model
$h_n(\omega)$	n^{th}-nearest neighbor coupling strength used in discrete 1D model
$\boldsymbol{k}$	Wave vector
K	Fixed x-component of wave vector parallel to boundary of half-infinite medium
$\boldsymbol{k}_r$	Wave vector of reflected wave
$\boldsymbol{k}_0$	Wave vector of incident wave
$\boldsymbol{k}^{(n)}$	Wave vector of n^{th} transmitted wave
L	Effective additional distance traveled by reflected polarization waves in discrete 1D model
L_i	Power series expression for $E_i^{(1)}$ found using iteration process
$L_i^{a,b}$	Coefficient of $(\alpha)^a(iz)^b$ in L_i
l_{eff}	Number of effective additional lattice constants traveled by reflected polarization waves in discrete 1D model
M	Total number of resonances in susceptibility
M_i	Power series expression for $E_i^{(2)}$ found using iteration process
$M_i^{a,b}$	Coefficient of $(\alpha)^a(iz)^b$ in M_i

Notation	Definition
m_{ex}, $m_{\mathrm{ex}\perp}$, $m_{\mathrm{ex}\parallel}$, m_h, m_l, $m_\perp$, $m_\parallel$	Exciton mass
m_{el}, m_{ho}	Electron and hole mass
N	Total number of transmitted waves in half-infinite medium
N_i	Power series expression for $E_i^{(3)}$ found using iteration process
$N_i^{a,b}$	Coefficient of $(\alpha)^a(iz)^b$ in N_i
$\boldsymbol{P}$	Polarization field
$\boldsymbol{\mathcal{P}}$	Polarization field associated with resonance in susceptibility
$p_n(t)$	Electric dipole moment of n^{th} particle in discrete 1D model
q	z-component of wave vector perpendicular to boundary of the half-infinite medium
q_n	z-component of $\boldsymbol{k}^{(n)}$
q_0	z-component of $\boldsymbol{k}_0$
$\boldsymbol{r}$	Position vector
r_s, r_p	Electromagnetic reflection coefficient of s- and p-polarized light
r_0	Atomic radius used in discrete 1D model
$\boldsymbol{S}$	Arbitrary source term used in iteration process
SS	Arbitrary source term used in iteration process (rescaled)
t	Time
T_i	Power series expression for E_i found using iteration process
$t_s^{(n)}, t_p^{(n)}$	Electromagnetic transmission coefficient of n^{th} wave in the s- and p-polarizations
U_i, U_{ij}	Phenomenological reflection coefficient of polarization waves
U_{mi}	Phenomenological reflection coefficient of polarization waves associated with m^{th} susceptibility resonance
u_{tot}	Spectral energy density
u_0	Spectral energy density (vacuum)
z_n	Lattice position of n^{th} particle in discrete 1D model
Z_s, Z_p	Surface impedance of s- and p-polarization
$\hbar$	Planck's reduced constant
α	Amplitude of susceptibility used in iteration process (Chapter 4)

Notation	Definition
Γ, Γ_m, $\Gamma_\perp$, $\Gamma_\parallel$	Pole of isotropic susceptibility models
Γ_i, $\Gamma_i^{(\pm)}$	Pole of anisotropic susceptibility models
γ, γ_m	Lorentz model damping coefficient
Δ	Relative difference between $D_\perp$ and $D_\parallel$
δ_{ij}	Kronecker Delta
ε_0	Permittivity of free space
ζ	Nonlocal $\pm k$ linear splitting parameter
$\eta^{(n)}$	Ratio of $E_z^{(n)}/E_x^{(n)}$ for transmitted waves
$\Theta(z)$	Heaviside step function
θ_i	Angle of incident wave
Λ_n	Effective susceptibility for infinite discrete 1D model
$\Lambda'_{n,m}$	Effective susceptibility for half-infinite discrete 1D model
$\Lambda^R_{n,m}$	Effective susceptibility term for reflected polarization waves in half-infinite discrete 1D model
μ_0	Permeability of free space
ξ	Nonlocal $\pm k$ linear splitting parameter (rescaled)
$\tau^{(n)}$	Ratio of $B_y^{(n)}/E_x^{(n)}$ for transmitted waves
φ	Electromagnetic scalar potential
$\phi_{ij}^{(n)}$, $\phi_{mj}^{(n)}$, $\psi_{ij}^{(n)}$	Coefficients of $E_j^{(n)}$ in effective ABC equations
χ, χ_{ij}	Susceptibility of infinite medium
χ'_{ij}	Susceptibility of half-infinite medium
χ_m	Individual resonance in susceptibility of infinite medium
χ'_m	Individual resonance in susceptibility of half-infinite medium
$\chi_\perp$	Transverse susceptibility
$\chi_\parallel$	Longitudinal susceptibility
$\chi_{\text{lin}}^{\perp}$	Susceptibility for $\boldsymbol{E} \perp \boldsymbol{c}$ in a uniaxial medium
$\chi_{\text{lin}}^{\parallel}$	Susceptibility for $\boldsymbol{E} \parallel \boldsymbol{c}$ in a uniaxial medium
χ_0	Lorentz model background susceptibility
ω	Angular frequency
ω_L, ω_{Lm}	Dispersion relation solutions when $\boldsymbol{k} = 0$
ω_p, ω_{pm}	Lorentz model resonance strength
ω_T, ω_{Tm}	Lorentz model resonant frequency
ABC	Additional boundary condition

List of Figures

List of Tables

List of Fourier transformations

Fourier transformations in time:

$$F(t) = \frac{1}{2\pi}\int_{-\infty}^{\infty} d\omega\, F(\omega)e^{-i\omega t}, \qquad F(\omega) = \int_{-\infty}^{\infty} dt\, F(t)e^{i\omega t}. \tag{1}$$

Fourier transformations in space:

$$F(\boldsymbol{r}) = \frac{1}{(2\pi)^3}\int_{-\infty}^{\infty} d^3\boldsymbol{k}\, F(\boldsymbol{k})e^{i\boldsymbol{k}\cdot\boldsymbol{r}}, \qquad F(\boldsymbol{k}) = \int_{-\infty}^{\infty} d^3\boldsymbol{r}\, F(\boldsymbol{r})e^{-i\boldsymbol{k}\cdot\boldsymbol{r}}. \tag{2}$$

$$F(z) = \frac{1}{2\pi}\int_{-\infty}^{\infty} dk\, F(k)e^{ikz}, \qquad F(k) = \int_{-\infty}^{\infty} dz\, F(z)e^{-ikz}. \tag{3}$$

$$f_n = \frac{a}{2\pi}\int_{-\pi/a}^{\pi/a} dq\, f(q)e^{iqan}, \qquad f(q) = \sum_{n=-\infty}^{\infty} f_n e^{-qan}. \tag{4}$$

Chapter 1

Introduction

The physics behind light-matter interactions are incredibly rich and diverse, with countless interactions and mechanisms at the microscopic level. However, at the macroscopic level this vast range of behaviour is encapsulated by the comparatively straightforward dielectric functions [1]. In particular, a simple model for the susceptibility can accurately describe the response of a material to an electromagnetic field without reference to the complex underlying physics. This thesis focuses on two important components of the electromagnetic susceptibility.

The first part provides a detailed calculation for a long-held assumption regarding the microscopic origin of absorption in dielectric models [2] that has formed the basis of a key piece of work on the subject [3]. Doing so provides a much-needed link between a successful, but unrealistic, phenomenological model and the microscopic behaviour of a real material.

The second part focuses on the effect of spatial dispersion near a planar boundary. While spatial dispersion is often overlooked when compared to temporal dispersion, there are many cases where it is essential to accurately describe the behaviour of a system. An existing derivation for reflection and transmission valid only for a simple, idealized medium [4] is extended to account for many more of the features that are present in real-world materials. The inclusion of spatial dispersion in this calculation has wider implications for a range of other physical quantities, including the spectral energy density of thermal and zero-point radiation [5], which is discussed in depth for a variety of materials.

1.1 Absorption

Temporal nonlocality, characterized by the frequency dependence of the dielectric functions, is central in describing the electromagnetic response of macroscopic materials. Absorption is a key feature of this and is characterized by the imaginary part of the susceptibility. Due to the Kramers-Kronig relations [6, 7] (a result of the causal nature of the electromagnetic response) absorption is therefore always present, but most important near resonant frequencies of the medium. A simple textbook derivation [1] that treats electrons in a sparse medium as damped harmonic oscillators leads to a susceptibility model that can provide an excellent fit for real materials and belies the complexity of the underlying microscopic physics. However, such an approach becomes difficult to justify [2] when one requires the absorption (or damping) to emerge from the model directly. Instead, it is typically added "by hand" at some point during calculations.

In 1958 Hopfield studied the effective description of light-matter interactions by a susceptibility [2]. He found that a simple model with linear coupling to the electromagnetic field absorbed light only at specific frequencies. He argued this was a result of the linear interaction terms, which lead to coupling between single modes of the medium and light. In terms of second-order perturbation theory [8], there was an insufficient density of final states for real transitions to occur between the excitations of the electromagnetic field and the medium. Instead, energy simply oscillated back and forth between the two.

To provide the coupling between a single mode and a continuum of modes required for real transitions, Hopfield suggested nonlinear interactions [2]. Each mode of the medium that interacted with light would also be nonlinearly coupled to the modes that were not directly coupled to the electromagnetic field. In his specific model, he proposed a polarization field nonlinearly coupled to lattice vibrations, where the energy absorbed from the electromagnetic field would be stored.

Hopfield subsequently assumed that such a model would be sufficient to provide broadband absorption, but gave no supporting calculations in his paper. Other authors continued his work, with the approaches broadly split into two groups. The first followed Hopfields approach in a quantum setting [9–13]. While this has been successful, a full quantum analysis remains challenging and part of the appeal of Hopfield's proposal is that it can be carried out classically.

The second took a phenomenological approach to introducing coupling to a continuum of modes. In 1992, Huttner and Barnett [3] modified Hopfield's model by linearly coupling a polarization field to a reservoir - a field of harmonic oscillators of every frequency.

Each mode of the polarization field was coupled to a continuum of reservoir modes, defined by the frequency of the oscillator. Absorption was found to emerge from the model without sacrificing the relative simplicity of linear coupling. This paper has proved hugely influential and has subsequently been improved upon to include more dielectric features such as inhomogeneity [14, 15], anisotropy [16] and magnetic response [17–20]. Some authors have taken this a step further by removing the polarization field entirely, after noting that only the reservoir was required for absorption [21, 22]. Each of the electromagnetic modes were directly coupled to a continuum, with the resulting susceptibility expressed in terms of the interaction function.

The continuum reservoir has proved an invaluable tool not just in macroscopic electromagnetism, but in other systems with dissipation or absorption, by providing a way to incorporate such behaviour directly in the model, without the need to add it "by hand". A prominent example of this is writing a time-independent Lagrangian for the damped harmonic oscillator [23], where previous attempts [24] had either failed or imposed strict conditions on the model that were unlikely to be satisfied by real materials.

Despite its success, the reservoir remains an abstract mathematical tool that is simply added to a model in order to account for the absorbed energy without a clear relationship to the underlying microscopic model and physics of the system. The first half of this thesis [25] returns to the proposal made by Hopfield [2], to verify his claim that an intuitive classical model leads to a susceptibility with broadband absorption that can be described by a simple resonance model. In doing so, the microscopic physics that allow the phenomenological reservoir to provide such an accurate description of the electromagnetic response of a medium are clarified.

1.2 Spatial dispersion

The electromagnetic response of a medium is nonlocal both in space and time. Known as spatial dispersion, spatial non-locality is characterized by the wave vector dependence of the dielectric functions [26, 27]. While the circumstances where temporal dispersion can be ignored are limited, spatial dispersion is often overlooked. Nevertheless there are circumstances where spatially nonlocal behaviour is required for an accurate description of the system, such as metallic nanoparticles and metamaterials [28–32].

One of the key differences between local and nonlocal media is the existence of additional solutions to the dispersion relation - waves with the same frequency, but different

wave vectors [27]. The resulting complications introduced to the calculation of electromagnetic reflection and transmission coefficients are well-known. While an incident monochromatic wave results in a single transmitted wave in a local medium, the presence of spatial dispersion can lead to several transmitted waves that satisfy the dispersion relation in a nonlocal medium [27]. The information provided by the Maxwell boundary conditions that gives the Fresnel coefficients in the local case [1] is insufficient to solve for the unknown amplitudes of the transmitted waves.

The need for extra information was historically resolved with the introduction of additional boundary conditions (ABCs) on the polarization field of the media [33–56]. The first of these was proposed by Pekar [53–56], based upon microscopic considerations of a system of Frenkel (tight-binding) excitons [57, 58], and specified that that polarization field must vanish at the boundary. While the Pekar ABC remains the most popular choice due to its simplicity, subsequent authors [33–52] have proposed alternative ABCs under certain assumptions that suit different types of material.

In 1984, Halevi and Fuchs collected all of these approaches into a single, generalized ABC model and derived the corresponding electromagnetic reflection coefficients [4]. While uniting the work of previous authors into a single formalism had many advantages, it was somewhat limited in its application to real materials. The model is valid only for single, isolated resonances in a scalar susceptibility with a specific wave vector dependence. While systems such as this do occur, it represents a small fraction of those found in nature [59, 60].

The second half of this thesis starts by extending the Halevi and Fuchs generalized ABC model to include many more of the features found in real materials [61, 62], including tensor susceptibilities [26], multiple or degenerate resonances [63] and alternative wave vector dependences [64–66]. While some of these cases have been individually studied by previous authors [67–73], they were typically for a specific ABC, and have greatly different formalisms that make direct comparisons challenging. The derivation presented in this thesis can include all of the above behaviour in a single model.

The inclusion of spatial dispersion in the derivation of the electromagnetic reflection and transmission coefficients has far-reaching consequences on other phenomena near the surface of a nonlocal medium. The modifications to the Green function of the electromagnetic field have significant effects on many calculations, including spontaneous emission [22, 74–77], radiative heat transfer [78, 79], Casimir forces [22, 80] and the spectral energy density of thermal and zero-point radiation [5]. The final part of this thesis

focuses on the last of these, where it is known that a local model of the medium leads to an unphysical divergence near the boundary. This is caused by evanescent electromagnetic waves with arbitrarily large wave vectors parallel to the surface of the medium. While this problem has previously been resolved by introducing an artificial wave vector cut-off to calculations [81, 82], the inclusion of spatial dispersion will be shown to naturally remove the unphysical divergence from the spectral energy density at the boundary of a half-infinite medium [61, 62].

1.3 Thesis outline

This thesis is organized as follows. Chapter 2 contains the background theory required for the remaining chapters. The first part describes the various properties of the electric susceptibility. The second part describes the various historic approaches to solve the challenge of absorption or dispersive behaviour emerging directly from a model. The third part focuses on the calculation of electromagnetic reflection and transmission coefficients, describing both the problems caused by the inclusion of spatial dispersion and the corresponding solutions in the form of additional boundary conditions (ABCs).

In chapter 3 the calculation behind a long-held assumption made by Hopfield is performed, showing that nonlinear interactions lead to a complex susceptibility in a simple classical model. The frequency and wave vector dependence of a simple one-dimensional model are calculated and compared to the widely-used Lorentz susceptibility model.

Chapter 4 sets the groundwork for subsequent chapters by verifying certain unsupported assumptions made in the derivation of both a specific ABC and the Halevi-Fuchs generalized ABC model. Chapters 5-7 extend the Halevi-Fuchs model to include many more of the features found in real materials. Chapter 5 considers the often overlooked tensor form of the susceptibility in an isotropic, nonlocal medium and chapter 6 replaces the single-resonance susceptibility used by Halevi and Fuchs with a multi-resonance model. Finally, chapter 7 considers uniaxial crystals, modifying the Halevi-Fuchs model to include both anisotropy and an alternate wave vector dependence. In each case, the subsequent effects on the spectral energy density are discussed, noting the differences to the result of both the local model and the original Halevi-Fuchs model.

Chapter 2

Background Theory

The central theme of this thesis is the electric susceptibility, which describes the macroscopic response of a material to an applied electromagnetic field. Section 2.1 discusses the various properties of the susceptibility, starting with the nonlocal behaviour in both space and time. The behaviour of light in a medium is described first for the susceptibility in general, before considering the specific case of the Lorentz model, which is widely used to describe a medium in terms of damped harmonic oscillators. The chapter then moves on to discuss the two key features of the susceptibility that are studied in this thesis.

Section 2.2 focuses on absorption in dielectrics, which is characterized by the imaginary part of the susceptibility. The origin of this term is discussed and a simple model [2] is used to demonstrate the difficulty in absorption naturally emerging from a model. The various phenomenological solutions to this problem are discussed, including the continuum reservoir [3], highlighting the point that they are abstract mathematical tools without a clear connection to the microscopic behaviour of the material.

Section 2.3 considers the effect of spatial dispersion in the susceptibility of a half-infinite medium, discussing the difficulties that nonlocal behaviour introduces to the calculation of electromagnetic reflection and transmission coefficients. The various historic solutions to these problems are described, culminating in a generalized model for a half-infinite, spatially dispersive medium [4]. The limitations of the model are highlighted and the potential improvements are identified. Finally, the inclusion of spatial dispersion in the calculation of the electromagnetic reflection coefficients has a knock-on effect on a range of other physical phenomena. The specific case of the electromagnetic energy density is discussed, where a local model leads to a well-known unphysical divergence at the boundary of the medium [5].

2.1 The electric susceptibility

At the microscopic scale, an external electromagnetic field exerts a force on the electrons and nuclei of atoms in a material. Providing an exact solution for a large system of interacting charges and currents is impossible due to the sheer number and complexity of the equations involved. Despite this, the interaction between light and matter at the macroscopic level is encapsulated by the comparatively simple dielectric functions.

The focus of this thesis is the electric susceptibility, which describes the relation between an applied electric field $\boldsymbol{E}$ and the induced polarization field $\boldsymbol{P}$ of a medium. It must be stressed that in this context, both of these quantities are macroscopic averages [1]. For example, $\boldsymbol{P}(\boldsymbol{r}, t)$ is the average value of the various atomic and molecular dipole moments in a region that is large in comparison to the atomic or lattice dimensions surrounding $\boldsymbol{r}$ at time t. For this reason, the macroscopic dielectric functions are not valid down to atomic scales.

2.1.1 Temporal nonlocality

The response of a medium to an applied field is not instantaneous. For any given point in a medium, the induced polarization field at any time depends on the history of the electric field. This relationship is therefore nonlocal in time and described by [1] :

$$P_i(\boldsymbol{r}, t) = \varepsilon_0 \int_{-\infty}^{t} dt' \sum_{j=x,y,z} \chi_{ij}(\boldsymbol{r}, t - t') E_j(\boldsymbol{r}, t'), \tag{2.1}$$

where ε_0 is the permittivity of free space and the electric susceptibility χ_{ij} is, in general, a tensor of rank two. It is convenient to perform a Fourier transformation on Eq. (2.1) using (1):

$$P_i(\boldsymbol{r}, \omega) = \varepsilon_0 \sum_{j} \chi_{ij}(\boldsymbol{r}, \omega) E_j(\boldsymbol{r}, \omega). \tag{2.2}$$

The dependence of the susceptibility on the frequency ω is known as *temporal dispersion*, or just simply *dispersion*.

Almost all crystals are anisotropic at the microscopic level. If χ_{ij} is symmetric, the correct choice of co-ordinates can bring the susceptibility to diagonal form [26] , with a component for each principal direction in the crystal. Those with three (biaxial crystals) or two (uniaxial crystals) unique χ_{ij} components must be described by a tensor susceptibility. Cubic crystals, with three identical components of the diagonalized susceptibility, are no different from isotropic bodies and can be described by the scalar susceptibility.

2.1.2 Spatial nonlocality

The assumption made so far, that $\boldsymbol{P}$ only depends on $\boldsymbol{E}$ at the same point in space, is not always valid. In general, it also depends on the field in the surrounding region [26]. The material response to an electromagnetic field is therefore nonlocal in both time and space. Subsequent references to *local* or *non-local* will therefore refer to *spatial* locality or nonlocality.

Rudkadze and Silin [27] provide an excellent overview of electrodynamics in nonlocal media and several of their key points are repeated here. With the inclusion of spatial nonlocality, the induced polarization now takes the form:

$$P_i(\boldsymbol{r},t) = \varepsilon_0 \int_{-\infty}^{t} dt' \int d^3\boldsymbol{r}' \sum_j \chi_{ij}(\boldsymbol{r},\boldsymbol{r}',t-t')E_j(\boldsymbol{r}',t'). \tag{2.3}$$

In a homogeneous, isotropic medium the susceptibility depends only on the difference $|\boldsymbol{r}-\boldsymbol{r}'|$. In this case, a Fourier transformation of (2.3) can be made both in space and time using (1) and (2) to give:

$$P_i(\boldsymbol{k},\omega) = \varepsilon_0 \sum_j \chi_{ij}(\boldsymbol{k},\omega)E_j(\boldsymbol{k},\omega). \tag{2.4}$$

The dependence of the susceptibility on the wave vector $\boldsymbol{k}$ is known as spatial dispersion.

With the inclusion of spatial dispersion, the electric susceptibility can be described by a tensor, even in an isotropic medium, as a distinctive direction is generated by the wave vector $\boldsymbol{k}$. In a homogeneous, isotropic, non-gyroscopic (i.e. it has a centre of symmetry) medium [26]:

$$\chi_{ij}(\boldsymbol{k},\omega) = \delta_{ij}\chi_\perp(k,\omega) + \frac{k_i k_j}{k^2}\left[\chi_\parallel(k,\omega) - \chi_\perp(k,\omega)\right], \tag{2.5}$$

where $\chi_\perp$ and $\chi_\parallel$ are the transverse and longitudinal susceptibilities, which apply to the components of the field $\boldsymbol{E}$ perpendicular and parallel to $\boldsymbol{k}$ respectively. This general form has frequently been overlooked in the past, with many authors simply setting $\chi_\perp = \chi_\parallel$ to return to a scalar susceptibility.

The importance of spatial dispersion in the dielectric depends on the medium in question. In conducting media, the motion of free charge carriers may lead to nonlocal behaviour at large distances. If the length scales $|\boldsymbol{r}-\boldsymbol{r}'|$ where χ_{ij} is nonzero are large in comparison to the wavelength of light in the medium, spatial dispersion will affect the behaviour of the macroscopic fields [26].

In contrast, the nonlocal susceptibility in most dielectrics rapidly decreases for distances $|\boldsymbol{r} - \boldsymbol{r}'|$ that are large in comparison to the lattice dimensions. Because the macroscopic fields are averaged over volume elements much larger than atomic scales, the local susceptibility can often provide an adequate approximation of the system [26]. As a result, spatial dispersion is often overlooked in calculations in favour of temporal dispersion. However, there are some circumstances where nonlocal behaviour must be included for accurate results. The second half of this thesis looks at one such case – the calculation of the electromagnetic reflection and transmission coefficients at planar boundaries. The small changes to the susceptibility are shown to have large consequences, leading to drastically different behaviour compared to the local model.

2.1.3 Properties of the electric susceptibility

The electric susceptibility is subject to a number of constraints [1]. As $\boldsymbol{P}(\boldsymbol{r}, t)$ and $\boldsymbol{E}(\boldsymbol{r}, t)$ are both real vector fields, $\chi_{ij}(\boldsymbol{r}, t)$ must also be real. This imposes certain symmetry conditions on the complex Fourier transformation of the susceptibility in (2.4):

$$\chi^*_{ij}(\boldsymbol{k}, \omega) = \chi_{ij}(-\boldsymbol{k}, -\omega). \tag{2.6}$$

Futhermore, if the system exhibits time-reversal symmetry then

$$\chi_{ij}(\boldsymbol{k}, \omega) = \chi_{ji}(-\boldsymbol{k}, \omega). \tag{2.7}$$

The tensor susceptibility in (2.5) satisfies both of these conditions. In each of the limits $\omega \to \infty$ and $k \to \infty$, the susceptibility must tend to zero, as the field varies either too rapidly or at scales too small for the medium to respond. In the $k \to 0$ limit, the tensor susceptibility (2.5) should tend to $\chi(\omega)\delta_{ij}$, which does not depend on the direction of $\mathbf{k}$. This implies that:

$$\chi_\perp(0, \omega) = \chi_\parallel(0, \omega) = \chi(\omega), \tag{2.8}$$

which will be important when defining expressions for $\chi_{\perp/\parallel}$.

The casual nature of (2.3) means that $\chi_{ij}(\boldsymbol{k}, \omega)$ is analytic in the upper half ω plane. The real and imaginary components of the susceptibility are therefore connected by the Kramers-Kronig relations [6, 7] for every value of $\boldsymbol{k}$:

$$\begin{aligned}
\mathbb{R}\mathrm{e}\left[\chi_{\perp/\parallel}(k, \omega)\right] =& \frac{2}{\pi} \int_0^\omega d\omega' \frac{\omega' \, \mathbb{I}\mathrm{m}\left[\chi_{\perp/\parallel}(k, \omega')\right]}{\omega'^2 - \omega^2}, \\
\mathbb{I}\mathrm{m}\left[\chi_{\perp/\parallel}(k, \omega)\right] =& -\frac{2\omega}{\pi} \int_0^\omega d\omega' \frac{\mathbb{R}\mathrm{e}\left[\chi_{\perp/\parallel}(k, \omega')\right]}{\omega'^2 - \omega^2}.
\end{aligned} \tag{2.9}$$

A key consequence of this is that $\mathbb{I}\mathrm{m}\left[\chi(k,\omega)\right]$, which describes the absorption of light by the medium, is present at all frequencies inside a medium. While this component may be considered small enough to ignore in some regimes, it is most important near the resonant frequencies of a material. The physical origin of this imaginary term, and how it emerges from the choice of dielectric model, is the focus of the first half of this thesis and is discussed in greater depth in section 2.2.

A similar function, the magnetic susceptibility, describes the relationship between an applied magnetic field $\boldsymbol{H}$ and the induced magnetization of a medium $\boldsymbol{M}$. While this thesis only deals with non-magnetic materials, the inclusion of spatial dispersion leads an interesting relationship between the dielectric functions. As the electric and magnetic fields are directly related by Maxwell's equations, there is some ambiguity between the electric and magnetic susceptibilities. Indeed, it has been shown [27] that the two tensor susceptibilities cannot be independent and that the expression in (2.4) is also completely equivalent to a scalar electric and magnetic susceptibility. In the absence of spatial dispersion, the local nature of the $\boldsymbol{P}$ response to $\boldsymbol{E}$ imposes the separation of the electric and magnetic susceptibilities, but this is not unique in general. It is therefore convenient to set $\boldsymbol{M}$ and the magnetic susceptibility to zero to simplify calculations.

2.1.4 The electromagnetic wave equation

In a medium, the macroscopic fields $\boldsymbol{E}$ and $\boldsymbol{H}$ must obey Maxwell's equations [1] :

$$\begin{aligned} \boldsymbol{\nabla}\cdot\boldsymbol{D} &= \rho_f, & \boldsymbol{\nabla}\cdot\boldsymbol{B} &= 0, \\ \boldsymbol{\nabla}\times\boldsymbol{E} &= -\,\partial_t\boldsymbol{B}, & \boldsymbol{\nabla}\times\boldsymbol{H} &= \boldsymbol{J}_f + \partial_t\boldsymbol{D}. \end{aligned} \tag{2.10}$$

Throughout this thesis, the free charge ρ_f and free current $\boldsymbol{J}_f$ densities are taken to equal zero. The displacement field $\boldsymbol{D}$ is defined in terms of the electric field $\boldsymbol{E}$ and the polarization field $\boldsymbol{P}$ of the medium:

$$\boldsymbol{D}(\boldsymbol{r},t) = \varepsilon_0\boldsymbol{E}(\boldsymbol{r},t) + \boldsymbol{P}(\boldsymbol{r},t). \tag{2.11}$$

A similar expression relates $\boldsymbol{H}$ to the magnetic induction $\boldsymbol{B}$ and the induced magnetization of the medium $\boldsymbol{M}$. As previously stated, this work only considers non-magnetic media where the magnetic susceptibility is set to zero. As a result:

$$\boldsymbol{H}(\boldsymbol{r},t) = \frac{1}{\mu_0}\boldsymbol{B}(\boldsymbol{r},t), \tag{2.12}$$

where μ_0 is the permeability of free space and $\mu_0\varepsilon_0 = 1/c^2$.

A wave equation can be derived by combining Maxwell's equations. This must be obeyed by the electromagnetic field at every point in space and plays a central role throughout each subsequent chapter. After a Fourier transform in time using (1), it can be expressed in terms of $\boldsymbol{E}$ and $\boldsymbol{P}$:

$$\boldsymbol{\nabla} \times \boldsymbol{\nabla} \times \boldsymbol{E}(\boldsymbol{r},\omega) - \frac{\omega^2}{c^2}\boldsymbol{E}(\boldsymbol{r},\omega) = \frac{\omega^2}{c^2}\frac{1}{\varepsilon_0}\boldsymbol{P}(\boldsymbol{r},\omega). \tag{2.13}$$

As described in section 2.1.1 and 2.1.2, $\boldsymbol{P}$ can be expressed in terms of the electric field, leaving an equation solely in terms of $\boldsymbol{E}$. After another Fourier transform in $\boldsymbol{r}$, the wave equation in an unbounded, homogeneous medium is

$$\boldsymbol{k} \times \boldsymbol{k} \times \boldsymbol{E}(\boldsymbol{k},\omega) + \left(\frac{\omega}{c}\right)^2 \left[1 + \underline{\boldsymbol{\chi}}(\boldsymbol{k},\omega)\right] \boldsymbol{E}(\boldsymbol{k},\omega) = 0 \tag{2.14}$$

in the linear regime. Nonlinear susceptibility terms would lead to higher powers of $\boldsymbol{E}$.

The wave equation (2.14) has solutions for $\boldsymbol{E}$ when the frequency and wave vector satisfy the dispersion relation. For an arbitrary tensor susceptibility, one must solve the equation [27]

$$\left|k^2\delta_{ij} - k_i k_j - (\omega/c)^2 \left[\delta_{ij} + \chi_{ij}(\boldsymbol{k},\omega)\right]\right| = 0, \tag{2.15}$$

where the vector identity

$$\boldsymbol{k} \times \boldsymbol{k} \times \boldsymbol{E}(\boldsymbol{k},\omega) = \boldsymbol{k}\left[\boldsymbol{k} \cdot \boldsymbol{E}(\boldsymbol{k},\omega)\right] - k^2\boldsymbol{E}(\boldsymbol{k},\omega) \tag{2.16}$$

has been used. However, for the general form of the nonlocal susceptibility in (2.5) describing a homogeneous, isotropic, non-gyroscopic medium, (2.16) reduces to two simpler equations. The first is for transverse waves with $\boldsymbol{k} \cdot \boldsymbol{E} = 0$, which must satisfy:

$$k_0^2\left[1 + \chi_\perp(\boldsymbol{k},\omega)\right] = k^2, \tag{2.17}$$

where $k_0 = \omega/c$. The electric and magnetic fields of transverse waves are perpendicular to both each other and the wave vector, as shown in Fig. 2.1. In a local medium there is only one solution ($k = k_0\sqrt{1+\chi(\omega)}$) to the dispersion relation for a given ω. In a nonlocal medium, the k dependence of χ leads to the possibility of additional solutions to (2.17). The presence of multiple waves inside a medium with the same frequency but different k is key result of spatial dispersion.

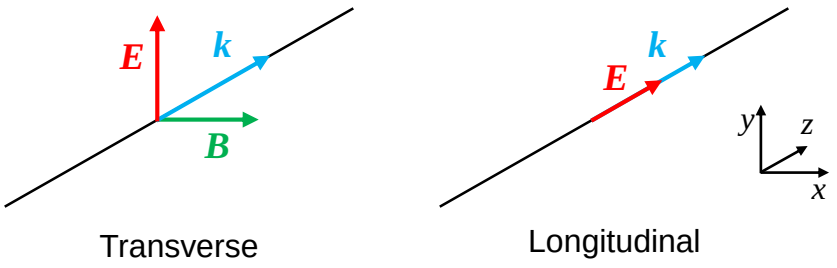

Figure 2.1: Comparison between transverse and longitudinal waves in an isotropic medium. The longitudinal wave has no magnetic field.

The second dispersion relation is for longitudinal waves, with $\boldsymbol{k} \times \boldsymbol{E} = 0$. These must satisfy:

$$1 + \chi_{\parallel}(\boldsymbol{k}, \omega) = 0. \tag{2.18}$$

As the electric field is parallel to the wave vector, Maxwell's equations mean that these waves have no associated magnetic field. These waves are less well-known in comparison to their transverse counterparts and are sometimes overlooked in calculations. In a local medium, longitudinal waves have zero group velocity and therefore do not carry energy. It is only when spatial dispersion is included that the frequency depends on $\boldsymbol{k}$ and energy propagates through the medium.

As with (2.17), there is a possibility for multiple solutions to the longitudinal dispersion relation (2.18). The presence of these additional transverse and longitudinal waves leads to difficulties in the calculations of physical phenomena. These problems, and their various historic solutions, form the basis of the second half of this thesis and are discussed in greater depth in section 2.3.

2.1.5 The Lorentz model

Everything up to this point has been in terms of a generic linear susceptibility. This section considers the specific case of the Lorentz model, which is widely used to describe the electromagnetic response of dielectrics. The fitting and optimisation of Lorentz model parameters to experimental data is an ongoing area of research, with continuous improvements being made to provide a closer fit to observations [83, 84]. Given its widespread usage, the benefits of improving calculations involving the Lorentz model are readily apparent.

The Lorentz model was derived by treating the electrons in a dielectric as damped oscillators that are harmonically bound to their parent nuclei. When subject to an applied electric field, the resulting displacement between electrons and nuclei leads to an electric dipole moment for each atom. Collectively, these correspond to the macroscopic polarization field, from which an electric susceptibility for the medium can be found. While the derivation is valid only for rarefied material, the resulting expression has proven to be equally applicable to dense materials such as crystals [85]. This treatment of a dielectric as a lattice of electric dipoles that respond to an applied electromagnetic field is widespread [2] and will be used throughout this thesis.

The general expression for the local Lorentz model is given by:

$$\chi(\omega) = \chi_0 + \sum_{m=1}^{M} \frac{\omega_{pm}^2}{\omega_{Tm}^2 - \omega^2 - i\gamma_m\omega}, \tag{2.19}$$

where ω_T is the resonant frequency of a transition in the medium, γ quantifies the absorption (or damping) and ω_p describes the strength of the resonance. The term χ_0 collects the contributions from other resonances not explicitly included in the model, and acts as a background susceptibility. While a more complete model would dispense with this term by including additional resonance terms, it is often sufficient to treat it as a constant. In general, the expression in (2.19) can also be used to describe the response of free electrons in a metal. Setting the resonant frequency, which corresponds to the binding force of the electrons, equal to zero gives the Drude model of the susceptibility.

The Lorentz model is analytic in the upper half-plane of complex ω and therefore obeys the Kramers-Kronig relations in section 2.1.3. Figure 2.2 compares the real and imaginary components of the susceptibility as a function of frequency. While the imaginary component is present for all ω, it is most important in the vicinity of the resonant frequency.

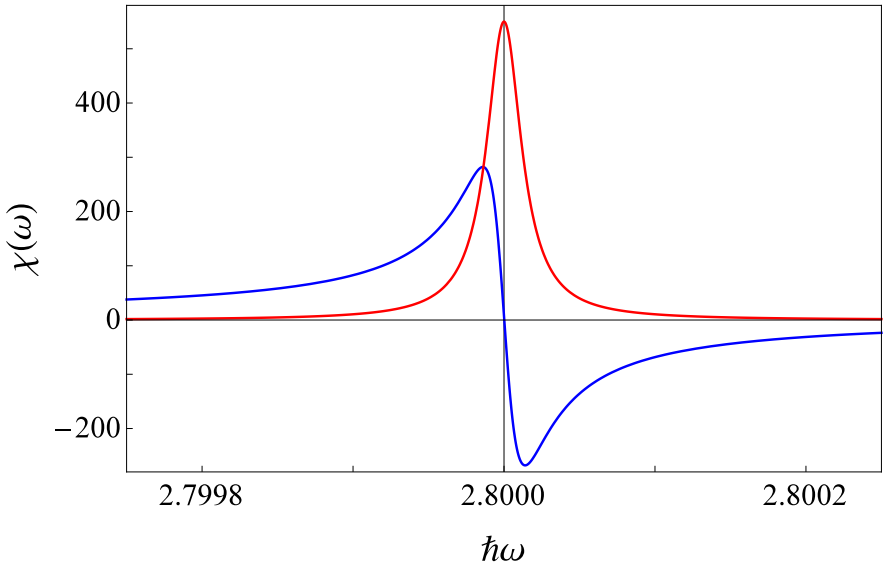

Figure 2.2: Comparison between the real (blue) and imaginary (red) parts of a single resonance in the Lorentz model of ZnSe. Model parameters used are $\chi_0 = 8.1$, $\hbar\omega_T = 2.8$eV, $\hbar\omega_p = 0.208$eV and $\hbar\gamma = 2.8 \times 10^{-5}$eV.

Figure 2.3 shows the dispersion relations for transverse electric waves that satisfy (2.17) in a medium described by a local single-resonance Lorentz model. In the absence of damping, each resonance leads to an ω gap in the dispersion relation. While the lower branch approaches the resonant frequency ω_T as $k \to \infty$, the upper branch minima are given by ω_L, which are the solutions of (2.17) at $k = 0$ in the absence of damping. In a single-resonance susceptibility this is defined as:

$$\omega_L^2 = \omega_T^2 + \frac{\omega_p^2}{1 + \chi_0}. \tag{2.20}$$

It is often ω_L that is measured in experiments [60], with ω_p calculated using (2.20). In the presence of damping, k is complex-valued for all real ω, with the largest differences in behaviour found in the bandgap region between ω_T and ω_L.

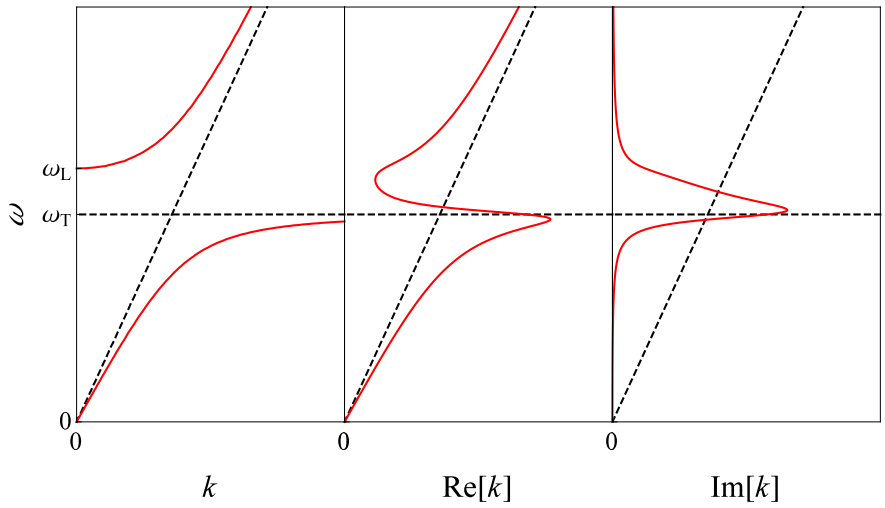

Figure 2.3: Solutions (not to scale) of the transverse wave dispersion relation (2.17) (red solid lines) for purely real ω using a single-resonance Lorentz model (2.19) with (centre, right) and without (left) the damping term γ. Note that k solutions are complex when γ is present. The minimum value of the upper branch in the undamped case at $k = 0$ is denoted ω_L and defined in (2.20). Dashed lines indicate the solutions to $k^2 = (\omega/c)^2(1 + \chi_0)$ (i.e. $\boldsymbol{E}$ in the medium without the resonance) and $\omega = \omega_T$.

In general, the parameters of the Lorentz model are also wave vector dependent. The k-dependence of ω_p does not introduce any significant differences to the local model and the k-dependence of γ is typically small enough to be ignored [86] . However, the presence of spatial dispersion in $\omega_T(k)$ has several far-reaching consequences. These are the focus of the second half of this thesis and are discussed in greater depth in section 2.3.

2.1.6 Excitons

Each resonance in the Lorentz model is associated with a transition in the medium with frequency $\omega_T(k)$. The nature of the k-dependence is determined by the physical parameters of the material and the type of transition. While this thesis focuses on excitonic transitions, the calculations presented in subsequent chapters are not specific to them and could be applied to other excitations, such as phonons.

When light is incident on a semiconductor or insulator, it can excite an electron in the valence band to the conduction band. An exciton is a bound state between an excited electron and a positively charged hole left behind in the valence band. First introduced in

the tight-binding limit by Frenkel in 1931 [57, 58], and later in the weak-binding limit by Wannier in 1937 [87], excitons are typically the lowest-energy excited states of insulating media and often have energies in the visible spectrum of light. A full description of excitons in crystals is beyond the scope of this thesis. Instead, the key results that will be used in subsequent chapters are presented here. For detailed derivations the reader is referred to the wealth of literature on the subject, in particular the work of Kane [59] and the review of Hönerlage *et al*. [60].

The exciton dispersion relations are determined by the structure, symmetries and degeneracies of the valence and conduction bands of a crystal [60]. When combined, these can lead to a large number of interacting exciton bands, each with their own resonance in the Lorentz model. In an ideal case of an isotropic medium with simple parabolic valence and conduction bands, the dispersion relation of an exciton band is:

$$\hbar\omega_T(\boldsymbol{k}) = \hbar\omega_T + \frac{\hbar^2 k^2}{2m_{\mathrm{ex}}}, \tag{2.21}$$

where $m_{\mathrm{ex}} = m_{\mathrm{el}} + m_{\mathrm{ho}}$ is the mass of the exciton and $m_{\mathrm{el/ho}}$ are electron and hole masses, respectively. Real materials exhibit more complex behaviour than this idealized case. If the valence band maximum is degenerate and there is a difference in hole masses, there are "heavy" and "light" excitons, with masses m_h and m_l [59]. While the definition of the exciton mass is slightly modified, the overall form of the dispersion relations remains the same as (2.21) and are degenerate at $k = 0$:

$$\hbar\omega_T^{(h)}(\boldsymbol{k}) = \hbar\omega_T + \frac{\hbar^2 k^2}{2m_h}, \qquad \hbar\omega_T^{(l)}(\boldsymbol{k}) = \hbar\omega_T + \frac{\hbar^2 k^2}{2m_l}. \tag{2.22}$$

Anisotropy can lead to exciton dispersion relations with additional k terms compared to (2.21). Uniaxial crystals, such as zincblende and wurtzite, are a notable example of this behaviour [64–66, 71–73]. The symmetry of these systems can lead to two exciton bands with a linear k term that are degenerate at $k = 0$:

$$\hbar\omega_T^{(\pm)}(\boldsymbol{k}) = \hbar\omega_T + \frac{\hbar^2 k_\perp^2}{2m_\perp} + \frac{\hbar^2 k_\parallel^2}{2m_\parallel} \pm \zeta k_\perp. \tag{2.23}$$

The inversion symmetry of the system is preserved with the inclusion of both $+$ and $-$ bands. Due to the anisotropy of the crystal, a distinction must be made between the wave vector components that are parallel or perpendicular to the crystal axis $\boldsymbol{c}$, denoted with the $\perp$ / $\parallel$ subscript.

In each case, $\omega_T(k)$ can be used to find an expression for the susceptibility. The simplest case is that of the isolated exciton band of the form (2.21). Upon substitution into the Lorentz model, only the k^2 term in the denominator is retained, giving:

$$\chi(\boldsymbol{k},\omega) = \chi_0 + \frac{\omega_p^2}{(\omega_T^2 + Dk^2) - \omega^2 - i\gamma\omega}, \tag{2.24}$$

where the contributions from the other exciton band resonances have been collected into χ_0. The higher order k terms in the denominator are omitted as they are considered to be small in comparison. By comparing (2.24) and (2.21) it can be seen that $D = \hbar\omega_T/m_{\mathrm{ex}}$.

The examples presented here are but a small selection from the wide range of behaviour found in exciton dispersion relations. It is therefore apparent that a generalized approach to calculations involving excitons is preferable, rather than treating every individual case separately.

2.2 Absorption in dielectrics

The widely used Lorentz susceptibility model (2.19) in section 2.1 was based on a simple argument treating a dielectric as a collection of polarizable particles described by a damped harmonic oscillator. It has been used extensively to successfully describe the electromagnetic response of a wide range of materials [85]. However, it becomes difficult to justify such a treatment with a more realistic model of a dielectric. The root of these problems lies in the damping term γ (responsible for broadband absorption) naturally emerging from the model. It is well known that dissipative behaviour leads to difficulties in general when writing a Lagrangian for such a system [2]. As a result, the damping term is usually added "by hand" at a point during calculations.

2.2.1 The Hopfield model

This problem can be traced back to a 1958 paper by Hopfield [2], in which he studied the relationship between a microscopic model of a polarizable medium interacting with the electromagnetic field and the effective description of such a system by a susceptibility. Hopfield's microscopic model consisted of non-interacting excitons in a medium linearly coupled to the photons of the electromagnetic field. This was compared to a classical model of a dielectric, represented by an oscillating polarization density $\boldsymbol{P}$ linearly coupled to the electromagnetic field. By quantizing the Lagrangians of the two systems and comparing the resulting equations of motion, it was shown that the microscopic system could be represented by an electromagnetic field linearly coupled to a quantized set of classical polarization fields, with one for each exciton band that interacted with radiation.

Hopfield noticed a key problem with both of these models. For the sake of simplicity, only the classical model is presented here. The Lagrangian density of the system is split into three parts:

$$\begin{aligned}\mathcal{L} = \quad & \frac{1}{2}\left[\varepsilon_0 \left(\partial_t \boldsymbol{A} + \boldsymbol{\nabla}\varphi\right)^2 - \frac{1}{\mu_0}\left(\boldsymbol{\nabla}\times\boldsymbol{A}\right)^2\right] \\ & + \frac{1}{2\varepsilon_0\beta}\left[(\partial_t \boldsymbol{P})^2 - \omega_0^2 \boldsymbol{P}^2\right] \\ & + \left[\varphi(\boldsymbol{\nabla}\cdot\boldsymbol{P}) + \boldsymbol{A}\cdot\partial_t\boldsymbol{P}\right], \end{aligned} \tag{2.25}$$

where the first line describes the electromagnetic field in terms of the vector ($\boldsymbol{A}$) and scalar (φ) potential , the second contains the polarization field and the final line contains the linear coupling term between the two. Using the definitions $\boldsymbol{E} = -\boldsymbol{\nabla}\varphi - \partial_t \boldsymbol{A}$ and

$\boldsymbol{B} = \boldsymbol{\nabla} \times \boldsymbol{A}$ [1], the Euler-Lagrange equations of motion for (2.25) were found to be equivalent to Maxwell's equations in (2.10) and the additional relation:

$$\partial_t^2 \boldsymbol{P}(\boldsymbol{r}, t) + \omega_0^2 \boldsymbol{P}(\boldsymbol{r}, t) = \varepsilon_0 \beta \boldsymbol{E}(\boldsymbol{r}, t). \tag{2.26}$$

After a Fourier transform in time, (2.26) can be rearranged to the form:

$$\boldsymbol{P}(\boldsymbol{r}, \omega) = G_P(\boldsymbol{r}, \omega)\boldsymbol{E}(\boldsymbol{r}, \omega) = \varepsilon_0 \frac{\beta}{\omega_0^2 - (\omega + i0^+)^2} \boldsymbol{E}(\boldsymbol{r}, \omega), \tag{2.27}$$

where G_p is the Green function of the polarization field and 0^+ is an infinitesimally small term used to account for the causal response of the system, shifting the pole into the lower half plane of complex ω to satisfy the Kramers-Kronig relations. By comparing (2.27) to the definition in (2.2), it can be seen that the electric susceptibility is directly analogous to the Green function of the polarization field, describing the propagation of the field in time. This treatment of the susceptibility as a Green function can be taken a step farther by considering (2.24). Here, $\chi(k, \omega)$ can be thought of as the Green function of the exciton, describing its propagation through the crystal in both space and time. This concept will be touched upon again in 2.3.4 and used throughout this thesis.

The electromagnetic response of the Hopfield model was therefore described by the Lorentz susceptibility, but with the key omission of the damping term γ. By using the identity:

$$\frac{1}{\omega_0^2 - (\omega + i0^+)^2} = \mathbb{P}\frac{1}{\omega_0^2 - \omega^2} + \frac{i\pi}{2\omega}\left[\delta(\omega - \omega_0) - \delta(\omega + \omega_0)\right], \tag{2.28}$$

where $\mathbb{P}$ denotes the principle-valued part, it could be seen that absorption was only present in the medium at the resonant frequency ω_0. This is in direct contrast to the broadband absorption found in real materials. Even the inclusion of an exciton-exciton interaction term to the Lagrangian of the corresponding microscopic model did not solve this problem.

Hopfield stated that the solution to this issue lay in the modes of the crystal that were not directly coupled to light and had been omitted in his original model. This idea had previously been proposed by other authors (see [88] for example), but Hopfield identified the *type* of coupling as the critical component responsible for broadband absorption. The linear interaction term in (2.25) leads to coupling between single modes of the EM field and the medium due to wave vector conservation. This could be seen by performing a spatial Fourier transform on (2.27), and seeing that $\boldsymbol{P}$ is coupled to $\boldsymbol{E}$ only for same $(\boldsymbol{k}, \omega)$ mode. In terms of second order perturbation theory, the $\mathrm{photon} \rightarrow \mathrm{exciton}$ process

did not have a density of final states at energies other than $\hbar\omega_0$. As a result, no real transitions occurred and energy simply oscillated back and forth between the field and the medium. Broadband absorption therefore requires a process with an energy continuum of final states, allowing real transitions for a range of frequencies.

There have been various approaches to including this behaviour into a dielectric model. Hopfield proposed many-body interactions as a solution to this problem [2]. These provided a way to transfer energy between modes with different $\boldsymbol{k}$ while conserving the total wave vector of the system. Furthermore, each process had an energy continuum of final states, giving the possibility of real transitions if the energy of the initial state overlapped this continuum. Energy was therefore not absorbed by states directly coupled to the electromagnetic field, but in the indirectly coupled crystal states. Hopfield suggested a range of processes, highlighting the $\mathrm{exciton} \rightarrow \mathrm{exciton}' + \mathrm{phonon}$ process in particular, which he claimed would lead to an effective damping term to (2.27) when included in his model. However, Hopfield states this result without providing any supporting calculations, instead relying on a heuristic argument.

The inclusion of nonlinear interactions was recently considered in a paper that extended the Hopfield model to inhomogeneous media [89]. However, thier work focused on the resulting nonlinear susceptibilty terms rather than the effect on the linear susceptibility. Other authors have followed Hopfield's suggestion in the quantum regime [9–13], with excitons nonlinearly coupled to lattice phonons. While this interaction was found to provide an effective damping term to the equations of motion, a full analysis in the quantum setting is very challenging. Part of the appeal of Hopfield's proposal is that it can be carried out classically, much like the textbook derivations [1] of the macroscopic Maxwell equations.

2.2.2 The phenomenological reservoir

An alternative solution to the problem of absorption has been to include coupling to a continuum in a phenomenological manner. An example of this is the reservoir - a collection of harmonic oscillators of various frequencies representing the additional modes of a medium into which the electromagnetic energy can dissipate. One of the more attractive features of this approach is that linear coupling can be used between the reservoir and the rest of the medium, which is comparatively simpler than the nonlinear coupling in Hopfield's proposal.

An early example of the reservoir can be seen in a paper by Fano [90]. He started

with a similar system to the Hopfield model, consisting of of harmonic oscillators with resonant frequency ω_n linearly coupled to a field. After encountering the same problem of absorption, his solution was to couple each oscillator to an infinite number of additional oscillators with $\omega_{n\nu}^2 = \omega_n^2 + \nu\delta$, where ν runs from $-\infty$ to ∞. After approximating the discrete spectrum of the reservoir as a continuum, Fano recovered a susceptibility similar to the Lorentz model with a nonzero damping term γ and broadband absorption.

Despite the obvious differences to his proposal, Hopfield used this as a justification for the introduction of a damping term via many-body interactions. Subsequent work on discrete reservoirs [24] has shown that recovering the widely used damped harmonic oscillator behaviour often requires a set of extremely contrived set of assumptions about the reservoir. A set of restrictions must be placed on both the spacing of the reservoir oscillator frequencies and the interaction strength with the rest of the model. In his paper, Tatarskiĭ highlighted the case where the ratio of each reservoir frequency must be a rational number, and the coupling strength must lie on a Lorentzian resonant curve based on the corresponding frequency.

The discrete reservoir is therefore of questionable use as a representation of the physics in a real medium. Its role as a purely phenomenological description of absorption is further reinforced by the wide range of materials that can accurately described by the Lorentz model. It is unlikely that the highly specific reservoir conditions can be simultaneously satisfied by such a broad range of materials.

In 1992, Huttner and Barnett [3] used a continuous reservoir coupled to the Hopfield model, as shown in Fig. 2.4. Each mode of the polarization field was linearly coupled to a continuum of reservoir modes of every frequency, which in turn provided the required density of final states for absorption. The corresponding susceptibility expression was given in terms of the frequency dependent coupling function between the polarization field and the reservoir. While there were also restrictions on this coupling function, they were not as strict as those of the discrete reservoir. This model has been subsequently improved to incorporate features such as inhomogeneity [14, 15], spatial dispersion [16] and magnetic response [17–20].

The continuum reservoir has proven to be a powerful tool in incorporating dissipative behaviour in a Lagrangian, while retaining the relative simplicity of linear coupling in calculations. It has been used to give a Lagrangian formalism of the Maxwell equations for an arbitrary susceptibility, even when directly coupled to the electromagnetic field, removing the need for the polarization field [21, 22] . More generally, it has been applied

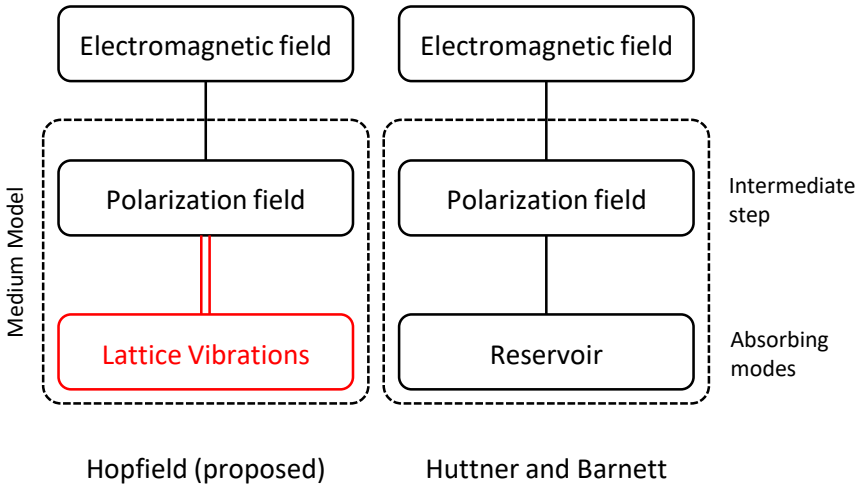

Figure 2.4: Comparison between the Hopfield model (left), with the proposed addition of nonlinear coupling between the harmonic polarization field and lattice vibrations, and the Huttner and Barnett model (right) with linear coupling to a continuum reservoir. In both cases the polarization field acts an intermediate step in the absorption process. The continuum of modes indirectly coupled to the electromagnetic field are responsible for the absorption of light.

to the damped harmonic oscillator [23] which formed the basis of the original Lorentz model derivation.

Despite the success of the reservoir, it is a phenomenological solution to the problem of absorption and remains an abstract mathematical tool without a detailed connection to the microscopic physics of a dielectric. The first aim of this thesis is to return to Hopfield's proposal and verify his claim that many-body interactions are responsible for absorption and lead to a damping term in the susceptibility. While this has been done before in the quantum setting, this calculation in chapter 3 is purely classical and demonstrates that quantum mechanical behaviour is not required for broadband absorption [25]. In doing so, the relationship between the widely used reservoir and the underlying microscopic model and physics of a real medium is clarified, showing that lattice vibrations can act as a "pseudo-reservoir" for the medium.

2.3 Reflection and transmission at planar boundaries

This section considers the behaviour of light at a planar interface between a vacuum and a medium, where the inclusion of spatial dispersion leads to several difficulties in the calculation of the electromagnetic reflection and transmission coefficients. These problems have historically been overcome through the use of additional boundary conditions (ABCs) on the polarization field at the boundary. Of particular interest is a generalized ABC model [4] that combines the work of several previous authors into a single formalism. The results and limitations of this model are outlined and potential improvements are identified to encompass many more of the features found in real materials. Finally, the applications of such a model beyond the calculation of electromagnetic reflection and transmission coefficients are described, highlighting the energy density of both the zero-point and thermal radiation of the electromagnetic field.

2.3.1 The local medium interface

To understand the difficulties caused by spatial dispersion at the vacuum/nonlocal medium interface, one must first consider the local medium. Figure 2.5 displays a schematic of a system where monochromatic light in one medium is incident on a planar interface with a second medium. The light is reflected back into the first medium and transmitted into the second. While the incident medium is taken to be a vacuum, subsequent derivations are also valid for a local medium with some slight changes.

The choice of co-ordinate system is made to simplify calculations. The plane of incidence is aligned with the xz-plane and the plane of the surface is aligned with the xy-plane. The wave vector of light is given by

$$\boldsymbol{k} = K\hat{\boldsymbol{x}} + 0\hat{\boldsymbol{y}} + q\hat{\boldsymbol{z}}, \tag{2.29}$$

where only the $\hat{\boldsymbol{z}}$ component differs between waves.

The electric field must satisfy the wave equation (2.13) at all points in space. There are two transverse wave solutions for a given ω and K in the $z < 0$ vacuum, corresponding to the incident ($\boldsymbol{E}_0$) and reflected wave ($\boldsymbol{E}_r$):

$$\begin{aligned} q_0 &= \quad \sqrt{k_0^2 - K^2} \\ q_r &= -\sqrt{k_0^2 - K^2} \end{aligned} \tag{2.30}$$

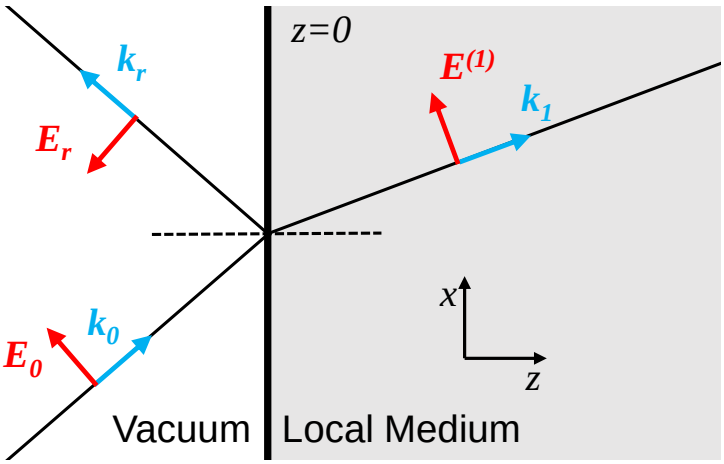

Figure 2.5: Schematic of reflection at the planar interface of a local medium. The coordinate system is chosen such that the xz-plane coincides with the plane of incidence and $k_y = 0$. The $z < 0$ vacuum half-space contains the incident wave $\boldsymbol{E}_0$ and the reflected wave $\boldsymbol{E}_r$, with the corresponding wave vectors $\boldsymbol{k}_0$ and $\boldsymbol{k}_r$. The $z > 0$ local medium contains the single transmitted wave $\boldsymbol{E}^{(1)}$ with wave vector $\boldsymbol{k}_1$.

Similarly, there are two transverse wave solutions in the $z > 0$ local medium described by $\chi(\omega)$. The $\mathbb{I}\mathrm{m}[q] < 0$ result is discarded as it diverges as $z \to \infty$, leaving a single transmitted wave ($\boldsymbol{E}^{(1)}$) with

$$q_1 = \sqrt{k_0^2[1 + \chi(\omega)] - K^2}, \qquad \mathbb{I}\mathrm{m}[q_1] > 0. \tag{2.31}$$

The overall electric field is given by:

$$\boldsymbol{E} = \begin{cases} \left(\boldsymbol{E}_0 e^{iq_0 z} + \boldsymbol{E}_r e^{iq_r z}\right) e^{iKx} e^{-i\omega t} & z < 0, \\ \left(\boldsymbol{E}^{(1)} e^{iq_1 z}\right) e^{iKx} e^{-i\omega t} & z > 0, \end{cases} \tag{2.32}$$

and the corresponding magnetic field is calculated using Maxwell's equations in (2.10).

The relationships between the various wave amplitudes are described by the reflection and transmission coefficients:

$$r = \frac{E_r}{E_0}, \qquad t^{(1)} = \frac{E^{(1)}}{E_0}. \tag{2.33}$$

These are found using the Maxwell boundary conditions [1], which impose the continuity of transverse ($\hat{\boldsymbol{x}}, \hat{\boldsymbol{y}}$) components of $\boldsymbol{E}$ and $\boldsymbol{H}$ and normal ($\hat{\boldsymbol{z}}$) components of $\boldsymbol{D}$ and $\boldsymbol{B}$ at the boundary. To simplify calculations, the electric field is split into two parts. The

s-polarization contains components that are perpendicular to the plane of incidence (E_y), while the p-polarization contains those that lie in the plane of incidence (E_x, E_z). These are also known as TM (transverse magnetic) and TE (transverse electric) polarizations. Each of these cases requires slightly different considerations in calculations.

The reflection coefficient for each polarization is expressed in terms of the surface impedance of the two media [44]:

$$r_s = \frac{Z_s(0^-) - Z_s(0^+)}{Z_s(0^-) + Z_s(0^+)} \tag{2.34}$$

$$r_p = \frac{Z_p(0^-) - Z_p(0^+)}{Z_p(0^-) + Z_p(0^+)} \tag{2.35}$$

where $0^\pm$ indicates the position either side of the $z = 0$ boundary. The surface impedances Z_s and Z_p are given by [44]:

$$Z_s = -\frac{E_y}{H_x} = -\frac{1}{\mu_0}\frac{E_y}{B_x} = \frac{k_0}{\mu_0}\frac{iE_y}{\partial_z E_y}, \tag{2.36}$$

$$Z_p = \frac{E_x}{H_y} = \frac{1}{\mu_0}\frac{E_x}{B_y} = \frac{k_0}{\mu_0}\frac{iE_x}{\partial_z E_x - \partial_x E_z}, \tag{2.37}$$

where $\boldsymbol{B}$ has been expressed in terms of $\boldsymbol{E}$ using the Maxwell equations (2.10) for a non-magnetic material. The results for the system in Fig. 2.5 are found by substituting (2.32) into (2.37) and (2.36). For the transverse waves in the $z < 0$ vacuum, these simplify to:

$$Z_s(0^-) = \frac{k_0}{\mu_0 q_0} = \frac{k_0}{\mu_0\sqrt{k_0^2 - K^2}}, \tag{2.38}$$

$$Z_p(0^-) = \frac{k_0 q_0}{\mu_0(q_0^2 + K^2)} = \frac{\sqrt{k_0^2 - K^2}}{\mu_0 k_0}. \tag{2.39}$$

Similarly, the single transverse wave in the $z > 0$ local medium gives:

$$Z_s(0^+) = \frac{k_0}{\mu_0 q_1} = \frac{k_0}{\mu_0\sqrt{k_0^2[1+\chi(\omega)] - K^2}}, \tag{2.40}$$

$$Z_p(0^+) = \frac{k_0 q_1}{\mu_0(q_1^2 + K^2)} = \frac{\sqrt{k_0^2[1+\chi(\omega)] - K^2}}{\mu_0 k_0[1+\chi(\omega)]}. \tag{2.41}$$

Substituting (2.38-2.41) into (2.34-2.35) gives the familiar Fresnel coefficients [1]:

$$r_s = \frac{\sqrt{k_0^2[1+\chi(\omega)] - K^2} - \sqrt{k_0^2 - K^2}}{\sqrt{k_0^2[1+\chi(\omega)] - K^2} + \sqrt{k_0^2 - K^2}}, \tag{2.42}$$

$$r_p = \frac{[1+\chi(\omega)]\sqrt{k_0^2 - K^2} - \sqrt{k_0^2[1+\chi(\omega)] - K^2}}{[1+\chi(\omega)]\sqrt{k_0^2 - K^2} + \sqrt{k_0^2[1+\chi(\omega)] - K^2}}. \tag{2.43}$$

Finally, by equating the transverse components of $\boldsymbol{E}$ at the boundary, the transmission coefficients can be derived for the s-polarization:

$$\begin{aligned} E_0 - E_r &= E_y^{(1)} \\ t_s &= 1 - r_s \end{aligned} \tag{2.44}$$

and p-polarization:

$$\begin{aligned} E_{0x} - E_{rx} &= E_x^{(1)} \\ t_p^{(1)} &= (1 - r_p)\frac{q_0\sqrt{q_1^2 + K^2}}{k_0 q_1} \end{aligned} \tag{2.45}$$

The problem of reflection and transmission at the vacuum/local medium interface can therefore be completely solved using only Maxwell's boundary conditions.

2.3.2 The nonlocal medium interface

Replacing the local medium occupying the $z > 0$ half-space with a nonlocal medium introduces difficulties to the derivation of the reflection and transmission coefficients. As described in chapter 2.1.4, spatial dispersion can lead to additional solutions of the electromagnetic dispersion relation for the bulk medium. In this section, the k-dependent susceptibility in (2.24) is used as an example to highlight the problems in the calculation. For the purposes of this calculation, the one-resonance Lorentz model is rewritten as:

$$\chi(K, 0, q) = \chi_0 + \frac{\omega_p^2/D}{q^2 - \Gamma^2}, \tag{2.46}$$

where

$$-\Gamma^2 = \frac{\omega_T^2 - \omega^2 - i\gamma\omega}{D} + K^2. \tag{2.47}$$

For this bulk medium there are two $\mathbb{I}\mathrm{m}[q] > 0$ solutions of the transverse dispersion relation:

$$\left[(1 + \chi_0)\, k_0^2 - K^2 - q^2\right]\left[\Gamma^2 - q^2\right] = k_0^2\omega_p^2/D, \tag{2.48}$$

for waves with $\boldsymbol{E} \perp \boldsymbol{k}$ and one solution of the longitudinal dispersion relation:

$$\left[\Gamma^2 - q^2\right] = \frac{\omega_p^2/D}{(1 + \chi_0)}, \tag{2.49}$$

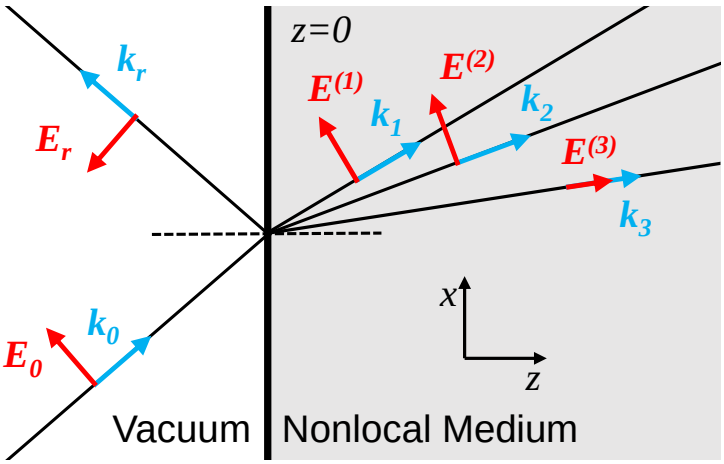

Figure 2.6: Schematic of reflection at the planar interface of a nonlocal medium. The coordinate system is chosen such that the xz-plane coincides with the plane of incidence and $k_y = 0$. The $z < 0$ vacuum half-space contains the incident wave $\boldsymbol{E}_0$ and the reflected wave $\boldsymbol{E}_r$, with the corresponding wave vectors $\boldsymbol{k}_0$ and $\boldsymbol{k}_r$. The $z > 0$ nonlocal medium contains two transverse waves $\boldsymbol{E}^{(1)}$ and $\boldsymbol{E}^{(2)}$ and one longitudinal wave $\boldsymbol{E}^{(3)}$, with the corresponding wave vectors $\boldsymbol{k}_1$, $\boldsymbol{k}_2$ and $\boldsymbol{k}_3$.

for waves with $\boldsymbol{E} \parallel \boldsymbol{k}$, giving a total of three waves. As $E_y = 0$ for all longitudinal waves, they do not contribute to s-polarization calculations.

In the half-infinite nonlocal medium, it is assumed that there are also three waves in the $z > 0$ region:

$$\boldsymbol{E} = \begin{cases} \left(\boldsymbol{E}_0 e^{iq_0 z} + \boldsymbol{E}_r e^{iq_r z}\right) e^{iKx} e^{-i\omega t} & z < 0, \\ \left(\boldsymbol{E}^{(1)} e^{iq_1 z} + \boldsymbol{E}^{(2)} e^{iq_2 z} + \boldsymbol{E}^{(3)} e^{iq_3 z}\right) e^{iKx} e^{-i\omega t} & z > 0, \end{cases} \tag{2.50}$$

where $\boldsymbol{E}^{(1)}$ and $\boldsymbol{E}^{(2)}$ are transverse and $\boldsymbol{E}^{(3)}$ is longitudinal. A schematic of the system is shown in Fig. 2.6. The presence of the boundary breaks the translational invariance of the system. The susceptibility is therefore spatially dependent, and while one would expect some authors to also consider the q_n values to be spatially dependent, only approaching the solutions of (2.48) and (2.49) in the $z \to \infty$ limit, most [33–56] considered them equal to the bulk result at all points within the medium. The correct choice of ansatz for the electric field is discussed in depth in chapter 4, but each case shares the same weakness in calculating the reflection coefficient.

If (2.50) is substituted into (2.36) or (2.37), the surface impedances of the nonlocal medium are found:

$$Z_s = \frac{k_0}{\mu_0}\frac{E_y^{(1)} + E_y^{(2)}}{q_1 E_y^{(1)} + q_2 E_y^{(2)}} = \frac{k_0}{\mu_0}\frac{1 + \frac{E_y^{(2)}}{E_y^{(1)}}}{q_1 + q_2\frac{E_y^{(2)}}{E_y^{(1)}}}, \tag{2.51}$$

$$Z_p = \frac{k_0}{\mu_0}\frac{E_x^{(1)} + E_x^{(2)} + E_x^{(3)}}{\frac{q_1^2+K^2}{q_1 k_0}E_x^{(1)} + \frac{q_2^2+K^2}{q_2 k_0}E_x^{(2)}} = \frac{k_0}{\mu_0}\frac{1 + \frac{E_x^{(2)}}{E_x^{(1)}} + \frac{E_x^{(3)}}{E_x^{(1)}}}{\frac{q_1^2+K^2}{q_1 k_0} + \frac{q_2^2+K^2}{q_2 k_0}\frac{E_x^{(2)}}{E_x^{(1)}}}, \tag{2.52}$$

where $E_z^{(n)}$ has been rewritten in terms of $E_x^{(n)}$ using simple trigonometry. Note that $E^{(3)}$ does not appear in (2.51), as it has no s-polarization component, or in the denominator of (2.52) as longitudinal waves do not have an associated magnetic field.

Unlike the local medium derivation, the field amplitudes in (2.51) and (2.52) do not cancel each other out, leaving a set of unknown field amplitude ratios. The Maxwell boundary conditions are therefore insufficient to calculate the reflection coefficients of a nonlocal medium. Extra information is required about the behaviour of the field inside the medium at the boundary.

2.3.3 Additional boundary conditions

The need for extra information was historically resolved with the introduction of additional boundary conditions (ABCs) on the behaviour of $\boldsymbol{\mathcal{P}}$, the polarization field associated with the resonance in the susceptibility. The exact nature of the ABC is usually determined based on the type of nonlocal medium being studied. Typically, each of these can be expressed in the general form [4]

$$\alpha_i \mathcal{P}_i(0^+) + \beta_i \partial_z \mathcal{P}_i(0^+) = 0, \tag{2.53}$$

where α_i and β_i may be frequency dependent.

The first and perhaps the most straightforward ABC was derived by Pekar [53–56] in 1958. In his model, the resonance in the susceptibility of the form (2.46) was due to Frenkel (tight-binding) excitons, typically found in molecular crystals. Considering only nearest-neighbour interactions and the symmetry of the system lead him to the conclusion that $\boldsymbol{\mathcal{P}} = 0$ at the boundary, corresponding to $\beta_i = 0$ in (2.53).

However, in his paper [55] Pekar mistakenly derived the conditions just outside, rather than inside, the boundary of the nonlocal medium. The details of this calculation and the

correct result for this system are presented in section 4.1. Despite this, the Pekar ABC can be used as an approximation to simplify calculations and remains the most commonly used ABC. Subsequent authors have presented many alternate ABCs, each derived under a set of assumptions that suit different types of material.

Some were derived starting from microscopic considerations of the system. Ting *et al.* [43] considered Wannier-Mott (weak binding) excitons, typically found in semiconductors, as the origin of the susceptibility resonance, finding $\partial_z \boldsymbol{\mathcal{P}}(0^+) = 0$. This corresponded to $\alpha_i = 0$ in (2.53) and is the second-most popular choice af ABC. Fuchs and Kliewer [44–47] considered the specular reflection of electrons on the interior surface of a metal by imaging the nonlocal medium to fill the $z < 0$ half-space and imposing symmetry conditions on the fields. This lead to alternate expressions for polarization wave components parallel ($\mathcal{P}_x$,$\mathcal{P}_y$) and normal ($\mathcal{P}_z$) to the planar surface, in particular $\partial_z \mathcal{P}_{x,y}(0^+) = 0$ and $\mathcal{P}_z(0^+) = 0$.

Other ABCs were found by starting with a desired behaviour and working backwards to find the ABC required for it to occur. Rimbey and Mahan [48–52] imposed the condition that only transverse waves were present inside the nonlocal medium. Using a similar approach to Fuchs and Kliewer they found that $\mathcal{P}_{x,y}(0^+) = 0$ and $\partial_z \mathcal{P}_z(0^+) = 0$ led to the complete absence of longitudinal waves. Agarwal *et al.* [33–42] derived their ABC under the assumption that any changes to the bulk susceptibility caused by the presence of the boundary were negligible, and could be ignored when considering bulk effects such as reflection and refraction.

Some authors have rejected the notion of ABCs entirely. In 1998 Henneberger [91] wrote a paper in which he described ABCs as a "historical mistake" and proposed an alternate approach. In it, the bulk expressions for the waves in the vacuum and the bulk medium are matched at the boundary provided that the region where surface effects are present is smaller than the wavelength. Excitations generated by the incident wave in the sub-surface layer of negligible width are then treated as the source of the transmitted waves. This paper was somewhat controversial [92, 93], but more importantly it was shown to be completely equivalent to the Ting *et al.* ABC. The ABC method has remained the dominant approach to solving the problem of reflection at the boundary of nonlocal media.

2.3.4 The generalized ABC model

Several of the authors proposing the various ABCs noted that they were equivalent to introducing an extra component to the susceptibility of the half-infinite nonlocal medium. An additional phenomenological scattering term in χ could be used to describe the behaviour of the medium at the boundary and was specific to each ABC. In 1984, Halevi and Fuchs [4] used this approach for the generalized ABC in (2.53) and developed a model applicable to the single-resonance scalar susceptibility in (2.46). This collected the work of all of the previous authors into a single, easy-to-use formalism to calculate the electromagnetic reflection coefficients.

Halevi and Fuchs defined the half-infinite susceptibility χ' in terms of the bulk expression. The presence of the boundary breaks the translational symmetry of the system. As a result, the susceptibility of the half-infinite medium is spatially-dependent. After a Fourier transform in the xy-plane, their expression took the form:

$$\chi_i'(K,0,z,z') = \begin{cases} \chi(K,0,z-z') + U_i\chi(K,0,z+z') & \text{if } z,z' > 0, \\ 0 & \text{otherwise.} \end{cases} \tag{2.54}$$

This could be understood by considering the susceptibility in terms of a Green function for $\boldsymbol{P}$, as described in section 2.2.1. The first part of (2.54) was the translation-invariant bulk response of the medium that described the propagation of a polarization wave from z' to z. The second term described a polarization wave traveling from z' to the boundary of the medium, before reflecting and continuing to z, as shown in Fig. 2.7. The U_i values phenomenologically described the reflection of the excitations by the surface. As previously mentioned, the behaviour of the polarization waves could differ for components transverse ($\hat{\boldsymbol{x}}, \hat{\boldsymbol{y}}$) and normal ($\hat{\boldsymbol{z}}$) to the surface, hence the dependence on $i \in \{x, y, z\}$. In general the U_i values are complex and dependent on K and ω, with $|U_i| = 1$ indicating perfect reflection.

The question of which ABC is "correct" for a given material is an open one. Either an ABC is chosen simply to get the best fit to experimental data, or it is chosen by comparing the assumptions made in the derivations to the type of medium in question. For a more detailed discussion regarding the comparison between expertimental and theoretical data, the reader is referred to the work of Halevi and Hernandez-Cocoletzi [94]. In their paper, they note that such comparisons often favour the Pekar ABC, as demonstrated in Fig. 2.8 for the model (2.54) in the scalar U case.

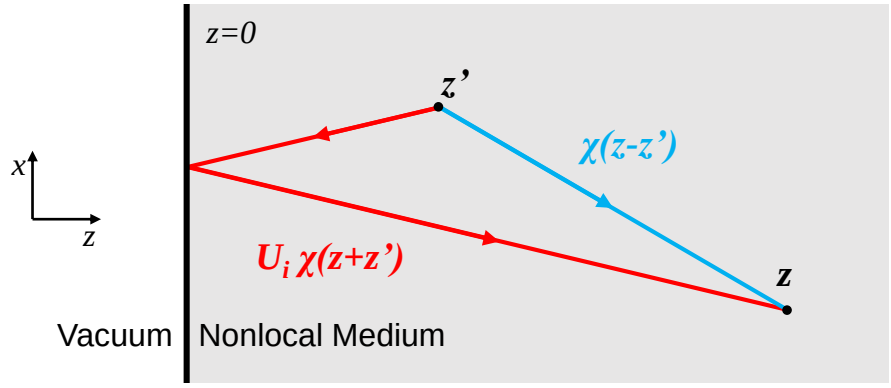

Figure 2.7: Schematic displaying the response at z due to an applied field at z' described by the nonlocal susceptibility (2.54) used by Halevi and Fuchs. The bulk response (blue) is spatially-independent and describes the direct propagation of the excitation in the medium. The spatially dependent surface response (red) contains the phenomenological term U_i describing the reflection of the excitation on the boundary.

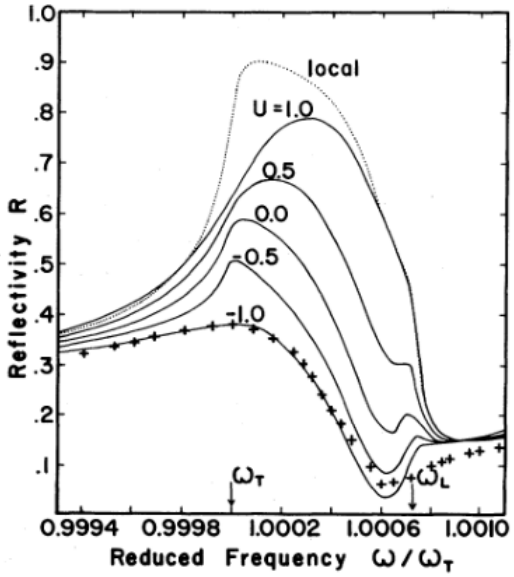

Figure 2.8: Normal incidence reflectivity as a function of frequency for the A_1 exciton of CdS comparing experimental data (points) to theoretical results (sold lines) using various scalar values of U in (2.54). The Pekar ABC provides the closest fit to experimental results [94]. Note that this is different to the exciton studied in chapter 7.

On its own, the susceptibility in (2.54) was insufficient to solve the wave equation (2.13). The other *critical* assumption made by Halevi and Fuchs was in their choice of ansatz for the electric field in the medium. The expression in (2.50) was used with spatially-independent values of q_n that satisfied the electromagnetic field dispersion relation in the infinite medium. While this is a safe assumption in the $z \to \infty$ limit, the susceptibility in the region of interest near the boundary is significantly different to that of the bulk medium.

Halevi and Fuchs gave no justification for the use of this ansatz and provided no argument that it was appropriate for the susceptibility in (2.54). This is quite a significant oversight on their part. If the values of q_n were spatially-dependent, the ∂_z acting on the electric field in (2.36) and (2.37) would lead to additional terms in the surface impedance, leading to a different final expression for the reflection coefficient. In addition, the field amplitude ratios derived by Halevi and Fuchs are given in terms of the wave vector components at the boundary, leading to further differences with the bulk q_n result.

In section 4.2, the choice of ansatz used by Halevi and Fuchs is tested by calculating the Green function for the electric field in the nonlocal medium. This is done using an iterative method that makes no assumptions about the form of the electric field. It will be shown that the susceptibility (2.54) does lead to the $\boldsymbol{E}$ expression used by Halevi and Fuchs and that the ansatz can safely be used.

With the choice of ansatz made, the rest of the Halevi and Fuchs derivation was straightforward. The details of the calculation are presented in chapter 5, but the key results are repeated here. The nonlocal susceptibility (2.54) and the ansatz for the electric field were substituted into (2.3) for $\boldsymbol{P}$ and the integrals were evaluated. By comparing the terms on each side of the wave equation (2.13), Halevi and Fuchs found that it could only hold for all points inside the medium if:

$$\sum_{n=1}^{3} \left(\frac{1}{q_n - \Gamma} + \frac{U_i}{q_n + \Gamma} \right) E_i^{(n)} = 0, \qquad i = x, y, z. \tag{2.55}$$

These equations provided the extra information required to calculate the electromagnetic reflection coefficients for the Halevi-Fuchs model. Converting $E_z^{(n)}$ to $E_x^{(n)}$ as in (2.52) gave two relations between the three $E_x^{(n)}$ components in the p-polarization and one relation between the two $E_y^{(n)}$ components of the s-polarization. This was sufficient to derive the field amplitude ratios used in the surface impedances (2.51-2.52) and the subsequent reflection coefficients (2.34-2.35). Furthermore, by re-arranging (2.55) to:

$$i\Gamma(1 - U_i)\mathcal{P}_i(0^+) + (1 + U_i)\partial_z \mathcal{P}_i(0^+) = 0, \tag{2.56}$$

Halevi and Fuchs were able to draw a link between their phenomenological reflection coefficients U_i and the generalized form of the ABC in (2.53). Table 2.1 contains the five previously mentioned ABCs that will be used for comparisons throughout the rest of this thesis in terms of both $\mathcal{P}_i$ and U_i.

Table 2.1: List of ABCs

	Parallel components		Normal components	
ABC	$\mathcal{P}_{x,y}$	$U_{x,y}$	$\mathcal{P}_z$	U_z
Agarwal *et al*. [33–42]	$i\Gamma\mathcal{P}_{x,y} + \partial_z\mathcal{P}_{x,y} = 0$	0	$i\Gamma\mathcal{P}_z + \partial_z\mathcal{P}_z = 0$	0
Ting *et al*. [43]	$\partial_z\mathcal{P}_{x,y} = 0$	-1	$\partial_z\mathcal{P}_z = 0$	-1
Fuchs-Kliewer [44–47]	$\partial_z\mathcal{P}_{x,y} = 0$	-1	$\mathcal{P}_z = 0$	1
Rimbey-Mahan [48–52]	$\mathcal{P}_{x,y} = 0$	1	$\partial_z\mathcal{P}_z = 0$	-1
Pekar [53–56]	$\mathcal{P}_{x,y} = 0$	1	$\mathcal{P}_z = 0$	1

The Halevi and Fuchs model allowed for comparisons between ABCs using a single formalism. Figure 2.9 shows typical plots for the reflection coefficients for an example medium as a function of frequency for a fixed incident angle. Many of the features of $r_s(\omega)$ and $r_p(\omega)$ were the same as the local medium with $D = 0$. The nonlocal effects were largely determined by $U_{x,y}$, with $U_{x,y} = -1$ (Pekar and Rimbey-Mahan) giving the greatest difference to the local results, followed by $U_{x,y} = 0$ (Agarwal *et al*.) and $U_{x,y} = 1$ (Fuchs-Kliewer and Ting *et al*.). The reflection minima also shifted to lower frequencies, with $U_{x,y} = -1$ again giving the greatest change compared to the local model. In contrast, the value of U_z only affected the frequency region near ω_L, with the largest difference near the reflection minimum.

The Halevi and Fuchs model has been used as the basis for more complex nonlocal models. In 1982, Halevi and Hernández-Cocoletzi [94] studied the effect of a small exciton-free surface layer. A region of fixed width L at the surface of the nonlocal medium was designated a "dead layer" and was described by a local susceptibility, effectively creating a double interface system. The vacuum/local medium interface was solved with Maxwell's boundary conditions and the local/nonlocal medium interface was solved with the generalized ABC of the Halevi model, leading to an L-dependent reflection coefficient for the entire system. Instead of adding extra components to the nonlocal model in this manner, this thesis seeks to improve the scope of the basic Halevi-Fuchs model by increasing the range of bulk susceptibility functions it can be applied to.

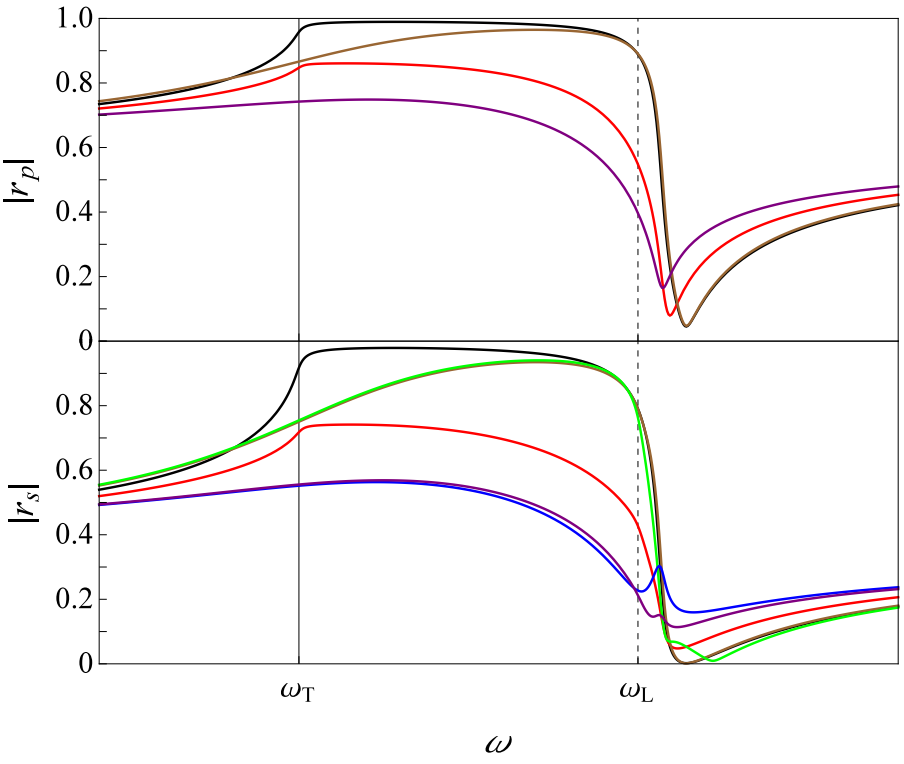

Figure 2.9: Reflection coefficients r_s (top) and r_p (bottom) as a function of ω for an example medium with the nonlocal susceptibility in (2.54) at an incident angle of $45°$. Vertical lines indicate ω_T (solid) and ω_L (dashed) values. Includes Agarwal *et al.* (Red), Ting *et al.* (Brown), Fuchs-Kliewer (Green), Rimbey-Mahan (Blue) and Pekar (Purple) ABCs compared to the local $D = 0$ result (Black). Model parameters used are $\chi_0 = 8.1$, $\hbar\omega_T = 2.8$eV, $\hbar\omega_p = 0.208$eV, $\hbar\gamma = 2.8 \times 10^{-5}$eV and $D = 6.17 \times 10^{-6}c^2$.

2.3.5 Additional work

While the Halevi-Fuchs model is valid for isolated scalar resonances in the susceptibility of the form (2.46), this represents a small fraction of the wide range of behaviour found in real materials. Several of the previously discussed ABCs have been taken and successfully applied to nonlocal media beyond these limitations.

Some of the various ABC authors had considered a tensor susceptibility as part of their derivations [48, 95]. As described in section 2.1.2, a distinctive direction is generated by the wave vector $\boldsymbol{k}$ when spatial dispersion is present. Even in an isotropic medium there may be a difference in the susceptibility for transverse and longitudinal waves. While the inequality between $\chi_\perp$ and $\chi_\parallel$ was included in their derivations, the authors did not in-

vestigate the effect this had on the electromagnetic reflection coefficients. This behaviour was also not carried over to the generalized ABC model and the effect the choice of ABC has on such a system remained to be investigated.

As discussed in section 2.1.6, a nonlocal medium can contain a large number of excitations in the medium, each with their own resonance in the susceptibility [59, 60]. Other authors have studied multi-resonance systems [67–73], but limited themselves to a maximum of two exciton bands. Despite the small number of resonances, a wide variety of exciton dispersion behaviour has been studied. The simplest examples contained two non-interacting parabolic bands of the form (2.21), but others dealt with degenerate exciton bands. Of particular interest is the work of Sell *et al.* [70] that dealt with the heavy/light exciton bands described by (2.22) with the Pekar ABC. These authors argued that such a system could be approximated using a single effective exciton band. This was done by simply taking the average energy of the heavy and light exciton for a given k, giving

$$D_{\text{eff}} = \frac{D_h + D_l}{2} \tag{2.57}$$

and reducing the problem to the previously solved single exciton band. This can also be thought of in terms of the susceptibility, where combining the two resonances to a single fraction gives:

$$\frac{\omega_p^2}{\omega_0^2 + D_h k^2 - \omega^2 - i\gamma\omega} + \frac{\omega_p^2}{\omega_0^2 + D_l k^2 - \omega^2 - i\gamma\omega} = \frac{2\omega_p^2(\omega_0^2 + D_{\text{eff}} k^2 - \omega^2 - i\gamma\omega)}{(\omega_0^2 + D_{\text{eff}} k^2 - \omega^2 - i\gamma\omega)^2 - \frac{1}{2}(D_h^2 + D_l^2)k^4}, \tag{2.58}$$

which is approximately equivalent to a single D_{eff} resonance with $\omega_p^2 \to 2\omega_p^2$ and an additional k^4 term. While Sell *et al.* noted that this approximation underestimated the amplitude of the features in $r_s(\omega)$ and $r_p(\omega)$, they were only interested in making semi-quantitative comparisons and not a detailed fit between theoretical and experimental results.

Not all features in the exciton band structure can be reduced to the simple k dependence in (2.24). In 1964, Mahan and Hopfield [71] applied the Pekar ABC to a more complex case by studying degenerate exciton bands with linear k terms, as in (2.23). This behaviour can be found in crystals with certain symmetry groups, including the uniaxial crystals zincblende and wurtzite [59]. The presence of anisotropy in the medium due to the crystal axis inevitably led to a tensor susceptibility that was not only dependant on the orientation of the field but also the wave vector. However, Mahan and Hopfield only considered a single orientation of the crystal axis, aligned normal to the plane of incidence.

This reduced the susceptibility to a scalar in each of the s- and p-polarization equations. The effect the choice of ABC and, more importantly, the orientation of the crystal axis has on the reflection coefficients had not been studied in detail and remained an open problem.

There is therefore a wide range of behaviour that is not covered by the Halevi and Fuchs model and has previously only been considered for specific ABCs. This provides the motivation for the second half of this thesis, in which the Halevi and Fuchs generalized ABC model is extended to include many more of the features found in real materials [61, 62]. The first part deals with incorporating the tensor nature of the susceptibility in (2.5) that is an inherent result of the wave vector dependence [61]. For the sake of simplicity, this is done for the isolated resonance. However, this will be equally applicable to the second part, where Halevi and Fuchs model is extended to multiple resonances [62]. This enables not only the study of closely spaced resonances in the susceptibility, but also degenerate resonances such as those found in the heavy/light exciton model. Finally, the restriction to k dependence of the form in (2.24) is lifted and the specific case of linear k terms in uniaxial crystals is studied [62].

2.3.6 Applications

The inclusion of spatial dispersion in the calculation of the electromagnetic reflection coefficients has significant knock-on effects on a range of other physical phenomena. The presence of a planar boundary modifies the Green tensor of the electric field. The Sipe representation [96] allows the Green tensor to be split into s- and p-polarization components. After a Fourier transform in the xy-plane, the Green tensor for two points in the half-space outside the medium can be written as:

$$\begin{aligned}\boldsymbol{G}^{EE}_{ij}(K,0,z,z',\omega) = \quad & \frac{1}{2q_0}\left(\hat{s}_i\hat{s}_j + \hat{p}_i^{\mathrm{sgn}(z'-z)}\hat{p}_j^{\mathrm{sgn}(z'-z)}\right)e^{iq_0|z'-z|} \\ & + \frac{1}{2q_0}\left(\hat{s}_i r_s \hat{s}_j + \hat{p}_i^{+} r_p \hat{p}_j^{-}\right)e^{iq_0(z'+z)} \\ & + \frac{i}{2k_0^2}\delta_{iz}\delta_{jz}\delta(z'-z), \end{aligned} \tag{2.59}$$

where $\hat{\boldsymbol{s}} = \hat{\boldsymbol{y}}$ picks out the s-polarization components and $\hat{\boldsymbol{p}}^{\pm} = (K\hat{\boldsymbol{z}} \mp q_0\hat{\boldsymbol{x}})/k_0$ picks out the p-polarization components of $\boldsymbol{E}$. In a similar manner to (2.54), the first part describes the direct propagation of light from z' to z, while the second position-dependent part describes waves reflecting on the surface of the medium.

The inclusion of spatial dispersion in the calculation of the electromagnetic reflection coefficients r_s and r_p therefore has wider implications for a large number of phenomena near the surface of the nonlocal medium that are based on the Green tensor. One example is radiative heat transfer between two semi-infinite parallel plates separated by a finite distance d. The radiative heat transfer was found to obey a $1/d^2$ law for distances below a few hundred nanometers if local models were used to describe the two media. By including spatial dispersion, the Halevi and Fuchs model has been shown [78] to remove the divergence from the system, instead approaching a finite value as $d \to 0$.

The neglect of spatial non-locality is also known to be responsible for several divergences in Casimir theory. The classic Lifshitz formula [97] for the Casimir force does not include spatial dispersion. At small separations and distances from material boundaries some components of the Casimir stress-energy tensor are dominated by the diverging integration over evanescent fields with arbitrarily large lateral wave vectors. A similar problem exists for curved boundaries, where the Casimir stress tensor perpendicular to the boundary leads to an infinite self-force for the simple example of the dielectric ball [98] or conducting shell [99]. Unlike the planar boundary, the Halevi and Fuchs model is inapplicable to such a system as it would require a completely different ansatz for the electric field inside either object. In each of these cases, the divergences are not simply due to the zero-point fields but are also present for purely thermal radiation [5].

The final part of this thesis investigates the effect of spatial dispersion on the energy density of thermal and zero-point radiation near the planar boundary of a half-infinite medium. The thermal energy density near metal surfaces has recently been probed using near-field microscopy [100] and the zero-point spectral energy density can be probed by measuring spontaneous emission rates close to a boundary [74–77]. It is well known that the use of a local model to describe the medium leads to an unphysical divergence in the energy density outside the boundary [5, 81, 101].

The average value of the energy density at a distance $|z|$ from the planar boundary is given by [5]:

$$\langle U \rangle = \frac{\varepsilon_0}{2} \langle |\boldsymbol{E}(\boldsymbol{r},t)|^2 \rangle + \frac{\mu_0}{2} \langle |\boldsymbol{B}(\boldsymbol{r},t)|^2 \rangle = \int_0^\infty d\omega \, u_{\mathrm{tot}}(z,\omega) \,. \tag{2.60}$$

The divergence is known to occur at the level of the spectral energy density $u_{\mathrm{tot}}(z,\omega)$, the energy density per unit frequency. Although the zero-point energy will diverge if it is not regularized, the spectral energy density of zero-point radiation should be finite without regularization [22].

The expression for u_{tot} can be calculated from the Green tensor of the electromagnetic fields by using the fluctuation-dissipation theorem [5]. The random thermal motion of charges, such as electrons or ions, in a material will generate small, fluctuating currents which radiate an electromagnetic field of their own. The fluctuation-dissipation theorem describes the statistical properties of these fluctuations and the radiated field. In thermal equilibrium, a relationship between the cross-correlation tensor and the Green tensor of the system at temperature T can be found [5]:

$$\langle E_i(\boldsymbol{r}, t+\Delta t) E_j(\boldsymbol{r}', t)\rangle = \mathbb{R}\mathrm{e}\left\{\int_0^\infty \frac{d\omega}{2\pi} e^{i\omega\Delta t} 4\omega\mu_0 \Theta(\omega, T)\, \mathbb{I}\mathrm{m}\left[G_{ij}^{EE}(\boldsymbol{r}, \boldsymbol{r}', \omega)\right]\right\}, \tag{2.61}$$

where

$$\Theta(\omega, T) = \hbar\omega\left(\frac{1}{2} + \frac{1}{e^{\hbar\omega/k_B T} - 1}\right) \tag{2.62}$$

is the mean energy of a harmonic oscillator in thermal equilibrium. The first term of (2.62) gives rise to the electromagnetic zero-point energy.

Equation (2.61) and the Green tensor (2.59) can be used to calculate u_{tot} by setting $\boldsymbol{r} = \boldsymbol{r}'$, $i = j$ and $\Delta t = 0$ and substituting into (2.60). Assuming that the nonlocal medium is in thermal equilibrium with its surroundings and the system is rotationally invariant around the z axis, the spectral energy density can be written in terms of the previously calculated reflection coefficients [102]:

$$\begin{aligned} u_{\mathrm{tot}}(z, \omega) = \quad & \frac{u_0}{k_0}\int_0^{k_0} \frac{K\,dK}{\sqrt{k_0^2 - K^2}}\left\{1 + \frac{K^2}{2k_0^2}\,\mathbb{R}\mathrm{e}\left[(r_s + r_p) e^{2i\sqrt{k_0^2 - K^2}|z|}\right]\right\} \\ & + \frac{u_0}{2k_0^3}\int_{k_0}^\infty \frac{K^3\,dK}{\sqrt{K^2 - k_0^2}}\left\{\mathbb{I}\mathrm{m}[r_s + r_p] e^{-2\sqrt{K^2 - k_0^2}|z|}\right\}. \end{aligned} \tag{2.63}$$

The term u_0 is the spectral energy density in the absence of the material, given by

$$u_0 = \frac{\Theta(\omega, T)\omega^2}{\pi^2 c^3}. \tag{2.64}$$

The integration over wave vector has been split into two parts. The first integral in (2.63) is the contribution from propagating waves with real q in the vacuum and contains both the incident and reflected electromagnetic waves. The second integral is the contribution from evanescent reflected waves with imaginary q. It is important to note that the result in (2.63) is for an ideal planar interface. It does not include surface roughness and quantum effects

such as "electron spill-out" that are not directly encoded in the susceptibility, which may affect the results in the $|z| \to 0$ limit.

While the exponential in the first term is complex and oscillates over the range of the integral, the exponential in the second term is real and decays as $K \to \infty$. The rate of decay is determined by the distance from the planar surface $|z|$. For this reason, the propagating wave contribution dominates the result for u_{tot} in the far field. It is only in the near field very close to the boundary, where $|z|$ is smaller than the wavelength of light and the second exponential decays slowly, that the evanescent term significantly contributes to the result.

It is in this region near the boundary that the divergence of the local medium is found. If spatial dispersion is ignored, then as $K \to \infty$ the Fresnel reflection coefficients (2.42) and (2.43) approach the constant values:

$$\lim_{K\to\infty} r_s = 0, \tag{2.65}$$

$$\lim_{K\to\infty} r_p = \frac{\chi(\omega)}{2+\chi(\omega)}. \tag{2.66}$$

The leading contribution to the evanescent wave integral therefore comes from the very large K values, where the function in (2.63) is proportional to K^2. In the $z \to 0$ limit, the exponential in the second integral decays slowly enough that this term becomes dominant, giving the approximate result [5]:

$$u_{\mathrm{tot}}(z,\omega) \approx \frac{u_0}{2k_0^3}\left\{\frac{\mathbb{I}\mathrm{m}[\chi(\omega)]}{|2+\chi(\omega)|^2}\frac{1}{4|z|^3}\right\}. \tag{2.67}$$

This contribution can be seen to dominate the result at small $|z|$ for an example local medium in Fig. 2.10. Due to the Kramers-Kronig relations between the real and imaginary components of the susceptibility, $\mathbb{I}\mathrm{m}[\chi(\omega)]$ is always present and therefore u_{tot} will contain an unphysical divergence at the boundary.

One can also consider the spectrum of $u_{\mathrm{tot}}(\omega)$ at a fixed distance from the boundary. This is shown in Fig. 2.11 for a range of $|z|$ values. At large distances, the result is approximately constant for all frequencies, but below 100nm, the evanescent wave contributions begin to appear. The main feature of the result is a large peak in $u_{\mathrm{tot}}(\omega)$ at ω_L due to the evanescent p-polarization that becomes significantly larger and broader as $|z|$ decreases. A much smaller peak due to the evanescent s-polarization is found at ω_T, however this is masked by the p-polarization peak as $|z| \to 0$.

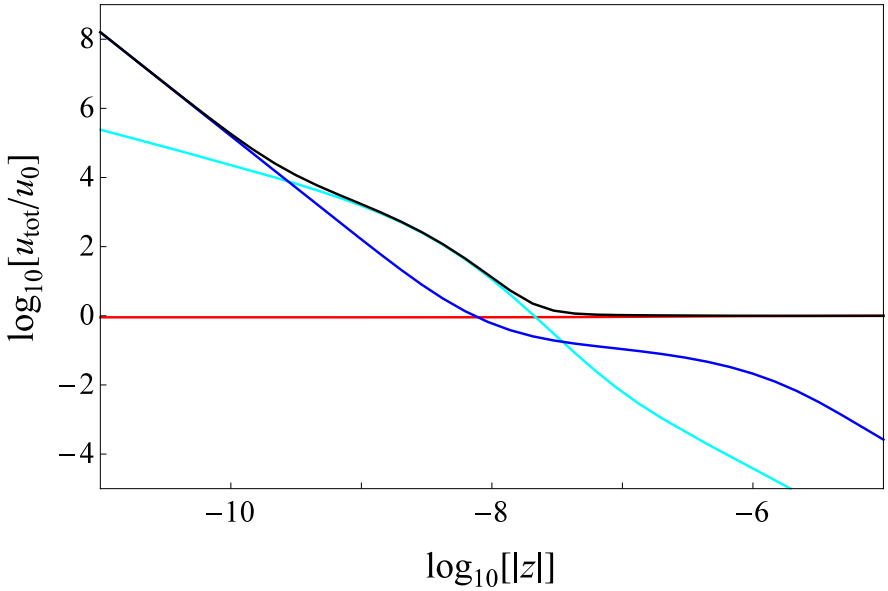

Figure 2.10: Spectral energy density u_{tot} (black line) as a function of distance $|z|$ from the boundary at the fixed frequency ω_T . Results include the propagating wave s and p-polarization contribution (red) and the evanescent wave s-(cyan) and p-polarization (blue) contributions. The evanescent p-polarization wave contribution diverges as $1/|z|^3$ as $z \to 0$. Model parameters used are $\chi_0 = 8.1$, $\hbar\omega_T = 2.8$eV, $\hbar\omega_p = 0.207$eV and $\hbar\gamma = 2.8 \times 10^{-5}$eV.

It has been argued that the divergent result in (2.67) is due to the assumption that the spatially local macroscopic susceptibility is valid down to the smallest scales, where the microscopic structure of the medium becomes apparent. Some authors have attempted to resolve this by either introducing a sharp cut-off to the K integral [81] or smoothing the spatial delta function $\delta^3(\boldsymbol{r} - \boldsymbol{r}')$ of the local susceptibility to a Gaussian [82] with a length scale based on either the lattice period or some finite correlation length. While this does remove the divergence in u_{tot}, it is a rather unsatisfactory approach. Much like the problem of absorption described in section 2.2, it must be added to the calculation "by hand" rather than simply emerging from the model.

Previous work [82] based on a different model as shown that the inclusion of spatial dispersion in the susceptibility can remove the $1/z^3$ divergence in u_{tot} outside the medium. The Linhard susceptibility, which is based on a semi-classical description of the electron gas, is applicable to the conduction electrons in a metal when the mean free path is longer than the Fermi wavelength. While successful, the susceptibility due to the core electrons still lead to an unphysical divergence unless their nonlocal behaviour is taken

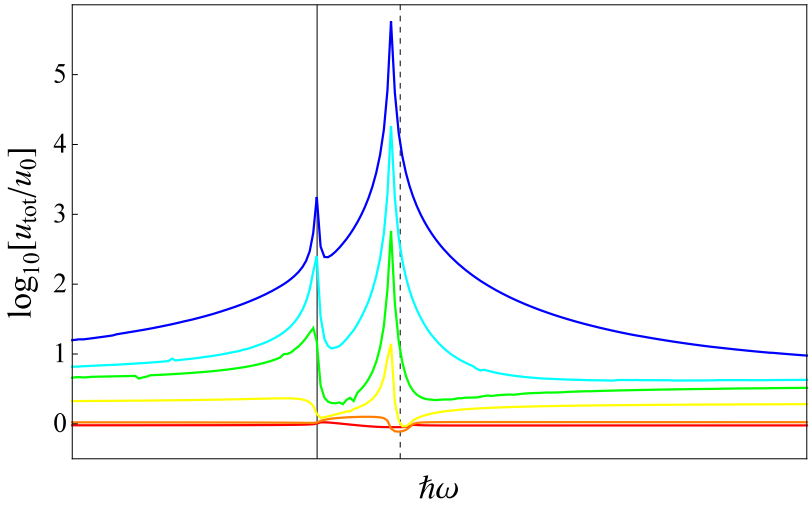

Figure 2.11: Spectral energy density $u_{\mathrm{tot}}(\omega)$ at a range of fixed distances $|z|$ from the boundary. Examples include $|z| = 10^{-6.5}$m (red), 10^{-7}m (orange), $10^{-7.5}$m (yellow), 10^{-8}m (green), $10^{-8.5}$m (cyan) and 10^{-9}m (blue). Vertical lines indicate ω_T (solid) and ω_L (dashed) values. The evanescent p-polarization contribution is responsible for the peak at ω_L that grows in magnitude closer to the boundary. Model parameters are the same as Fig. 2.10.

into consideration.

The final part of this thesis applies both Halevi and Fuchs' original generalized ABC model and the extensions described in section 2.3.5 to the calculation of the spectral energy density. In each case the unphysical $1/|z|^3$ divergence is removed and the differences caused by the choice of ABC are investigated and found to be significant even for distances $|z|$ much larger than the lattice spacing [61, 62].

Chapter 3

Absorption in Dielectrics

In 1958 Hopfield [2] proposed many-body interactions, described by nonlinear coupling, as a solution to the lack of broadband absorption found in linear dielectric models. While such a calculation has been performed in the quantum regime [9–13], a full analysis remains challenging. Instead, the use of a phenomenological reservoir has become widespread [3, 14–22], despite the unclear link between this mathematical tool and the microscopic physics and interactions of a real medium.

This chapter verifies Hopfield's claim with a purely classical calculation, demonstrating that quantum mechanical behaviour is not required for broadband absorption [25]. The model used is a discrete version of the Hopfield model presented in section 2.2.1, with an additional degree of freedom in the form of lattice vibrations. While this new model is one-dimensional, chosen to simplify calculations, the work presented throughout this chapter is also applicable to 3D crystals, under certain assumptions.

In section 3.1, a basic 1D dipole model of a dielectric with linear coupling is described and the corresponding equations of motion are derived. The assumptions required for application to a 3D lattice are outlined and the corresponding susceptibility is found. This model is modified in section 3.2 with the inclusion of nonlinear interactions between the dipoles and the new displacement degree of freedom. A method to extract an effective linear susceptibility from this new model using an iteration process is discussed in section 3.3. In section 3.4, a diagrammatic approach to the iteration method is described and applied to the linear model. This method is subsequently applied to the nonlinear model in section 3.5. A numerical calculation of the leading-order terms in the perturbation theory is performed in section 3.6, giving an effective linear susceptibility that can be accurately described by the Lorentz model, confirming Hopfield's proposal. The wave

vector dependence of these results are also investigated, highlighting the role of higher-order terms in the perturbation series.

3.1 The linear model

This chapter starts by considering a simple microscopic model with linear coupling between a scalar field and an infinite lattice of electric dipoles, in what is essentially a 1D, discrete version of the Hopfield model [2] in section 2.2.1. While this model will prove inadequate in providing broadband absorption, it will subsequently be used as a basis for a nonlinear model. A schematic of the microscopic linear (ML) model is shown in Fig. 3.1. Each "atom" is located at the position $z_n = na$, where a is the lattice spacing and n labels each particle. The corresponding electric dipole p_n is linearly coupled to the scalar field A, which represents a projection of the electromagnetic vector potential. This treatment of a medium as a lattice of dipoles is applicable to solid dielectrics with a regular crystal structure. However, just like the Lorentz model, systems outside the restrictions of the initial derivation will show features that are similar to this model.

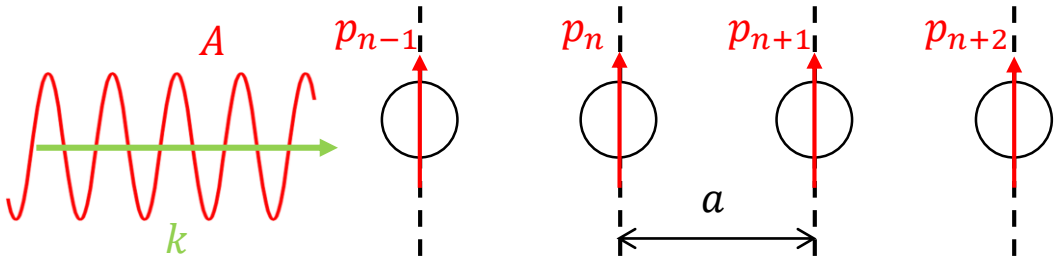

Figure 3.1: Schematic of the 1D microscopic linear (ML) model, consisting of an infinite lattice of finite sized "atoms" with an electric dipole moment p_n linearly coupled to the field A.

While the model was chosen with microscopic physics in mind, it is possible to construct a system of dielectric spheres on a macroscopic scale. Metamaterials based on arrays of dielectric nanoparticles are an example of this [103, 104] and are actively being investigated as a low-loss alternative to metallic systems [105–107]. However, the discrete model in Fig. 3.1 does not consider the internal structure and physics of each particle in the system. It therefore fails to capture several important aspects of the medium, such as using the size of nanoparticles to control a magnetic response [105]. In addition,

the coupling between dipoles in the macroscopic case is usually investigated for altering the already present broadband response of the material [106, 107], rather than inducing lattice vibrations that act as the origin of the response in the microscopic case.

Although the ML model is one-dimensional, the resulting equations of motion are equivalent to those of a 3D model consisting of a cubic lattice of electric dipoles $\boldsymbol{p_n}$ and the electromagnetic vector potential $\boldsymbol{A}$ under the following conditions:

- The vector potential $\boldsymbol{A}$ and all electric dipoles $\boldsymbol{p_n}$ are aligned with one of the principal axes (e.g. $\hat{\boldsymbol{x}}$).
- All wave vectors $\boldsymbol{k}$ are aligned with a principal axis perpendicular to $\boldsymbol{A}$ and $\boldsymbol{p_n}$ (e.g. $\hat{\boldsymbol{z}}$).
- The electromagnetic scalar potential ϕ is set to zero.

In other words, the 1D ML model is applicable to transverse electromagnetic waves propagating along one of the principal axes of a cubic crystal. The differences between this scenario and the 1D model are minor, but will be highlighted throughout the following derivation.

The Lagrangian of the linear model in Fig. 3.1 consists of three parts:

$$L_A = \frac{1}{2}\int_{-\infty}^{\infty} dz \left\{ \left[\partial_t A(z,t)\right]^2 - c^2 \left[\partial_z A(z,t)\right]^2 \right\}, \tag{3.1}$$

$$L_p = \frac{1}{2a}\sum_{n=-\infty}^{\infty} \left\{ \left[\partial_t p_n(t)\right]^2 - \omega_0^2 \left[p_n(t)\right]^2 + \frac{1}{2}\tau_1^2 \left[p_n p_{n-1} + p_n p_{n+1}\right] \right\}, \tag{3.2}$$

$$L_{pA} = -\beta \sum_{n=-\infty}^{\infty} \int_{-\infty}^{\infty} dz \left\{ \alpha(z-na) p_n(t) \left[\partial_t A(z,t)\right] \right\}, \tag{3.3}$$

where A and p_n have been rescaled to reduce notation throughout the chapter. The first two terms L_A and L_p are the respective "free" Lagrangians of the field and the dipoles and describe their behaviour in the absence of L_{pA}, which contains the linear coupling between the two.

The lattice of dipoles in (3.2) are described as simple harmonic oscillators with the resonant frequency ω_0. The p_n values are coupled to each other via τ_1, which arises from the r^{-3} dipole-dipole interaction [1]:

$$V_{nm} = V_0 \frac{p_n p_m}{|z_n - z_m|^3} = \frac{V_0}{a^3 |n-m|^3} p_n p_m = \frac{1}{2a}\tau_{n-m}^2 p_n p_m, \tag{3.4}$$

As the interaction strength rapidly decays with distance, only the nearest-neighbour term

$$\tau_1^2 = \frac{V_0}{a^2} \tag{3.5}$$

is retained in (3.2). In a 3D model, there would also be coupling between nearest neighbours in the $\hat{\boldsymbol{x}}$ and $\hat{\boldsymbol{y}}$ directions.

One feature not present in the Hopfield model is the term $\alpha(z - na)$ in the interaction Lagrangian L_{pA} (3.3). This is used to account for the finite size of the particles in the model and is taken to be the normalized Gaussian function

$$\alpha(z) = \frac{1}{z_0(2\pi)^{1/2}} e^{-\frac{z^2}{2z_0^2}} \tag{3.6}$$

throughout this chapter, with the convenient feature that (3.6) becomes the Dirac delta function $\delta(z)$ in the $z_0 \to 0$ limit.

The first step in calculating an effective susceptibility for the ML model is to perform a spatial Fourier transformation on (3.1)-(3.3) using (3) for the continuous field and (4) for the discrete dipoles. This leads to an important distinction between the wave vector range for A (which runs over all values) and p (which is limited to the first Brillouin zone). The resulting expressions are:

$$L_A = \frac{1}{2}\left(\frac{1}{2\pi}\right)\int_{-\infty}^{\infty} dk \left\{ [\partial_t A(k,t)]\,[\partial_t A(-k,t)] - c^2k^2\,[A(k,t)]\,[A(-k,t)] \right\}, \tag{3.7}$$

$$L_p = \frac{1}{2}\left(\frac{1}{2\pi}\right)\int_{-\pi/a}^{\pi/a} dq \left\{ [\partial_t p(q,t)]\,[\partial_t p(-q,t)] - \omega_0^2(q)\,[p(q,t)]\,[p(-q,t)] \right\}, \tag{3.8}$$

$$L_{pA} = -\beta\left(\frac{1}{2\pi}\right)\int_{-\infty}^{\infty} dk \int_{-\pi/a}^{\pi/a} dq \left\{ \alpha(-k)p(q,t)\,[\partial_t A(k,t)] \sum_{j=-\infty}^{\infty} \delta\left(k + q + j\tfrac{2\pi}{a}\right) \right\}, \tag{3.9}$$

where the resonant frequency of the dipoles in L_p is now wave vector-dependent:

$$\omega_0^2(q) = \omega_0^2 + \tau_1^2\cos(qa). \tag{3.10}$$

The inclusion of m^{th}-nearest neighbour coupling terms would lead to additional terms of $\tau_m^2\cos(qam)$ in (3.10). Due to the decrease in coupling strenght with distance, these terms will not have a significant effect on results. While the 3D model would contain additional terms in (3.10) due to coupling between dipoles in the $\hat{\boldsymbol{x}}$ and $\hat{\boldsymbol{y}}$ directions,

these would amount to a simple shift of ω_0 under the assumption that all wave vectors are aligned with $\hat{\boldsymbol{z}}$. The Dirac delta function in (3.9) contains terms where the wave vector q is displaced by an integer number j of reciprocal lattice vectors. The $j \neq 0$ terms describe Umklapp processes [108], where momentum is transferred to the centre of mass of the crystal. While the large mass of the infinite crystal means there is no accompanying energy transfer, Umklapp processes will still play an important role in subsequent calculations.

After an additional Fourier transform in time using (1), the equations of motion for the ML model are:

$$\left[c^2k^2 - \omega^2\right] A(k,\omega) = -i\omega\beta\alpha(k) \int_{-\pi/a}^{\pi/a} dq \left\{ p(q,\omega) \sum_{j=-\infty}^{\infty} \delta(q + j\tfrac{2\pi}{a} - k) \right\}, \quad (3.11)$$

$$\left[\omega_0^2(q) - \omega^2\right] p(q,\omega) = i\omega\beta \sum_{j'=-\infty}^{\infty} \alpha^*(q + j'\tfrac{2\pi}{a}) A(q + j'\tfrac{2\pi}{a}, \omega), \quad (3.12)$$

where the symmetry property $\alpha(-k) = \alpha^*(k)$ has been used. The integral in (3.11) picks out the specific value of j that translates k back into the first Brillouin zone, while (3.12) retains all values of j'. It is important to note that while Umklapp processes in (3.12) couple each (q,ω) dipole mode to a number of modes of the A field, these modes are discrete and all have the same frequency. Even with the inclusion of these terms, the system lacks the coupling to a continuum required by Hopfield [2] for broadband absorption.

Equation (3.12) can be solved to give

$$p(q,\omega) = p_h(q,\omega) + i\omega\beta G_p(q,\omega) \sum_{j'=-\infty}^{\infty} \alpha^*(q + j'\tfrac{2\pi}{a}) A(q + j'\tfrac{2\pi}{a}, \omega), \quad (3.13)$$

where p_h is the homogeneous solution of p satisfying the equation of motion in the absence of the A field:

$$\left[\omega_0^2(q) - \omega^2\right] p_h(q,\omega) = 0 \quad (3.14)$$

and G_p is the retarded Green function which takes the same form as (2.27) in the Hopfield model:

$$\begin{aligned} G_p(q,\omega) =& \frac{1}{\omega_0^2(q) - (\omega + i0^+)^2} \\ =& \mathbb{P}\frac{1}{\omega_0^2(q) - \omega^2} + \frac{i\pi}{2\omega}\left[\delta(\omega - \omega_0(q)) - \delta(\omega + \omega_0(q))\right]. \end{aligned} \quad (3.15)$$

The poles at $\omega^2 = \omega_0^2(q)$ in G_p have again been shifted into the lower half-plane of complex ω to preserve causality and satisfy the Kramers-Kronig relations. The resulting expression can be split into a real principal-valued term, denoted by $\mathbb{P}$, and two imaginary Dirac delta functions.

Equation (3.13) is then substituted into (3.11) to give an equation solely in terms of the field A and the homogeneous solutions p_h:

$$\begin{aligned}\left[c^2k^2 - \omega^2\right] A(k,\omega) =& \omega^2\beta^2 G_p(k,\omega)\alpha(k) \sum_{j=-\infty}^{\infty} \alpha^*(k + j\tfrac{2\pi}{a}) A(k + j\tfrac{2\pi}{a}, \omega) \\ &- i\omega\beta\alpha(k) \int_{-\pi/a}^{\pi/a} dq \left\{ p_h(q,\omega) \sum_{j'=-\infty}^{\infty} \delta(q + j'\tfrac{2\pi}{a} - k) \right\}. \quad (3.16)\end{aligned}$$

If Umklapp processes are ignored by only considering the $j = 0$ term in (3.16), a transverse wave equation can be recovered:

$$\begin{aligned}\left\{ k^2 - \frac{\omega^2}{c^2}\left[1 + \chi(k,\omega)\right] \right\} A(k,\omega) =& \\ &- i\omega\beta\alpha(k) \int_{-\pi/a}^{\pi/a} dq \left\{ p_h(q,\omega) \sum_{j'=-\infty}^{\infty} \delta(q + j'\tfrac{2\pi}{a} - k) \right\},\end{aligned} \quad (3.17)$$

which is the equivalent of the Maxwell electromagnetic wave equation (2.14) for the ML model, with A taking the role of the electric field and the effective susceptibility of the system given by:

$$\chi(k,\omega) = |\alpha(k)|^2\beta^2 G_p(k,\omega) = \frac{|\alpha(k)|^2\beta^2}{\omega_0^2(k) - (\omega + i0^+)^2}. \quad (3.18)$$

As previously discussed in section 2.2.1 for the Hopfield model, the Green function G_p is directly related to the susceptibility. While $\omega_0(k)$ in (3.10) is periodic in k due to the discrete nature of the system, the $\alpha(k)$ term ensures that $\chi \to 0$ as $k \to \infty$ for any non Dirac-delta spatial coupling term, satisfying the conditions in section 2.1.3. It can be seen that the ML model suffers from the same issues as the Hopfield model in section 2.2, as separating (3.18) into real and imaginary components using (3.15) gives absorption only at the resonant frequency $\omega_0(k)$ for a given wave vector k. The ML model, which contains only linear coupling, therefore lacks the broadband absorption found in real materials.

This problem is not alleviated through the inclusion of Umklapp processes. While this does introduces coupling between a single mode and a discrete set of modes, similar to

the various discrete reservoir models [3], they are all of the same frequency. Hopfield's required energy continuum [2], described in section 2.2.1, is not present in the ML model and broadband absorption is absent even when Umklapp processes are included. This behaviour is explicitly calculated later in section 3.4.1.

3.2 The nonlinear model

The previous section has shown that the simple ML model of a dielectric lacks the broadband absorption found in real materials. This leads to the aim of this chapter — to verify Hopfield's claim [2] that the inclusion of many-body interactions via nonlinear coupling leads to a susceptibility that is similar to the Lorentz model (2.19) with a non-zero damping term γ.

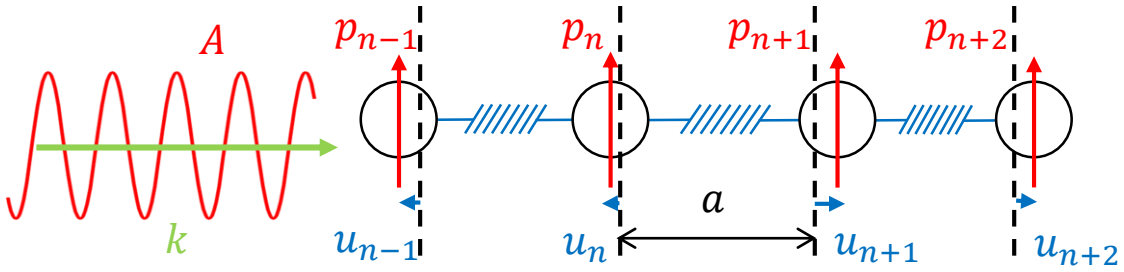

Figure 3.2: Schematic of the 1D microscopic nonlinear (MN) model. The electric dipoles p_n are linearly coupled to the field A and nonlinearly coupled to the particle displacements u_n. Both the dipoles and the displacements are coupled to their nearest neighbours, represented by the blue springs.

To test his proposal, an additional degree of freedom not directly coupled to the field A is added to the ML model. Each particle now has two associated variables - the dipole moment p_n and the physical displacement of the particle from the equilibrium position $z_n = na$, denoted by u_n. This can be thought of as adding the acoustic modes of vibration to the model. A schematic of the new microscopic nonlinear (MN) model is shown in Fig. 3.2. For the 1D MN model to apply to the 3D lattice, the second condition in section 3.1 must be modified to:

- All wave vectors $\boldsymbol{k}$ *and displacements* $\boldsymbol{u_n}$ are aligned with the same principal axis perpendicular to $\boldsymbol{A}$ and $\boldsymbol{p_n}$ (e.g. $\hat{\boldsymbol{z}}$).

Two additional terms are added to the Lagrangian as a result of these changes. The L_u term is the "free" Lagrangian of the u displacements in the MN model and takes a similar form to L_p in (3.19):

$$L_u = \frac{1}{2}M \sum_{n=-\infty}^{\infty} \left\{ \left[\partial_t u_n(t)\right]^2 - \nu_0^2 \left[u_n(t)\right]^2 - \frac{1}{2}\kappa_1^2 \left[u_n(t) - u_{n-1}(t)\right]^2 \right\}, \tag{3.19}$$

where κ_1^2 is the nearest-neighbour coupling strength and M is the mass of the particle. This expression contains several parts, the first of which is the usual kinetic energy term for a particle with mass M. The second part contains a harmonic confining potential with resonant frequency ν_0 that anchors the particle to the lattice site. While this term is not strictly required and ν_0 can be set to equal zero, its inclusion does not significantly affect the overall results and a small nonzero value of ν_0 can simplify later numerical calculations. The final term contains the coupling between nearest-neighbours, shown in Fig. 3.2 and modelled in the usual way [86, 108] by connecting particles with springs of a rest length a.

As in the case of L_p in (3.19), the 3D model would also contain nearest-neighbour coupling terms with particles separated in the $\hat{\boldsymbol{x}}$ and $\hat{\boldsymbol{y}}$ directions. However, the extension of the spring would no longer be given by a simple difference in u values. For example, the spring extension for particles separated in the $\hat{\boldsymbol{x}}$ direction is given by:

$$\sqrt{a^2 + (u_n - u_{n-1})^2} - a, \tag{3.20}$$

under the assumption that all displacements are in the $\hat{\boldsymbol{z}}$ direction. A small u expansion can be made for (3.20), but the leading term will be of the order u^4. The corresponding nonlinear Lagrangian term would need to be considered separately to the linear terms in (3.19).

The nonlinear interaction term between the dipole moments and the displacements naturally emerges from the r^{-3} dipole-dipole interaction previously used in (3.4):

$$V_{n,n+m} = V_0 \frac{p_n p_{n+m}}{|(z_n + u_n) - (z_{n+m} + u_{n+m})|^3} = \frac{V_0}{|ma|^3} \frac{1}{|1 + \frac{u_n - u_{n+m}}{ma}|^3} p_n p_{n+m}. \tag{3.21}$$

A small u expansion can be performed on this expression to give a series of Lagrangian terms with increasing powers of u. Retaining only nearest-neighbour interactions, the zeroth-order term has already been included in (3.2) and the first-order term gives the nonlinear Lagrangian:

$$L_{ppu} = -\frac{6V_0}{a^4} \sum_{n=-\infty}^{\infty} \Big\{ p_n(t) p_{n-1}(t) [u_n(t) - u_{n-1}(t)] \Big\}. \tag{3.22}$$

Once again, the 3D model will also contain nearest-neighbour coupling terms with particles separated in the $\hat{\boldsymbol{x}}$ and $\hat{\boldsymbol{y}}$ directions. However, for reasons similar to (3.20), these do not modify (3.22) as the leading order terms of the Lagrangian in the small u expansion contain $ppuu$ nonlinear interactions.

The process of calculating the effective susceptibility of the nonlinear model starts once again with a spatial Fourier transformation, with (3.19) and (3.22) taking the form:

$$L_u = \frac{1}{2}Ma\left(\frac{1}{2\pi}\right)\int_{-\pi/a}^{\pi/a} dq\left\{\left[\partial_t u(q,t)\right]\left[\partial_t u(-q,t)\right] - \nu_0^2(q)\left[u(q,t)\right]\left[u(-q,t)\right]\right\}, \tag{3.23}$$

$$L_{ppu} = \frac{3iV_0}{\pi a^2}\left(\frac{1}{2\pi}\right)\int_{-\pi/a}^{\pi/a} dq_1 \int_{-\pi/a}^{\pi/a} dq_2 \int_{-\pi/a}^{\pi/a} dq_3 \Big\{ \left[\sin(q_1 a) + \sin(q_2 a)\right] \times p(q_1,t)p(q_2,t)u(q_3,t)\delta(q_1+q_2+q_3)\Big\}, \tag{3.24}$$

where the u resonant frequency in (3.23) is now wave vector dependent.

$$\nu_0^2(q) = \nu_0^2 + \kappa_1^2 - \kappa_1^2\cos(qa). \tag{3.25}$$

A visual representation of (3.25) is shown in Fig. 3.3. Umklapp processes are also present in (3.24), but are omitted for notational brevity as the integrals will pick out a specific scattering process to ensure all wave vectors lie within the first Brillouin zone.

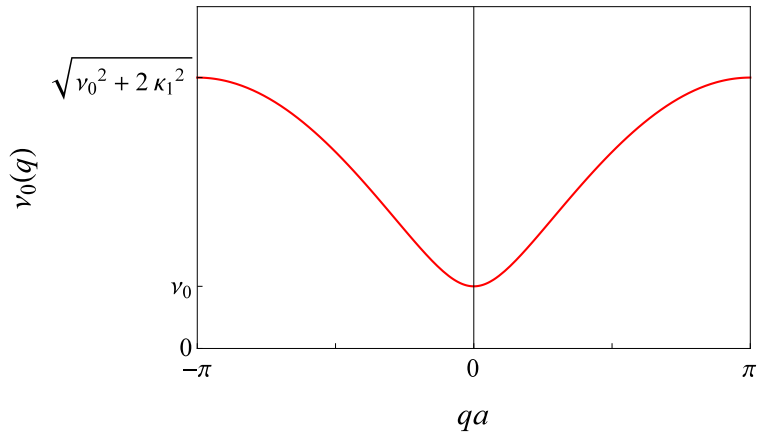

Figure 3.3: Wave vector dependence of the u resonant frequency $\nu_0(q)$ in (3.25), which covers the frequency range $\nu_0 \to \sqrt{\nu_0^2 + 2\kappa_1^2}$.

After using (1) to perform a Fourier transform in time and evaluating the Dirac delta functions, the equations of motion become:

$$A(k,\omega) = A_h(k,\omega) + G_A(k,\omega)\left[-i\omega\beta\alpha(k)\right]\int_{-\pi/a}^{\pi/a} dq\left\{p(q,\omega)\sum_{j=-\infty}^{\infty}\delta(q+j\tfrac{2\pi}{a}-k)\right\}, \tag{3.26}$$

$$\begin{aligned} p(q,\omega) =& p_h(q,\omega) + G_p(q,\omega)\sum_{j'=-\infty}^{\infty}\left[i\omega\beta\alpha^*(q+j'\tfrac{2\pi}{a})\right]A(q+j'\tfrac{2\pi}{a},\omega) \\ &+ G_p(q,\omega)\int_{-\pi/a}^{\pi/a} dq_1\int_{-\infty}^{\infty} d\omega_1\left[\sigma f_1(q,q_1)\right]\left[u(q_1,\omega_1)p(q-q_1,\omega-\omega_1)\right], \end{aligned} \tag{3.27}$$

$$\begin{aligned} u(q,\omega) =& u_h(q,\omega) \\ &+ \frac{1}{Ma}G_u(q,\omega)\int_{-\pi/a}^{\pi/a} dq_1\int_{-\infty}^{\infty} d\omega_1\left[\sigma f_2(q,q_1)\right]\left[p(q_1,\omega_1)p(q-q_1,\omega-\omega_1)\right], \end{aligned} \tag{3.28}$$

where the nonlinear coupling constant σ is given by:

$$\sigma = \frac{3V_0}{2\pi^2 a^2} \tag{3.29}$$

and the coupling functions are given by:

$$\begin{aligned} f_1(q,q_1) =& 2i\left\{\sin[(q-q_1)a] - \sin[qa]\right\}, \\ f_2(q,q_1) =& i\left\{\sin[(q-q_1)a] - \sin[q_1 a]\right\}. \end{aligned} \tag{3.30}$$

The homogeneous solutions and Green functions are given by

$$\left[(ck)^2-\omega^2\right]A_h(q,\omega) = 0, \qquad G_A(k,\omega) = \frac{1}{(ck)^2-(\omega+i0^+)^2}, \tag{3.31}$$

$$\left[\nu_0^2(q)-\omega^2\right]u_h(q,\omega) = 0, \qquad G_u(q,\omega) = \frac{1}{\nu_0^2(q)-(\omega+i0^+)^2}, \tag{3.32}$$

while equations (3.14) and (3.15) for p_h and G_p remain the same.

The introduction of nonlinear coupling has lead to a form of "pesudo-reservoir" in the equations of motion, with each mode of $p(q,\omega)$ in (3.27) now coupled to a continuum of modes. However, attempting to repeat the previous section and rearranging equations (3.26)-(3.28) to a wave equation solely in terms of A and homogeneous solutions presents several challenges as the nonlinear coupling makes it difficult to express p in a closed form. Instead, a perturbative solution to the equations of motion is sought.

3.3 The perturbative solution

This section presents a method for extracting an effective linear susceptibility from the MN model by deriving a wave equation for A similar to (3.17). This is done by treating the nonlinear interaction as a perturbation to the initial ML model in section 3.1 and taking the coupling coefficient σ in (3.29) to be small. The process to find a perturbative solution is performed in stages, with the initial aim of finding an equation solely in terms of A and homogeneous solutions, similar (3.17) in the ML model.

The first step is to consider the equation for the displacement u, as it is not directly coupled to the field A. While the expression for u in (3.28) can be immediately substituted into the p equation in (3.27), this is not always the case. For example, the small u expansion of the dipole-dipole interaction (3.21) used in section 3.2 could be continued to the next term in the series. The resulting $ppuu$ interaction would lead to a ppu term on the right-hand side (RHS) of (3.28) that must be dealt with before it can be substituted in to the equation for p.

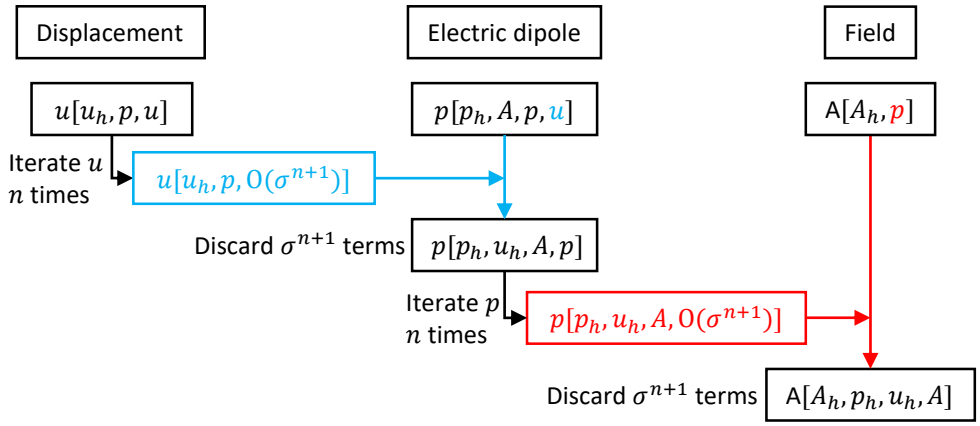

Figure 3.4: Schematic of the first iteration process used to derive an equation for the MN model solely in terms of the field A and homogeneous solutions.

An iteration process is performed by taking the solution to the u equation of motion, which depends on the homogeneous solution u_h, p and yet more u terms, and substituting it in the place of every RHS u term. While there are still RHS terms of u after this iteration, they will have gained an additional power of the nonlinear coupling constant σ. This process of substituting for RHS u terms is repeated to give a solution that is a power series in σ. After n iterations, all RHS terms up to the n^{th} power of σ contain only p and the homogeneous solution u_h. The remaining RHS terms of u are only found with a

coefficient of σ^{n+1} or higher. Removing these terms leaves an expression for u in terms of p and u_h that is accurate up to order σ^n that can be substituted into (3.27). A visual representation of this process is shown in Fig. 3.4.

This process is repeated with the new p equation of motion, which is given in terms of the homogeneous solutions u_h and p_h, the field A and the RHS p terms that must be iterated. After n iterations, where the entire expression for p has been substituted into the RHS p terms, all terms up to σ^n contain only the field A and the homogeneous solutions, while those containing p have a coefficient of σ^{n+1} or higher. Once again, the σ^{n+1} terms are discarded and the expression is substituted into the A equation of motion, giving:

$$\left[(ck)^2 - \omega^2\right] A(k,\omega) = H + \omega^2 \left|\beta\alpha(k)\right|^2 G_p(k,\omega) A(k,\omega) + Z_{\mathrm{L}}[A] + Z_{\mathrm{NL}}[A], \quad (3.33)$$

where the various RHS terms have been split into groups. The first term H contains only homogeneous solutions (u_h and p_h) and will subsequently be omitted from calculations, as it will not contribute to the calculation of the linear susceptibility upon rearranging (3.33) as a wave equation. The second terms is the linear A term that was already present in the ML model. This will give the leading-order term in the perturbation series of the effective linear susceptibility of the MN model. The remaining terms of A are contained within integrals over ω and k and are collected into Z_{L} and Z_{NL}, which are linear and nonlinear functionals of A respectively.

The nonlinear terms of A contained in Z_{NL} can be used to find an effective nonlinear susceptibility for the MN model. This could subsequently be used to analyse the re-emission of frequency-converted A waves by the dielectric. However, the focus of this derivation is the introduction of broadband absorption to the linear susceptibility. As the leading-order term of Z_{NL} contains more powers of σ than the leading-order linear A term (the second term in (3.33) from the ML model) and is dependent upon higher powers of A, Z_{NL} can be considered negligible for weak fields and as such is omitted from the rest of this derivation.

After removing H and Z_{NL} , the only remaining RHS components in (3.33) are the term from the linear model and the linear functional $Z_{\mathrm{L}}[A]$. A different iteration process is required to extract an effective susceptibility from this expression. Each of the RHS A terms in (3.33) are split into two groups: those that are in the same mode as the initial wave (k,ω) and those in a different mode ($k' \neq k, \omega' \neq \omega$). However, the (k,ω) terms are a set of measure zero in the integration $\int dk' \int d\omega'$ over all modes in Z_{L}. This is a direct result of the continuous nature of the wave vector in the Fourier transform of an infinite discrete system. The current infinite model must instead be considered as an approximation of a

large, but finite, chain of N atoms. In this more realistic case, the possible wave vectors are a closely spaced set of N values. The integrals over continuous q in the equations of motion become a sum over discrete modes, where it is perfectly acceptable to consider a single term of the sum. For the purposes of the iteration process, it is therefore necessary to treat the integration over modes as a sum over discrete values. This is similar to some calculations in quantum optics, where the discretization of modes can be used to simplify certain calculations, such as the treatment of thermal radiation [109].

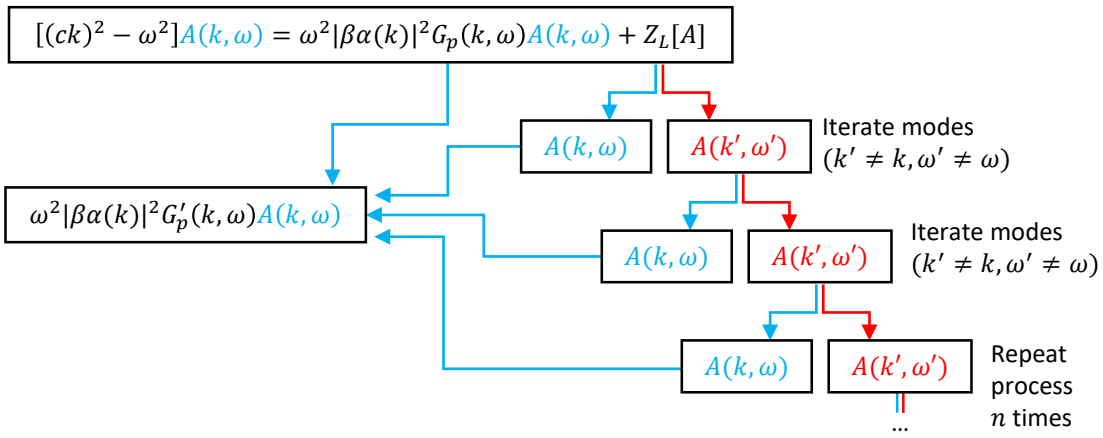

Figure 3.5: Schematic of the second iteration process used to derive a wave equation for the field A. Terms in the initial (k,ω) mode are collected together and those that are not are iterated. The process is ideally repeated until only terms in the initial mode remain, but in practice is terminated after a finite number of steps.

Figure 3.5 describes the second iteration process used to rearrange (3.33) to the form of a wave equation similar to (3.17) of the ML model. At the start of each step, each of the RHS terms of A in the mode (k,ω) of the initial wave are moved to the LHS of the equation and grouped with the existing terms. The equation is then iterated by substituting the new expression into the remaining RHS terms of A in the modes $(k' \neq k, \omega' \neq \omega)$. The RHS terms of A that have returned to the initial mode (k,ω) are once again moved to the LHS and the process is repeated. Each step in the iteration can be thought of as a scattering process, with the overall aim of extracting the waves that scatter back into their initial mode.

The process is terminated after n iterations, at which point all terms up to the order σ^n contain only A terms that have returned to the initial mode and terms of order σ^{n+1} and higher contain those that have not. The higher order terms are once again discarded and

(3.33) now takes the form of a 1D wave equation, similar to (3.17) in the ML model, that is accurate up to the order σ^n:

$$\left\{(ck)^2 - \omega^2 \left[1 + |\beta\alpha(k)|^2 G'_p(k,\omega)\right]\right\} A(k,\omega) = 0, \tag{3.34}$$

where the RHS homogeneous solutions have been omitted and G'_p is identified as the effective Green function of p in the MN model:

$$G'_p(k,\omega) = G_p(k,\omega) + O\left[\sigma\right]. \tag{3.35}$$

Just as the susceptibility (3.18) was extracted from the wave equation (3.17) in the case of the ML model in section 3.1, the effective linear susceptibility of the MN model can be extracted from the wave equation (3.34) in terms of the modified Green function:

$$\chi_{\text{eff}}(k,\omega) = \beta^2 |\alpha(k)|^2 G'_p(k,\omega). \tag{3.36}$$

All that remains is to calculate the $O[\sigma]$ terms in (3.35) resulting from the iteration of the linear A terms in ($k' \neq k, \omega' \neq \omega$) modes due to the nonlinear interaction term. However, even in this simplified 1D model, the iteration procedure rapidly becomes notationally cumbersome. In the next section, a graphical solution to this problem is proposed.

3.4 Nonlinear equations and diagrams

To simplify the vast amount of notation produced using the methods of the previous section, the iteration process is instead expressed through diagrams. While this is hardly a new concept, with Feynman diagrams extensively used in quantum field theory (QFT) [110], it is not typically used outside of a quantum setting. A set of Feynman rules can also be found when solving classical field equations perturbatively [111]. These rules are similar to those of QFT, but with the key difference that Wick contraction cannot be used to close loops and remove pairs of fields. Only tree diagrams are therefore permitted.

Returning to the equations of motion in (3.26)-(3.28), it can be seen that upon iterating a field, it is replaced with either a homogeneous solution (which terminates the iteration process) or the associated Green function accompanied by a coupling term and another field (or fields) that can be iterated further. For example, in (3.28) u is replaced by u_h plus the Green function G_u multiplied by the coupling term σf_2 and an integral over a pp term that can be iterated further.

After every step in the iteration process, each field is represented by a line: A, p and u are wavy, straight and dashed respectively. Green functions for the free fields, which precede additional fields that can be iterated are drawn as full lines, while homogeneous solutions, which cannot be further iterated, are represented by terminated lines. Examples of these are given in Fig. 3.6.

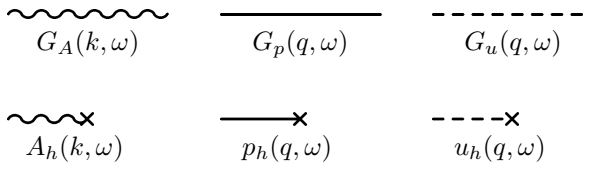

Figure 3.6: Diagram representation of Green functions and homogeneous solutions in the iteration process.

The diagrams are read from left to right and contain these lines joined together in a limited number of ways, determined by the type of coupling in the Lagrangian. Figure 3.7 displays all possible vertices for the current MN model. The linear coupling term in L_{pA} gives a two-line vertex, while the nonlinear coupling in L_{ppu} gives a three-line vertex. Each vertex in a diagram has an associated coupling function from the equations of motion. Both wave vector and frequency must be conserved at each vertex, although Umklapp processes mean this is only true up to multiples of the reciprocal lattice vector. Each undetermined q and ω in the nonlinear vertices must be integrated over all possible values.

In summary:

- Intermediate lines give the corresponding Green function of the free field.
- Terminated lines give the corresponding homogeneous solution.
- Vertices give the corresponding coupling function determined by the Lagrangian.
- Frequency is conserved at each vertex.
- Wave vector is conserved at each vertex, up to multiples of the reciprocal lattice vector for a discrete system.
- An integral is performed over each unknown q and ω.
- Only tree diagrams are permitted.

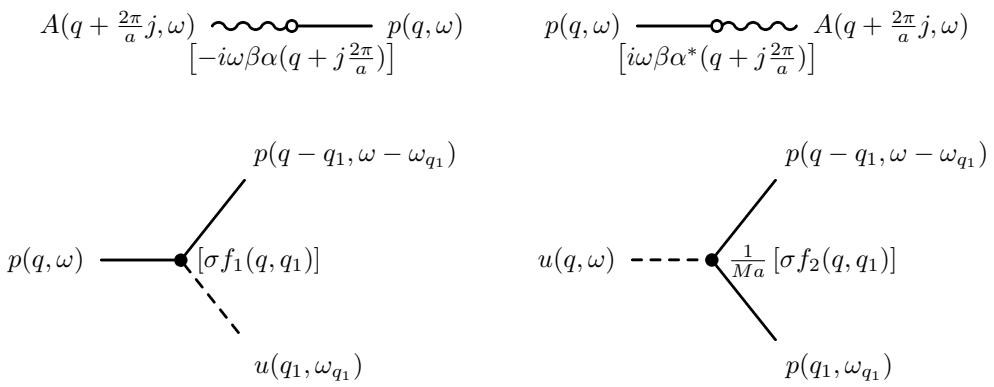

Figure 3.7: The allowed vertices and the corresponding coupling factors for the nonlinear model.

This diagrammatic representation gives an intuitive way of calculating the total Green function in a coupled system by summing over all diagrams that start and end with a field in the same mode. In the absence of coupling, only the "bare" Green function satisfies this condition, but with the addition of vertices due to Lagrangian interactions new diagrams can be found that contribute to the new Green function. This is somewhat similar to the calculation of self-energy in QFT [110].

3.4.1 Applications to the linear model

To demonstrate the capabilities of this diagrammatic approach, the ML model of section 3.1 is considered. In calculating the modified Green function of p dressed with A, denoted G_p^d, an infinite series of diagrams beginning and ending with p in the same mode can be found:

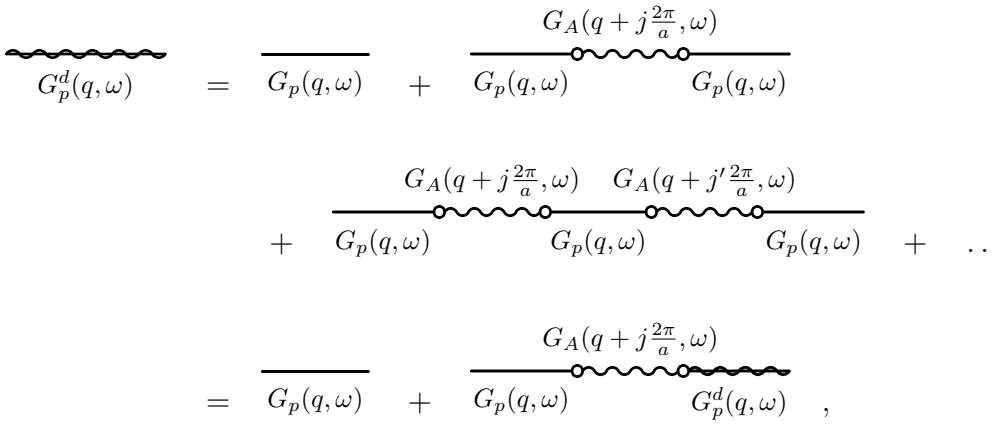

(3.37)

where the infinite sum has been simplified using the Dyson equation [110]. While the wave vector of the p field is limited to the first Brillouin zone, the intermediate A fields are under no such restriction. As a result, Umklapp processes have been included explicitly in these diagrams.

Using the rules previously described, the diagrams in (3.37) can be evaluated to give the equation:

$$\begin{aligned} G_p^d(q,\omega) &= G_p(q,\omega) \\ &+ G_p(q,\omega)\left\{\sum_{j=-\infty}^{\infty}\left[i\omega\beta\alpha^*(q+\tfrac{2\pi}{a}j)\right]G_A(q+\tfrac{2\pi}{a}j,\omega)\left[-i\omega\beta\alpha(q+\tfrac{2\pi}{a}j)\right]\right\}G_p(q,\omega) \\ &+ G_p(q,\omega)\left\{\sum_{j=-\infty}^{\infty}\left[i\omega\beta\alpha^*(q+\tfrac{2\pi}{a}j)\right]G_A(q+\tfrac{2\pi}{a}j,\omega)\left[-i\omega\beta\alpha(q+\tfrac{2\pi}{a}j)\right]\right\}^2 G_p^2(q,\omega) \\ &+ \ldots. \end{aligned} \tag{3.38}$$

This infinite sum can simplified in a similar manner to the diagrams in (3.37) using the Dyson equation to give:

$$\begin{aligned} G_p^d(q,\omega) &= G_p(q,\omega) \\ &+ G_p(q,\omega)\left\{\sum_{j=-\infty}^{\infty}\left[i\omega\beta\alpha^*(q+\tfrac{2\pi}{a}j)\right]G_A(q+\tfrac{2\pi}{a}j,\omega)\left[-i\omega\beta\alpha(q+\tfrac{2\pi}{a}j)\right]\right\}G_p^d(q,\omega). \end{aligned} \tag{3.39}$$

The modified Green function G_p^d can be found by dividing (3.39) by $G_pG_p^d$ to give:

$$\left[G_p^d(q,\omega)\right]^{-1} = \left[G_p(q,\omega)\right]^{-1} - \left\{\omega^2\beta^2\sum_{j=-\infty}^{\infty}\left|\alpha(q+\tfrac{2\pi}{a}j)\right|^2 G_A(q+\tfrac{2\pi}{a}j,\omega)\right\}. \tag{3.40}$$

It can be seen that with the exception of the Dirac delta terms from the expansion of G_A, the sum over reciprocal lattice vectors does not contain any imaginary components. In the $\alpha(z)=\delta(z)$ limit, the identity [112]

$$\pi\cot(\pi x) = \frac{1}{x} + 2x\sum_{j=1}^{\infty}\frac{1}{x^2-j^2} \tag{3.41}$$

can be used to evaluate (3.40) exactly to give

$$G_p^d(q,\omega) = \frac{1}{\omega_0^2(q) - \omega^2 - \frac{\beta^2}{2}\left(\frac{\omega a}{c}\right)\frac{\sin(\omega a/c)}{\cos(\omega a/c)-\cos(qa)}}, \tag{3.42}$$

where the $(\omega + i0^+)$ pole prescription has been omitted for notational brevity.

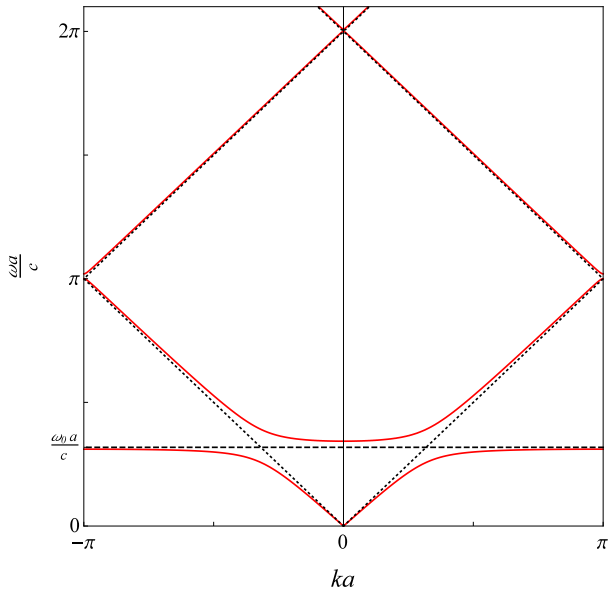

Figure 3.8: The dispersion relation for the modes of p dressed with A in the ML model (red lines), found by equating the denominator of the dressed Green function G_p^d to zero, compared to the "bare" dispersion relations of p (dashed black line) and A (dotted black lines) folded back into the first Brillouin zone by reciprocal lattice vector scattering.

The dispersion relation for p dressed with A is found by satisfying the equation:

$$\left[G_p^d(q,\omega)\right]^{-1} = 0 \tag{3.43}$$

and is shown in Fig. 3.8. The Umklapp processes have the effect of folding the "bare" dispersion relation of A back into the first Brillouin zone, with each j term in (3.40) adding an additional branch. While the Dirac delta function approximation of $\alpha(z)$ is accurate for small k, and therefore small ω in Fig. 3.8, it may not hold at larger frequencies corresponding to the $j \neq 0$ branches of the dispersion relation.

3.5 The effective susceptibility

From a diagrammatic point of view, deriving the effective linear susceptibility χ_{eff} of the MN model is equivalent to calculating the expression for the effective Green function G_p', represented by a straight double line, in the following diagram:

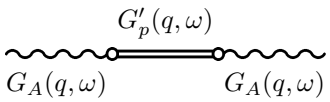

The Green function G'_p is the "free" Green function for p dressed by nonlinear interactions with the lattice vibrations, and represents a sum over the intermediate steps of all diagrams that start and end with A in the same mode, with certain exceptions. The first are diagrams containing intermediate A terms in the initial mode (q, ω), as these can be reduced to multiple copies of the above diagram. The second are diagrams where A appears in multiple "branches" of the various tree diagrams. These can be traced back to the Z_{NL} term in (3.33) that was previously dropped from calculations, as it instead contributed to the nonlinear susceptibility of the MN model. Note that the wave vector q of the initial and final field A is taken to lie within the first Brillouin zone as the primary focus are fields with $\lambda \gg a$ that vary over macroscopic scales.

To calculate G'_p, a summation is performed over all diagrams that start and end with p in the (q, ω) mode, with the exception of those with intermediate terms of $A(q, \omega)$ for the reason described above. Each of the tree diagrams contributing to G'_p will have a "main" branch that starts and ends with $G_p(q, \omega)$ and a number of "side" branches that terminate in homogeneous solutions. The infinite series of diagrams can be collected according to the number of intermediate p steps in the "main" branch of the tree diagram that are in the initial (q, ω) mode:

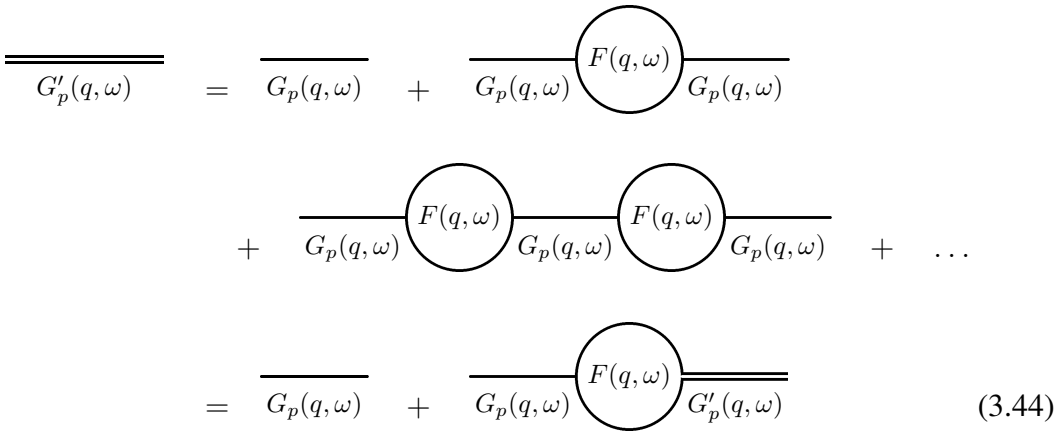

(3.44)

where the Dyson equation [110] has once again been used to simplify the infinite series. The term $F(q, \omega)$ represents a sum over all possible intermediate steps for processes that start and end with $p(q, \omega)$, but do not contain terms of $A(q, \omega)$ (for the reasons described previously) and $p(q, \omega)$ (as the diagram would belong to another term in this series). This entire process can be thought of as the classical counterpart to the calculation of particle self-energy in QFT [110], with the F term playing the role of the one-particle-irreducible diagram.

The derivation of the corresponding expression for G'_p is similar to that of G^d_p in section 3.4.1. The diagram rules in section 3.4 are first used to find the expression for the sum in (3.44):

$$\begin{aligned} G'_p(q,\omega) =& G_p(q,\omega) + G_p(q,\omega)\,[F(q,\omega)]\,G_p(q,\omega) \\ &+ G_p(q,\omega)\,[F(q,\omega)]\,G_p(q,\omega)\,[F(q,\omega)]\,G_p(q,\omega) + \dots \\ =& G_p(q,\omega) + G_p(q,\omega)\,[F(q,\omega)]\,G'_p(q,\omega), \end{aligned} \tag{3.45}$$

which has also been shortened using the Dyson equation. This equation is then divided by $G_pG'_p$ to give:

$$\left[G'_p(q,\omega)\right]^{-1} = [G_p(q,\omega)]^{-1} - F(q,\omega). \tag{3.46}$$

The modified Green function of p in the MN model is therefore expressed in terms of the "free" Green function G_p and the (in general) complex function F. This expression can be substituted into (3.36) to find the effective linear susceptibility for the MN model:

$$\chi_{\text{eff}}(q,\omega) = \frac{\beta^2|\alpha(q)|^2}{\{\omega_0^2(q) - \mathbb{R}\text{e}\,[F(q,\omega)]\} - \omega^2 - i\,\mathbb{I}\text{m}\,[F(q,\omega)]}, \tag{3.47}$$

where the real and imaginary parts of F have been separated. By comparing (3.47) to the Lorentz model in (2.19), it can be seen that $\mathbb{R}\text{e}[F]$ acts to rescale the resonant frequency of the ML model and, more importantly, $\mathbb{I}\text{m}[F]$ acts as an effective damping term $\gamma\omega$, which is required for broadband absorption.

All that remains is to calculate the expression for $F(q,\omega)$. When considering the diagrams in (3.44) that start and end with G_p, it is important to remember that in the iteration process described in section 3.3, only the wave vector and frequency of the initial mode are known. Nonlinear interactions lead to an integration over q and ω of the final mode. The terms that contribute to the effective linear susceptibility are found by picking out just a single term from these integrals, a process that is justified by treating the infinite chain MN model as the limit of a large, but finite medium.

This process must be repeated in the calculation of $F(q,\omega)$ from the diagrams that start and end with G_p. In each case, the expression for the diagrams must be derived for the general case when all q and ω beside the initial mode are left unspecified. Once this is calculated, the contribution to F and the resulting effective linear susceptibility χ_{eff} are found by picking out the term in the final integral that returns the p to the initial mode (q,ω).

The various terms in $F(q,\omega)$ can be grouped according to the number of nonlinear coupling coefficients to give a power series in σ:

$$F(q,\omega) = \sigma^2 F_2(q,\omega) + \sigma^3 F_3(q,\omega) + \sigma^4 F_4(q,\omega) + \ldots, \tag{3.48}$$

with each term F_n representing a sum over all diagrams containing n nonlinear vertices. Note that there is no F_1 term, as the nonlinear coupling function f_1 is zero in this case. As it would be impossible to calculate every F_n expression, the next sections focus on the first few terms in the series.

3.5.1 Leading-order F terms

To calculate the expression for F_2, the leading-order term in the F power series, diagrams that start and end with G_p and contain two nonlinear vertices must be considered. These are shown in Fig. 3.9 for the general case where only the initial mode of p is specified. The Green function G_p^d of p dressed with A, defined in (3.40), has been used to sum over all possible diagrams where the intermediate p field has coupled to A and back again. For each diagram, the contribution to F_2 is found by using the rules in section 3.4 to find the expression in the general case, before picking out the specific term in the final integral that returns p to the initial mode. By specifying that $(q - q_1 - q_2, \omega - \omega_{q_1} - \omega_{q_2}) = (q,\omega)$, the expression for each diagram reduces to $G_p(q,\omega)F_{2p}(q,\omega)G_p(q,\omega)$ and $G_p(q,\omega)F_{2u}(q,\omega)G_p(q,\omega)$, which are labeled according to the type of intermediate field in the diagram.

The diagram in Fig. 3.9 with intermediate p terms is first considered. In the case where only the initial mode is specified, the diagrams rules in section 3.4 give the corresponding function:

$$\begin{aligned} G_p(q,\omega)\Bigg\{ &\int_{-\pi/a}^{\pi/a} dq_1 \int_{-\infty}^{\infty} d\omega_1 \left[\sigma f_1(q,q_1)\right] u_h\left(q_1,\omega_1\right) G_p^d(q-q_1,\omega-\omega_1) \\ \times &\int_{-\pi/a}^{\pi/a} dq_2 \int_{-\infty}^{\infty} d\omega_2 \left[\sigma f_1(q-q_1,q_2)\right] u_h\left(q_2,\omega_2\right) G_p(q-q_1-q_2,\omega-\omega_1-\omega_2)\Bigg\}, \end{aligned} \tag{3.49}$$

where the integration runs over all possible final modes. This expression contains the homogeneous solution u_h, which must satisfy the equation in (3.32) and is usually expressed using delta functions in frequency:

$$u_h(q,\omega) = U(q)\delta\left[\omega - \nu_0(q)\right] + U^*(-q)\delta\left[\omega + \nu_0(q)\right]. \tag{3.50}$$

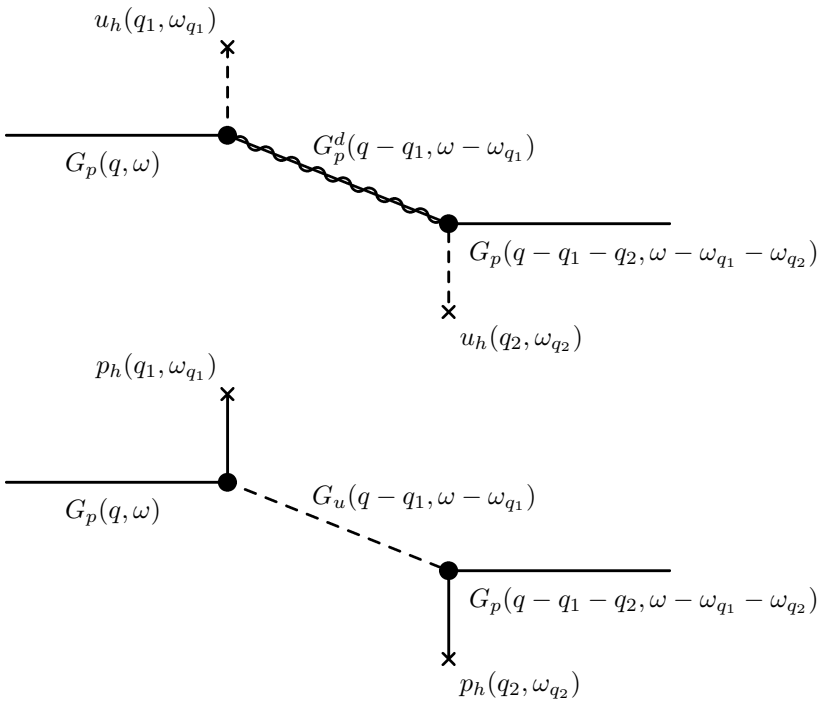

Figure 3.9: All diagrams starting and ending with G_p and containing two nonlinear vertices. The dressed Green function G_p^d in (3.42) is used due to the linear coupling term. After only considering diagrams that return to the initial mode by specifying that $(q - q_1 - q_2, \omega - \omega_{q_1} - \omega_{q_2}) = (q, \omega)$, the expression for each diagram reduces to $G_p(q,\omega)F_{2p}(q,\omega)G_p(q,\omega)$ (top) and $G_p(q,\omega)F_{2u}(q,\omega)G_p(q,\omega)$ (bottom).

The complex conjugate term is to ensure u_h satisfies the required symmetry conditions. The product of homogeneous solutions in (3.49) can therefore be expanded to four terms:

$$\begin{aligned} u_h(q_1,\omega_1)u_h(q_2,\omega_2) = \quad & U(q_1)U^*(-q_2)\delta\left[\omega_1 - \nu_0(q_1)\right]\delta\left[\omega_2 + \nu_0(q_2)\right] \\ & + U^*(-q_1)U(q_2)\delta\left[\omega_1 + \nu_0(q_1)\right]\delta\left[\omega_2 - \nu_0(q_2)\right] \\ & + U(q_1)U(q_2)\delta\left[\omega_1 - \nu_0(q_1)\right]\delta\left[\omega_2 - \nu_0(q_2)\right] \\ & + U^*(-q_1)U^*(-q_2)\delta\left[\omega_1 + \nu_0(q_1)\right]\delta\left[\omega_2 + \nu_0(q_2)\right]. \end{aligned} \tag{3.51}$$

However, the contribution to F is extracted from (3.49) only when the final mode of the corresponding diagram in Fig. 3.9 is equal to the initial mode (q, ω). This requirement imposes the conditions $q_1 + q_2 = 0$ and $\omega_1 + \omega_2 = 0$, which can only be satisfied by the first two terms in (3.51) because $\nu_0(q) > 0$, as defined in (3.25). The latter two terms are therefore omitted in subsequent calculations as they will not contribute to F_{2p}.

A functional form of $U(q)$ must also be specified to evaluate the integral in (3.49) and the thermal state is a natural choice for the homogeneous solution. The average amplitude of a harmonic oscillator in thermal equilibrium is inversely proportional to the frequency [113], giving:

$$U(q) = U_0 \left[\frac{\nu_0(0)}{\nu_0(q)}\right]. \tag{3.52}$$

Equation (3.52) and the first two terms of (3.51) are substituted into (3.49) to give:

$$\begin{aligned} G_p(q,\omega) \int_{-\pi/a}^{\pi/a} dq_1 \int_{-\pi/a}^{\pi/a} dq_2 \left[\sigma^2 f_1(q,q_1) f_1(q-q_1,q_2)\right] |U_0|^2 \left[\frac{\nu_0^2(0)}{\nu_0(q_1)\nu_0(q_2)}\right] \\ \times \Big[\; G_p^d(q-q_1,\omega-\nu_0(q_1)) G_p(k-q_1-q_2,\omega-\nu_0(q_1)+\nu_0(q_2)) \\ + G_p^d(q-q_1,\omega+\nu_0(q_1)) G_p(q-q_1-q_2,\omega+\nu_0(q_1)-\nu_0(q_2)) \Big], \end{aligned} \tag{3.53}$$

which still describes the diagram in Fig. 3.9 that ends in an arbitrary mode. The contribution to $F(q,\omega)$ is found by extracting the specific terms in the integrals of (3.53) that ensure the final mode is equal to the initial mode. As discussed previously in section 3.3, this is performed by treating the q integral of the infinite chain as a limit of the q_n sum of the finite chain, where it is perfectly acceptable to consider only a single wave vector.

The specific term $q_2 = -q_1$ is extracted from the second integral of (3.53) and the entire expression can be reduced to the form:

$$G_p(q,\omega)\Big\{\sigma^2 F_{2p}(q,\omega)\Big\}G_p(q,\omega), \tag{3.54}$$

where

$$\begin{aligned} F_{2p}(q,\omega) = \int_{-\pi/a}^{\pi/a} dq_1 \, a|f_1(q,q_1)|^2 \left|\frac{U_0}{a}\right|^2 \left[\frac{\nu_0(0)}{\nu(q_1)}\right]^2 \\ \times \left[G_p^d(q-q_1,\omega-\nu_0(q_1)) + G_p^d(q-q_1,\omega+\nu_0(q_1))\right] \end{aligned} \tag{3.55}$$

and the additional factor of $1/a$ is to account for the switch between the continuous integral and the discrete sum. It is important to note that this choice of q_2 leads to complex conjugate pairs of both the homogeneous solution $U(q)$ and the nonlinear coupling function f_1. The resulting factors of $|U_0|^2$ and $|f_1(q,q_1)|^2$ in (3.55) ensure that the integral over the intermediate modes gives a constructively adding quantity, which is not always the case for the higher-order terms of F.

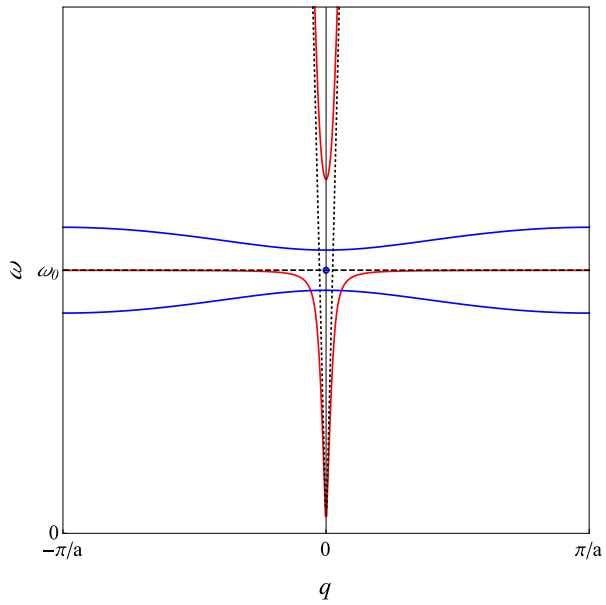

Figure 3.10: Graphical representation (not to scale) of the q_1 integration in (3.55) used to calculate F_{2p}. Starting from an initial mode $(q_{\text{in}} = 0, \omega_{\text{in}} = \omega_0)$, denoted by the blue dot, the integration is performed over the intermediate modes $(q_{\text{in}} - q_1, \omega_{\text{in}} \pm \nu_0(q_1))$ (blue lines). Intersections with the dispersion relation of the intermediate step (red line) in the diagram indicate the presence of a pole in the integrand, which lead to an imaginary component of F_{2p}.

Figure 3.10 shows a graphical representation of the q_1 integral in (3.55) for the example initial mode $(q = 0, \omega = \omega_0)$. The blue lines indicate the q_1 integration over the intermediate modes $(q - q_1, \omega - \nu_0(q_1))$ and $(q - q_1, \omega + \nu_0(q_1))$, while the red lines indicate the modes where the denominator of the Green function G_p^d is equal to zero. It can be seen that the integrand in (3.55) can contain one or more of poles of the intermediate G_p^d terms, which present several challenges when evaluating the integral.

The $(\omega + i0^+)$ pole prescription of G_p^d makes it preferable to perform an integration over frequency and the relationship between q_1 and ω_1 imposed by the homogeneous solutions in (3.50) provides the obvious choice for the a new integration variable using (3.25):

$$\nu_1 = \nu_0(q_1) = \sqrt{\nu_0^2 + \kappa_1^2 - \kappa_1^2 \cos(q_1 a)}. \tag{3.56}$$

Using the standard rules for integration by substitution, the q_1 integral over the range $-\pi/a \to \pi/a$ becomes a ν_1 integral over the range $\nu_0 \to \sqrt{\nu_0^2 + 2\kappa_1^2}$, demonstrated here

for the arbitrary functional Φ:

$$\int_{-\pi/a}^{\pi/a} dq_1 \Phi[q_1, \nu_0(q_1)] = \int_{\nu_0}^{\sqrt{\nu_0^2+2\kappa_1^2}} d\nu_1 \rho(\nu_1) \Big\{ \Phi[Q(\nu_1), \nu_1] + \Phi[-Q(\nu_1), \nu_1] \Big\}, \quad (3.57)$$

where:

$$\frac{1}{\rho(\nu_1)} = \left| \frac{d\nu_1}{dq_1} \right| \quad (3.58)$$

and

$$Q(\nu_1) = \arccos\left(1 + \frac{\nu_0^2 - \nu_1^2}{\kappa_1^2}\right), \quad (3.59)$$

which is the inverse of (3.56) with the properties $Q(\nu_1) = Q(-\nu_1)$ and $Q(\nu_1) > 0$. After changing the integration variable in to ν_1 and changing the sign of ν_1 in the second Green function, F_{2p} takes the form:

$$F_{2p}(q,\omega) = \int_\nu d\nu_1 \left| \frac{U_0}{a} \right|^2 \left(\frac{\nu_0}{\nu_1} \right)^2 \frac{a}{\rho(\nu_1)} \times \Big[\; |f_1(q, Q(\nu_1))|^2 G_p^d(q - Q(\nu_1), \omega - \nu_1) + |f_1(q, -Q(\nu_1))|^2 G_p^d(q + Q(\nu_1), \omega - \nu_1) \Big]. \quad (3.60)$$

where the integral $\int_\nu$ is over the two ranges $-\sqrt{\nu_0^2 + 2\kappa_1^2} \to -\nu_0$ and $\nu_0 \to \sqrt{\nu_0^2 + 2\kappa_1^2}$, representing the upper and lower branches in Fig. 3.10 respectively.

The integrand of (3.60) contains a number of poles of G_p^d, labeled $\nu_{\text{pole}}^{(n)}$, which are found when

$$\left[G_p^d(q - Q(\nu_1), \omega - \nu_1)\right]^{-1} = 0 \qquad \text{or} \qquad \left[G_p^d(q + Q(\nu_1), \omega - \nu_1)\right]^{-1} = 0. \quad (3.61)$$

The $(\omega + i0^+)$ pole prescription in G_p^d conveniently splits the calculation into two parts: a real principal-value integral and an imaginary component associated with the poles of G_p^d. While the real part of F_{2p}, which acts to rescale the resonant frequency of χ_{eff} in (3.47), must be calculated numerically, the imaginary part can be found analytically using the residue theorem [114].

The pole prescription shifts the pole of G_p^d in (3.60) into the upper-half complex plane of ν_1. By performing an integral over a semi-circle with radius r centred on each of the poles $\nu_1 = \nu_{\text{pole}}^{(n)}$ in the lower-half complex plane and taking the limit $r \to 0$, an expression

for the imaginary part of F_{2p} can be found [114] :

$$\begin{aligned}
&\mathbb{Im}[F_{2p}(q,\omega)] = \\
&\pi \sum_n \mathrm{Res}\left[\left|\frac{U_0}{a}\right|^2 \left(\frac{\nu_0}{\nu_1}\right)^2 \frac{a}{\rho(\nu_1)} |f_1(q, Q(\nu_1))|^2 G_p^d(q - Q(\nu_1), \omega - \nu_1), \nu_{\mathrm{pole}}^{(n)} \right] \\
&+ \pi \sum_n \mathrm{Res}\left[\left|\frac{U_0}{a}\right|^2 \left(\frac{\nu_0}{\nu_1}\right)^2 \frac{a}{\rho(\nu_1)} |f_1(q, -Q(\nu_1))|^2 G_p^d(q + Q(\nu_1), \omega - \nu_1), \nu_{\mathrm{pole}}^{(n)} \right],
\end{aligned} \tag{3.62}$$

where $\mathrm{Res}[f(z), z_0]$ denotes the residue of $f(z)$ at $z = z_0$. For the simple poles in (3.62), the following definition is used [114]:

$$\mathrm{Res}\left[\frac{a(z)}{b(z)}, z_0\right] = \frac{a(z_0)}{b'(z_0)}. \tag{3.63}$$

The $\mathbb{Im}[F_{2p}]$ result can then be used, along with the Kramers-Kronig relations in (2.9), to check the numerical calculation of $\mathbb{Re}[F_{2p}]$.

The presence of an imaginary component in the terms of F confirms Hopfield's proposal that nonlinear interactions, specifically between electric dipoles and lattice vibrations, can lead to an effective damping term in the susceptibility. While the mode of the p field directly coupled to light did not satisfy the dispersion relation $[G_p]^{-1} = 0$, the indirectly coupled modes of u and p dressed with A did satisfy their respective dispersion relations $[G_u]^{-1} = 0$ and $[G_p^d]^{-1} = 0$ and thus acted as the absorbing states of the medium. Once again, comparisons can be made to the calculation of self-energy [110] in QFT, where imaginary components of the propagator are found when the virtual particles lie "on-shell" and satisfy their respective dispersion relations.

A similar expression to (3.60) exists for the other diagram in Fig. 3.9, denoted F_{2u}, but there are significant differences in the result. The intermediate step in F_{2p} is p dressed with A and the corresponding dispersion relation in (3.43) runs over almost all frequencies, as seen in Fig. 3.8. As a result of this, poles are almost always present in the integrand (3.60) and F_{2p} has an imaginary component for most frequencies of the initial mode. In contrast, the intermediate step in the F_{2u} is the "bare" field u. The corresponding dispersion relation $\nu_0^2(q) - \omega^2 = 0$ runs over the significantly smaller frequency range $-\sqrt{\nu_0^2 + 2\kappa^2} \to -\nu_0$ and $\nu_0 \to \sqrt{\nu_0^2 + 2\kappa^2}$, as seen in Fig. 3.3. The first few leading order F terms with an intermediate u step will therefore not contain poles in the integral for a large range of initial frequencies. For example, F_{2u} has no imaginary component near ω_0 for the model parameters used later in this chapter. The F_{2u} term is subsequently ignored in calculations, leaving the F_{2p} term the sole contribution to F_2.

3.5.2 Higher-order F terms

The higher-order terms of F can be calculated in a similar manner to F_{2p}, but additional considerations must be made when extracting the expressions from diagrams that end in an arbitrary mode. In the two-vertex cases in Fig. 3.9, the calculation of F terms requires the final mode $(q - q_1 - q_2, \omega - \omega_1 - \omega_2)$ to equal the initial mode (q, ω). This imposes the conditions $q_2 = -q_1$ and $\omega_2 = -\omega_1$. The second nonlinear interaction is therefore exactly the opposite of the first one. The resulting expressions for F_2 contains complex conjugate pairs of both coupling functions and homogeneous solutions. The higher order terms of F are under no such restriction, and as such the corresponding expressions for a diagram can contain a mixture of homogeneous solutions and coupling functions of different frequencies and wave vectors. Upon integration, these can interfere destructively. As a result, only diagrams with complex conjugate pairs that interfere constructively are retained, as these will be the dominant contributions to F.

As none of the diagrams with an odd number of nonlinear vertices can satisfy the conditions for complex conjugate pairs, the next contribution to F belongs to the F_4 group. While there are a number of diagrams within this group, only the diagram in Fig. 3.11 is considered as the intermediate steps of p dressed with the A field are the same as in the diagram for F_{2p}. As previously stated, the corresponding dispersion relation in (3.43) runs over almost all frequencies, ensuring the presence of poles (and the resulting imaginary residue terms) in the integrand, which is not the case for all F_4 diagrams

The corresponding F expression for Fig. 3.11, denoted F_{4p}, is found by choosing the specific homogeneous solutions

$$u_h(q_1, \omega_1) = u_h(-q_4, -\omega_4), \qquad u_h(q_2, \omega_2) = u_h(-q_3, -\omega_3), \tag{3.64}$$

to give complex conjugate pairs in the resulting integral. Under these conditions, the expression for this diagram reduces to $G_p(q,\omega)F_{4p}(q,\omega)G_p(q,\omega)$ and the central part of the diagram is the same as the one used to calculate F_{2p} in Fig. 3.9. The final expression for F_{4p} can therefore be expressed in terms of the previously calculated F_{2p}:

$$\begin{aligned} &F_{4p}(q,\omega) = \\ &\int_\nu d\nu \left|\frac{U_0}{a}\right|^2 \left(\frac{\nu_{\min}}{\nu}\right)^2 \frac{a}{\rho(\nu)} \Big\{ |f_1(q, Q(\nu))|^2 \left[G_p^d(q - Q(\nu), \omega - \nu)\right]^2 F_{2p}(q - Q(\nu), \omega - \nu) \\ &\qquad + |f_1(q, -Q(\nu))|^2 \left[G_p^d(q + Q(\nu), \omega - \nu)\right]^2 F_{2p}(q + Q(\nu), \omega - \nu) \Big\}, \end{aligned} \tag{3.65}$$

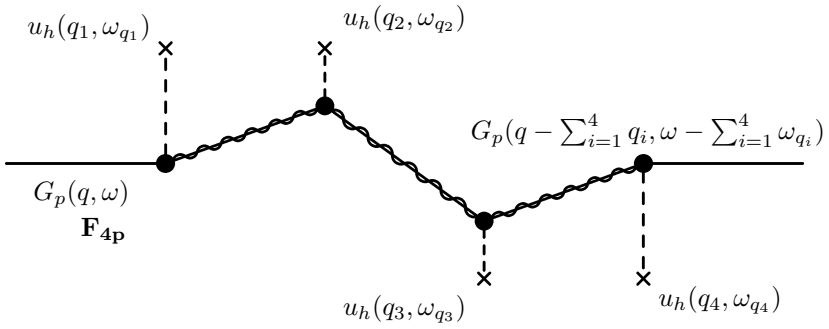

Figure 3.11: Diagram starting and ending with G_p and containing four nonlinear vertices, which gives a contribution to F_4, which we denote F_{4p} based on the intermediate steps. After only considering diagrams that return to the initial mode, the expression for this diagram reduces to $G_p(q,\omega)F_{4p}(q,\omega)G_p(q,\omega)$ The additional restrictions on higher order F terms to give complex conjugate pairs of homogeneous solutions and vertex coupling functions reduce the middle portion to the F_{2p} diagram in Fig. 3.9.

where the poles in the intermediate G_p^d terms are dealt with in the same manner as those in the F_{2p} calculations.

When calculating the imaginary components of F_{4p}, it is important to note that if the middle step in the iteration process in Fig. 3.11 satisfies the dispersion relation $[G_p^d]^{-1} = 0$, the relatively small frequency range of the homogeneous solutions u_h mean the denominator of the other Green functions in (3.65) will also be close to zero. Because of this, the magnitude of the resulting term $\sigma^4 F_{4p}$ may be comparable to the lower-order terms in the F power series (3.48), even with the additional powers of the small nonlinear coupling coefficient σ.

3.6 Numerical calculations

The frequency and wave vector dependence of the F terms, and the resulting effective susceptibility, in section 3.5 are not readily apparent from an inspection of (3.60) and (3.65). This section presents the results of a numerical calculation for F_{2p} and χ_{eff} using the model parameters in Table 3.1. These have been rescaled to dimensionless variables, taking inspiration from the G_p^d expression in (3.42) to rescale frequencies by a/c, where $a = 3\text{Å}$ is a typical dielectric lattice constant and c is the speed of light.

The resonant frequency $\omega_0 a/c = 0.003$ corresponds to a photon energy of 1.975eV (477.44THz), which lies in the visible region. The values of τ_1 (3.5) and σ (3.29) are related to each other, as both given in terms of V_0, which dictates the strength of the r^{-3} dipole-dipole in (3.21). The value of $\tau_1 a/c = 0.0001$ was chosen so that $\omega_0(q)$ remained approximately constant over the first Brillouin zone, simplifying the numeric calculations. The corresponding value of σ and the amplitude U_0 of the homogeneous solution (3.52) ensure that F_{2p} is the dominant term in $\sigma^n F_n$ series (3.48) for small q and perturbation theory is valid. The confining potential strength ν_0 and the nearest-neighbour coupling strength κ_1 in the particle displacement Lagrangian (3.23) lead to an expression for $\nu_0(q)$ in (3.25) that runs over a typical frequency range for lattice vibrations in a solid of approximately $1.6 \rightarrow 10\text{THz}$ [115]. Finally, the $z_0 \rightarrow 0$ limit of $\alpha(z)$ was taken, reducing the expression in (3.6) to a Dirac delta function. This allowed the sum over reciprocal lattice constants in the expression for G_p^d (3.40) to be evaluated exactly to the result in (3.42). The general formulas presented in section 3.5 are not specific to these values and can be used for any medium, under the condition that perturbation theory must be valid.

Table 3.1: List of model parameters, rescaled to dimensionless quantities

Parameter	Value
a	3Å
$\omega_0 a/c$	0.003
$\tau_1 a/c$	0.0001
$\nu_0 a/c$	0.00001
$\kappa_1 a/c$	0.000049
$\beta a/c$	0.0012
$\sigma a^2/c^2$	7.6×10^{-10}
U_0/a	0.04

The model parameters in Table 3.1 are not intended to represent a specific medium and are partly chosen to ensure that F_{2p} is the dominant term in F for small q. The choice of β, which is the coupling coefficient of the linear interaction between p and A in (3.3), is especially important due to the role it plays in the Green function of p dressed with A given in (3.42). The dispersion relation of intermediate step in the F_{2p} process in Fig. 3.9 is given by $[G_p^d]^{-1} = 0$ and is shown in Fig. 3.8. The size of the frequency gap in the

dispersion relation near ω_0 is determined by the value of β. If β and the band gap are too large, the F_{2p} integral over intermediate modes in (3.60) will not include any poles of the intermediate G_p^d Green functions for initial frequencies near ω_0. As a result, the imaginary terms of F_{2p} in (3.62) will not be present. Conversely, if β is too small, the integral will contain poles from both the upper and lower branches of the dispersion relation in Fig. 3.8. In this case, the imaginary residues in (3.62) can act to cancel each other out. In both of these scenarios, one of the higher-order terms in the $\sigma^n F_n$ series (3.48), such as F_{4p} in (3.65), will become the dominant term of F. The value of β was therefore chosen to lie in the intermediate range, where $\mathbb{I}\mathrm{m}[F_{2p}(q,\omega)]$ dominates the F result for small values of the initial wave vector q.

3.6.1 Frequency dependence

The frequency dependence of $F(q,\omega)$ and the resulting χ_{eff} were considered by setting the initial wave vector $q = 0$. Figure 3.12 shows the real and imaginary components of F_{2p} for a frequency range centred around $\omega_0 a/c = 0.003$, which were found to satisfy the Kramers-Kronig relations. The dominant features in the results are the large peaks in $\mathbb{I}\mathrm{m}[F_{2p}(q,\omega)]$ above and below ω_0. These occur when the F_{2p} integration (3.60) contains poles of the intermediate Green function G_p^d that lie of the "flat" part of the lower branch dispersion relation, as seen in Fig. 3.8. The shape of the peaks is determined by the coupling function $f_1(q,q_1)$ in (3.30) and the specific form of the homogeneous solutions $U(q)$ in (3.52). The value of $\mathbb{I}\mathrm{m}[F_{2p}]$ in the intermediate region is smaller, but nonzero, providing the sought after damping term in the effective susceptibility (3.47) at the resonant frequency.

With a nonzero imaginary component of F, the imaginary part of the effective susceptibility in (3.47) can be written as:

$$\mathbb{I}\mathrm{m}[\chi_{\text{eff}}(q,\omega)] = \frac{|\alpha(q)|^2\beta^2\,\mathbb{I}\mathrm{m}\left[F(q,\omega)\right]}{\left\{\omega_0^2(q) - \mathbb{R}\mathrm{e}\left[F(q,\omega)\right] - \omega^2\right\}^2 + \left\{\mathbb{I}\mathrm{m}\left[F(q,\omega)\right]\right\}^2}, \tag{3.66}$$

in contrast to the Dirac-delta function (3.15) of the ML model in section 3.1. The resonant peak in (3.66) now occurs when $\omega^2 = \omega_0^2(q) - \mathbb{R}\mathrm{e}\left[F(q,\omega)\right]$, but the small value of σ and the shape of $\mathbb{R}\mathrm{e}\left[F_{2p}(q,\omega)\right]$ in Fig. 3.12 mean that the difference to resonant frequency is negligible. The peaks of $\mathbb{I}\mathrm{m}\left[F_{2p}\right]$ in Fig. 3.12 will also give features in the imaginary susceptibility above and below ω_0. However, these will be several orders of magnitude smaller than the $\mathbb{I}\mathrm{m}[\chi_{\text{eff}}]$ resonant peak as the previously mentioned resonance condition will not be satisfied.

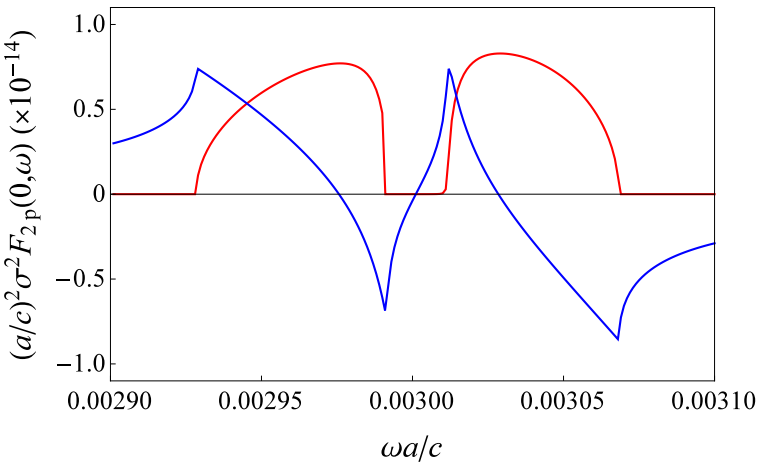

Figure 3.12: $\mathbb{I}\mathrm{m}[F_{2p}]$ (red) and $\mathbb{R}\mathrm{e}[F_{2p}]$ (blue) rescaled to dimensionless variables in the frequency region near $\omega_0 = 0.003$ for $q = 0$. Note that the imaginary part of F_{2p} is small, but nonzero at ω_0. The real and imaginary parts are related by the Kramers-Kronig relations.

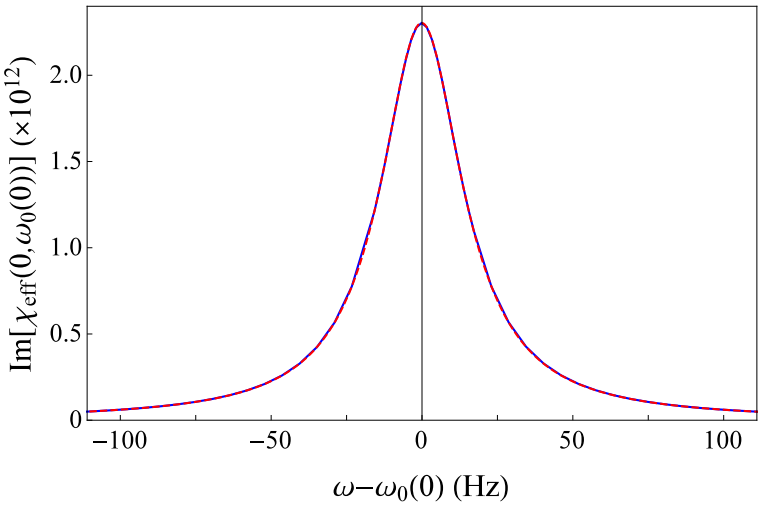

Figure 3.13: The frequency dependence of $\mathbb{I}\mathrm{m}\left[\chi_{\mathrm{eff}}\right]$ in (3.66) (blue line) using the leading-order term F_{2p} when $q = 0$. The resonant frequency of the susceptibility is effectively unchanged by $\mathbb{R}\mathrm{e}\left[F_{2p}\right]$. The calculated susceptibility is extremely well fitted by the Lorentz model (red dashed line) in (2.19).

Figure 3.13 shows the frequency dependence of the imaginary part of the effective linear susceptibility in (3.66) at $q = 0$, using only the F_{2p} component of the F power series in (3.48). A peak in $\mathbb{I}\mathrm{m}\left[\chi_{\mathrm{eff}}\right]$ is found at the resonant frequency $\omega = \omega_0(0)$, which has remained effectively unchanged by the presence of $\mathbb{R}\mathrm{e}[F_{2p}]$ in the denominator of

(3.66). Most importantly, the resonant peak in Fig. 3.13 now displays the broadband absorption that has been the goal of this chapter, verifying the original proposal made by Hopfield. In addition to this, the complex effective linear susceptibility χ_{eff} can also be described almost exactly by the Lorentz model:

$$\chi(\omega) = \frac{\omega_p^2}{\omega_T^2 - \omega^2 - i\gamma\omega}, \qquad \mathbb{Im}[\chi(\omega)] = \frac{\omega_p^2 \gamma\omega}{(\omega_T^2 - \omega^2)^2 + (\gamma\omega)^2}, \tag{3.67}$$

once again matching the predictions made by Hopfield in his original paper. The imaginary part of (3.67) is shown in Fig.3.13 for the model parameters $\omega_T = \omega_0(0) \approx 477\text{THz}$, $\omega_p \approx \beta \approx 190\text{THz}$ and $\gamma \approx 33\text{Hz}$, which provide an almost-perfect fit to $\mathbb{Im}\left[\chi_{\text{eff}}\right]$. This result is in stark contrast to the phenomenological reservoir [23], where a specific and highly artificial frequency-dependent coupling function must be used to recover the Lorentz model. The agreement between the resonant peak in Fig. 3.13 and the Lorentz model in (3.67) was found without any special considerations to the form of nonlinear coupling, which was found to emerge naturally from the r^{-3} dipole-dipole interaction.

The excellent fit to the Lorentz model is likely due to the shape of F_{2p} in Fig. 3.12. By comparing (3.66) to (3.67), it can be seen that $\mathbb{Im}\left[F_{2p}\right]$ is the equivalent term to $\gamma\omega$ in the Lorentz model. The imaginary part of F_{2p} does not vary rapidly over the central frequency range between the two peaks in Fig. 3.12 and so $\mathbb{Im}\left[F_{2p}\right]$ in (3.66) can therefore be treated as a constant over the narrow frequency range of the resonant peak in Fig. 3.13. The same argument can also be applied to the corresponding term of $\gamma\omega$ in the Lorentz model (3.67), which does not vary significantly over the small range of the resonant peak in Fig. 3.13. The excellent agreement between χ_{eff} and the Lorentz model is therefore due to the fact that the damping term of each model can be treated as a constant over the width of the resonant peak. Wider peaks in the susceptibility will require the value of F to increase with frequency to match the $\gamma\omega$ term of the Lorentz model, which is already found in Fig. 3.13.

While the resulting values for the susceptibility are clearly unrealistic, with the maximum value of 2.4×10^{12} for $\mathbb{Im}[\chi_{\text{eff}}]$ in Fig. 3.13 being several orders of magnitude larger than the values found in a real dielectric [85], the aim of this chapter was simply to verify Hopfield's proposal that nonlinear interactions would lead to broadband absorption and a damping term in the susceptibility. The extreme size and sharpness of the imaginary susceptibility peak is due to the small value of σ and the use of perturbation theory to find F. A larger σ would mean that a higher-order term in the F power series would dominate the final expression, which would require calculating the expressions for more advanced

diagrams with a larger number of nonlinear interactions. Achieving realistic results for F would likely require the consideration of significantly more diagrams than described here, in addition to many of the other nonlinear interaction terms that were previously omitted. Examples include the higher-order expansions of the r^{-3} dipole-dipole coupling in (3.21) or non-parabolic terms in the confining potential of the Lagrangian L_u (3.19). Such a calculation is far beyond the scope of this thesis and would require significant computational power.

3.6.2 Wave vector dependence

Information on the spatial dispersion of materials is somewhat limited in comparison to temporal dispersion. Typically, this is restricted to the q-dependent resonant frequency in the Lorentz model, as described in section 2.1.5. This section investigates the wave vector dependence of $\mathbb{I}\mathrm{m}\left[F(q,\omega)\right]$, which corresponds to the damping term $\gamma\omega$ in the Lorentz model. Although this has been measured in some cases [116], this behaviour is generally overlooked [86].

Figure 3.14 compares imaginary parts of the leading-order term $[F_{2p}]$ in (3.60) and the higher-order term $[F_{4p}]$ in (3.65) as a function of q. These values determine the effective damping of the resonance in the effective susceptibility (3.66) and are given for the initial frequency $\omega_0(q)$, as the shift in the resonant frequency due to $\mathbb{R}\mathrm{e}[F]$ was found to be negligible. It can be seen that $\mathbb{I}\mathrm{m}[F_{2p}]$ increases with q at first, before approaching zero as q approaches the edge of the Brillouin zone. Using the model parameters in table 3.1, the imaginary components of F_{2p} for initial frequencies near ω_0 are a result of the q_1 integral overlapping the lower branch of the G_p^d dispersion relation. For small initial q, as seen in Fig. 3.10, the residue terms have similar values due to the symmetry of the system. The sum over residues in (3.62) is therefore constructive and F_{2p} is the dominant term in the F sum. However, as the initial wave vector moves outside the "light cone" described by $\omega = ck$, the residue in the same half of the Brillouin zone as q_{in} changes sign and begins to cancel out the other residue. The underlying reasons behind this behaviour are quite complex. Thanks to the definition in (3.63), the residue can roughly be thought of in terms of the gradient of the dispersion relation at the intersection with the integration path, which is the location of the pole. When q is outside of the light cone, as seen in Fig. 3.15, the gradients of the function at the two intersections are roughly equal and opposite. The corresponding residues therefore also act to cancel each other out.

In cases such as this, where cancellations cause a leading-order term in the F sum to

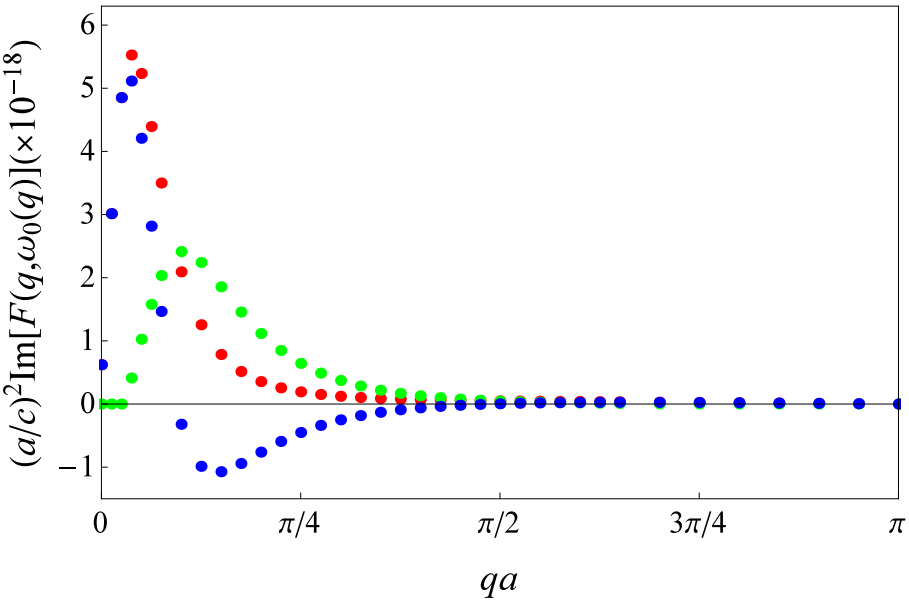

Figure 3.14: Imaginary components of $\sigma^2 F_{2p}$ (blue) and $\sigma^4 F_{4p}$ (green) rescaled to a dimensionless quantity. The overall sum (red) is dominated by the leading-order term F_{2p} near $q = 0$. At larger q, the residues in F_{2p} cancel each other out and the higher-order term F_{4p} dominates the result. The residues of this term also begin to cancel as $q \to \pi/a$ and a full q dependence would require calculating many more higher-order F terms.

approach zero, one of the higher-order terms will instead dominate the result. This can be seen in Fig. 3.14, where F_{4p} gives the largest contribution to the F sum for intermediate q values. As previously described in section 3.5.2, if the denominators of the additional G_p^d Green functions in (3.65) are close to zero, the magnitude of $\sigma^4 F_{4p}$ can be comparable to that of the lower-order term despite the extra factors of the small nonlinear coupling coefficient σ. However, as q increases the various imaginary residue terms in F_{4p} begin to cancel in a similar manner to those of F_{2p}. Such behaviour is to be expected, as F_{4p} (3.65) is expressed in terms of F_{2p}. As the higher-order term also approaches zero as $qa \to \pi$, it is presumed that one of the even higher-order terms of F will dominate the result.

In the very small q range, where F_{2p} dominates the result, the value of the fitted Lorentz model damping term γ can be described by a power series in q:

$$\gamma(q) = \gamma_0 + \gamma_2 (qa)^2 + \gamma_4 (qa)^4 + \ldots, \tag{3.68}$$

where the symmetry of the system restricts this series to even powers only. The expansion up to q^2 provides a good fit to the calculated susceptibility up to $qa = 0.1$. This matches

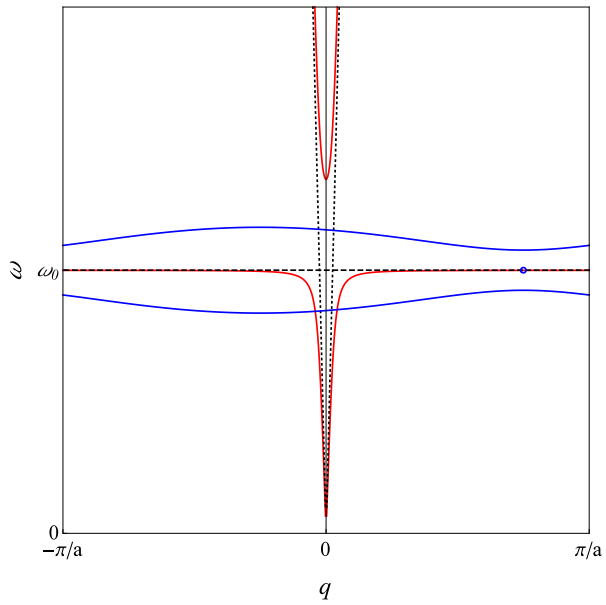

Figure 3.15: Graphical representation (not to scale) of the q_1 integration in (3.55) used to calculate F_{2p} for an initial mode with large q, denoted by the blue dot. The integration is performed over the intermediate modes $(q - q_1, \omega \pm \nu_0(q_1))$ (blue lines) which contain poles of the intermediate Green function G_p^d when this intersects the dispersion relation $[G_p^d]^{-1} = 0$ (red lines), The imaginary residue terms associated with these poles can cancel each other out, causing a higher-order term to dominate the result for $F(q_{\text{in}}, \omega)$.

another model proposed by Hopfield and Thomas [86] , which was made under different considerations to the current MN model. The full q dependence of F as $q \to \pi/a$ would require the calculation of many higher-order F_n terms, which lies beyond the scope of this thesis.

3.7 Chapter summary

This chapter has verified the proposal made by Hopfield made in his 1958 paper [2] — that the introduction of nonlinear interactions will solve the lack of broadband absorption in the susceptibility of linear dielectric models, instead giving a susceptibility described by the Lorentz model with a nonzero damping term. While previous work on this subject has been in the quantum regime [9–13], where a complete treatment of the system is incredibly challenging, the derivation in this chapter was performed classically [25].

The nonlinear microscopic dielectric model used consisted of a chain of particles, with a displacement from the lattice sites and an electric dipole that was linearly coupled to a field representing a projection of the electromagnetic vector potential. While the model was one-dimensional, the results could be applied to a three-dimensional cubic lattice under certain restrictions. The nonlinear coupling was found to naturally emerge from the r^{-3} dipole-dipole interaction, with the particle displacements acting as a "pseudo-reservoir" and providing the coupling to a continuum of modes required by Hopfield [2].

The resulting nonlinear equations of motion for the model were solved by treating the nonlinear interaction term as a small perturbations of the system. The expressions were rearranged using an iteration process to a find an expression in the form of a wave equation, from which an effective linear susceptibility could be extracted. This notationally cumbersome process was performed using a diagrammatic method, similar to the calculation of self-energy in quantum filed theory using Feynman diagrams. The calculation of the effective linear susceptibility amounted to the summation over all diagrams that start and end with the dipole field in the same mode.

Exact expressions were derived for one of the leading-order and one of the higher-order terms contributing to the effective linear susceptibility χ_{eff}. Imaginary components were found when the intermediate fields in the iteration process satisfied their corresponding dispersion relations.

Numerical calculations of these terms were preformed to investigate the frequency and wave vector dependence of the susceptibility. While the resulting values for the effective linear susceptibility were unrealistically large in comparison to real dielectrics (a limitation of perturbation theory), χ_{eff} was found to have the broadband absorption predicted by Hopfield. In addition to this, the results were found to be an excellent fit to the Lorentz model of susceptibility without the need for a specific frequency-dependent coupling, which is the case for the phenomenological reservoir. The wave vector dependence was found to be more complex, with the various imaginary contributions in the lower-order terms of the perturbation series cancelling each other out as q increased, leaving a higher-order term to dominate the result. At small q, the damping term γ of the fitted Lorentz model was found to obey an even power series in q, agreeing with a proposal made by Hopfield and Thomas under a different set of considerations [86], while the full q dependence would require the calculation of a large number of higher-order terms.

Chapter 4

Assumptions in ABC models

The second half of this thesis extends the Halevi and Fuchs [4] model of a half-infinite nonlocal medium to include many more of the features found in real materials [61, 62]. Before these improvements are made, this chapter takes a closer look at the derivations behind a specific ABC [55] and the generalized ABC model [4]. In both cases, certain assumptions are made during the derivation that initially appear to be straightforward and trivial, but actually require careful consideration upon closer inspection. The aim of this chapter is to fill the gaps in these derivations and asses the validity of the assumptions made in each case.

Section 4.1 takes a second look at the derivation of the Pekar ABC [55], focusing on the choice of the medium boundary position that is made in the transition from the microscopic to macroscopic regime. Taking inspiration from the previous chapter, an iteration process is used to independently check Pekar's calculation before making several improvements to his work.

Section 4.2 considers the choice of ansatz made by Halevi and Fuchs [4] for the electric field in a half-infinite nonlocal medium. Their paper assumes the field is described by a sum of plane waves, with wave vectors that satisfy the dispersion relation of the infinite medium. While this is a safe assumption to make far from the boundary, the derivation of the reflection and transmission coefficients in section 2.3 depends on the behaviour of the field *at* the boundary, where the susceptibility of the half-infinite nonlocal medium is significantly different to the infinite case. Despite the fact that the behaviour of the field is critical to their final result, Halevi and Fuchs gave no justification for the use of this ansatz and provided no argument that it was appropriate for the susceptibility of the half-infinite medium. Once again, an iteration procedure is used to independently derive

an expression for the electric field without making any assumptions other than the form of the nonlocal susceptibility and the shape of the boundary.

4.1 The Pekar ABC

In section 2.3.2, it was shown that the Maxwell boundary conditions were insufficient to calculate the reflection and transmission coefficients of a nonlocal medium. The additional information was provided in the form of Additional Boundary Conditions (ABCs) on the behaviour of the polarization field just inside the planar boundary of the half-infinite medium. A wide variety of ABCs were proposed [33–56], each derived under different assumptions specific to the type of material considered. The first, and perhaps the simplest, of these was derived by Pekar [53–56], which states that the polarization field must vanish at the boundary of the nonlocal medium.

The Pekar ABC [55] was derived from a microscopic model of discrete atoms in a crystal at positions $\boldsymbol{n} = n_1\boldsymbol{a_1} + n_2\boldsymbol{a_2} + n_3\boldsymbol{a_3}$, where $\boldsymbol{a_i}$ were the lattice vectors. To consider the case of Frenkel (tight-binding) excitons [57, 58] in the medium, nearest-neighbour coupling was added between each of the atoms in the lattice. After considering a slab bounded by the planes $n_3 = 1$ and $n_3 = N$, where N is an arbitrarily large integer, Pekar used various symmetry arguments to show that the polarization field $\boldsymbol{P}$ must vanish at the $n_3 = 0$ origin.

At this point in his derivation, Pekar states that the $n_3 = 1$ plane is, in a macroscopic sense, a plane through the $n_3 = 0$ origin of co-ordinates and thus $\boldsymbol{P} = 0$ at the boundary of the medium. However, from a microscopic perspective, Pekar had derived a condition for $z = 0^-$ just outside the boundary of the medium, rather than $z = 0^+$ just inside the boundary, which was required for the calculation of reflection and transmission in spatially dispersive media as described in section 2.3.

This section takes an independent approach to find the ABC for this system, and investigates the impact, if any, the discrepancy in the boundary position has on the result. This is done by calculating the expression for the microscopic susceptibility of a half-infinite chain of atoms with nearest-neighbour coupling. By comparing to the generalized ABC model used by Halevi and Fuchs [4]:

$$\chi_i'(z, z') = \chi(z - z') + U_i\chi(z + z'), \tag{4.1}$$

an expression for U_i and the corresponding ABC is found. This is first performed for a system with nearest-neighbour coupling similar to Pekar's, before being extended to the

more general case of j^{th}-nearest-neighbour coupling with interaction strengths that decay with distance.

4.1.1 Nearest-neighbour coupling

To derive the susceptibility of the half-infinite medium in a form similar to the one used by Halevi and Fuchs in (4.1), the infinite case must first be considered. The model chosen is a simplified one-dimensional version of Pekar's model [55] and consists of a chain of atoms with radius r_0 located at $z_n = na$, where $n = -\infty \to \infty$ and a is the lattice spacing. Note that this includes the possible case where $r_0 > a/2$, which leads to an overlap between neighbouring atoms. Each atom has an electric dipole p_n that is linearly coupled both to the electric field E at the lattice site and the dipole of the nearest-neighbour atoms.

The equation of motion for each dipole in the infinite model is assumed to take the simplified form:

$$p_n(\omega) = g(\omega)E(z_n, \omega) + h(\omega)\left[p_{n+1}(\omega) + p_{n-1}(\omega)\right] \tag{4.2}$$

where $g(\omega)$ and $h(\omega)$ are arbitrary functions. Frequency dependence will be subsequently omitted for notational brevity as it plays no role in the subsequent derivation. The first term describes the linear coupling to the electric field, while the second contains the nearest-neighbour interactions. Rearranging (4.2) to give p solely in terms of E is usually done by performing a spatial Fourier transformation. Instead, an iteration process is performed by substituting the entire expression for p_n in (4.2) into each of the right-had side (RHS) terms of p_n. The first few steps of this process are displayed below:

$$\begin{aligned} p_n =& gE(z_n) + h\left[p_{n+1} + p_{n-1}\right] \\ =& gE(z_n) + gh\left[E(z_{n+1}) + E(z_{n-1})\right] + h^2\left[p_{n+2} + 2p_n + p_{n-2}\right] \\ =& gE(z_n) + gh\left[E(z_{n+1}) + E(z_{n-1})\right] + gh^2\left[E(z_{n+2}) + 2E(z_n) + E(z_{n-2})\right] + O[h^3]. \end{aligned} \tag{4.3}$$

The resulting expression for p_n is a sum over $E(z_m)$, with each coefficient expressed as a power series in h. As the model is for an infinite medium is invariant under transformations of the lattice constant, the coefficients only depend on the difference $|n - m|$:

$$p_n = \sum_m \Lambda_{|n-m|} E(z_m), \tag{4.4}$$

where some examples of Λ_n are given by:

$$\begin{aligned}
\Lambda_0 &= g\left(1 + 2h^2 + 6h^4 + 20h^6 + 70h^8 + \dots\right), \\
\Lambda_1 &= g\left(h + 3h^3 + 10h^5 + 34h^7 + 126h^9 \dots\right), \\
\Lambda_2 &= g\left(h^2 + 4h^4 + 15h^6 + 56h^8 + \dots\right), \\
\Lambda_5 &= g\left(h^5 + 7h^7 + 36h^9 + \dots\right).
\end{aligned} \tag{4.5}$$

Note that the leading-order term in Λ_n is always gh^n. By comparing to the definition of the nonlocal susceptibility in (2.3), $\Lambda_{|n-m|}$ can be seen as the equivalent of $\chi(z_n - z_m)$ for this infinite discrete model.

The half-infinite model is then considered, with n now running from $0 \to \infty$. The equations of motion for p_n remain the same as (4.2), with the exception of the p_0 equation, where the p_{-1} term is removed as this dipole no longer exists in the half-infinite medium. The iteration process used in (4.3) for infinite medium is repeated to once again find an expression for p_n:

$$p_n = \sum_m \Lambda'_{n,m} E(z_m), \tag{4.6}$$

where $\Lambda'_{n,m}$ no longer depends on $|n-m|$. Upon closer inspection, each term of $\Lambda'_{n,m}$ can be expressed in terms of the infinite medium coefficient Λ_n using

$$\Lambda'_{n,m} = \Lambda_{|n-m|} - \Lambda_{n+m+2}. \tag{4.7}$$

An example of this is $\Lambda'_{2,1}$, which can be rewritten in terms of the coefficients in (4.5):

$$\begin{aligned}
\Lambda'_{2,1} =& g\left(h + 3h^3 + 9h^5 + 28h^7 + 90h^9 + \dots\right) \\
=& g\left(h + 3h^3 + 10h^5 + 34h^7 + 126h^9 \dots\right) - g\left(h^5 + 7h^7 + 36h^9 + \dots\right) \\
=& \Lambda_1 - \Lambda_5.
\end{aligned} \tag{4.8}$$

The first term in (4.7) is translation invariant and gives the non-local bulk response, while the second term depends on the distance of n and m from the boundary and describes reflection on the surface. This way of expressing the behaviour of the half-infinite medium in terms of the infinite bulk response is very similar to the model used by Halevi and Fuchs [4] in (4.1). However, the reflected component appears to be traveling past the boundary to a "phantom" dipole p_{-1}, located at $z = -a$ before reflecting with an amplitude coefficient of -1. This is illustrated in Fig. 4.1. The location of this "phantom" dipole coincides with the $n_3 = 0$ origin of Pekar's model [55], which was subsequently

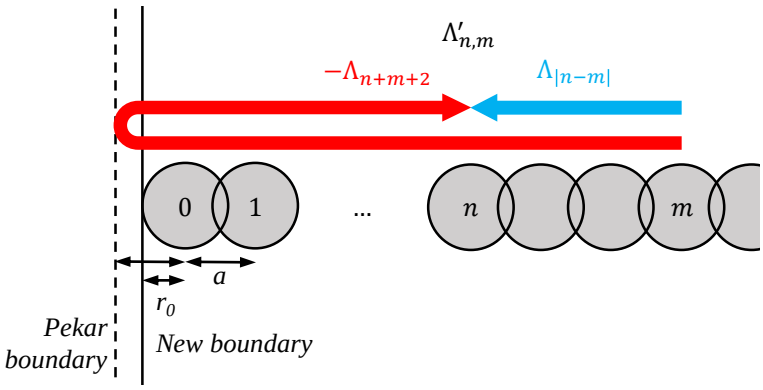

Figure 4.1: Diagram comparing the components of $\Lambda'_{n,m}$ in (4.7) for a 1D chain of atoms with radius r_0 and lattice spacing a between the centers. The bulk response (blue) $\Lambda_{|n-m|}$is identical to that of the infinite medium, while the Λ_{n+m+2} term describes the reflection of p at the "phantom" dipole p_{-1}. The vertical lines indicate the choice of $z = 0$ boundary for Pekar (dashed), which actually lies outside the medium, and the modified position used in this chapter (solid).

used as the boundary of the medium. It can be seen that the p wave acts as if it has reflected at a point outside the medium.

The next step is to take this result to the macroscopic limit so a comparison can be made to the form (4.1) used by Halevi and Fuchs. An important part of this is defining where the $z = 0$ boundary lies, as this determines the position where the ABCs are applicable. The microscopic location of this plane therefore has an effect on the macroscopic reflection and transmission coefficients, as they are entirely dependent on the behaviour of the electric field at the position $z = 0^+$ just inside the boundary.

Pekar defined the $z = 0$ surface a distance of one lattice constant a from the position of the dipole at the end of the chain. This is the location of the "phantom" dipole p_{-1} that the second term in (4.7) appears to reflect on. Assuming $\chi(z)$ is the macroscopic limit of Λ_n, the discrete expression in (4.7) becomes:

$$\chi'(z, z') = \chi(z - z') - \chi(z + z'), \tag{4.9}$$

which agrees with the value $U_i = -1$ used by Halevi and Fuchs for the Pekar ABC. In reality, this position can lie outside the medium. Figure 4.1 demonstrates this for the case when $r_0 < a$.

To ensure the resulting ABCs can be applied to the calculation of the surface impedance, a new $z = 0$ position inside the medium must be defined. Figure 4.1 presents the case

where the edge of the $n = 0$ atom has been chosen as the new boundary. The macroscopic susceptibility for this case is given by:

$$\chi'(z, z') = \chi(z - z') - \chi(z + z' + L). \tag{4.10}$$

where $L = 2(a - r_0)$. The expression in (4.10) can potentially be rearranged to the form in (4.1). Using the same bulk susceptibility as Halevi and Fuchs [4]:

$$\chi(q) \propto \frac{1}{q^2 - \Gamma^2}, \qquad -\Gamma^2 = \frac{\omega_T^2 - \omega^2 - i\gamma\omega}{D} + K^2, \tag{4.11}$$

which corresponds to the real-space expression:

$$\chi(z) \propto e^{i\Gamma|z|}, \tag{4.12}$$

the expression in (4.10) can be rewritten as:

$$\chi'(z, z') = \chi(z - z') + U\chi(z + z'), \qquad U = -e^{i\Gamma L}, \tag{4.13}$$

where $\mathrm{Im}[\Gamma] > 0$ ensures the $|U| < 1$ condition made by Halevi and Fuchs is satisfied. The apparent shift of the reflection plane in Fig. 4.1 can instead be thought of as a phase factor in the reflection coefficient. While similar behaviour is also found in the Goos-Hänchen effect (specifically the second-order Focal Shift) [117], the origin of this effect is different as it relies upon the angular spectrum of a finite-sized beam at non-normal incidence.

Unlike the values of U previously obtained from ABC's in Table 2.1, the expression in (4.13) is complex and dependent on both ω and K. In most cases, $|\Gamma L| \ll 1$ near the resonant frequency, leading to a result that is almost identical to the Pekar value of $U = -1$. However, far from the resonance, or when the wavelength of the polarization field becomes comparable to L, the result in (4.13) may be significantly different to that of Pekar. This may prove to be important in the calculation of spectral energy, where the integral in (2.63) runs over all values of K.

It must be noted that the same result can be found by following Pekar's derivation, but instead focusing on $\boldsymbol{P}$ at $z = a - r_0$. Using the susceptibility in (4.11) and the relation in (2.53), the subsequent equation for $\boldsymbol{P}$ leads to:

$$\frac{\alpha_i}{\beta_i} = \frac{-\Gamma}{\tan[\Gamma(a - r_0)]}, \qquad \rightarrow \qquad U_i = -e^{i\Gamma 2(a - r_0)}, \tag{4.14}$$

which matches the result in (4.13). However, the iterative method has several advantages as it can be applied to models with next-nearest-neighbour coupling or greater.

4.1.2 j^{th}-nearest-neighbour coupling

The iterative method in 4.1.1 is far more general than Pekar's derivation and can be applied to models with j^{th}-nearest-neighbour interactions with the corresponding coupling strengths h_j. While the nonlocal $\Lambda'_{n,m}$ can once again be split into a bulk and reflection term, as in (4.7), the latter of these will no longer be an exact match to a Λ_n term of the infinite medium. Instead, it will correspond to p propagating a non-integer number of lattice constants. The exact distance the reflected component travels must be found by substituting numeric values for the h_j coefficients and interpolating between the Λ_n values of the infinite medium.

As an example, a model with next-nearest-neighbour coupling is considered. The simplified equation of motion for p_n in this system is given by:

$$p_n = gE(z_n, \omega) + h_1 \left[p_{n+1}(\omega) + p_{n-1}(\omega)\right] + h_2 \left[p_{n+2}(\omega) + p_{n-2}(\omega)\right], \tag{4.15}$$

where h_1 and h_2 are the relative coupling strengths. The process is the same as in section 4.1.1, with the infinite medium first considered. The entire expression for p_n in (4.15) is substituted into each of the RHS p_n terms repeatedly to give an expression of the form (4.4). The Λ_n coefficients are expressed as a power series of both h_1 and h_2.

The half-infinite medium containing the dipoles $n = 0$ to ∞ is then considered. The equations of motion remain the same as (4.15), but with the removal of the p_{-1} and p_{-2} terms from the p_0 and p_1 equations. The same iteration is then performed for the half-infinite medium to find the coefficients $\Lambda'_{n,m}$. The Λ_n result for the infinite medium can be used to split each of the coefficients into two parts:

$$\Lambda'_{n,m} = \Lambda_{|n-m|} - \Lambda^R_{n,m} \tag{4.16}$$

where Λ^R contains all terms not included in the bulk response $\Lambda_{|n-m|}$. Unlike the previous section, Λ^R does not correspond to one of the Λ_n terms of the infinite medium. However, by substituting numeric values for h_1 and h_2, $\Lambda^R_{n,m}$ can be compared to the values of Λ_n to find the *effective* distance travelled by the reflected term.

A comparison between $\Lambda^R_{n',m'}$ and the values of Λ_n is shown in Fig. 4.2 for the specific case of $\Lambda^R_{n'=6,m'=8}$. The interaction between the electric dipoles in the model is assumed to obey a $1/r^N$ power law, where r is the distance between the dipoles, similar to that of the dipole-dipole potential (3.4) used in chapter 3. Figure 4.2 compares the results for several N values, using the coupling strengths $h_1 = 0.1$ and $h_2 = h_1/2^N$. It must be noted that the iteration process described in this section is in no way specific to these values, or the r-dependence of the coupling strengths.

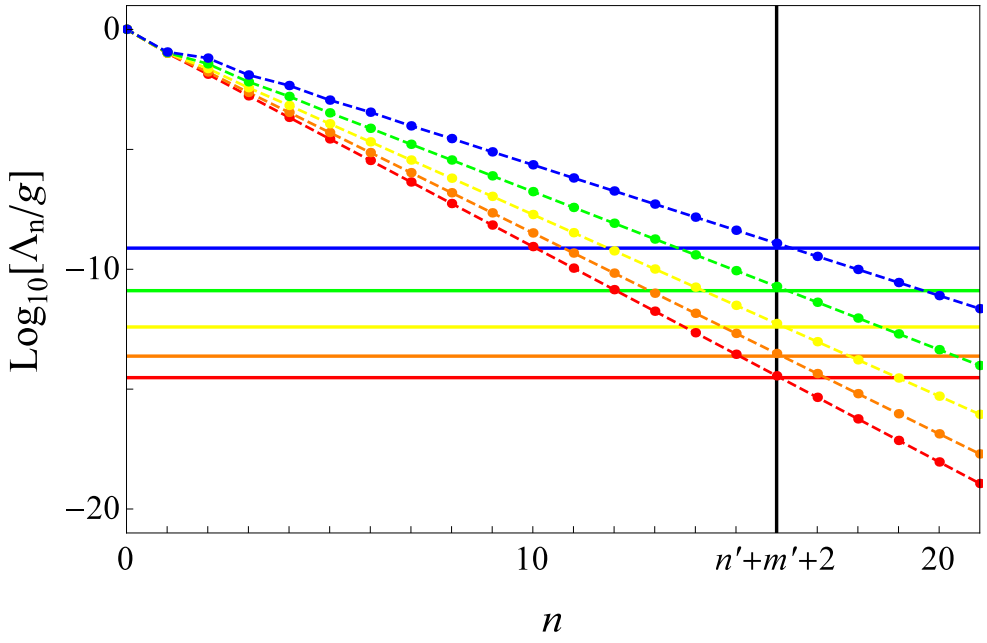

Figure 4.2: Diagram comparing values of the bulk expression Λ_n/g for a system with next-nearest-neighbour coupling, with $h_1 = 0.1$ and h_2 determined by an $1/r^N$ power law. Includes $N = 1$ (blue), $N = 2$ (green), $N = 3$ (yellow), $N = 4$ (orange) and $N = 5$ (red). Horizontal lines indicate the value of $\Lambda^R_{n',m'}$ in each case for the example values $n' = 6, m' = 8$. With the introduction of next-nearest neighbour coupling, the reflection term corresponds to a distance travelled that is very slightly larger than the $n' + m' + 2$ lattice constants of the nearest-neighbour model.

The values of Λ_n shown as points in Fig. 4.2 describe the p wave traveling a distance na in the infinite medium. These values are interpolated to give the dashed lines, which represent the p wave traveling a non-integer number of lattice constants. The horizontal lines indicate the value of $\Lambda^R_{n'=6,m'=8}$ for each N and the intersection with the dashed lines can be used to calculate the effective distance travelled by the reflected p wave in the next-nearest-neighbour model.

It can be seen that the presence of next-nearest-neighbour coupling increases the effective distance travelled by the reflected p wave in comparison to the $n' + m' + 2$ lattice constants of the nearest-neighbour model in section 4.1.1. This new distance depends on the values of N, approaching $n'+m'+2.5$ for the slowly decaying $1/r$ potential. Potentials that decay rapidly, such as the $M = 5$ case, return to the result of the nearest-neighbour coupling model as h_2 becomes negligibly small. These new distances are largely inde-

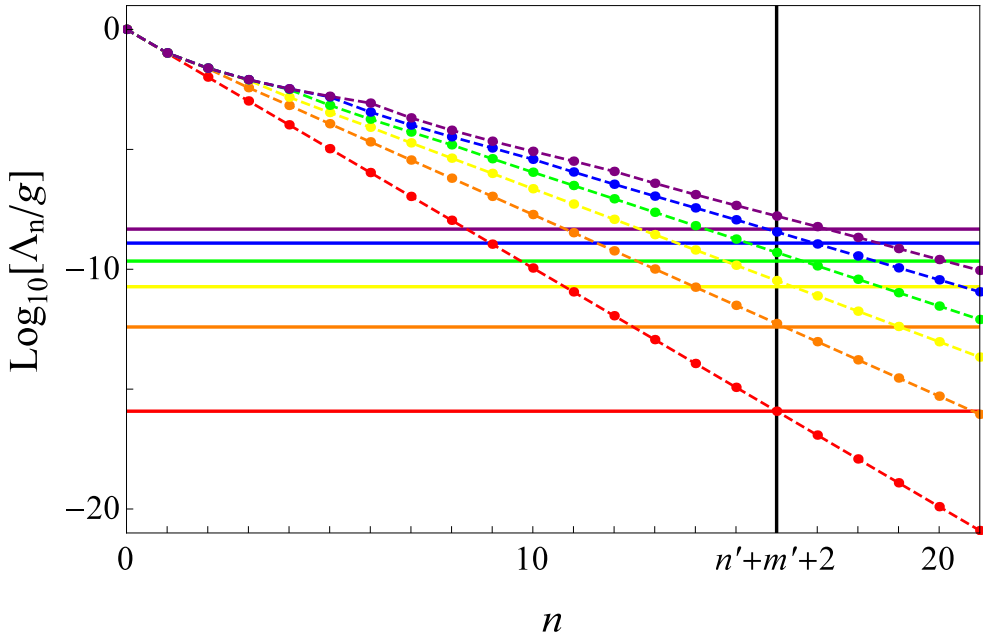

Figure 4.3: Diagram comparing values of the bulk expression Λ_n/g for a system with j^{th}-nearest-neighbour coupling, with $h_1 = 0.1$ and other terms determined by an $1/r^3$ power law. Includes $j = 1$ (red), $j = 2$ (orange), $j = 3$ (yellow), $j = 4$ (green), $j = 5$ (blue) and $j = 6$ (purple). Horizontal lines indicate the value of $\Lambda^R_{n',m'}$ in each case for the example values $n' = 6, m' = 8$. The greater the number of coupling terms, the larger the effective distance travelled by the reflected term, exceeding $n'+m'+3$ for 6^{th}-nearest-neighbour coupling.

pendent of the value of h_1 and the specific choice of n' and m', provided they are not too close to the end of the chain.

The inclusion of additional j^{th}-nearest-neighbour coupling terms also affects the effective distance travelled by the reflected p wave. Figure 4.3 compares the values of Λ_n and $\Lambda^R_{n'=6,m'=8}$ in models with j^{th}-nearest-neighbour interactions. The coupling strength $h_1 = 0.1$ is used once again, and higher-order terms of h_j are taken to obey a $1/r^3$ power law. The inclusion of additional coupling terms can be seen to have a much stronger effect on the the effective distance travelled by the reflected p wave compared to the effect of N in Fig. 4.2. The distance is found to increase with every additional coupling term, exceeding $n' + m' + 3$ lattice constants for 6^{th}-nearest-neighbour coupling. Once again, these results are largely independent of the value of h_1 and the specific choice of n' and m', provided they are not too close to the end of the chain.

In each of these cases, the coefficients of the half-infinite medium can now be written as

$$\Lambda'_{n,m} = \Lambda_{|n-m|} - \Lambda_{n+m+l_{\text{eff}}}, \tag{4.17}$$

where the second term describes the reflected p wave traveling the non-integer number of lattice constants $n + m + l_{\text{eff}}$. After taking the macroscopic limit of (4.17) to the form in (4.10), the expression for L is now given by

$$L = l_{\text{eff}} - 2r_0. \tag{4.18}$$

Increasing the number of nearest-neighbour coupling terms and decreasing the decay of the coupling strengths both cause l_{eff} to increase, further changing the corresponding value of U in (4.13) from the -1 value used by Pekar. However, the Pekar ABC will act as a good approximation to this result in the $|\Gamma L| \ll 1$ regime.

4.1.3 Conclusions

This section provided an alternate derivation of the Pekar ABC and investigated the effect of coupling strength and j^{th}-nearest-neighbour coupling between dipoles. At the microscopic scale, the reflected polarization waves act as if they reflect on a point outside the medium, which is equivalent to the additional phase term in the result $U_i = -\exp(i\Gamma L)$. In the macroscopic limit, the Pekar ABC $U_i = -1$ provides a good approximation for the model, although this will fail to hold when Γ becomes large either far from the resonance or for wavelengths that are comparable to the lattice spacing. The validity of the expression used by Halevi and Fuchs [4] in (4.13) is questionable in the latter case, as it is expressed in terms of the macroscopic susceptibility which by definition describes the electromagnetic response of a medium over scales much larger than the lattice spacing. The Pekar ABC $U_i = -1$ is therefore a safe approximation to use for systems with tight binding.

4.2 The Halevi-Fuchs ansatz

In 1985, Halevi and Fuchs introduced a generalized ABC model for the half-infinite nonlocal medium [4], collecting the various ABCs that were previously derived [33–56] into a single, easy-to-use formalism. Their work is described in greater detail in section 2.3.4,

but the key points are repeated here. The susceptibility χ' of the half-infinite medium used in their paper was expressed in terms of the infinite medium susceptibility χ:

$$\chi_i'(x-x',y-y',z,z') = \begin{cases} \chi(x-x',y-y',z-z') \\ \quad + U_i\chi(x-x',y-y',z+z') & \text{if } z,z'>0, \\ 0 & \text{otherwise.} \end{cases} \tag{4.19}$$

where the $z = 0$ plane has been taken as the boundary of the medium. The $(z - z')$-dependent term described the usual bulk response of the medium and the $(z + z')$-dependent term described the polarization waves reflecting on the interior surface of the dielectric. The ABC information was contained within the reflection coefficients U_i of the polarization waves.

Halevi and Fuchs found the specific form of the nonlocal susceptibility in (4.19) insufficient to solve the wave equation:

$$\boldsymbol{\nabla}\times\boldsymbol{\nabla}\times\boldsymbol{E}(\boldsymbol{r}) - k_0^2\boldsymbol{E}(\boldsymbol{r}) - k_0^2\int_{-\infty}^{\infty} d^3\boldsymbol{r}'\underline{\boldsymbol{\chi}}(\boldsymbol{r},\boldsymbol{r}')\boldsymbol{E}(\boldsymbol{r}') = 0 \tag{4.20}$$

where $k_0 = \omega/c$. The other critical assumption made by Halevi and Fuchs was the expression for the monochromatic electric field inside the half-infinite nonlocal medium:

$$\boldsymbol{E}(\boldsymbol{r},t) = \left(\sum_{n=1}^{N}\boldsymbol{E}^{(n)}e^{iq_nz}\right)e^{iKx}e^{-i\omega t} \qquad z>0, \tag{4.21}$$

where the N wave vectors $\boldsymbol{k}_n = K\hat{\boldsymbol{x}} + 0\hat{\boldsymbol{y}} + q_n\hat{\boldsymbol{z}}$ are the $\mathbb{I}\mathrm{m}[q_n] > 0$ solutions of the infinite-medium dispersion relation (2.15). It is important to note that Halevi and Fuchs were not alone in their choice of ansatz for the electric field, as this expression was also used in several of the papers deriving the individual ABCs.

The ansatz in (4.21) is a safe assumption for a medium described by the susceptibility (4.19) in the $z, z' \to \infty$ limit, as the $(z + z')$ term in χ' becomes negligible in comparison to the $(z - z')$ bulk response of the medium due to the exponential dependence in (4.12). However, the electromagnetic reflection and transmission coefficients described in section 2.3 depend on the behaviour of the field in the $z \to 0$ limit. In the region near the boundary, there are significant differences in the wave equation (4.20) between the infinite and half-infinite medium. This is true even in the $U_i = 0$ case, as the integration over z' is limited to the $z > 0$ half-space for the half-infinite medium. Halevi and Fuchs provided no justification for the use of the ansatz (4.21) in this critical region.

This aim of this section is to perform an independent check for the validity of the electric field ansatz used by Halevi and Fuchs, specifically in the region near the boundary.

A calculation of the electric field in the half-infinite medium is made using an iteration process. No assumptions about the system are made other than the expression for χ' and the shape of the boundary.

4.2.1 Calculating the electric field

This section starts by returning to the electric field wave equation in a nonlocal medium:

$$\boldsymbol{\nabla} \times \boldsymbol{\nabla} \times \boldsymbol{E}(\boldsymbol{r}) - k_0^2 \boldsymbol{E}(\boldsymbol{r}) - k_0^2 \int d^3\boldsymbol{r}' \underline{\boldsymbol{\chi}}(\boldsymbol{r}, \boldsymbol{r}') \boldsymbol{E}(\boldsymbol{r}') = \boldsymbol{S}(\boldsymbol{r}), \tag{4.22}$$

where $\boldsymbol{S}$ is an arbitrary source term. The susceptibility of the half-infinite medium in (4.22) is treated as a perturbation and an iteration process is used to find $\boldsymbol{E}$ inside the medium in terms of a source $\boldsymbol{S}$ outside the medium.

The Halevi and Fuchs [4] susceptibility model in (4.1) is used to describe the nonlocal medium occupying the $z > 0$ half-space, with some minor changes. The first is the choice of U_i. While the derivation can be performed for general U_i values, this chapter uses the $U_i = 0$ Agarwal ABC [33–42]. This choice is made simply to reduce the amount of notation and the overall findings of this chapter are not specific to these values. The second change replaces the scalar bulk susceptibility used by Halevi and Fuchs with the general expression for a homogeneous, isotropic, non-gyroscopic medium:

$$\chi_{ij}(\boldsymbol{k}, \omega) = \delta_{ij}\chi_\perp(k, \omega) + \frac{k_i k_j}{k^2}\left[\chi_\parallel(k, \omega) - \chi_\perp(k, \omega)\right], \tag{4.23}$$

which makes it easier to distinguish between transverse and longitudinal components of $\boldsymbol{E}$ inside the medium. The $\chi_\parallel = \chi_\perp$ limit can subsequently be taken to compare the results to the scalar χ basis of the Halevi-Fuchs model.

The setup is the same as described in section 2.3, with the xz-plane aligned with the plane of incidence and the wave vectors given by:

$$\boldsymbol{k} = K\hat{\boldsymbol{x}} + 0\hat{\boldsymbol{y}} + q\hat{\boldsymbol{z}}, \tag{4.24}$$

where only the $\hat{\boldsymbol{z}}$ component can vary. Under these conditions, only the χ_{xx}, χ_{yy}, χ_{zz}, χ_{xz} and χ_{zx} terms of (4.23) are nonzero. Upon making a Fourier transformation in x and y, the wave equation (4.22) reduces to a single equation for E_y corresponding to the s-polarization:

$$\left[-\partial_z^2 - q_0^2\right] E_y(z) = S_y(z) + k_0^2 \int_{-\infty}^{\infty} dz_1 \Theta(z)\Theta(z_1)\chi_{yy}(z, z_1)E_y(z_1) \tag{4.25}$$

and a pair of coupled equations for E_x and E_z corresponding to the p-polarization:

$$\begin{aligned}\left[-\partial_z^2 - k_0^2\right] E_x(z) =& S_x(z) + k_0^2 \int_{-\infty}^{\infty} dz_1 \Theta(z)\Theta(z_1)\chi_{xx}(z-z_1)E_x(z_1) \\ &- iK\partial_z E_z(z) + k_0^2 \int_{-\infty}^{\infty} dz_1 \Theta(z)\Theta(z_1)\chi_{xz}(z-z_1)E_z(z_1), \quad (4.26)\\ \left[-q_0^2\right] E_z(z) =& S_z(z) + k_0^2 \int_{-\infty}^{\infty} dz_1 \Theta(z)\Theta(z_1)\chi_{zz}(z-z_1)E_z(z_1) \\ &- iK\partial_z E_x(z) + k_0^2 \int_{-\infty}^{\infty} dz_1 \Theta(z)\Theta(z_1)\chi_{zx}(z-z_1)E_x(z_1). \quad (4.27)\end{aligned}$$

In each case $q_0^2 = k_0^2 - K^2$ and the boundary of the medium is described by the Heaviside step function $\Theta(z)$. The pair of equations (4.26) and (4.27) are first considered, as the p-polarization contains both transverse and longitudinal waves, unlike the s-polarization described by (4.25). The integrals make it difficult to find expressions for E_x and E_z in a closed form. Instead, the susceptibility χ_{ij} is treated as a perturbation of the vacuum wave equation and an iteration process is used to remove the RHS terms of both E_x and E_z.

The process starts with the RHS term of E_z in (4.27). The equation is divided by $-q_0^2$ and the entire expression for E_z is substituted into the RHS E_z term to give:

$$\begin{aligned}E_z(z) =& -\frac{1}{q_0^2} S_z(z) \\ &+ \frac{iK}{q_0^2}\partial_z E_x(z) \\ &- \frac{k_0^2}{q_0^2}\int_{-\infty}^{\infty} dz_1 \Theta(z)\Theta(z_1)\chi_{zx}(z-z_1)E_x(z_1) \\ &+ \frac{k_0^2}{q_0^4}\int_{-\infty}^{\infty} dz_1 \Theta(z)\Theta(z_1)\chi_{zz}(z-z_1)S_z(z_1) \\ &- \frac{iKk_0^2}{q_0^4}\int_{-\infty}^{\infty} dz_1 \Theta(z)\Theta(z_1)\chi_{zz}(z-z_1)\partial_{z_1}E_x(z_1) \\ &+ \frac{k_0^4}{q_0^4}\int_{-\infty}^{\infty} dz_1 \Theta(z)\Theta(z_1)\chi_{zz}(z-z_1)\int_{-\infty}^{\infty} dz_2 \Theta(z_1)\Theta(z_2)\chi_{zx}(z_1-z_2)E_x(z_2) \\ &+ \frac{k_0^4}{q_0^4}\int_{-\infty}^{\infty} dz_1 \Theta(z)\Theta(z_1)\chi_{zz}(z-z_1)\int_{-\infty}^{\infty} dz_2 \Theta(z_1)\Theta(z_2)\chi_{zz}(z_1-z_2)E_z(z_2).\end{aligned} \quad (4.28)$$

The $S_z(z_1)$ term is subsequently discarded, as the source lies in the $z < 0$ half-space outside the medium. This expression is once again substituted into the remaining RHS E_z term in (4.28) and the process is repeated n times, after which the remaining RHS E_z

terms are discarded. The remaining expression for E_z is accurate up to the order $(\chi_{\perp/\parallel})^n$ and contains only terms of S_z and E_x. To second order, E_z is given by:

$$\begin{aligned}
E_z(z) &= -\frac{1}{q_0^2}S_z(z) + \frac{iK}{q_0^2}\partial_z E_x(z) \\
&- \frac{q_0^2 k_0^2}{q_0^4}\int_{-\infty}^{\infty} dz_1 \Theta(z)\Theta(z_1)\chi_{zx}(z-z_1)E_x(z_1) \\
&- \frac{iKk_0^2}{q_0^4}\int_{-\infty}^{\infty} dz_1 \Theta(z)\Theta(z_1)\chi_{zz}(z-z_1)\partial_{z_1}E_x(z_1) \\
&+ \frac{q_0^2 k_0^4}{q_0^6}\int_{-\infty}^{\infty} dz_1 \Theta(z)\Theta(z_1)\chi_{zz}(z-z_1)\int_{-\infty}^{\infty} dz_2 \Theta(z_1)\Theta(z_2)\chi_{zx}(z_1-z_2)E_x(z_2) \\
&+ \frac{iKk_0^4}{q_0^6}\int_{-\infty}^{\infty} dz_1 \Theta(z)\Theta(z_1)\chi_{zz}(z-z_1)\int_{-\infty}^{\infty} dz_2 \Theta(z_1)\Theta(z_2)\chi_{zz}(z_1-z_2)\partial_{z_1}E_x(z_2).
\end{aligned} \tag{4.29}$$

The expression for E_z in (4.29) is substituted into (4.26) to give an equation solely in terms of E_x, S_x and S_z. After some slight rearranging, (4.26) becomes:

$$\begin{aligned}
&\left[-\partial_z^2 - q_0^2\right]E_x(z) = SS(z) \\
&+ \frac{q_0^4}{q_0^2}\int_{-\infty}^{\infty} dz_1 \Theta(z)\Theta(z_1)\chi_{xx}(z-z_1)E_x(z_1) \\
&+ \frac{iKq_0^2}{q_0^2}\int_{-\infty}^{\infty} dz_1 \Theta(z)\Theta(z_1)\chi_{xz}(z-z_1)\partial_{z_1}E_x(z_1) \\
&+ \frac{iKq_0^2}{q_0^2}\int_{-\infty}^{\infty} dz_1 \partial_z\Theta(z)\Theta(z_1)\chi_{zx}(z-z_1)E_x(z_1) \\
&- \frac{K^2}{q_0^2}\int_{-\infty}^{\infty} dz_1 \partial_z\Theta(z)\Theta(z_1)\chi_{zz}(z-z_1)\partial_{z_1}E_x(z_1) \\
&- \frac{q_0^4 k_0^2}{q_0^4}\int_{-\infty}^{\infty} dz_1 \Theta(z)\Theta(z_1)\chi_{xz}(z-z_1)\int_{-\infty}^{\infty} dz_2 \Theta(z_1)\Theta(z_2)\chi_{zx}(z_1-z_2)E_x(z_2) \\
&- \frac{iKq_0^2k_0^2}{q_0^4}\int_{-\infty}^{\infty} dz_1 \Theta(z)\Theta(z_1)\chi_{xz}(z-z_1)\int_{-\infty}^{\infty} dz_2 \Theta(z_1)\Theta(z_2)\chi_{zz}(z_1-z_2)\partial_{z_2}E_x(z_2) \\
&- \frac{iKq_0^2k_0^2}{q_0^4}\int_{-\infty}^{\infty} dz_1 \partial_z\Theta(z)\Theta(z_1)\chi_{zz}(z-z_1)\int_{-\infty}^{\infty} dz_2 \Theta(z_1)\Theta(z_2)\chi_{zx}(z_1-z_2)E_x(z_2) \\
&+ \frac{K^2k_0^2}{q_0^4}\int_{-\infty}^{\infty} dz_1 \partial_z\Theta(z)\Theta(z_1)\chi_{zz}(z-z_1)\int_{-\infty}^{\infty} dz_2 \Theta(z_1)\Theta(z_2)\chi_{zz}(z_1-z_2)\partial_{z_2}E_x(z_2),
\end{aligned} \tag{4.30}$$

where the source terms have been collected to $SS(z) = \left[\frac{q_0^2}{k_0^2}S_x(z) + \frac{iK}{k_0^2}\partial_z S_z(z)\right]$. Equa-

tion (4.30) can be rewritten using the Green function

$$g(z,z') = \frac{i}{2q_0} e^{-iq_0|z-z'|} \tag{4.31}$$

that satisfies:

$$\left[-\partial_z^2 - q_0^2\right] g(z,z') = \delta(z-z') \tag{4.32}$$

to give an expression of the form:

$$E_x(z) = \int_{-\infty}^{\infty} dz' \frac{i}{2q_0} e^{-iq_0|z-z'|} \Bigg[SS(z') + \frac{q_0^4}{q_0^2} \int_{-\infty}^{\infty} dz_1 \Theta(z')\Theta(z_1)\chi_{xx}(z'-z_1)E_x(z_1) + \dots \Bigg]. \tag{4.33}$$

The entire expression in (4.33) is substituted into each of the RHS E_x terms and the process is repeated n times, after which the remaining E_x terms are discarded. An expression for E_x is left that is accurate up to the order $(\chi_{\perp/\parallel})^n$ and solely in terms of the source components S_x and S_z. Under the condition that E_x lies in the $z > 0$ half-space inside the medium and $\boldsymbol{S}$ lies outside the medium in the $z < 0$ half-space, (4.33) takes the form:

$$E_x(z) = T_x(z) \left[\frac{i}{2q_0} \int_{-\infty}^{\infty} dz' e^{-iq_0 z'} SS(z') \right] \tag{4.34}$$

where $T_x(z)$ is a series of integrals containing increasing powers of $\chi_\perp$ and $\chi_\parallel$ describing the field in the medium.

The exact form of the susceptibility must be specified to evaluate the integrals in $T_x(z)$. The single-resonance model from the Halevi and Fuchs model [4] is used for the transverse and longitudinal susceptibilities:

$$\chi_{\perp/\parallel} = \frac{\alpha}{\omega_T^2 + D_{\perp/\parallel}(q^2+K^2) - \omega^2 - i\gamma\omega} = \frac{\alpha/D_{\perp/\parallel}}{q^2 - \Gamma_{\perp/\parallel}^2}. \tag{4.35}$$

which reduces (4.23) to the scalar χ model in the $D_\perp = D_\parallel$ limit. The expression in (4.35) leads to three distinct sets of terms in $T_x(z)$:

$$T_x(z) = L_x(z)e^{iq_0 z} + M_x(z)e^{i\Gamma_\perp z} + N_x(z)e^{i\Gamma_\parallel z}, \tag{4.36}$$

where L_x, M_x and N_x are power series in (iz) and the susceptibility magnitude α. The use of the tensor susceptibility in (4.23) with $\Gamma_\perp \neq \Gamma_\parallel$ allows the terms of M and N to be distinguished from one another.

A similar result can be found for the z-component by substituting (4.34) into the previously calculated expression for E_z in terms of S_x and E_x shown in (4.29). After once again evaluating the various z_n-integrals, the expression for E_z inside the half-infinite nonlocal medium is given by

$$E_z(z) = T_z(z)\left[\frac{i}{2q_0}\int_{-\infty}^{\infty} dz' e^{-iq_0 z'} SS(z')\right] \tag{4.37}$$

and

$$T_z(z) = L_z(z)e^{iq_0 z} + M_z(z)e^{i\Gamma_\perp z} + N_z(z)e^{i\Gamma_\parallel z}, \tag{4.38}$$

where L_z, M_z and N_z are also power series in (iz) and the susceptibility magnitude α. The terms in L_i, M_i and N_i can be collected into various groups according to these powers. For example, the expression for L_j can be split into $L_j^{a,b}$ terms, where a and b denote the powers of α and (iz) respectively:

$$\begin{aligned} L_j(z) = \Big(& \left\{[L_j^{0,0}]\right\} \\ & + \left\{[L_j^{1,0}] + (iz)[L_j^{1,1}]\right\}\alpha \\ & + \left\{[L_j^{2,0}] + (iz)[L_j^{2,1}] + (iz)^2[L_j^{2,2}]\right\}\tfrac{\alpha^2}{2} + \dots\Big) e^{iq_0 z}, \qquad j = x, z. \end{aligned} \tag{4.39}$$

To compare with the ansatz used by Halevi and Fuchs, the iteration process was performed up to the order α^2. Expressions for the various terms in (4.38) will not be included in this chapter as they are extremely long and would not provide any additional insight.

4.2.2 Comparisons to the Halevi-Fuchs ansatz

If the ansatz in (4.21) used by Halevi and Fuchs is correct, then the expressions in (4.36) and (4.38) must correspond to the general expression for three plane waves in the medium:

$$E_j(z) = \left[t_j^{(1)}(\alpha)e^{iq_1(\alpha)z} + t_j^{(2)}(\alpha)e^{iq_2(\alpha)z} + t_j^{(3)}(\alpha)e^{iq_3(\alpha)z}\right] E_0, \tag{4.40}$$

where $E_0 t_j^{(n)}$ are the amplitude of the wave components. The wave vectors $q_1(\alpha)$ and $q_2(\alpha)$ are the $\mathbb{Im}[q] > 0$ solutions to the transverse $\boldsymbol{E}$ dispersion relation:

$$\alpha/D_\perp^2 = \left(q^2 - q_0^2\right)\left(q^2 - \Gamma_\perp^2\right), \tag{4.41}$$

and $q_3(\alpha)$ is the $\mathbb{Im}[q] > 0$ solution to the longitudinal $\boldsymbol{E}$ dispersion relation:

$$-\alpha/D_\parallel^2 = \left(q^2 - \Gamma_\parallel^2\right). \tag{4.42}$$

A small α expansion can be made to rewrite each term in (4.40) as a power series:

$$\begin{aligned} t_j^{(n)}(\alpha) &= [t_j^{(n)}(0)] + [t_j^{(n)\prime}(0)]\alpha + [t_j^{(n)\prime\prime}(0)]\tfrac{\alpha^2}{2} + \ldots, \\ q_n(\alpha) &= [q_n(0)] + [q_n'(0)]\alpha + [q_n''(0)]\tfrac{\alpha^2}{2} + \ldots, \end{aligned} \tag{4.43}$$

where $q_1(0) = q_0$, $q_2(0) = \Gamma_\perp$ and $q_3(0) = \Gamma_\parallel$ and the various terms of $t_j^{(n)}$ are currently unknown. The expressions in (4.43) are used to give an overall expansion for (4.40) as a power series in both α and (iz):

$$\begin{aligned} &t_j^{(n)}(\alpha)e^{iq_n(\alpha)z} \\ &\quad= \Big(\quad \Big\{[t_j^{(n)}(0)]\Big\} \\ &\qquad + \Big\{[t_j^{(n)\prime}(0)] + (iz)[t_j^{(n)}(0)q_n'(0)]\Big\}\alpha \\ &\qquad + \Big\{[t_j^{(n)\prime\prime}(0)] + (iz)[t_j^{(n)}(0)q_n''(0) + 2t_j^{(n)\prime}(0)q_n'(0)] + (iz)^2[t_j^{(n)}(0)q_n'^2(0)]\Big\}\tfrac{\alpha^2}{2} \\ &\qquad + \ldots\Big)e^{iq_n(0)z}. \end{aligned} \tag{4.44}$$

The validity of the Halevi and Fuchs ansatz can be checked by comparing (4.44) to the expressions for L_j, M_j and N_j in (4.34) and (4.37), which were found using the iteration process in section 4.2.1. Comparing the exponential terms indicates L_j, M_j and N_j correspond to the $n = 1, 2$ and 3 waves respectively.

As an example, the L_j power series in (4.39) and the expression in (4.44) are compared for $n = 1$. The structure of the two power series are identical, which allows each $L_j^{a,b}$ expression to be matched to the various terms in (4.43); $L_j^{(0,0)}$ is matched to $t_j^{(1)}(0)$, $L_j^{(1,1)}$ is matched to $t_j^{(1)}(0)q_1'(0)$ and so on. The results of this comparison are all consistent with the known terms of the $q_1(\alpha)$ expansion in (4.43), supporting the choice of the Halevi and Fuchs ansatz. For example, $L_j^{(1,1)}/L_j^{(0,0)}$, which corresponds to the fraction $t_j^{(1)}(0)q_1'(0)/t_j^{(1)}(0)$, gives the correct result for $q_1'(0)$.

Comparisons between the L_j, M_j and N_j power series and (4.44) allowed the various terms in the small α expansion of the previously unknown $t_j^{(n)}$ to be found. Additional support for the Halevi and Fuchs ansatz was found using the definitions of transverse ($\boldsymbol{k}\cdot\boldsymbol{E} = 0$) and longitudinal ($\boldsymbol{k}\times\boldsymbol{E} = 0$) waves given in section 2.1.4. It was found that:

$$\begin{pmatrix} K \\ 0 \\ q_n \end{pmatrix} \cdot \begin{pmatrix} t_x^{(n)} \\ 0 \\ t_z^{(n)} \end{pmatrix} E_0 e^{iq_n z} = 0, \qquad\qquad n = 1, 2, \tag{4.45}$$

for all orders in α, confirming that $n = 1, 2$ are p-polarized transverse waves and

$$\begin{pmatrix} K \\ 0 \\ q_n \end{pmatrix} \times \begin{pmatrix} t_x^{(n)} \\ 0 \\ t_z^{(n)} \end{pmatrix} E_0 e^{iq_n z} = 0, \qquad n = 3, \tag{4.46}$$

similarly confirming $n = 3$ is a p-polarized longitudinal wave.

Further evidence for the validity of this perturbative method can be found in comparisons to the transmission coefficients later derived in chapter 5. The expressions for $t_j^{(n)}$ in (4.43) can be combined to find the transmission coefficients for the waves in (4.40). In the case of the p-polarization:

$$|\boldsymbol{E}^{(n)}| = \sqrt{E_x^{(n)2} + E_z^{(n)2}} = \sqrt{t_x^{(n)2} + t_z^{(n)2}} E_0 = t_p^{(n)} E_0. \tag{4.47}$$

The resulting power series in α for $t_p^{(n)}$ (up to α^2) were found to be an exact match to the small α expansions of the p-polarization transmission coefficients derived in section 5.4.2 for the tensor susceptibility.

Similar results were found for the s-polarization by applying an iteration process to the E_y equation of motion in (4.25). A power series of the form (4.38) was found, but with the absence of the N_y term, as the s-polarization cannot contain longitudinal waves.

4.2.3 Conclusions

The matching forms of the L_j, M_j and N_j power series in (4.34) and (4.37) and the expansion of the ansatz in (4.44), and the transverse/longitudinal behaviour shown in (4.45)-(4.46) all support the use of the Halevi and Fuchs ansatz for the field throughout the half-infinite medium. Further support for the ansatz can be found by comparing transmission coefficients for the iteration method in this section to the modified Halevi and Fuchs method derived in chapter 5. The ansatz containing solutions to the infinite dispersion relations used by Halevi and Fuchs is therefore suitable to describe the electric field in a half-infinite nonlocal medium.

4.3 Chapter summary

This chapter took a closer look at some of the assumptions in the derivations of a specific ABC [55] and the generalized ABC model [4]. In the case of the Pekar ABC [55], derived from microscopic medium with nearest-neighbour interactions, it was shown that his assumption regarding the macroscopic position of the boundary meant his conditions were for a position just outside, rather than inside, the half-infinite medium. An iterative method was used to independently derive the microscopic susceptibility for his nonlocal model, before extending the results to include j^{th}-nearest neighbour interactions of varying strength. By taking the macroscopic limit of these results, a new frequency and wave-vector dependent function was found for U_i in the generalized ABC model susceptibility. The Pekar ABC was found to be a reasonable approximation near the resonant frequency for fields with wavelengths much larger than the lattice spacing.

The second half of the chapter looked at the choice of ansatz made by Halevi and Fuchs [4] for the electric field in a half-infinite nonlocal medium. While the use of wave vectors that satisfy the infinite medium dispersion relations is certainly valid far from the boundary, the calculation of the electromagnetic reflection coefficients requires the electric field behaviour just inside the boundary, where the susceptibility is significantly different to that of the infinite medium. Halevi and Fuchs provided no reasoning or argument for the validity of the ansatz in this critical region. An iteration process was applied to the nonlocal wave equation to independently derive an expression for the electric field inside the medium with no assumptions other than the form of the susceptibility and the shape of the boundary. The results were found to be in perfect agreement to the Halevi and Fuchs ansatz throughout the entire half-infinite medium, including the critical region just inside the boundary.

Chapter 5

Extending the Halevi-Fuchs model I. The single-resonance susceptibility

In 1984, Halevi and Fuchs developed a generalized ABC model [4] for a half-infinite nonlocal medium occupying the $z > 0$ half-space, described by:

$$\chi_i'(x-x',y-y',z,z') = \begin{cases} \chi(x-x',y-y',z-z') \\ \quad + U_i\chi(x-x',y-y',z+z') & \text{if } z,z' > 0, \\ 0 & \text{otherwise.} \end{cases} \tag{5.1}$$

where χ is the bulk susceptibility of the infinite medium and U_i are the phenomenological reflection coefficients of polarization waves at the interior boundary of the medium. Each of the previously derived ABCs [33–56]. corresponded to a specific set of U_i values, as shown in Table 2.1. However, the Halevi-Fuchs model was limited to materials described by a specific scalar susceptibility χ containing a single resonance with a k^2 dependence in the denominator. This represents a very limited range of the nonlocal behaviour outlined in chapter 2.1. Chapters 5-7 describe several improvements to the Halevi-Fuchs model that incorporate many more of the features found in real materials, starting with the single-resonance susceptibility [61].

The inclusion of spatial dispersion ($\boldsymbol{k}$-dependence) means that the wave vector generates a distinct direction, even in an isotropic medium. As a result, the susceptibility in a homogeneous, isotropic, non-gyroscopic (i.e. it has a centre of symmetry) medium is given by a tensor, with the general form [26]:

$$\chi_{ij}(\boldsymbol{k},\omega) = \left\{ \delta_{ij}\chi_\perp(k,\omega) + \frac{k_i k_j}{k^2}\left[\chi_\parallel(k,\omega) - \chi_\perp(k,\omega)\right] \right\}, \tag{5.2}$$

where $\chi_\perp$ and $\chi_\parallel$ are the transverse and longitudinal susceptibilities, which apply to the components of the field $\boldsymbol{E}$ perpendicular and parallel to $\boldsymbol{k}$ respectively. The susceptibility reduces to the scalar form $\delta_{ij}\chi_\perp$ used by Halevi and Fuchs in the $\chi_\perp = \chi_\parallel$ case.

While the tensor nature of the susceptibility is generally overlooked, several of the original ABC authors did consider this behaviour. Rimbey and Mahan [48–52] used the expression (5.2) in their calculations, but their specific ABC led to the absence of longitudinal waves in the medium. Garcia-Moliner and Flores [95] also included this behaviour in their attempt at a generalized ABC model, similar to that of Halevi and Fuchs in (5.1). However, this model was limited to a scalar U describing the reflection of polarization waves at the interior boundary and the resulting electromagnetic reflection coefficients were given in integral form.

The aim of this chapter is to modify the single-resonance bulk susceptibility used in the Halevi-Fuchs model (5.1) to the tensor form in (5.2) and derive the corresponding electromagnetic reflection and transmission coefficients [61]. These results are then applied to the calculation of electromagnetic thermal and zero-point energy density outside the planar boundary of a medium, in an attempt to remove the unphysical divergence described in section 2.3.6 that is encountered in the case of a local medium [5, 81, 101].

The infinite medium is first considered in section 5.1, where the specific form of the susceptibility and the resulting dispersion relations are discussed. Section 5.2 considers the half-infinite medium and modifies the model in (5.1) to the case of the tensor susceptibility, before applying the derivation used by Halevi and Fuchs to find a set of equations relating the various waves inside the nonlocal medium. Section 5.3 derives general expressions for the electromagnetic reflection and transmission coefficients in the p-polarization, before presenting numeric results for the specific case of ZnSe in section 5.4 for a range of ABCs. Note that the s-polarization is not included as the derivation is identical to that of the Halevi-Fuchs model. The difference in $\chi_\perp$ and $\chi_\parallel$ is found to have a negligible effect on the reflection coefficient of propagating waves, except for the reflection minima in the frequency region near ω_L, where the longitudinal transmitted wave plays a greater role in reflection calculations. The effect is also found to be similarly small for the transverse wave transmission coefficients, but can be significantly larger for the longitudinal wave depending on the choice of ABC. Finally, in section 5.5 the derived expressions for the electromagnetic reflection coefficients are used in the calculation of the spectral energy density near the boundary of a nonlocal medium. The inclusion of spatial dispersion is found to remove the unphysical divergence found at the boundary of

a local medium [5, 81, 101] caused by evanescent waves with arbitrarily large transverse wave vectors. The difference between $\chi_\perp$ and $\chi_\parallel$ is also found to have a significant effect on the result, in contrast to the electromagnetic reflection coefficient for propagating waves in section 5.4.

5.1 The infinite medium

This chapter starts by considering the infinite nonlocal medium described by the tensor susceptibility in (5.2). The transverse and longitudinal bulk susceptibilities are chosen to contain a single resonance of the form used by Halevi and Fuchs, corresponding to excitonic transitions in the medium. The dispersion relation of the exciton band in the isotropic medium is taken as [86] :

$$\hbar\omega_{T\perp/\parallel}(k) = \hbar\omega_T + \frac{\hbar^2 k^2}{2m_{\perp/\parallel}}, \quad \omega^2_{T\perp/\parallel}(k) \approx \omega_T^2 + D_{\perp/\parallel}k^2, \quad D_{\perp/\parallel} = \frac{\hbar\omega_T}{m_{\perp/\parallel}}, \tag{5.3}$$

where $m_{\perp/\parallel}$ is the mass of the exciton in the directions perpendicular or parallel to $\boldsymbol{k}$. Equation (5.3) is substituted into the Lorentz model (2.19) to give the single-resonance susceptibility:

$$\chi_{\perp/\parallel}(\boldsymbol{k},\omega) = \chi_0 + \frac{\omega_p^2}{\left(\omega_T^2 + D_{\perp/\parallel}k^2\right) - \omega^2 - i\gamma\omega}, \tag{5.4}$$

where ω_T is the resonant frequency, γ quantifies the absorption (or damping) and ω_p describes the strength of the resonance. The term χ_0 contains contributions from the other resonances not explicitly described in (5.4) and acts as a background susceptibility. The tensor expression in (5.2) therefore reduces to the scalar susceptibility used by Halevi and Fuchs in the $D_\perp = D_\parallel$ limit.

In the infinite nonlocal medium, the polarization field $\boldsymbol{P}$ is given by:

$$P_i(\boldsymbol{r},\omega) = \varepsilon_0 \sum_j \int d^3\boldsymbol{r}' \chi_{ij}(\boldsymbol{r}-\boldsymbol{r}',\omega) E_j(\boldsymbol{r}',\omega), \tag{5.5}$$

which can be rewritten using the spatial Fourier transformation (2) to give:

$$P_i(\boldsymbol{k},\omega) = \varepsilon_0 \sum_j \chi_{ij}(\boldsymbol{k},\omega) E_j(\boldsymbol{k},\omega). \tag{5.6}$$

The exact relationship for the infinite medium can be found by substituting (5.2) and (5.4) into (5.6) to give:

$$P_i(\boldsymbol{k},\omega) = \varepsilon_0\chi_0 E_i(\boldsymbol{k},\omega) + \varepsilon_0 \sum_j \left\{ \delta_{ij} \left[\frac{\omega_p^2}{(\omega_T^2 + D_\perp k^2) - \omega^2 - i\gamma\omega} \right] + \frac{k_i k_j}{k^2} \left[\frac{\omega_p^2}{\left(\omega_T^2 + D_\parallel k^2\right) - \omega^2 - i\gamma\omega} - \frac{\omega_p^2}{(\omega_T^2 + D_\perp k^2) - \omega^2 - i\gamma\omega} \right] \right\} E_j(\boldsymbol{k},\omega). \tag{5.7}$$

This expression can be inverted to find the equation of motion for $\boldsymbol{P}$ in a form similar to the one used by Hopfield in section 2.2.1. In the absence of χ_0, which represents the other resonances in the medium, this is given by:

$$\varepsilon_0\omega_p^2 E_i(\boldsymbol{k},\omega) = \left[(\omega_T^2 + D_\perp k^2) - \omega^2 - i\gamma\omega\right] P_i(\boldsymbol{k},\omega) + \sum_j \left[(D_\parallel - D_\perp)k_i k_j\right] P_j(\boldsymbol{k},\omega). \tag{5.8}$$

Equation (5.8) is identical to that of the medium described by the scalar susceptibility, with the exception of the final term that depends on the difference between the nonlocal parameters $D_\perp$ and $D_\parallel$. These coefficients are defined to have the relationship:

$$D_\parallel = (1+\Delta)D_\perp, \tag{5.9}$$

so that the tensor susceptibility (5.2) returns to the scalar expression $\delta_{ij}\chi_\perp$ in the $\Delta \to 0$ limit.

The electric field $\boldsymbol{E}$ and the polarization field $\boldsymbol{P}$ in (5.5) must satisfy the wave equation

$$\boldsymbol{\nabla} \times \boldsymbol{\nabla} \times \boldsymbol{E}(\boldsymbol{r},\omega) - \frac{\omega^2}{c^2}\boldsymbol{E}(\boldsymbol{r},\omega) = \frac{\omega^2}{c^2}\frac{1}{\varepsilon_0}\boldsymbol{P}(\boldsymbol{r},\omega) \tag{5.10}$$

at all points in space [1]. After performing a spatial Fourier transformation using (2) and substituting the expression for $\boldsymbol{P}$ in (5.7), the wave equation in (5.10) has solutions when the frequency and wave vector satisfy the dispersion relation

$$\frac{\omega^2}{c^2}\left[1 + \chi_0 + \frac{\omega_p^2}{(\omega_T^2 + D_\perp k^2) - \omega^2 - i\gamma\omega}\right] = k^2 \tag{5.11}$$

for transverse waves with $\boldsymbol{E}\cdot\boldsymbol{k} = 0$ and

$$\left[1 + \chi_0 + \frac{\omega_p^2}{\left(\omega_T^2 + D_\parallel k^2\right) - \omega^2 - i\gamma\omega}\right] = 0 \tag{5.12}$$

for longitudinal waves with $\boldsymbol{E} \times \boldsymbol{k} = 0$. With the field dependence $\exp(ik_z z)$, solutions to (5.11) and (5.12) are restricted to those with $\mathbb{I}\mathrm{m}[k_z] > 0$. This is to avoid waves that grow exponentially in the $z > 0$ half-space. The two solutions of (5.11) and the single solution to (5.12) that satisfy this condition are subsequently used in the ansatz for the electric field in the half-infinite medium, in the same manner as Halevi and Fuchs [4].

5.2 The half-infinite medium

The rest of this chapter considers the half-infinite nonlocal medium occupying the $z > 0$ half-space. The following derivation is based on the Halevi-Fuchs scalar single-resonance model in (5.1), with some changes to account for the tensor nature of the susceptibility. In section 2.3.2, it was shown that the main problem in the calculation of the electromagnetic reflection and transmission coefficients was insufficient information regarding the relative amplitudes of the multiple waves in the nonlocal medium. This section will derive a set of equations that act as the ABCs for the half-infinite nonlocal medium that provide the required relationships between the field amplitudes.

Before starting, several notes must be made regarding the half-infinite medium and the assumptions made in this calculation. First, the following work is based on macroscopic electromagnetism. Quantum-mechanical features, such as "electron spill-out", that are not directly encoded in the bulk susceptibility are not included in the derivation. The results of this chapter will therefore not be accurate for distances below a few nanometres from the planar boundary of the half-infinite medium. However, it has been found that some quantum features of the boundary can be included through a spatially-dispersive term in the susceptibility [9].

The derivation also assumes that the surface of the nonlocal medium is perfectly smooth. While boundary roughness has previously been studied in the case of the local medium [118, 119], and could potentially be incorporated in a similar manner, this lies beyond the scope of this thesis. Boundary layers containing slits [120] or other non-trivial structures [121] are similarly not covered by this derivation, as this would require additional considerations of the field inside the interface layer.

Finally, this derivation is not applicable to materials such as thin films or nanospheres due to the more complex behaviour of the polarization waves in such a system, such as multiple reflections from closely-spaced boundaries. However, an exception can be made for spatially-dispersive metamaterials when the wavelength is such that an effective

description can be used for the susceptibility.

The model set-up and choice of co-ordinates shown in Fig. 5.1 are identical to those used by Halevi and Fuchs and described in section 2.3. The $z < 0$ vacuum half-space contains the incident ($\boldsymbol{E_0}$) and reflected ($\boldsymbol{E_r}$) monochromatic plane waves with wave vectors $\boldsymbol{k_0}$ and $\boldsymbol{k_r}$ respectively ($k_0 = k_r = \omega/c$). The $z > 0$ nonlocal medium half-space contains two transverse plane waves ($\boldsymbol{E}^{(1)}$, $\boldsymbol{E}^{(2)}$) and a single longitudinal wave ($\boldsymbol{E}^{(3)}$) with wave vectors $\boldsymbol{k_n}$. The xz-plane is chosen to coincide with the plane of incidence, fixing the wave vector components $k_{nx} = K$ and $k_{ny} = 0$. Only the component $k_{nz} = q_n$ can vary between the different waves.

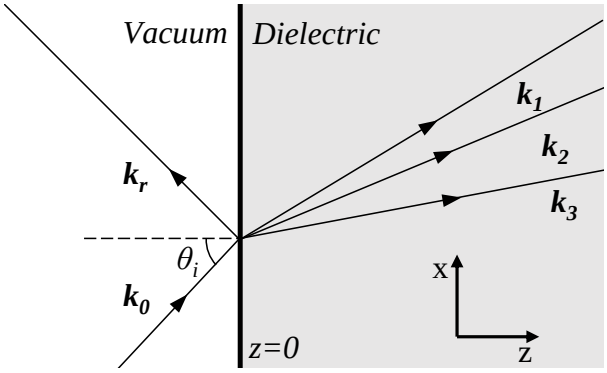

Figure 5.1: Schematic of reflection at the planar interface of a nonlocal medium. The coordinate system is chosen such that the xz-plane coincides with the plane of incidence and $k_y = 0$. The $z < 0$ vacuum half-space contains the incident wave $\boldsymbol{E}_0$ and the reflected wave $\boldsymbol{E}_r$, with the corresponding wave vectors $\boldsymbol{k}_0$ and $\boldsymbol{k}_r$. The $z > 0$ nonlocal medium contains two transverse waves ($\boldsymbol{E}^{(1)}$, $\boldsymbol{E}^{(2)}$) and one longitudinal wave ($\boldsymbol{E}^{(3)}$), with the corresponding wave vectors $\boldsymbol{k}_n$.

The presence of the boundary at $z = 0$ means the polarization field $\boldsymbol{P}$ in the nonlocal medium now depends on a position-dependent susceptibility, denoted χ'. Instead of (5.5), the expression for $\boldsymbol{P}$ takes the form:

$$P_i(\boldsymbol{r}) = \varepsilon_0 \sum_j \int d^3\boldsymbol{r}' \chi'_{ij}(\boldsymbol{r}, \boldsymbol{r}') E_j(\boldsymbol{r}'), \tag{5.13}$$

where ω dependence has been omitted to reduce notation. Following the Halevi-Fuchs model in (5.1), the susceptibility of the half-infinite medium in (5.13) is expressed in

terms of the bulk susceptibility (5.2):

$$\chi'_{ij}(x-x',y-y',z,z') = \begin{cases} \chi_{ij}(x-x',y-y',z-z') \\ \quad + U_{ij}\chi_{ij}(x-x',y-y',z+z') & \text{if } z,z'>0, \\ 0 & \text{otherwise,} \end{cases} \tag{5.14}$$

where both χ_{ij} and U_{ij} are now rank-2 tensors. The first term in (5.14) is the nonlocal bulk response describing the direct propagation of the polarization wave between two points. The second term describes a polarization wave traveling from z' to the boundary of the medium, before reflecting and continuing to z, as shown in Fig. 2.7 of section 2.3.4.

The expression for the susceptibility of the half-infinite medium in (5.14) can be substituted into the $\boldsymbol{P}$ definition in (5.13). After a spatial Fourier transformation is performed in the xy-plane using (3), the polarization field is given by:

$$\begin{aligned} P_i(K,0,z) =& \varepsilon_0\chi_0 E_i(K,0,z) \\ &+ \frac{\varepsilon_0}{2\pi}\int_0^\infty dz' \int_{-\infty}^\infty dq \sum_j \left[e^{iq(z-z')} + U_{ij}e^{iq(z+z')}\right]\chi_{ij}(K,0,q)E_j(K,0,z'). \end{aligned} \tag{5.15}$$

The expressions for the bulk susceptibilities in (5.4) that appear in (5.15) can each be rewritten in terms of q:

$$\chi_{\perp/\parallel}(K,0,q,\omega) = \chi_0 + \frac{\omega_p^2/D_{\perp/\parallel}}{q^2 - \Gamma_{\perp/\parallel}(K)}, \tag{5.16}$$

where

$$-\Gamma^2_{\perp/\parallel}(K) = \frac{\omega_T^2 - \gamma^2 - i\gamma\omega}{D_{\perp/\parallel}} + K^2. \tag{5.17}$$

The $k_x = K$ and $k_y = 0$ dependences will subsequently omitted as they are the same in all arguments.

At this point in the derivation, an ansatz for the electric field must be introduced to evaluate the integrals in (5.15). Halevi and Fuchs used a sum of monochromatic plane waves with wave vectors that satisfied the dispersion relations of the infinite medium. While they provided no supporting arguments for this particular ansatz, the derivation in section 4.2 has shown that this was a suitable choice for the electric field at all points inside the medium. The same expression is used for the single-resonance tensor susceptibility model:

$$\boldsymbol{E}(z) = \begin{cases} \boldsymbol{E}_0 e^{iq_0 z} + \boldsymbol{E}_r e^{-iq_0 z} & z<0, \\ \displaystyle\sum_{n=1}^{3} \boldsymbol{E}^{(n)} e^{iq_n z} & z>0, \end{cases} \tag{5.18}$$

where the $z < 0$ half-space contains the incident ($\boldsymbol{E}_0$) and reflected ($\boldsymbol{E}_r$) waves, with the corresponding wave vector

$$q_0 = \sqrt{k_0^2 - K^2}. \tag{5.19}$$

The $z > 0$ half-space contains the transverse waves $\boldsymbol{E}^{(1)}$ and $\boldsymbol{E}^{(2)}$ and the longitudinal wave $\boldsymbol{E}^{(3)}$. The corresponding wave vectors q_1 and q_2 are the $\mathbb{I}\mathrm{m}[q] > 0$ solutions to the transverse dispersion relation (5.11), rewritten as:

$$k_0^2 \frac{\omega_p^2}{D_\perp^2} = \left[q^2 - k_0^2(1+\chi_0) + K^2\right]\left[q^2 - \Gamma_\perp^2\right], \tag{5.20}$$

and q_3 is the $\mathbb{I}\mathrm{m}[q] > 0$ solution to the longitudinal dispersion relation (5.12), rewritten as:

$$-\frac{\omega_p^2}{(1+\chi_0)D_\parallel^2} = \left(q^2 - \Gamma_\parallel^2\right). \tag{5.21}$$

Substituting the ansatz (5.18) for $\boldsymbol{E}(z')$ into (5.15) allows the z' integral to be evaluated, leaving:

$$P_i(z) = \varepsilon_0\chi_0 E_i(z) + \varepsilon_0 \frac{i}{2\pi}\int_{-\infty}^{\infty} dq \sum_j \sum_{n=1}^{3} e^{iqz}\left[\frac{1}{q_n - q} + \frac{U_{ij}}{q_n + q}\right]\chi_{ij}(q) E_j^{(n)}. \tag{5.22}$$

The q integral in (5.22) is evaluated by performing a contour integration in the upper half-plane [114] of complex q, enclosing the poles at $q = q_n$ in the square brackets and the poles at $q = \Gamma_{\perp/\parallel}$ and $q = iK$ in the susceptibility χ_{ij}. The residue associated with the pole $q = iK$ is equal to zero, leaving a final expression for the polarization field in the half-infinite nonlocal medium that contains three distinct parts:

$$P_i(z) = \sum_j \sum_{n=1}^{3} \varepsilon_0 \chi_{ij}(q_n) E_j^{(n)} e^{iq_n z} + \sum_j \sum_{n=1}^{3} \varepsilon_0 \phi_{ij}^{(n)} E_j^{(n)} e^{i\Gamma_\perp z} + \sum_j \sum_{n=1}^{3} \varepsilon_0 \psi_{ij}^{(n)} E_j^{(n)} e^{i\Gamma_\parallel z}, \tag{5.23}$$

where χ_{ij} is the susceptibility of the infinite medium. The electric field coefficients in the last two terms are given by:

$$\phi_{ij}^{(n)} = -\frac{q_n(1+U_{ij}) + \Gamma_\perp(1-U_{ij})}{2\Gamma_\perp}\left[\delta_{ij} - \frac{k_i^{(\perp)} k_j^{(\perp)}}{\Gamma_\perp^2 + K^2}\right]\chi_\perp(q) \tag{5.24}$$

and:

$$\psi_{ij}^{(n)} = -\frac{q_n(1+U_{ij}) + \Gamma_\parallel(1-U_{ij})}{2\Gamma_\parallel}\left[\frac{k_i^{(\parallel)}k_j^{(\parallel)}}{\Gamma_\parallel^2 + K^2}\right]\chi_\parallel(q), \tag{5.25}$$

where $\boldsymbol{k}^{(\perp/\parallel)} = (K, 0, \Gamma_{\perp/\parallel})$.

The electric field given by the ansatz (5.18) and the polarization field in (5.23) must satisfy the electromagnetic wave equation (5.10) at all points inside the medium. A simple inspection reveals that all LHS terms are proportional to the exponential $\exp(iq_nz)$. If the wave equation is to hold for all values of z, the RHS sums proportional to $\exp(i\Gamma_{\perp/\parallel}z)$ in (5.23) must each equal zero:

$$\sum_j \sum_{n=1}^{3} \phi_{ij}^{(n)} E_j^{(n)} = 0, \qquad \sum_j \sum_{n=1}^{3} \psi_{ij}^{(n)} E_j^{(n)} = 0. \tag{5.26}$$

This set of equations act as the ABCs for this model and can be used to calculate the field amplitude ratios of the waves in the nonlocal medium. The next section uses the sums in (5.26) to derive exact expressions for the electromagnetic reflection and transmission coefficients of the single-resonance tensor susceptibility model.

5.3 The p-polarization

It is at this point in the calculation that the electric field is split into two parts, which each require slightly different considerations in the calculation of the electromagnetic reflection and transmission coefficients. The s-polarization contains the components of the electric field that are perpendicular to the plane of incidence, which corresponds to E_y in the current model. It can be seen in (5.2) that the current choice of co-ordinate system, with $k_y = 0$, means $\chi_{yy} = \chi_\perp$ is the only nonzero component of the susceptibility for the s-polarization. As a result, the derivation of the electromagnetic reflection and transmission coefficients is identical to that of the Halevi-Fuchs model and will not be repeated here. This section focuses on the p-polarization, which contains the components of the electric field E_x and E_z that lie in the plane of incidence. In this case there are four relevant nonzero components of the tensor susceptibility (5.2), compared to two in the Halevi-Fuchs model in (5.1).

5.3.1 The surface impedance

Halevi and Fuchs used an expression for the electromagnetic reflection coefficient in terms of the surface impedance of the vacuum and the nonlocal medium [4]. In the p-polarization the surface impedance Z_p is given by [44]:

$$Z_p = \frac{E_x}{H_y} = \frac{1}{\mu_0}\frac{E_x}{B_y}, \tag{5.27}$$

where the nonmagnetic nature of both the vacuum and the nonlocal medium ($\boldsymbol{H} = \mu_0 \boldsymbol{B}$) has been used. Inside the nonlocal medium, the field component B_y of the ansatz (5.18) can be rewritten using the Maxwell equation [1] $k_0 \boldsymbol{B} = \boldsymbol{k} \times \boldsymbol{E}$:

$$B_y(z) = \sum_{n=1}^{3} \frac{1}{k_0}\left[q_n E_x^{(n)} - K E_z^{(n)}\right] e^{iq_n z}. \tag{5.28}$$

Simple geometry can be used to rewrite E_z in terms of E_x:

$$E_z^{(n)} = \eta^{(n)} E_x^{(n)}, \tag{5.29}$$

where $\eta^{(n)} = -K/q_n$ for transverse waves and $\eta^{(n)} = q_n/K$ for longitudinal waves. The magnetic field in (5.27) can subsequently be expressed solely in terms of E_x components:

$$B_y(z) = \sum_{n=1}^{3} \tau^{(n)} E_x^{(n)} e^{iq_n z} \qquad \tau^{(n)} = \begin{cases} \dfrac{q_n^2 + K^2}{q_n k_0}, & \text{transverse waves,} \\ 0, & \text{longitudinal waves.} \end{cases} \tag{5.30}$$

The surface impedance (5.27) of the nonlocal medium can therefore be expressed in terms of the field amplitude ratios:

$$Z_p(0^+) = \frac{1}{\mu_0}\frac{\sum_{n=1}^{3} E_x^{(n)}}{\sum_{n=1}^{3} \tau^{(n)} E_x^{(n)}} = \frac{k_0}{\mu_0}\frac{1 + \frac{E_x^{(2)}}{E_x^{(1)}} + \frac{E_x^{(3)}}{E_x^{(1)}}}{\frac{q_1^2+K^2}{q_1} + \frac{q_2^2+K^2}{q_2}\frac{E_x^{(2)}}{E_x^{(1)}}}. \tag{5.31}$$

Note that $E_x^{(3)}$ does not appear in the denominator of (5.31) as longitudinal waves do not have an associated magnetic field, as described in section 2.1.4. This behaviour can also be seen in (5.30), where $\tau^{(n)} = 0$.

5.3.2 Field amplitude ratios

The field amplitude ratios of the transmitted waves in the nonlocal medium are required to proceed with the calculation of the electromagnetic reflection coefficient. The relationship

in (5.29) was used to rewrite each of the relevant effective ABC equations in (5.26) solely in terms of E_x. For example:

$$\sum_j \sum_{n=1}^{3} \phi_{ij}^{(n)} E_j^{(n)} = \sum_{n=1}^{3} \left[\phi_{ix}^{(n)} E_x^{(n)} + \phi_{iz}^{(n)} E_z^{(n)} \right] = \sum_{n=1}^{3} \left[\phi_{ix}^{(n)} + \eta^{(n)} \phi_{iz}^{(n)} \right] E_x^{(n)} = 0, \tag{5.32}$$

where $i = x$ or z. In each case, the $E_x^{(n)}$ coefficients are grouped together to the new variables a_n and b_n:

$$\sum_{n=1}^{3} \left[\phi_{xx}^{(n)} + \eta^{(n)} \phi_{xz}^{(n)} \right] E_x^{(n)} = \sum_{n=1}^{3} a_n E_x^{(n)} = 0, \tag{5.33}$$

$$\sum_{n=1}^{3} \left[\phi_{zx}^{(n)} + \eta^{(n)} \phi_{zz}^{(n)} \right] E_x^{(n)} = \sum_{n=1}^{3} b_n E_x^{(n)} = 0. \tag{5.34}$$

Similar expressions were found by rearranging the ψ equations in (5.26) to give the variables c_n and d_n:

$$\sum_{n=1}^{3} \left[\psi_{xx}^{(n)} + \eta^{(n)} \psi_{xz}^{(n)} \right] E_x^{(n)} = \sum_{n=1}^{3} c_n E_x^{(n)} = 0, \tag{5.35}$$

$$\sum_{n=1}^{3} \left[\psi_{zx}^{(n)} + \eta^{(n)} \psi_{zz}^{(n)} \right] E_x^{(n)} = \sum_{n=1}^{3} d_n E_x^{(n)} = 0. \tag{5.36}$$

It can be seen that the current model has four equations that must be satisfied by the three wave amplitudes, in contrast to the two equations of the Halevi-Fuchs derivation.

Any two of the equations (5.33-5.36) can be combined to find the required expressions for the field amplitude coefficients:

$$\frac{E_x^{(2)}}{E_x^{(1)}} = \frac{(3,1)_{\mu\nu}}{(2,3)_{\mu\nu}}, \qquad \frac{E_x^{(3)}}{E_x^{(1)}} = \frac{(1,2)_{\mu\nu}}{(2,3)_{\mu\nu}}, \qquad \mu \neq \nu, \tag{5.37}$$

where $\mu, \nu \in \{a, b, c, d\}$ and

$$(i,j)_{\mu\nu} = \mu_i \nu_j - \mu_j \nu_i. \tag{5.38}$$

The field amplitude ratios in (5.37) must give the same value for any combination of μ and ν ($\mu \neq \nu$). This imposes the conditions $U_{xx} = U_{zx}$ and $U_{xz} = U_{zz}$, which reduce b_n and d_n to $(-k/\Gamma_\perp)a_n$ and $(\Gamma_\parallel/k)c_n$ respectively. The set of four equations in (5.33-5.36) similarly reduce to two unique equations relating the field amplitudes of the three

transmitted waves. These conditions on U_{ij} lead to obvious comparisons to the values of U_i used by Halevi and Fuchs. Subsequent calculations for specific ABCs will assume $U_{xx} = U_{zx}$ and $U_{xz} = U_{zz}$ in the current model correspond to the values of U_x and U_z in Table 2.1.

The field amplitude ratios (5.37) can be substituted into (5.31) to give a final expression for the surface impedance of the nonlocal medium:

$$Z_p(0^+) = \frac{k_0}{\mu_0} \frac{(2,3)_{ac} + (3,1)_{ac} + (1,2)_{ac}}{\frac{q_1^2+K^2}{q_1}(2,3)_{ac} + \frac{q_2^2+K^2}{q_2}(3,1)_{ac}}. \tag{5.39}$$

The subscripts $\mu = a$ and $\nu = c$ will subsequently be omitted for notational simplicity. The full expression for (5.39) is a function of the three wave vectors q_n. In the simplest case of $U_{ij} = 0$, the surface impedance is given by:

$$Z_p = -\frac{k_0}{\mu_0}\left\{\Gamma_\perp - \frac{\left[K^4+K^2(q_1^2+q_1q_2+q_2^2)+(q_1+q_2)q_1q_2q_3\right] - \frac{\left(\Gamma_\parallel-\Gamma_\perp\right)(K^2+q_3^2)}{\left(\Gamma_\perp^2+K^2\right)+\left(\Gamma_\parallel-\Gamma_\perp\right)(\Gamma_\perp+q_3)}[q_1q_2(q_1+q_2)]}{[K^2(q_1+q_2-q_3)+q_1q_2q_3] + \frac{\left(\Gamma_\parallel-\Gamma_\perp\right)(K^2+q_3^2)}{\left(\Gamma_\perp^2+K^2\right)+\left(\Gamma_\parallel-\Gamma_\perp\right)(\Gamma_\perp+q_3)}[K^2-q_1q_2]}\right\}^{-1}. \tag{5.40}$$

In the general case where $U_{xx} = U_{zx}$ and $U_{xz} = U_{zz}$, setting $D_\perp = D_\parallel$ (and therefore $\Gamma_\perp = \Gamma_\parallel$ and $\chi_{ij} = \delta_{ij}\chi_\perp$) reduces (5.39) to the Halevi-Fuchs model result for the scalar bulk susceptibility with $U_x = U_{xx}$ and $U_z = U_{zz}$. The results presented in this chapter are therefore consistent with those of the Halevi-Fuchs model.

5.3.3 Electromagnetic reflection and transmission coefficients

The p-polarization reflection coefficient r_p can be written in terms of the surface impedance [44]:

$$r_p = \frac{E_r}{E_0} = \frac{Z_p(0^-) - Z_p(0^+)}{Z_p(0^-) + Z_p(0^+)}, \tag{5.41}$$

where the nonlocal medium surface impedance (5.39) and the vacuum surface impedance [44]

$$Z_p(0^-) = \frac{q_0}{\mu_0 k_0} \tag{5.42}$$

can be used to find an exact expression for r_p.

The transmission coefficients for each of the three waves in the nonlocal medium are found by imposing Maxwell boundary conditions, specifically the continuity of transverse

$\boldsymbol{E}$ components, at the $z = 0$ planar boundary. In the current choice of co-ordinate system in Fig. 5.1, this means equating the E_x components in the ansatz (5.18):

$$E_{0x} + E_{rx} = E_x^{(1)} + E_x^{(2)} + E_x^{(3)}. \tag{5.43}$$

Simple geometry and the definition of the reflection coefficient in (5.41) can be used to rewrite (5.43) in terms of the previously calculated amplitude coefficients:

$$E_0 \left[\frac{q_0}{k_0}(1 - r_p)\right] = E_x^{(1)} \left[1 + \frac{E_x^{(2)}}{E_x^{(1)}} + \frac{E_x^{(3)}}{E_x^{(1)}}\right] = E_x^{(1)} \left[\frac{(2,3) + (3,1) + (1,2)}{(2,3)}\right], \tag{5.44}$$

with similar expressions for $E_x^{(2)}$ and $E_x^{(3)}$. Equation (5.29) can be used to rewrite the x-component of the field in terms of the total amplitude:

$$E^{(n)} = \sqrt{E_x^{(n)2} + E_z^{(n)2}} = \sqrt{1 + \eta^{(n)2}} E_x^{(n)}, \tag{5.45}$$

which leads to the final expressions for the transmission coefficients of the three waves:

$$\begin{aligned}
t_p^{(1)} = \frac{E^{(1)}}{E_0} &= (2,3) \frac{\sqrt{q_1^2 + K^2}}{q_1} \left\{\frac{q_0}{k_0} \frac{[1 - r_p]}{[(2,3) + (3,1) + (1,2)]}\right\}, \\
t_p^{(2)} = \frac{E^{(2)}}{E_0} &= (3,1) \frac{\sqrt{q_2^2 + K^2}}{q_2} \left\{\frac{q_0}{k_0} \frac{[1 - r_p]}{[(2,3) + (3,1) + (1,2)]}\right\}, \\
t_p^{(3)} = \frac{E^{(3)}}{E_0} &= (1,2) \frac{\sqrt{q_3^2 + K^2}}{K} \left\{\frac{q_0}{k_0} \frac{[1 - r_p]}{[(2,3) + (3,1) + (1,2)]}\right\}.
\end{aligned} \tag{5.46}$$

Note that the last set of brackets is identical for each expression in (5.46).

It has previously been mentioned in section 2.3.3 that the choice of $U_x = -1$ and $U_z = 1$ in the Rimbey-Mahan ABC leads to the absence of the longitudinal wave in the nonlocal medium [48–52]. This behaviour can be seen in (5.46), where these specific choices for U_{xx} and U_{zz} lead to the result $(1,2) = 0$ and $E^{(3)} = 0$. It is interesting to consider the possibility of the opposing case, where the choice of U_{ij} leads to the absence of transverse waves in the nonlocal medium. This would have significant consequences for the surface impedance, as the remaining longitudinal wave in the medium does not have an associated magnetic field. The definition in (5.27) would lead to $Z_p = \infty$ and perfect reflection with $r_p = -1$.

The absence of transverse waves in the nonlocal medium would require $(2,3) = (3,1) = 0$ and $(1,2) \neq 0$ in (5.46). The definition (5.38) leads to the condition $a_3 = c_3 = 0$, which can only be satisfied by the following conditions in the general $U_{xx} =$

$U_{zx}, U_{xz} = U_{zz}$ case:

$$U_{xx} = 1 + \frac{2q_3(\Gamma_\parallel^2 + K^2)}{(\Gamma_\perp\Gamma_\parallel + K^2)(\Gamma_\parallel - q_3)},$$
$$U_{zz} = -1 + \frac{2\Gamma_\perp(\Gamma_\parallel^2 + K^2)}{(\Gamma_\perp\Gamma_\parallel + K^2)(\Gamma_\parallel - q_3)}. \tag{5.47}$$

In the $\Delta = 0$ case, which corresponds to the Halevi-Fuchs model, the conditions for perfect reflection in (5.47) reduce to:

$$U_{zz} = U_{xx} = \frac{\Gamma_\perp + q_3}{\Gamma_\perp - q_3} = \frac{1 + \sqrt{1 + \frac{1}{1+\chi_0}\frac{\omega_p^2}{\omega_T^2 + D_\perp K^2 - \omega^2 - i\gamma\omega}}}{1 - \sqrt{1 + \frac{1}{1+\chi_0}\frac{\omega_p^2}{\omega_T^2 + D_\perp K^2 - \omega^2 - i\gamma\omega}}}, \tag{5.48}$$

where the q_3 definition in (5.21) has been used. It can be seen that the square root in (5.48) does not vanish for any real values of K and ω. The resulting value of $|U_{xx}| > 1$ conflicts with the definition of U_{ij} as a phenomenological reflection coefficient for the polarization waves inside the medium. The nonlocal medium therefore must contain transverse transmitted waves.

5.4 Results

The exact expressions for r_p and $t_p^{(n)}$ in section 5.3.3 are dependent on both $\Gamma_{\perp/\parallel}$ and the wave vectors q_n. The ω and K dependence of the electromagnetic reflection and transmission coefficients and their differences to the Halevi-Fuchs results are not readily apparent from a simple inspection of (5.41) and (5.46). This section presents numeric results for Zinc Selenide (ZnSe) [122], the same medium used by Halevi and Fuchs [4], and investigates the effects caused by the inequality between $D_\perp$ and $D_\parallel$.

Table 5.1: List of ZnSe model parameters [4, 122]

	ZnSe
χ_0	8.1
$\hbar\omega_T$ (eV)	2.80
$\hbar\omega_p$ (eV)	2.07
$\hbar\gamma$ (meV)	0.028
$D_\perp c^2$ ($\times 10^{-6}$)	5.49
$\hbar\omega_L$ (eV)	2.80085

The model parameters of the nonlocal medium ZnSe are shown in Table 5.1. The value of ω_L, which is the solution of the dispersion relation (5.11) with $k = 0$ and $\gamma = 0$, is calculated using (2.20). The transverse nonlocal parameter $D_\perp$ takes the same value used in the Halevi-Fuchs paper. The corresponding longitudinal parameter $D_\parallel = (1+\Delta)D_\perp$ is unknown. Results are instead presented over the range of Δ values -0.5 to 0.5. Table 5.2 contains the values of U_{ij} for a range of ABCs. In each case, the $U_{xx} = U_{zx}, U_{xz} = U_{zz}$ condition in section 5.3.3 were used to convert the values used by Halevi and Fuchs to the tensor susceptibility.

Table 5.2: List of ABC parameters for the single-resonance tensor χ'_{ij} in (5.14)

ABC	U_{xx}, U_{zx}, U_{yy}	U_{xz}, U_{zz}
Agarwal *et al.* [33–42]	0	0
Ting *et al.* [43]	1	1
Fuchs-Kliewer [44–47]	1	-1
Rimbey-Mahan [48–52]	-1	1
Pekar [53–56]	-1	-1

5.4.1 The p-polarization reflection coefficient

The reflection coeffcient of ZnSe is first considered as a function of the incident angle θ_i in Fig. 5.1. Figure 5.2 shows the absolute value of r_p at the resonant frequency ω_T for the Agarawal *et al.*, Ting *et al.*, Fuchs-Kliewer, Rimbey-Mahan and Pekar ABCs using the corresponding U_{ij} values in Table 5.2. The behaviour of r_p is mostly determined by the value of U_{xx}, with $U_{xx} = -1$ of the Rimbey-Mahan and Pekar ABCs displaying the greatest differences to the local model with $D_\perp = D_\parallel = 0$. This is followed by $U_{xx} = 0$ of the Agarwal *et al.* ABC and finally $U_{xx} = 1$ of the Ting *et al.* and Fuchs-Kliewer ABC. The values of U_{zz} and Δ have a much smaller effect, leading to minor differences near the reflection minima.

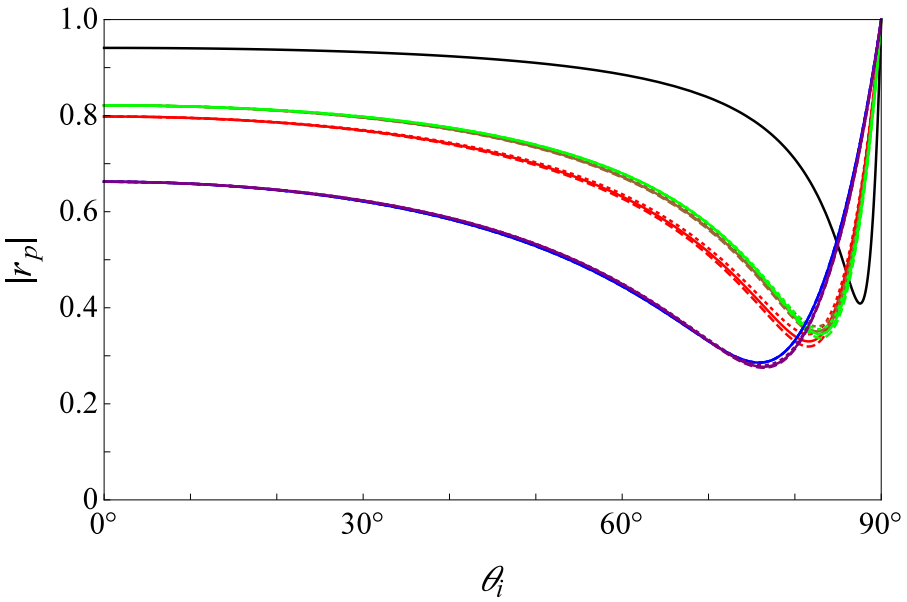

Figure 5.2: Absolute value of r_p as a function of incident angle θ_i in Fig. 5.1 for ZnSe at $\omega = \omega_T$. Results are shown for Agarwal et al. (red), Ting et al. (brown), Fuchs-Kliewer (green), Rimbey-Mahan (blue), and Pekar (purple) ABCs in addition to the local model with spatial dispersion removed ($D_\perp = D_\parallel = 0$) (black). Includes the $\Delta = 0$ results of the Halevi-Fuchs model (solid line) compared to $\Delta = 0.5$ (dashed) and $\Delta = -0.5$ (dotted), which are found to differ slightly at the reflection minima.

Figure 5.3 performs the same comparisons for r_p as a function of ω with the fixed incident angle $\theta_i = 45°$. A peak in $|r_p|$ is found between the values of ω_T and ω_L, indicated by solid and dashed vertical lines, respectively. The size of the peak and the overall behaviour of r_p is once again mostly determined by the value of U_{xx}, with $U_{xx} = 1$ giving the largest peak that is closest to the local medium result. The values of U_{zz} and Δ were found to play a more significant role in the frequency range above ω_L containing the reflection minima.

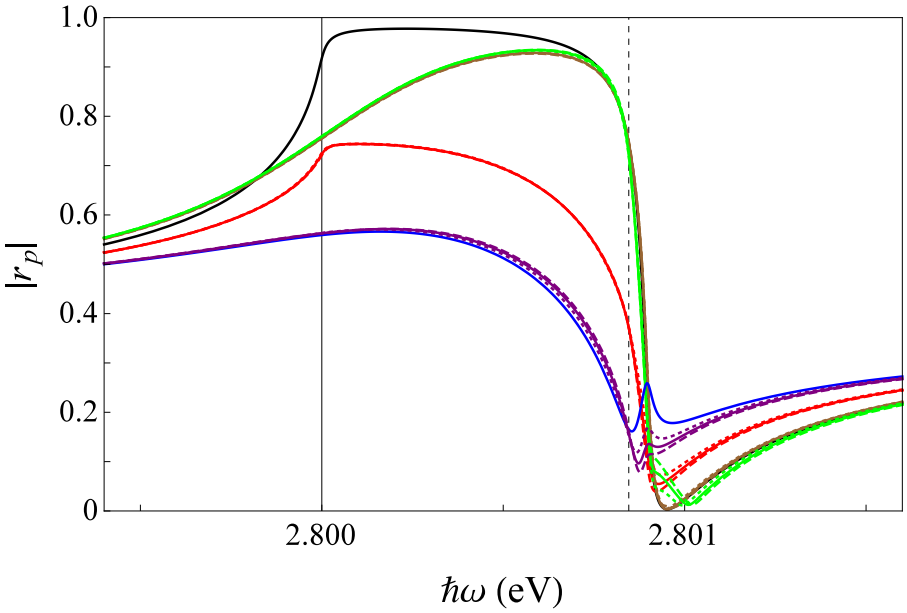

Figure 5.3: Absolute value of r_p as a function of ω for ZnSe at a fixed incident angle $\theta_i = 45°$. Vertical lines indicate ω_T (solid line) and ω_L (dashed line) values. Results are shown for Agarwal et al. (red), Ting et al. (brown), Fuchs-Kliewer (green), Rimbey-Mahan (blue), and Pekar (purple) ABCs in addition to the local model with spatial dispersion removed ($D_\perp = D_\parallel = 0$) (black). Includes the $\Delta = 0$ results of the Halevi-Fuchs model (solid line) compared to $\Delta = 0.5$ (dashed) and $\Delta = 0.5$ (dotted).

Figure 5.4 shows a closer comparison between the various ABCs in the frequency range near the reflection minima for a range of incident angles between $\theta_i = 15°$ and $75°$. At very small θ_i, r_p is determined almost entirely by the value of U_{xx}. This is because the E_z components of the both the incident and transmitted transverse waves are small near normal incidence. The effect of U_{zz} increases with θ_i and K, providing a split between the ABCs with the same U_{xx}. This behaviour was noted in Halevi and Fuchs' paper [4].

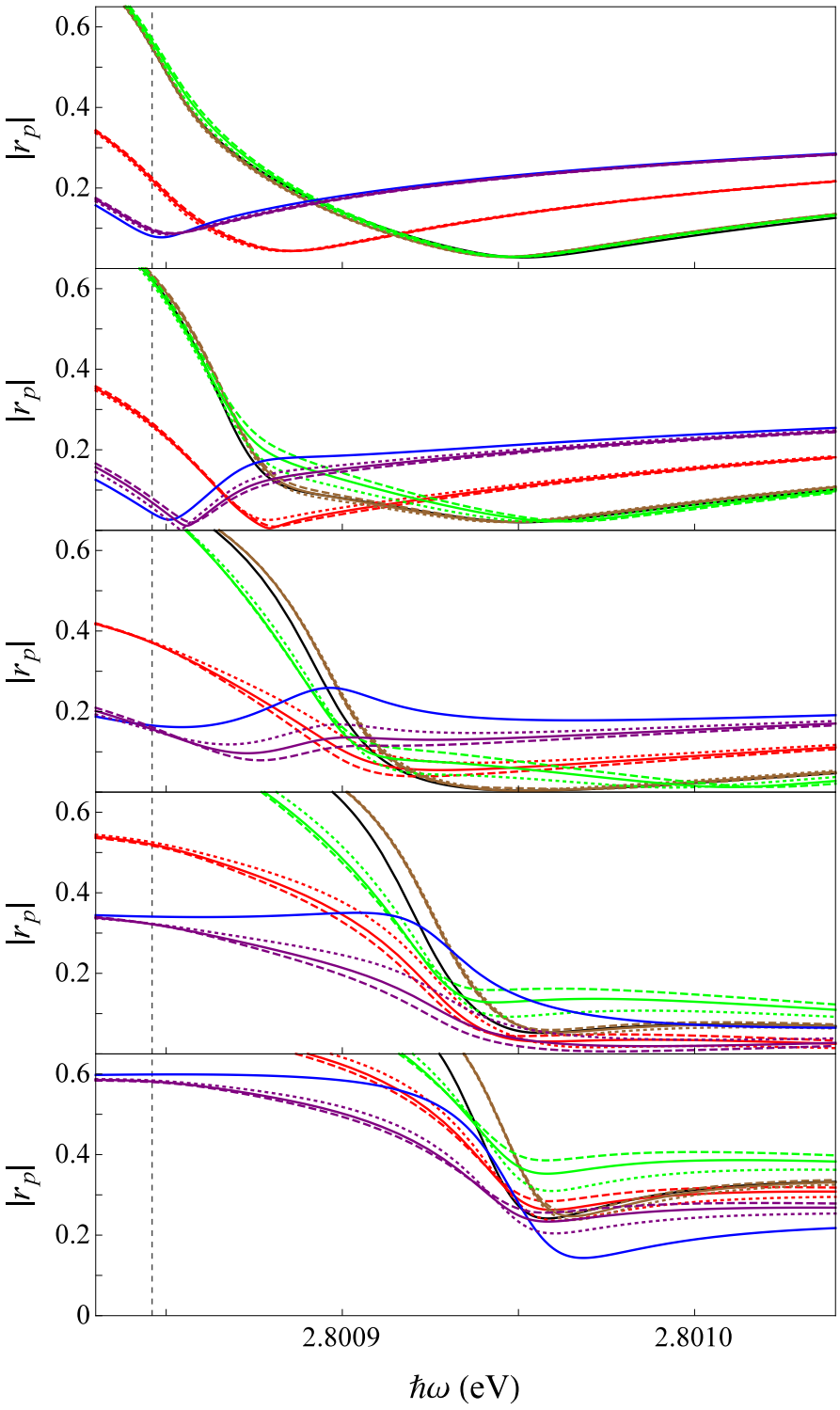

Figure 5.4: Absolute value of r_p as a function of ω for ZnSe near the reflection minima for the incident angle $\theta_i = 15°$ (top), $30°$, $45°$, $60°$ and $75°$ (bottom). Plot styles follow the conventions in Fig. 5.3.

The parameter Δ, describing the difference between the nonlocal parameters $D_\perp$ and $D_\parallel$ in (5.9), also has the largest effect on r_p in the frequency range near the reflection minima. The greatest differences were found in the Pekar and Fuchs-Kleiwer ABCs, followed closely by the Agarwal ABC. The Ting ABC, which was the closest result to that of the local model, was largely unaffected by the value of Δ, with only minor differences found in the $\theta_i = 30°$ result. The result for the Rimbey-Mahan ABC remained unchanged by Δ, as the values of U_{ij} lead to the complete absence of the longitudinal wave in the medium. The value of $D_\parallel$ and Δ therefore had no effect on r_p in this case.

5.4.2 The p-polarization transmission coefficients

Figure 5.5 compares the absolute values of the transmission coefficients $t_p^{(n)}$ at the resonant frequency ω_T as a function of the incident angle θ_i. The behaviour of $t_p^{(1)}$ and $t_p^{(2)}$ for the transverse waves is similar to that of r_p in Fig. 5.2. In these cases the result is mostly determined by the value of U_{xx}, while U_{zz} only leads to minor differences between the ABCs. The parameter Δ has a negligible effect on $t_p^{(1)}$ result, which corresponds to the transverse wave that is present even in the local medium with $D_\perp = D_\parallel = 0$, but has a slightly larger effect on $t_p^{(2)}$ for the wave introduced by the nonlocal behaviour of the susceptibility.

The transmission coefficient $t_p^{(3)}$ of the longitudinal wave displays significantly different behaviour to its transverse counterparts. The main difference is the lack of the $n = 3$ wave at normal incidence. This is because the incident transverse wave $\boldsymbol{E}_0$ lacks a $\hat{\boldsymbol{z}}$ component in this case to excite the longitudinal wave inside the nonlocal medium. The effect U_{ij} and Δ have on behaviour of $t_p^{(3)}$ is also different. The result is no longer mostly determined by the value of U_{xx}, and Δ can have a greater effect compared to the transverse waves. This can be seen for the Pekar ABC in Fig. 5.5, which is very different to the Rimbey-Mahan ABC with the same U_{xx} value and varies greatly over the Δ range -0.5 to 0.5. This behaviour is strongly dependent on both the model parameters and the frequency. For example, in Fig. 5.5, the Agarwal *et al.* and Ting *et al.* ABCs lead to similar results for $t_p^{(3)}$, but this is not true in general. The exception to this is the Rimbey-Mahan ABC, as the choice of U_{ij} leads to $(1, 2) = 0$ in (5.46) and the absence of the longitudinal wave in the medium.

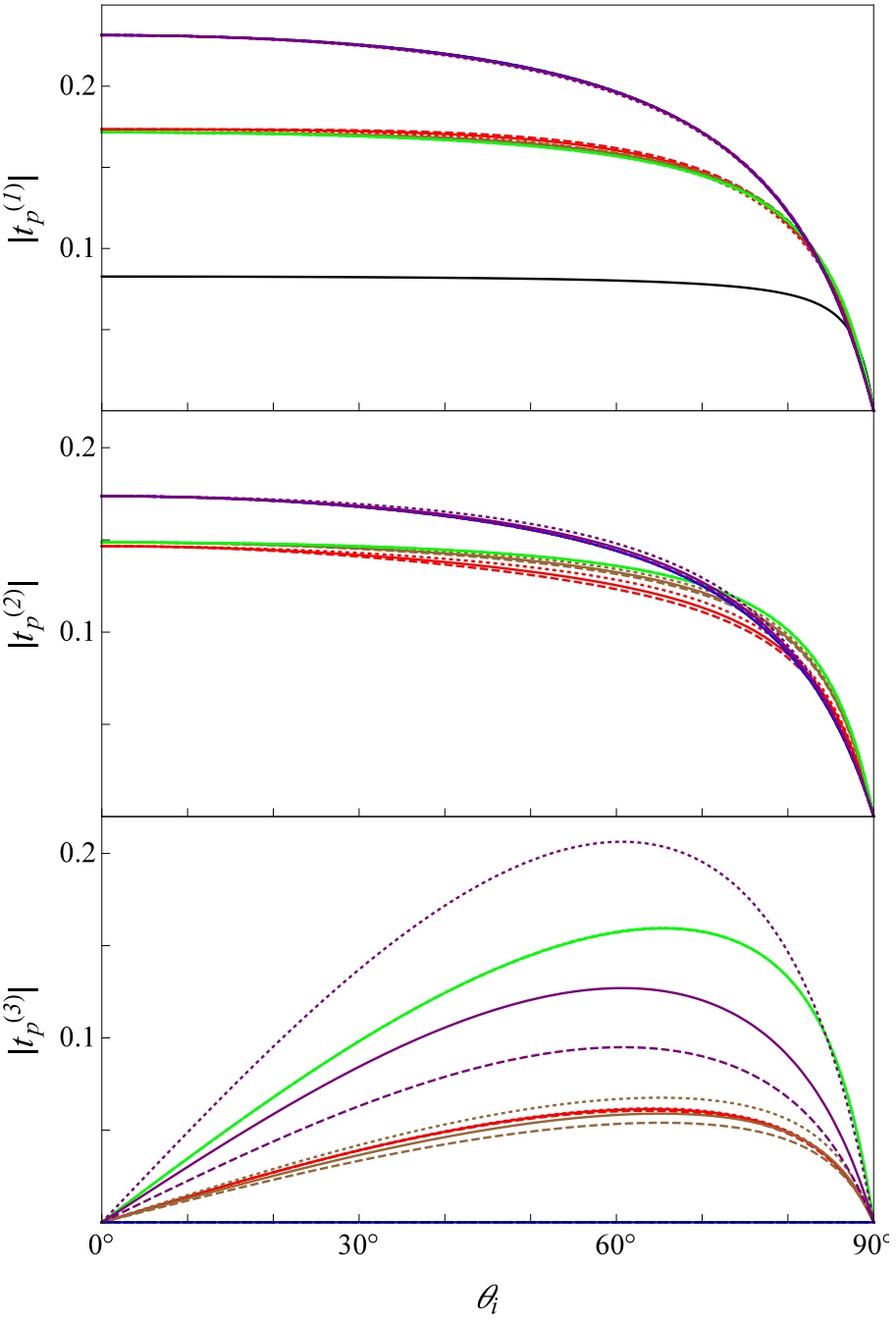

Figure 5.5: Absolute value of $t_p^{(n)}$ as a function of incident angle θ_i for ZnSe at $\omega = \omega_T$. Plot styles follow the conventions in Fig. 5.2. The parameter Δ has a minor effect on the $n = 1, 2$ transverse waves, but has a significant effect on the $n = 3$ longitudinal wave in the Pekar ABC. Note the absence of the longitudinal wave in the Rimbey-Mahan ABC.

5.5 Spectral energy density

This section takes the expression derived for r_p in the section 5.3 and applies it to the problem of the electromagnetic energy density of zero-point and thermal radiation near planar boundaries. The zero-point component can be probed by measuring spontaneous emission rates close to a boundary [74–77] and the thermal energy density has previously been measured for a metal using near-field microscopy [100]. Section 2.3.5 described the unphysical divergences in the energy density of the electromagnetic field encountered near the planar boundary of a local half-infinite medium. These divergences occurred at the level of the spectral energy density u_{tot} defined in (2.60) and could be traced back to the integral (2.63), repeated here [102]:

$$\begin{aligned} u_{\mathrm{tot}}(z,\omega) = \quad & \frac{u_0}{k_0}\int_0^{k_0} \frac{K\,dK}{\sqrt{k_0^2-K^2}} \left\{1+\frac{K^2}{2k_0^2}\,\mathbb{R}\mathrm{e}\left[(r_s+r_p)e^{2i\sqrt{k_0^2-K^2}|z|}\right]\right\} \\ & + \frac{u_0}{2k_0^3}\int_{k_0}^{\infty} \frac{K^3\,dK}{\sqrt{K^2-k_0^2}} \left\{\mathbb{I}\mathrm{m}[r_s+r_p]e^{-2\sqrt{K^2-k_0^2}|z|}\right\}, \end{aligned} \tag{5.49}$$

where u_0 is the spectral energy density in the absence of the material, given by (2.64). The first integral in (5.49) is the contribution from propagating waves with real k_z in the vacuum. The unphysical divergence is a result of the second integral over evanescent waves with imaginary k_z. Unlike r_s, the imaginary component of r_p does not vanish in the $K \to \infty$ limit in the absence of spatial dispersion. In the $z \to 0$ limit, the exponential decays slowly enough that this term becomes dominant, leading to the approximate result [5]:

$$u_{\mathrm{tot}}(z,\omega) \approx \frac{u_0}{2k_0^3}\left\{\frac{\mathbb{I}\mathrm{m}[\chi(\omega)]}{|2+\chi(\omega)|^2}\frac{1}{4|z|^3}\right\}. \tag{5.50}$$

This section will show that this unphysical divergence is naturally removed with the inclusion of spatial dispersion in the resonance of the susceptibility (5.4). This is in contrast to previous attempts by other authors that introduce a sharp [81] or smooth [82] cut-off to the K integral by hand based on parameters such as the lattice spacing or coherence length. It must be noted that a complex background susceptibility χ_0 will still lead to a divergence in u_{tot}. However, it has already been noted in section 2.1.5 that this is the contribution from other resonances in the medium. A full treatment of such a system must therefore contain multiple spatially-dispersive resonances in the susceptibility for an accurate result. Multi-resonance susceptibilities are covered in greater detail in chapter 6. Thankfully, this does not apply to the current system as the value of χ_0 in Table 5.1 is purely real.

5.5.1 The p-polarization

The p-polarization contribution to u_{tot} is first considered, using the expression for r_p derived in section 5.3. The result of the second integral in (5.49) depends greatly on the frequency ω. Figure 5.6 shows the behaviour of $\mathbb{Im}[r_p]$ for evanescent waves at frequencies both smaller ($\omega = 0.999\omega_T$) and larger ($\omega = 1.01\omega_T$) than the resonant frequency for each of the ABCs in Table 5.2. At very small K, the reflection coefficient closely matches the local medium result. At very large K, spatial dispersion causes $\mathbb{Im}[r_p]$ to fall off as $1/K^4$. This behaviour ensures that the integral over evanescent waves in (5.49) converges to a finite result, even in the $z \to 0$ limit.

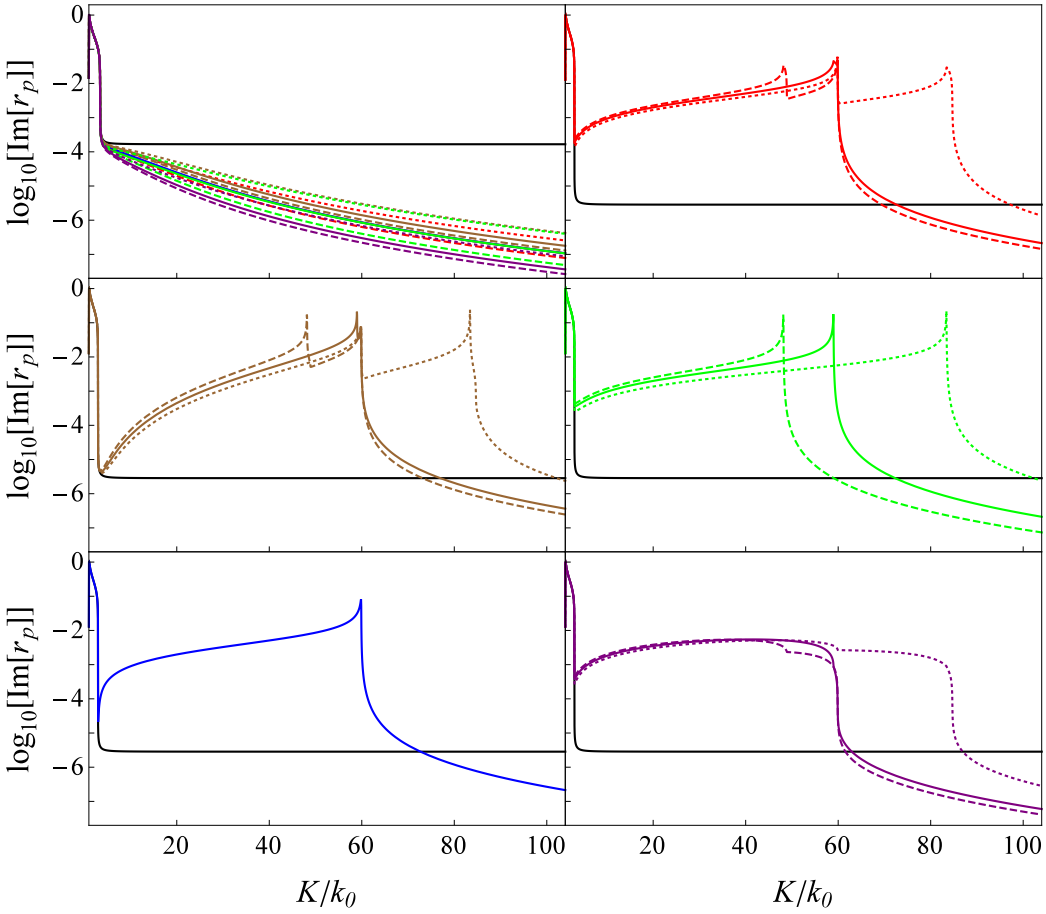

Figure 5.6: Logarithmic plot of $\mathbb{Im}[r_p]$ used in the u_{tot} integration as a function of K for evanescent waves at $\omega = 0.999\omega_T$ (top left) and $\omega = 1.01\omega_T$ (all others). Results are proportional to $1/K^4$ in the $K \to \infty$ limit, compared to the constant value of the local model. Plot styles follow the conventions in Fig. 5.2.

The behaviour for intermediate K differs significantly between the $\omega < \omega_T$ and $\omega > \omega_T$ regimes. For frequencies larger than ω_T, there are a series of peaks in $\mathbb{I}\mathrm{m}[r_p]$ followed by sharp drops. These occur at the values of K where the wave vectors q_n used in the ansatz (5.18) change from mostly real values (indicating propagating waves) to mostly

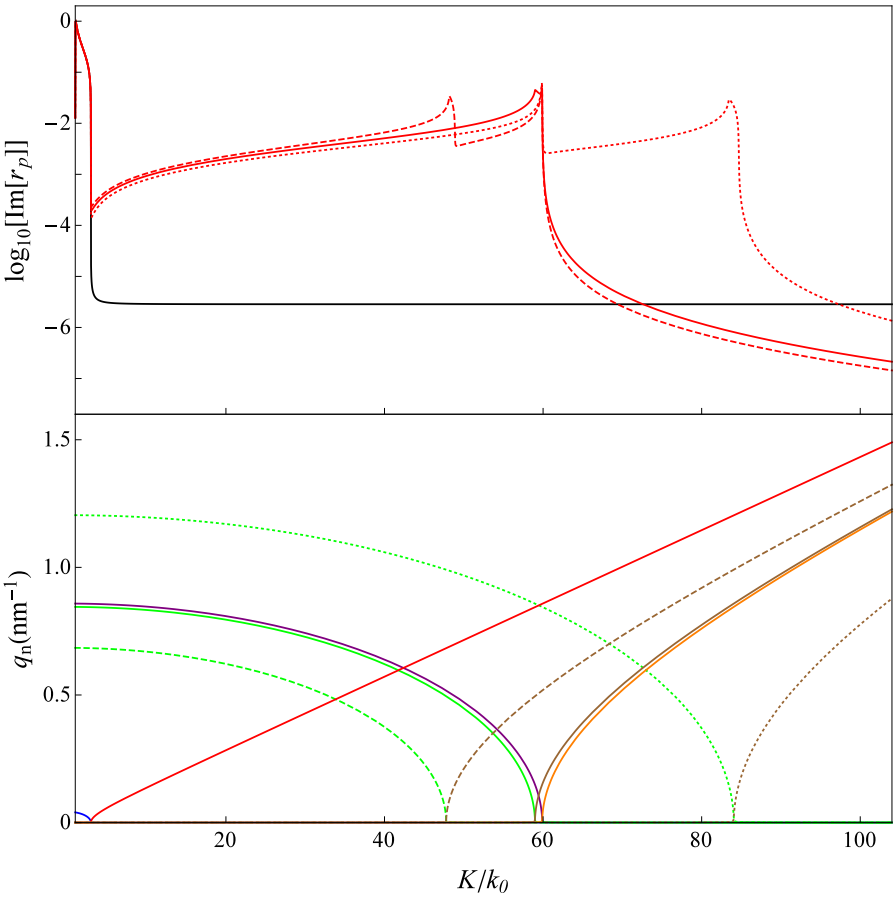

Figure 5.7: Comparison between $\mathbb{I}\mathrm{m}[r_p]$ using the Agarwal ABC (top) and the wave vectors q_n used in the electric field ansatz (5.18) (bottom) as functions of K when $\omega = 1.01\omega_T$. The real (blue, purple) and imaginary (red, orange) components of the transverse wave vectors (q_1, q_2) do not depend on the value of Δ, as it does not appear in the dispersion relation (5.20). In contrast, the real (green) and imaginary (brown) components of the longitudinal wave vector (q_3) strongly depend on Δ, with results given for $\Delta = 0$ (solid line), 0.5 (dashed line) and -0.5 (dotted line). In each case, the peaks in $\mathbb{I}\mathrm{m}[r_p]$ coincide with the values of K where the dominant component of q_n changes from $\mathbb{R}\mathrm{e}[q_n]$ (propagating wave) to $\mathbb{I}\mathrm{m}[q_n]$ (evanescent wave).

imaginary values (evanescent waves). This behaviour can be seen in Fig. 5.7, which compares $\mathbb{I}\mathrm{m}[r_p]$ with the Agarwal ABC to the real and imaginary components of q_n as a function of K. The position of these peaks can be estimated by calculating the values of K when $\mathbb{R}\mathrm{e}[\Gamma^2_{\perp/\parallel}] = 0$. The exceptions to this behaviour are the Rimbey-Mahan ABC, which does not display the corresponding peak for the longitudinal wave q_3, and the Fuchs-Kleiwer ABC, which does not display the corresponding peak for the transverse wave q_2. The peaks in $\mathbb{I}\mathrm{m}[r_p]$ associated with q_2 and q_3 are not observed in the $\omega < \omega_T$ regime, as these wave vectors are mostly imaginary for all values of K. Instead, the result simply obeys the same $1/K^4$ behaviour found in the $K \to \infty$ limit.

The longitudinal wave vector q_3, and the location of the corresponding peak in $\mathbb{I}\mathrm{m}[r_p]$, depends on the longitudinal nonlocal parameter $D_\parallel$ in (5.21). The value of Δ can therefore have a significant effect on r_p for waves with $K > k_0$, especially in the $\omega > \omega_T$ regime. This strongly contrasts with the results for waves with $K < k_0$ in section 5.4.1, where Δ had only a minor effect on r_p. The Rimbey-Mahan ABC is once again an exception to this rule, as the choice of U_{ij} values leads to the absence of the longitudinal wave and the peak in $\mathbb{I}\mathrm{m}[r_p]$ corresponding to q_3. In the $\Delta = 0$ case, the changeover values of K for q_2 and q_3 are close enough that the corresponding peaks of $\mathbb{I}\mathrm{m}[r_p]$ in Fig. 5.6 overlap and appear as a single peak.

5.5.2 The s-polarization

It has already been noted in section 5.3 that $\chi_{yy} = \chi_\perp$ is the only nonzero component of the tensor susceptibility (5.2) in the s-polarization. The expression for the reflection coefficient is therefore identical to the one derived by Halevi and Fuchs [4]:

$$r_s = \frac{E_r}{E_0} = \frac{Z_s(0^-) - Z_s(0^+)}{Z_s(0^-) + Z_s(0^+)}, \tag{5.51}$$

where

$$Z_s(0^-) = \frac{k_0}{\mu_0 q_0} \tag{5.52}$$

is the vacuum surface impedance and

$$Z_s(0^+) = \frac{(1+U_{yy})k_0(q_1q_2 + \Gamma_\perp^2) + (1-U_{yy})k_0\Gamma_\perp(q_1+q_2)}{(1+U_{yy})q_1q_2(q_1+q_2) + (1-U_{yy})\Gamma_\perp(q_1^2 + q_1q_2 + q_2^2 - \Gamma_\perp^2)} \tag{5.53}$$

is the surface impedance of the nonlocal medium.

Figure 5.8 shows the K dependence of $\mathbb{I}\mathrm{m}[r_s]$ for evanescent waves at $\omega = 1.01\omega_T$. Unlike the p-polarization in Fig. 5.6, the local medium result decays to zero in the large K limit, obeying a $1/K^4$ power law. The nonlocal medium results display many of the features found in Fig. 5.6 for the p-polarization. The reflection coefficient closely matches the local medium result at very small K and obeys a $1/K^6$ power law in the $K \to \infty$ limit. Peaks in $\mathbb{I}\mathrm{m}[r_s]$ are once again found at the points when the dominant component of q_1 and q_2 changes from $\mathbb{R}\mathrm{e}[q_n]$ to $\mathbb{I}\mathrm{m}[q_n]$, although these are typically smaller than those in the p-polarization.

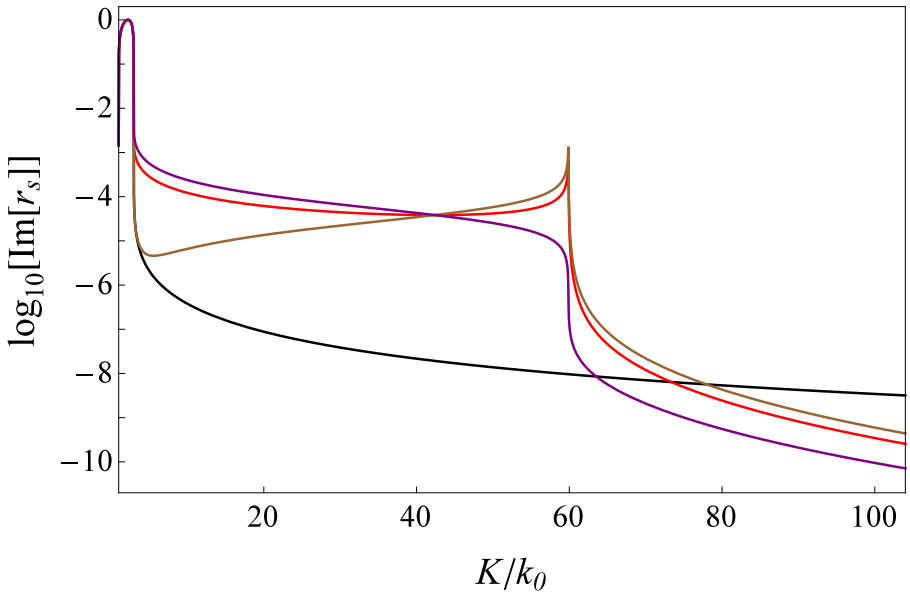

Figure 5.8: Logarithmic plot of $\mathbb{I}\mathrm{m}[r_s]$ used in the u_{tot} integration as a function of K for evanescent waves at $\omega = 1.01\omega_T$. Plot styles follow the conventions in Fig. 5.2. Peaks occur when the dominant component of q_1 and q_2 changes from $\mathbb{R}\mathrm{e}[q_n]$ (propagating wave) to $\mathbb{I}\mathrm{m}[q_n]$ (evanescent waves). Results are proportional to $1/K^4$ for the local model (black line) and $1/K^6$ for the nonlocal model in the $K \to \infty$ limit.

5.5.3 Results

This section presents the numerical results for the spectral energy density outside ZnSe using the expression (5.49) and the derived electromagnetic reflection coefficients. The z-dependence of $u_{\mathrm{tot}}(z, \omega)$ is first considered in both the $\omega < \omega_T$ and $\omega > \omega_T$ regimes. Figures 5.9 and 5.10 display the results for $u_{\mathrm{tot}}(z)$ at the frequencies $\omega = 0.999\omega_T$ and

$\omega = 1.01\omega_T$, respectively. In the large $|z|$ limit, the results closely match those of the local medium. However, below $20\mathrm{nm}$ for $0.999\omega_T$ and $8\mathrm{nm}$ for $1.01\omega_T$, the result for the nonlocal medium begins to differ from the local result. These distances coincide the wavelength of the polarization waves in the medium, approximately given by

$$D_\perp \left(\frac{2\pi}{|z|}\right)^2 = \left|\omega_T^2 - \omega^2 - i\gamma\omega\right|. \tag{5.54}$$

Furthermore, the value of u_{tot} begins to saturate to a finite value below $1\mathrm{nm}$, removing the unphysical $1/|z|^3$ divergence of the local result. This distance can also be traced back to the physical parameters of the model, and is given by:

$$D_\perp \left(\frac{2\pi}{|z|}\right)^2 = \omega_T^2, \tag{5.55}$$

below which the nonlocal term dominates the expression for the resonant frequency $\omega_T^2(k)$ in (5.3). This also marks the changeover point for the corresponding susceptibility:

$$\frac{\omega_p^2}{\omega_T^2(k) - \omega^2 - i\gamma\omega} \tag{5.56}$$

when it goes from $\omega_T^2(k) \approx \omega_T^2$ in the long wavelength limit, describing bulk oscillations of the polarization field, to $\omega_T^2(k) \approx Dk^2$ in the short wavelength limit, describing wave-like behaviour of the polarization field.

At the smaller frequency $\omega = 0.999\omega_T$, $\mathbb{I}\mathrm{m}[r_p]$ decays rapidly with a $1/K^4$ dependence. The second integral in (5.49) is therefore dominated by the small K contribution from Fig. 5.6, where the choice of ABC has very little effect on $\mathbb{I}\mathrm{m}[r_p]$. The resulting spectral energy density in Fig. 5.9 is found to approach a finite value in the $|z| \to 0$ limit, removing the unphysical $1/|z|^3$ divergence of the local model, and displays very little difference between the various ABCs. The effect of Δ is also negligible, as this only affects the large-K values of $\mathbb{I}\mathrm{m}[r_p]$ in the $\omega < \omega_T$ regime.

The u_{tot} result for the larger frequency $\omega = 1.01\omega_T$ in Fig. 5.10 also approaches a finite value in the $|z| \to 0$ limit. However, in this case the second integral in (5.49) is dominated by the peaks in $\mathbb{I}\mathrm{m}[r_p]$ shown in Fig. 5.6. The choice of ABC and Δ determine both the size and shape of these peaks and therefore have a significantly larger effect on u_{tot} compared to Fig. 5.10. In the $\Delta = 0$ limit, the Ting *et al.* and Pekar ABC give the largest and smallest values, respectively, while the Agarwal *et al.*, Fuchs-Kleiwer and Rimbey-Mahan results are almost identical. The Fuchs-Kleiwer ABC is most affected by the value of Δ, as it determines the location of the sole $\mathbb{I}\mathrm{m}[r_p]$ peak in Fig. 5.6, followed by

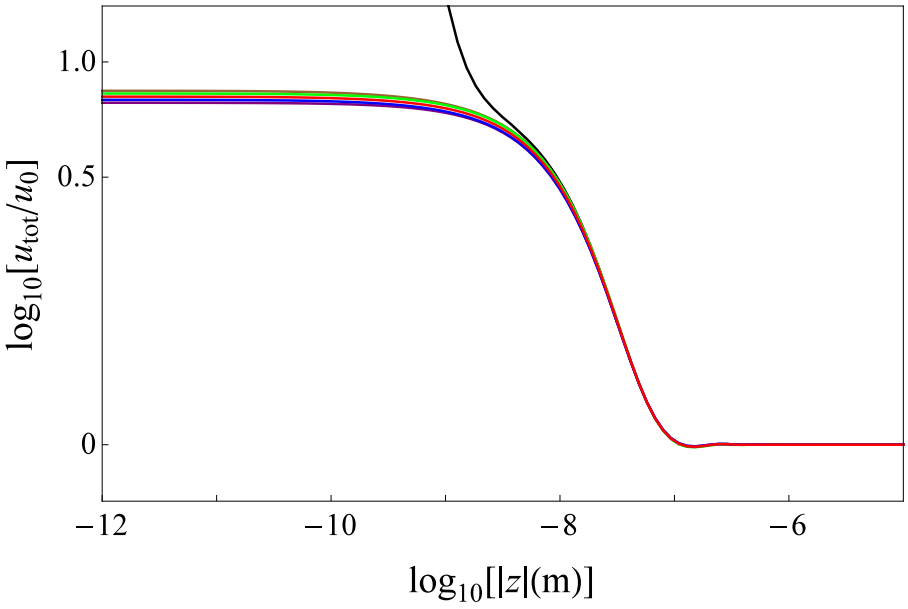

Figure 5.9: Rescaled spectral energy density u_{tot} as a function of distance z from the planar boundary of the nonlocal medium ZnSe at $\omega = 0.999\omega_T$. The inclusion of spatial dispersion has removed the unphysical $1/|z|^3$ divergence of the local model result (black line). Plot styles follow the conventions in Fig. 5.2.

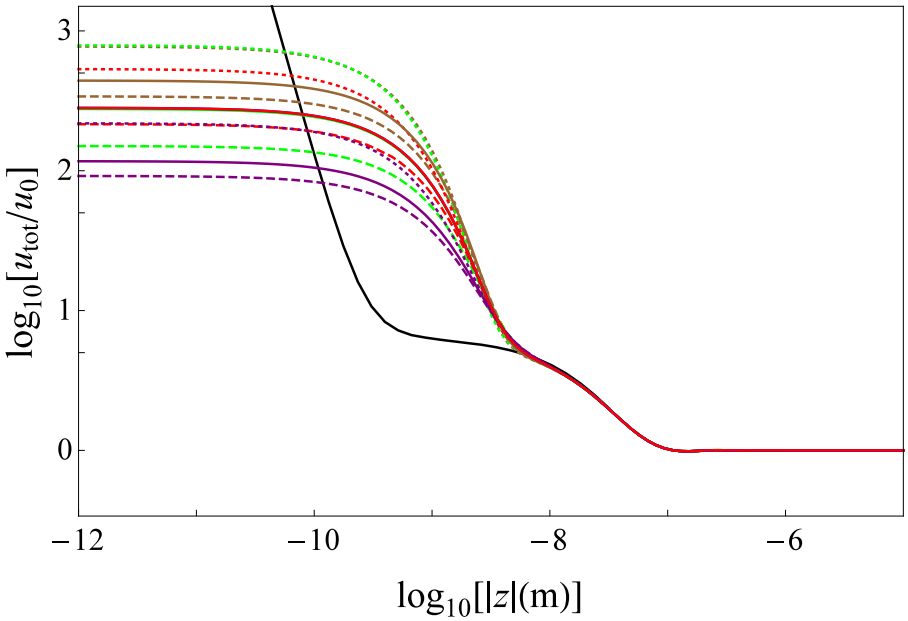

Figure 5.10: Rescaled spectral energy density u_{tot} as a function of distance z from the planar boundary of the nonlocal medium ZnSe at $\omega = 1.01\omega_T$. Plot styles follow the conventions in Fig. 5.2.

Ting *et al.*, Agarwal *et al.* and finally Pekar. The Rimbey-Mahan ABC remains unchanged by Δ due to the absence of the longitudinal wave in the medium.

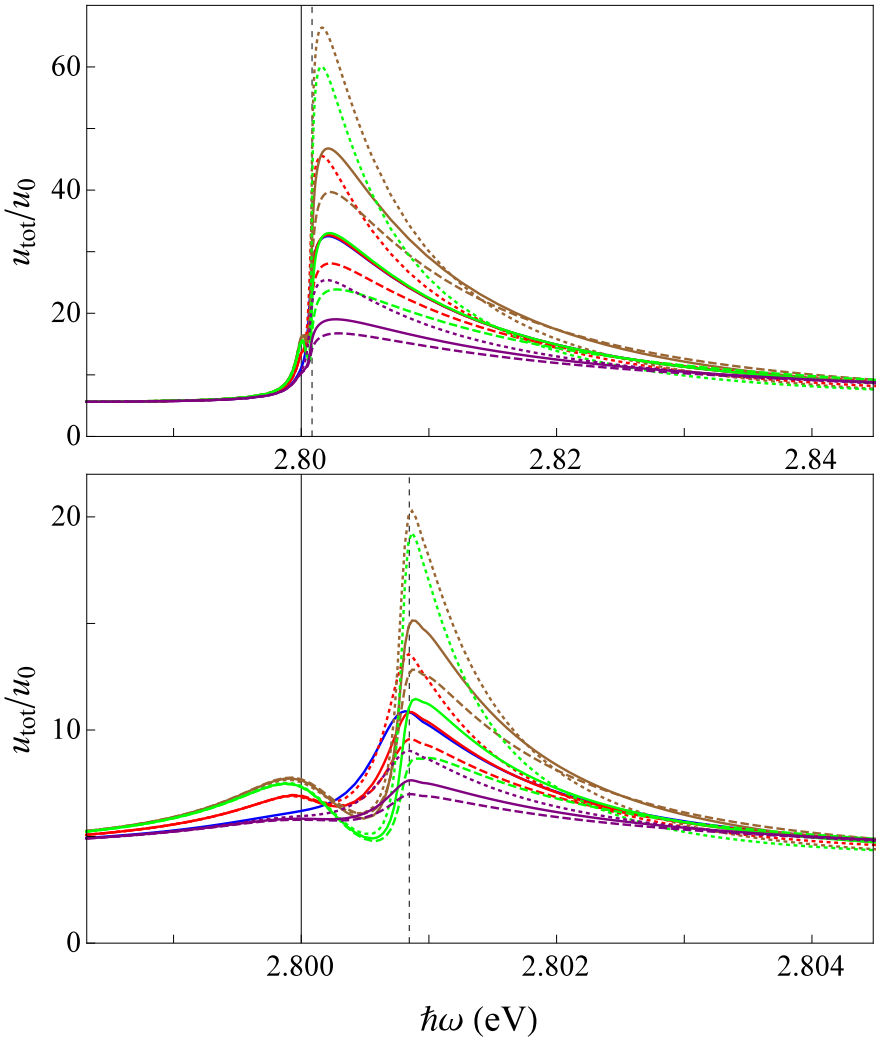

Figure 5.11: Rescaled spectral energy density $u_{\rm tot}$ as a function of ω at a distance of 3nm (top) and 10nm (bottom) from the planar boundary of the nonlocal medium ZnSe. Note the difference in scale between the two cases. Plot styles follow the conventions in Fig. 5.2, with vertical lines indicating the values ω_T (solid) and ω_L (dashed).

Figure 5.11 shows the frequency dependence of $u_{\rm tot}$ at a distance of $3\mathrm{nm}$ and $10\mathrm{nm}$ from the planar surface of ZnSe. The results display the same basic features as the local model in Fig. 2.11 of section 2.3.6. The first is a small peak in $u_{\rm tot}$ at ω_T, which is due to the s-polarization contribution to the evanescent wave integral in (5.49). The peak

height is mostly determined by the value of U_{yy}, as χ_{yy} is the only non-zero susceptibility component for the s-polarization. The peak is unaffected by Δ for the same reasons, as $\chi_{\parallel}$ does not apply to the s-polarization.

This second feature in the $u_{\mathrm{tot}}(\omega)$ result is a significantly larger peak at ω_L, which is due to the p-polarization contribution to the evanescent wave integral in (5.49). This peak increases in both height and width as the surface is approached, in a manner similar to the local result in Fig. 2.11. This can act to mask the smaller peak at ω_T, as seen Fig. 5.11 for the Rimbey-Mahan and Pekar ABCs at both $3\mathrm{nm}$ and $10\mathrm{nm}$ from the surface. The U_{ij} dependence is similar to that found in Fig. 5.10, with the Ting *et al.* ABC giving the largest peak in the $\Delta = 0$ limit, followed by the Agarwal *et al.*, Fuchs-Kleiwer and Rimbey-Mahan ABCs, which give similar results, and lastly the Pekar ABC.

The most striking feature of the peak in u_{tot} at ω_L is the dependence on Δ. In the case of the Fuchs-Kleiwer ABC, the u_{tot} result varies by a nearly a factor of 3 over the range $\Delta = -0.5$ to 0.5, even at a distance of 10nm from the surface. This is followed by the Ting *et al.*, Agarwal *et al.* and finally the Pekar ABC. These strongly contrast with the r_p results in Fig. 5.3 and 5.4, where Δ has a negligible effect, except for a frequency region near ω_L that is significantly smaller than the peak widths in Fig. 5.11.

From these results, it is clear that the tensor nature of the susceptibility and the difference between $\chi_{\perp}$ and $\chi_{\parallel}$ in a spatially-dispersive medium cannot be overlooked when considering the spectral energy density of zero point and thermal radiation near the boundary of a nonlocal medium.

5.6 Chapter summary

This chapter has extended the Halevi-Fuchs generalized ABC model to the general tensor form of the susceptibility in a homogeneous, isotropic, non-gyroscopic, nonlocal medium, which contains a separate expression for the transverse and longitudinal components of the electric field. The original Halevi-Fuchs derivation was modified to find exact expressions for the electromagnetic reflection and transmission coefficients, with minor restrictions upon the phenomenological reflection coefficients for the polarization waves in the half-infinite medium [61].

The difference between the transverse and nonlocal parameters was found to have little effect on the reflection and transmission coefficients for propagating incident waves compared to the choice of ABC, with the exception of the transmitted longitudinal wave for certain ABCs. The derived expressions for the reflection coefficients were subsequently applied to the calculation of the spectral energy density u_{tot} of thermal and zero-point radiation outside the half-infinite medium. The inclusion of spatial dispersion caused the imaginary part of the reflection coefficients to approach zero for evanescent waves with arbitrarily large wave vectors parallel to the surface of the medium, instead of the finite value found when using the local model. This had the knock-on effect of naturally removing the unphysical $1/|z|^3$ divergence in u_{tot} found close to the boundary of the medium without the need for an arbitrary wave vector cut-off or other phenomenological changes to the calculation. In contrast to the results for propagating waves, the difference between transverse and longitudinal parameters was found to have a significant impact on the spectral energy density, even at a distance of $10\mathrm{nm}$ from the surface.

Chapter 6

Extending the Halevi-Fuchs model II. Multiple parabolic exciton bands

The Halevi-Fuchs generalized ABC model [4] and the improvements made in the previous chapter [61] both use a susceptibility containing a single resonance that describes an isolated excitonic transition in the medium. As previously described in section 2.3.5, this represents a small fraction of the wide range of behaviour found in real materials. The structure, symmetry and degeneracies of the valence and conduction bands in a crystal [59, 60] all determine the exciton dispersion relations. In real semiconductors, this leads to a large number of interacting exciton bands in a medium, each with an associated resonance in χ. The susceptibility can contain behaviour that is not covered by the Halevi-Fuchs model, including resonances that are closely-spaced, degenerate [63] or contain nonlocal terms other than Dk^2 used in the previous chapter [64–66].

While the majority of work on the subject of reflection in nonlocal media has focused on the single-resonance susceptibility, culminating in the Halevi-Fuchs generalized ABC model, some authors [67–69] have considered the multi-resonance case. However, this work has been comparatively limited in scope and is typically restricted to the two-resonance susceptibility and a specific set of ABCs.

Chapters 6 and 7 further extend the Halevi-Fuchs generalized ABC model to nonlocal susceptibilities containing an arbitrary number of resonances and derive expressions for the electromagnetic reflection and transmission coefficients [62]. This chapter considers the case of parabolic exciton bands, with the same $\boldsymbol{k}$ dependence used by the Halevi-Fuchs model, while the next chapter deals with more complex wave vector dependences. These results are once again applied to the calculation of the spectral energy density outside the

nonlocal medium.

The assumptions made in the previous chapter also apply to the following derivation. Quantum-mechanical effects not encoded in the macroscopic susceptibility are omitted and the boundary is considered to be smooth and free of any features such as slits or structures. Boundaries are considered to be sufficiently separated, such that multiple reflections can be ignored.

The contents of this chapter are arranged in a similar manner to the previous chapter. Section 6.1 first considers the simple case of multiple isotropic, parabolic exciton bands in an infinite medium and discusses the resulting dispersion relations for the electric field. The half-infinite medium is then considered in section 6.2, where the Halevi-Fuchs model is modified to include multiple resonances. The Halevi-Fuchs derivation is repeated to find a set of equations relating the amplitude of the various waves inside the nonlocal medium. These are used in sections 6.3 and 6.4 to derive exact expressions for the electromagnetic reflection and transmission coefficients in both the p- and s-polarizations. Numerical results are presented in section 6.5 for two different nonlocal media and the differences with the single-resonance model are discussed. Improved parameters are found for the single band approximation to the heavy/light exciton band model. Finally, section 6.6 uses these results to calculate the spectral energy density outside each nonlocal medium and identifies the key differences to the single resonance results in section 2.3.6.

6.1 The infinite medium

This chapter starts by considering an infinite medium described by a scalar Lorentz model with M resonances

$$\chi(\boldsymbol{k},\omega) = \chi_0 + \sum_{m=1}^{M} \chi_m(\boldsymbol{k},\omega), \qquad \chi_m(\boldsymbol{k},\omega) = \frac{\omega_{pm}^2}{\omega_{Tm}^2(k) - \omega^2 - i\gamma_m\omega}, \tag{6.1}$$

where each of the parameters have the same definition as in chapter 5. The exciton bands have the same parabolic dispersion relations used in the Halevi-Fuchs model:

$$\hbar\omega_T(k) = \hbar\omega_T + \frac{\hbar^2 k^2}{2m_{\text{ex}}}, \qquad \omega_T^2(k) \approx \omega_T^2 + Dk^2, \qquad D = \frac{\hbar\omega_T}{m_{\text{ex}}}, \tag{6.2}$$

although it has been shown [59] that the previously used definition of the exciton mass $m_{\text{ex}} = m_{\text{el}} + m_{\text{ho}}$ must be modified if there are degenerate exciton bands. While a scalar susceptibility is used in (6.1), the following derivations are equally applicable to the tensor

expression in (5.2) by applying the same modifications described in chapter 5 to each of the resonances.

The susceptibility in (6.1) leads to the dispersion relation

$$\frac{\omega^2}{c^2}\left[1+\chi_0+\sum_{m=1}^{M}\chi(\boldsymbol{k},\omega)\right]=k^2 \tag{6.3}$$

for transverse waves with $\boldsymbol{E}\cdot\boldsymbol{k}=0$ and

$$\left[1+\chi_0+\sum_{m=1}^{M}\chi(\boldsymbol{k},\omega)\right]=0 \tag{6.4}$$

for longitudinal waves with $\boldsymbol{E}\times\boldsymbol{k}=0$. After making the restriction to solutions with $\mathbb{I}\mathrm{m}[k_z]>0$, (6.3) and (6.4) lead to $M+1$ transverse and M longitudinal waves inside the nonlocal medium described by (6.1) and (6.2).

6.2 The half-infinite medium

The half-infinite medium shown in Fig. 6.1 is now considered. The $z<0$ vacuum half space contains the incident ($\boldsymbol{E}_0$) and reflected ($\boldsymbol{E}_r$) waves with the corresponding wave vectors $\boldsymbol{k}_0$ and $\boldsymbol{k}_r$. The $z>0$ half space contains $M+1$ transverse and M longitudinal waves ($\boldsymbol{E}^{(n)}$), for a total of $N=2M+1$, with wave vectors $\boldsymbol{k}_n$ that satisfy the dispersion relations (6.3) and (6.4). The co-ordinate system is identical to the one used both in the Halevi and Fuchs paper and chapter 5, fixing the wave vector components $k_{nx}=K$ and $k_{ny}=0$ and only leaving the component k_{nz} to vary between waves.

The following derivation is very similar to the one found in chapter 5, with some slight modifications to account for the multiple resonances in the system. The Halevi-Fuchs model in (2.54) is once again modified, with the susceptibility of the half-infinite medium χ_i' given by:

$$\chi_i'(x-x',y-y',z,z')=\begin{cases}\chi_0\delta(x-x')\delta(y-y')\delta(z-z') & \\ \quad+\displaystyle\sum_{m}^{M}\chi_{mi}'(x-x',y-y',z,z') & \text{if } z,z'>0,\\ 0 & \text{otherwise,}\end{cases} \tag{6.5}$$

where each of the M resonances now contain two parts:

$$\chi_{mi}'(x-x',y-y',z,z')=\chi_m(x-x',y-y',z-z')+U_{mi}\chi_m(x-x',y-y',z+z'). \tag{6.6}$$

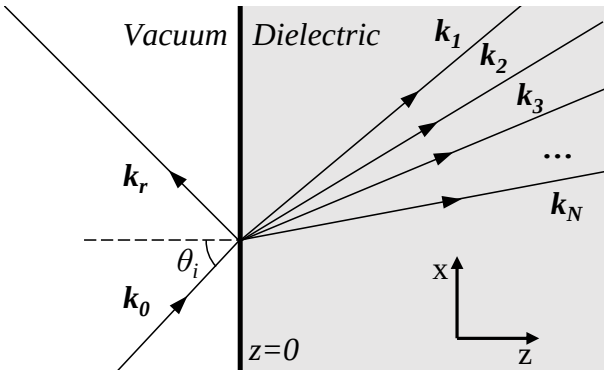

Figure 6.1: Schematic of reflection at the planar interface of the nonlocal medium described by the multi-resonance susceptibility in (6.1) and (6.2). The coordinate system is chosen such that the xz-plane coincides with the plane of incidence and $k_y = 0$. The $z < 0$ vacuum half-space contains the incident wave $\boldsymbol{E}_0$ and the reflected wave $\boldsymbol{E}_r$, with the corresponding wave vectors $\boldsymbol{k}_0$ and $\boldsymbol{k}_r$. The $z > 0$ nonlocal medium contains $M + 1$ transverse ($\boldsymbol{E}^{(1)}, \ldots, \boldsymbol{E}^{(M+1)}$) and M longitudinal waves ($\boldsymbol{E}^{(M+2)}, \ldots, \boldsymbol{E}^{(2M+1)}$), for a total of $N = 2M + 1$ waves with the corresponding wave vectors $\boldsymbol{k}_n$.

The first term in (6.6) is the bulk response of the nonlocal medium and the second describes the reflection of polarization waves on the interior boundary of the medium. Each of the resonances can have independent values of the phenomenological reflection coefficient U_{mi}, to account for the different behaviour of the various excitations in the medium. However, results presented later in this chapter assume that values of U_{mi} are the same for each resonance in the medium.

The expression for the multi-resonance susceptibility in (6.5) and (6.6) can once again be substituted in to the $\boldsymbol{P}$ definition in (2.3). After a spatial Fourier transformation in time and the xy-plane, the polarization field is given by:

$$\begin{aligned} P_i(K,0,z) =& \varepsilon_0 \chi_0 E_i(K,0,z) + \\ & \frac{\varepsilon_0}{2\pi} \int_0^\infty dz' \int_{-\infty}^\infty dq \sum_{m=1}^{M} \left[e^{iq(z-z')} + U_{mi} e^{iq(z+z')} \right] \chi_m(K,0,q) E_i(K,0,z'). \end{aligned} \tag{6.7}$$

The resonances in the bulk susceptibility (6.1) can once again be rewritten in terms of q:

$$\chi_m(q) = \frac{\omega_{pm}^2 / D_m}{q^2 - \Gamma_m^2}, \qquad -\Gamma_m^2 = \frac{\omega_{Tm}^2 - \omega^2 - i\gamma_m \omega}{D_m} + K^2, \tag{6.8}$$

where the $k_x = K$ and $k_y = 0$ dependences have been omitted.

An ansatz for the electric field must be introduced at this point in the derivation:

$$\boldsymbol{E}(z) = \begin{cases} \boldsymbol{E}_0 e^{iq_0 z} + \boldsymbol{E}_r e^{-iq_0 z} & z < 0, \\ \displaystyle\sum_{n=1}^{N} \boldsymbol{E}^{(n)} e^{iq_n z} & z > 0, \end{cases} \tag{6.9}$$

where the $z < 0$ half-space contains the incident ($\boldsymbol{E}_0$) and reflected ($\boldsymbol{E}_r$) waves, with the corresponding wave vector q_0, defined in (5.19). The $z > 0$ half-space contains $M + 1$ transverse and M longitudinal waves ($\boldsymbol{E}^{(n)}$), for a total of $N = 2M + 1$ waves. The corresponding wave vectors q_n are the $\mathbb{I}\mathrm{m}[q] > 0$ solutions to the transverse and longitudinal dispersion relations (6.3) and (6.4).

Substituting the ansatz (6.9) into (6.7) allows the z' integral to be evaluated, giving:

$$P_i(z) = \chi_0 E_i(z) + \frac{i}{2\pi} \int_{-\infty}^{\infty} dq e^{iqz} \sum_{m=1}^{M} \sum_{n=1}^{N} \left[\frac{1}{q_n - q} + \frac{U_{mi}}{q_n + q} \right] \chi_m(q) E_i^{(n)}, \quad z > 0. \tag{6.10}$$

The q integral in (6.10) can once again evaluated [114] by performing a contour integration in the upper half-plane of complex q, enclosing the poles at $q = q_n$ in the square brackets and $q = \Gamma_m$ in $\chi_m(q)$. The resulting expression for the polarization field can be split into $M + 1$ distinct sets of terms:

$$\begin{aligned} P_i(z) = & \sum_{n=1}^{N} \chi(q_n) E_i^{(n)} e^{iq_n z} \\ & - \frac{\omega_{p1}^2}{2D_1\Gamma_1} \sum_{n=1}^{N} \left(\frac{1}{q_n - \Gamma_1} + \frac{U_{1i}}{q_n + \Gamma_1} \right) E_i^{(n)} e^{i\Gamma_1 z} \\ & - \frac{\omega_{p2}^2}{2D_2\Gamma_2} \sum_{n=1}^{N} \left(\frac{1}{q_n - \Gamma_2} + \frac{U_{2i}}{q_n + \Gamma_2} \right) E_i^{(n)} e^{i\Gamma_2 z} \\ & - \ldots \\ & - \frac{\omega_{pM}^2}{2D_M\Gamma_M} \sum_{n=1}^{N} \left(\frac{1}{q_n - \Gamma_M} + \frac{U_{Mi}}{q_n + \Gamma_M} \right) E_i^{(n)} e^{i\Gamma_M z}. \end{aligned} \tag{6.11}$$

For the wave equation (5.10) to be valid for all values of z, each of the right-hand side sums proportional to $\exp(i\Gamma_m z)$ in (6.11) must equal zero. This leads to a set of M equations that relate each of the $E_i^{(n)}$ components:

$$\sum_{n=1}^{N} \phi_{mi}^{(n)} E_i^{(n)} = 0, \qquad m = 1, \ldots, M, \tag{6.12}$$

where:

$$\phi_{mi}^{(n)} = \left(\frac{1}{q_n - \Gamma_m} + \frac{U_{mi}}{q_n + \Gamma_m} \right). \tag{6.13}$$

This set of equations acts as the ABCs for the multi-resonance model in (6.5) and (6.6), similar to (5.26) for the tensor single-resonance susceptibility in chapter 5.

6.3 The p-polarization

The $\boldsymbol{E}$ field can be decomposed into terms perpendicular (s-polarized) or parallel (p-polarized) to the xz-plane of incidence. This section considers p-polarized light, with $E_y = 0$, $E_x \neq 0$ and $E_z \neq 0$.

6.3.1 The surface impedance

The methods used in section 5.3 can be used to rewrite the surface impedance of the nonlocal medium solely in terms of the transmitted waves' E_x components. This can be further rearranged to express $Z_p(0^+)$ in terms of the field amplitude ratios:

$$Z_p(0^+) = \frac{E_x}{H_y} = \frac{1}{\mu_0} \frac{\sum_{n=1}^{N} E_x^{(n)}}{\sum_{n=1}^{N} \tau^{(n)} E_x^{(n)}} = \frac{1}{\mu_0} \frac{1 + \sum_{n=2}^{N} \frac{E_x^{(n)}}{E_x^{(1)}}}{\tau^{(1)} + \sum_{n=2}^{N} \tau^{(n)} \frac{E_x^{(n)}}{E_x^{(1)}}}, \tag{6.14}$$

where $\tau^{(n)}$ relates $B_y^{(n)}$ and $E_x^{(n)}$ in (5.30).

6.3.2 Field amplitude ratios

Calculating the surface impedance in (6.14) requires the E_x field amplitude ratios of the $2M + 1$ transmitted waves in the p-polarization. These can be calculated using the previously derived effective ABCs in (6.13). The E_z equation can be rewritten in terms of E_x using the relationship in (5.29), giving:

$$\sum_{n=1}^{N} \left[\phi_{mx}^{(n)} \right] E_x^{(n)} = 0, \qquad \sum_{n=1}^{N} \left[\eta^{(n)} \phi_{mz}^{(n)} \right] E_x^{(n)} = 0, \qquad m = 1, \ldots, M, \tag{6.15}$$

where $\eta^{(n)} = -K/q_n$ for transverse and $\eta^{(n)} q_n / K$ for longitudinal waves. The $2M$ equations relating the $2M + 1$ waves inside the medium are sufficient information to calculate the field amplitude ratios and the resulting electromagnetic reflection coefficient. The

$n = 1$ term can be moved to the RHS of (6.15) and the entire expression divided by $E_x^{(1)}$ to give:

$$\sum_{n=2}^{N} \left[\phi_{mx}^{(n)}\right] \frac{E_x^{(n)}}{E_x^{(1)}} = -\phi_{mx}^{(1)}, \qquad \sum_{n=2}^{N} \left[\eta^{(n)}\phi_{mz}^{(n)}\right] \frac{E_x^{(n)}}{E_x^{(1)}} = -\phi_{mz}^{(1)}, \qquad m = 1, \ldots, M, \tag{6.16}$$

which can subsequently be expressed in matrix form. In the case of the two-resonance susceptibility, this is given by:

$$\begin{pmatrix} \phi_{1x}^{(2)} & \phi_{1x}^{(3)} & \phi_{1x}^{(4)} & \phi_{1x}^{(5)} \\ \phi_{2x}^{(2)} & \phi_{2x}^{(3)} & \phi_{2x}^{(4)} & \phi_{2x}^{(5)} \\ \eta^{(2)}\phi_{1z}^{(2)} & \eta^{(3)}\phi_{1z}^{(3)} & \eta^{(4)}\phi_{1z}^{(4)} & \eta^{(5)}\phi_{1z}^{(5)} \\ \eta^{(2)}\phi_{2z}^{(2)} & \eta^{(3)}\phi_{2z}^{(3)} & \eta^{(4)}\phi_{2z}^{(4)} & \eta^{(5)}\phi_{2z}^{(5)} \end{pmatrix} \begin{pmatrix} E_x^{(2)}/E_x^{(1)} \\ E_x^{(3)}/E_x^{(1)} \\ E_x^{(4)}/E_x^{(1)} \\ E_x^{(5)}/E_x^{(1)} \end{pmatrix} = - \begin{pmatrix} \phi_{1x}^{(1)} \\ \phi_{2x}^{(1)} \\ \eta^{(1)}\phi_{1z}^{(1)} \\ \eta^{(1)}\phi_{2z}^{(1)} \end{pmatrix}, \tag{6.17}$$

where $n = 1, 2, 3$ are transverse waves and $n = 4, 5$ are longitudinal waves. The $2M \times 2M$ matrix in (6.17) can be inverted to find the field amplitude ratios of the system and the surface impedance of the nonlocal medium in (6.14). The large number of matrix components made it impractical to derive analytic expressions for the field amplitude ratios, as in (5.3.2) for the single-resonance susceptibility. Instead, the matrix inversion was typically performed after the numerical values of $\eta^{(n)}$ and $\phi_{mi}^{(n)}$ had been calculated.

6.3.3 Electromagnetic reflection and transmission coefficients

The nonlocal medium surface impedance (6.14) and the vacuum surface impedance $Z_p(0^-) = q_0/\mu_0 k_0$ can be used to calculate the p-polarization reflection coefficient r_p using the definition [44] in (5.41). The Maxwell boundary condition requiring the continuity of transverse $\boldsymbol{E}$ components [1] is imposed at the $z = 0$ boundary, using the E_x components of the ansatz (6.9):

$$E_{0x} - E_{rx} = E_0 \left[\frac{q_o}{k_0}(1 - r_p)\right] = \sum_{n=1}^{N} E_x^{(n)} = E_x^{(1)} \sum_{n=1}^{N} \left[\frac{E_x^{(n)}}{E_x^{(1)}}\right], \tag{6.18}$$

which has been rewritten in terms of the field amplitude ratios calculated in section 6.3.2. The transmission coefficients $t_p^{(n)}$ are derived in the same manner as section 5.3.3 by using the relation in (5.45), to give:

$$t_p^{(n)} = \frac{E^{(n)}}{E_0} = \frac{\sqrt{q_n^2 + K^2}}{q_n} \frac{E_x^{(n)}}{E_x^{(1)}} \left\{ \frac{q_0}{k_0} \frac{[1 - r_p]}{\left[1 + \sum_{n=2}^{N} \frac{E_x^{(n)}}{E_x^{(1)}}\right]} \right\}, \tag{6.19}$$

for transverse waves and:

$$t_p^{(n)} = \frac{E^{(n)}}{E_0} = \frac{\sqrt{q_n^2 + K^2}}{K} \frac{E_x^{(n)}}{E_x^{(1)}} \left\{ \frac{q_0}{k_0} \frac{[1 - r_p]}{\left[1 + \sum_{n=2}^{N} \frac{E_x^{(n)}}{E_x^{(1)}}\right]} \right\}. \tag{6.20}$$

for longitudinal waves. While the final expressions for r_p and $t_p^{(n)}$ are quite long, numerically calculating the results is a straightforward process of finding the q_n solutions to the dispersion relations (6.3) and (6.4) and inverting a $2M \times 2M$ matrix similar to the one in (6.17).

6.4 The s-polarization

This section considers the simpler case of the s-polarization, which contains the components of $\boldsymbol{E}$ perpendicular to the plane of incidence. The current choice of co-ordinates mean the only nonzero component of s-polarized light is $E_y \neq 0$, with $E_x = 0$ and $E_z = 0$. All wave vectors must, by definition, lie in the xz-plane of incidence. The s-polarization therefore lacks the longitudinal waves discussed in the previous section, leaving $M + 1$ transverse waves inside the nonlocal medium.

6.4.1 The surface impedance

The Maxwell equations (2.10) can be used to rewrite the surface impedance solely in terms of the E_y components of the s-polarization, as in equation (2.36). This expression reduces to $Z_s(0^-) = k_0/\mu_0 q_0$ in the vacuum and

$$Z_s(0^+) = \frac{k_0}{\mu_0} \frac{\sum_{n=1}^{M+1} E_y^{(n)}}{\sum_{n=1}^{M+1} q_n E_y^{(n)}} = \frac{k_0}{\mu_0} \frac{1 + \sum_{n=2}^{M+1} \frac{E_y^{(n)}}{E_y^{(1)}}}{q_1 + \sum_{n=2}^{M+1} q_n \frac{E_y^{(n)}}{E_y^{(1)}}} \tag{6.21}$$

in the nonlocal medium, where Z_s has been rewritten in terms of the field amplitude ratios. Note that the sum in (6.21) only contains the $M + 1$ transverse waves.

6.4.2 Field amplitude ratios

The E_y sum in (6.12) can be rewritten in terms of the field amplitude ratios, giving a set of M expressions of the form:

$$\sum_{n=2}^{M+1} \left[\phi_{my}^{(n)}\right] \frac{E_y^{(n)}}{E_y^{(1)}} = -\phi_{my}^{(1)}, \qquad m = 1, \ldots, M \tag{6.22}$$

that relate the $M+1$ transverse waves in the medium for the s-polarization. Once again, there is sufficient information to calculate the field amplitude ratios by writing (6.22) in matrix form and inverting the expression. In the two-resonance case, this is given by:

$$\begin{pmatrix} \phi_{1y}^{(2)} & \phi_{1y}^{(3)} \\ \phi_{2y}^{(2)} & \phi_{2y}^{(3)} \end{pmatrix} \begin{pmatrix} E_y^{(2)}/E_y^{(1)} \\ E_y^{(3)}/E_y^{(1)} \end{pmatrix} = - \begin{pmatrix} \phi_{1y}^{(1)} \\ \phi_{2y}^{(1)} \end{pmatrix}, \tag{6.23}$$

which comparatively simpler than the p-polarization expression in (6.17).

6.4.3 Electromagnetic reflection and transmission coefficients

Now that the field amplitude ratios have been found, the surface impedance of the vacuum in (5.52) and the nonlocal medium in (6.21) can be used to calculate the reflection coefficient using the definition [44] in (2.34). The transmission coefficients are once again derived by imposing the continuity of transverse $\boldsymbol{E}$ components at the $z=0$ boundary [1]. As only E_y components are nonzero in the s-polarization, this leads to:

$$E_0 - E_r = E_0\left[1 - r_s\right] = \sum_{n=1}^{M+1} E_y^{(n)} = E_y^{(1)} \left[1 + \sum_{n=2}^{M+1} \frac{E_y^{(n)}}{E_y^{(1)}}\right], \tag{6.24}$$

which has been rearranged in terms of the reflection coefficient r_s and the field amplitude ratios calculated in section 6.4.2. The final expressions for the electromagnetic transmission coefficients in the s-polarization are given by:

$$t_s^{(n)} = \frac{E^{(n)}}{E_0} = \frac{E_y^{(n)}}{E_y^{(1)}} \left\{ \frac{\left[1 - r_s\right]}{\left[1 + \sum_{n=2}^{M+1} \frac{E_y^{(n)}}{E_y^{(1)}}\right]} \right\}. \tag{6.25}$$

This concludes the derivation of the electromagnetic reflection and transmission coefficients for the generalized ABC multi-resonance susceptibility in (6.5) and (6.6).

6.5 Results

This section, like much of the previous literature on ABCs and multi-resonance susceptibility models [67–69], focuses exclusively on the electromagnetic reflection coefficients r_s and r_p derived in sections 6.3 and 6.4. Two example materials are considered, each with different exciton band behaviour. The first is Zinc Oxide (ZnO), which contains three simple non-interacting parabolic exciton bands, while the second is Gallium Arsenide (GaAs), which contains two parabolic exciton bands that are degenerate at $k = 0$. This behaviour is shown in Fig. 6.2 (not to scale) along with the corresponding dispersion relations for transverse $\boldsymbol{E}$ waves in the absence of damping.

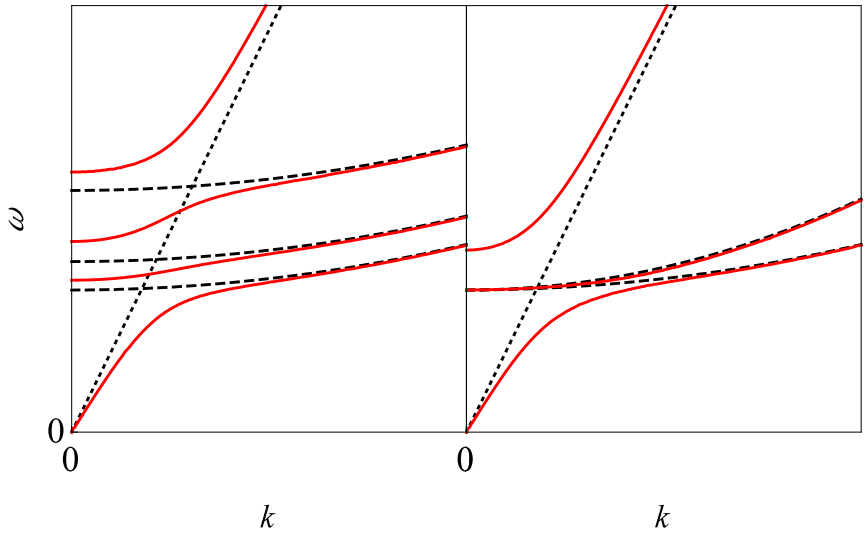

Figure 6.2: Exciton band behaviour (black dashed) compared to the light line (black dotted) and dispersion relations for transverse $\boldsymbol{E}$ waves in an infinite medium (solid red) when γ_m is set to zero. Examples include multiple non-interacting parabolic bands (left), such as those found in ZnO, and degenerate parabolic exciton bands with the same ω_T but different k^2 terms (right), such as those found in GaAs. The latter are also known as heavy/light exciton bands [59, 63] .

Model parameters for each of the materials are presented in Table 6.1. The values of ω_p are calculated from the measured values of ω_L, which are the solutions to the transverse wave equation (6.3) at $k = 0$ in the absence of the damping term γ. The nonlocal parameters D are similarly calculated from the measured exciton masses m_{ex}. While the exciton mass is typically the sum of the electron and hole masses, a different expression

must be used in the degenerate band case [59] .

Table 6.1: List of ZnO [68] and GaAs [70] model parameters, where m labels the resonances in the susceptibility, m_{e0} is the rest electron mass and c is the speed of light in the vacuum.

	ZnO			GaAs	
m	1	2	3	1	2
χ_0	5.2	5.2	5.2	11.6	11.6
$\hbar\omega_T$ (eV)	3.3758	3.3810	3.4198	1.514	1.514
$\hbar\omega_L$ (eV)	3.3776	3.3912	3.4317	1.515	1.515
$\hbar\gamma$ (meV)	0.7	0.7	0.7	0.05	0.05
m_{ex} (m_{e0})	0.87	0.87	0.87	0.183	0.805
$\hbar\omega_p$ (eV)	0.5334	0.6055	0.5983	0.138	0.138
Dc^2 ($\times 10^{-6}$)	7.58	7.61	7.69	16.19	3.68

6.5.1 Non-interacting exciton bands

The simpler case of non-interacting exciton bands is first considered. While this type of system has been considered previously [67–69] in reflection coefficient calculations, work has typically been limited to a maximum of two resonances and a specific ABC. The model used in this section for ZnO is a three resonance susceptibility involving the A, B and C excitons, which are labelled $m = 1, 2$ and 3 respectively. This is based on the work by Lagois [67,68], who considered the $m = 1, 2$ and the $m = 3$ resonances separately. As a result, each frequency region required a different derivation for the reflection coefficient, in contrast to the single, unified approach detailed in sections 6.3 and 6.4.

Figure 6.3 compares $r_p(\omega)$ and $r_s(\omega)$ at a fixed incident angle for the range of ABCs detailed in Table 6.1. The overall result is similar to that to the local model with $D_m = 0$, with the location of the peaks determined by the values of ω_{Tm} and ω_{Lm}, represented by solid and dashed vertical lines, respectively. The U_i dependence is similar to that found in section 5.4.1, with the results mostly determined by the value of U_x and U_y. The Ting *et al.* and Fuchs-Kleiwer ABCs with $U_x = U_y = 1$ display the smallest differences to the local result, followed by the Agarwal *et al.* and finally the Rimbey-Mahan and Pekar ABCs.

While the frequency region around the $m = 3$ resonance can be accurately described by the single-resonance model, due to the very small contributions to χ from the other resonances in the susceptibility, the same is not true for the $m = 1$ and 2 resonances. Large changes in behaviour are found in the frequency region between ω_{T1} and ω_{T2}, where the significant overlap of the two resonances in the susceptibility leads to the failure of the one-resonance model. Unlike the r_p minima associated with the $m = 2$ and 3 resonances, the minima at ω_{L1} is not affected by the value of U_z. This behaviour is found at all angles and is not present in the single-resonance model. Instead, the behaviour of r_p and r_s in this frequency range is solely determined by U_x or U_y, with $U_{x,y} = 1$ giving the largest contrast between the minima and maxima.

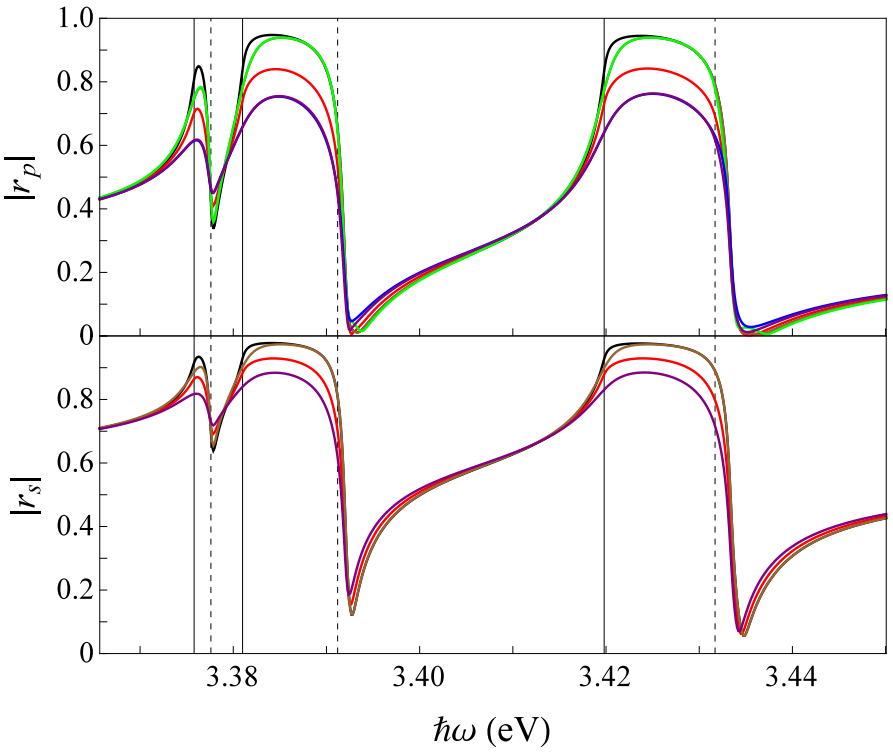

Figure 6.3: Absolute value of r_p (top) and r_s (bottom) for the ZnO 3-exciton model at a fixed incident angle of $50°$. Vertical lines indicate ω_{Tm} (solid) and ω_{Lm} (dashed) values. Includes Agarwal *et al.* (red), Ting *et al.* (brown), Fuchs-Kliewer (green), Rimbey-Mahan (blue) and Pekar (purple) ABC's compared to the result of the local model with $D_m = 0$ (black).

6.5.2 Heavy/light exciton bands

Interactions in a medium can lead to the splitting of otherwise degenerate exciton bands. In the simplest case of a medium with isotropic valence electron bands this leads to two parabolic exciton bands that are degenerate at $k = 0$ [59, 63]. These are labelled as "heavy" and "light" exciton bands, with the corresponding dispersion relations:

$$\begin{aligned} \hbar\omega_{Th}(k) =& \hbar\omega_T + \frac{\hbar^2 k^2}{2m_h}, \qquad \omega_{Th}^2(k) \approx \omega_T^2 + D_h k^2, \qquad D_h = \frac{\hbar\omega_T}{m_h}, \\ \hbar\omega_{Tl}(k) =& \hbar\omega_T + \frac{\hbar^2 k^2}{2m_l}, \qquad \omega_{Tl}^2(k) \approx \omega_T^2 + D_l k^2, \qquad D_l = \frac{\hbar\omega_T}{m_l}. \end{aligned} \tag{6.26}$$

This sections considers a two-resonance model for GaAs using the heavy/light exciton bands in (6.26) and the parameters in Table 6.1. Figure 6.4 shows the frequency dependence of r_p for a fixed incident angle. The result displays the same basic features as the single-resonance model. The behaviour is mostly determined by the value of U_x, with U_z only affecting the frequency region near the reflection minima.

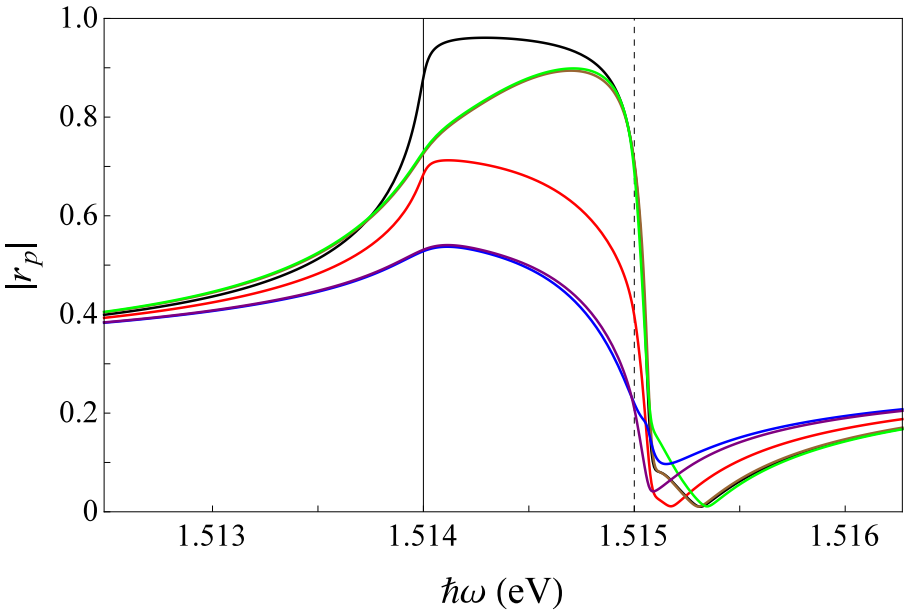

Figure 6.4: Absolute value of $r_p(\omega)$ for the GaAs heavy/light exciton model at a fixed incident angle of $50°$. Plot styles follow the conventions in Fig. 6.3.

Previous work [70] on heavy/light exciton bands has suggested that the susceptibility of the system can be approximated by a one-resonance model with ω_p^2 multiplied by 2 and

an effective nonlocal parameter, given by:

$$D_{\text{eff}} = \frac{D_h + D_l}{2}. \tag{6.27}$$

Figure 6.5 compares the r_p results of the full two-resonance model to a single-resonance approximation using the effective parameter in (6.27) for the Agarwal ABC at a range of incident angles. The effective parameter D_{eff} provides a reasonable approximation for most values of ω, but underestimates the result over the range of the peak in r_p, especially at the resonant frequency ω_T. The discrepancy between the single-band approximation and the heavy/light exciton band results increases with the difference in D_h and D_l values and is greatest for ABCs with $U_x = -1$.

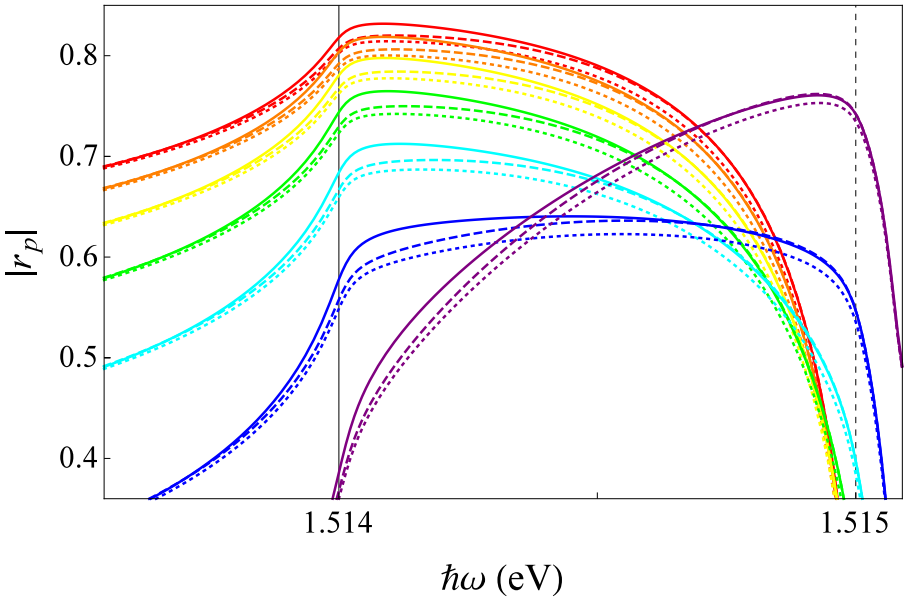

Figure 6.5: Detail of the peak in $|r_p(\omega)|$ for the GaAs heavy/light exciton model at a fixed incident angle $\theta_i = 20°$ (red), $30°$ (orange), $40°$ (yellow), $50°$ (green), $60°$ (cyan), $70°$ (blue) and $80°$ (purple) using the Agarwal ABC. Compares the two-resonance model (solid lines) to the single-resonance approximations using D_{eff} (dotted lines) in (6.27) and the newly proposed D^* (dashed lines) in (6.29), which provides a better fit all values of ω and θ_i.

The paper [70] that proposed the effective nonlocal parameter D_{eff} also noted this discrepancy in results near ω_T. However, as the aim of their work was not to provide a detailed fit between experimental and theoretical results, the approximation in in (6.27) was considered adequate as no qualitatively new features were introduced to the susceptibility.

An improved single-resonance approximation to the heavy/light exciton model can be made by re-expressing the nonlocal term in the susceptibility as

$$Dk^2 = \left(\sqrt{D}k\right)^2 \tag{6.28}$$

and instead taking the average value of $\sqrt{D}$, which is the coefficient of k. The new effective nonlocal parameter D^* is given by:

$$\sqrt{D^*} = \frac{\sqrt{D_h} + \sqrt{D_l}}{2}. \tag{6.29}$$

Results for the single-resonance approximation in (6.29) are also displayed in Fig. 6.5. While there are still differences in the result near ω_T, the newly proposed effective parameter D^* provides a much better fit than D_{eff} to the two-resonance model at every frequency and incident angle, especially in the frequency region near ω_L. This behaviour is found to hold for all values of $D_{h/l}$ and U_i and can also be applied to the s-polarization with a similar degree of success.

6.6 Spectral energy density

This section applies the newly-derived expressions for the electromagnetic reflection coefficients to the calculation of the spectral energy density in the presence of multiple exciton bands. It was previously shown in chapter 5 that the inclusion of spatial dispersion removed the unphysical $1/|z|^3$ divergence near the $z = 0$ surface of the medium. The aim of this section is to investigate differences in the behaviour of u_{tot} introduced by the presence of multiple resonances in the susceptibility.

6.6.1 Non-interacting exciton bands

The simpler case of non-interacting exciton bands in ZnO is first considered. Figure 6.6 shows the behaviour of $\mathbb{I}\text{m}[r_p]$ as a function of K for ZnO at $\hbar\omega = 3.44\text{eV}$, compared to the real and imaginary parts of q_n for the seven waves inside the medium. The results display the same general features as the single-resonance model in section 5.5, with peaks in $\mathbb{I}\text{m}[r_p]$ occurring at the values of K where each wave goes from propagating (dominated by $\mathbb{R}\text{e}[q_n]$) to evanescent (dominated by $\mathbb{I}\text{m}[q_n]$) behaviour, followed by a $1/K^4$ decay to zero in the $K \to \infty$ limit. The exceptions to this are the Fuchs-Kleiwer ABC, which only displays peaks for longitudinal waves, and the Rimbey-Mahan ABC, which only displays

peaks for transverse waves. The results for $\mathbb{I}\mathrm{m}[r_s]$, which are not included here, display similar behaviour, but with the absence of longitudinal waves and their associated peaks and a $1/K^6$ decay to zero in the $K \to \infty$ limit.

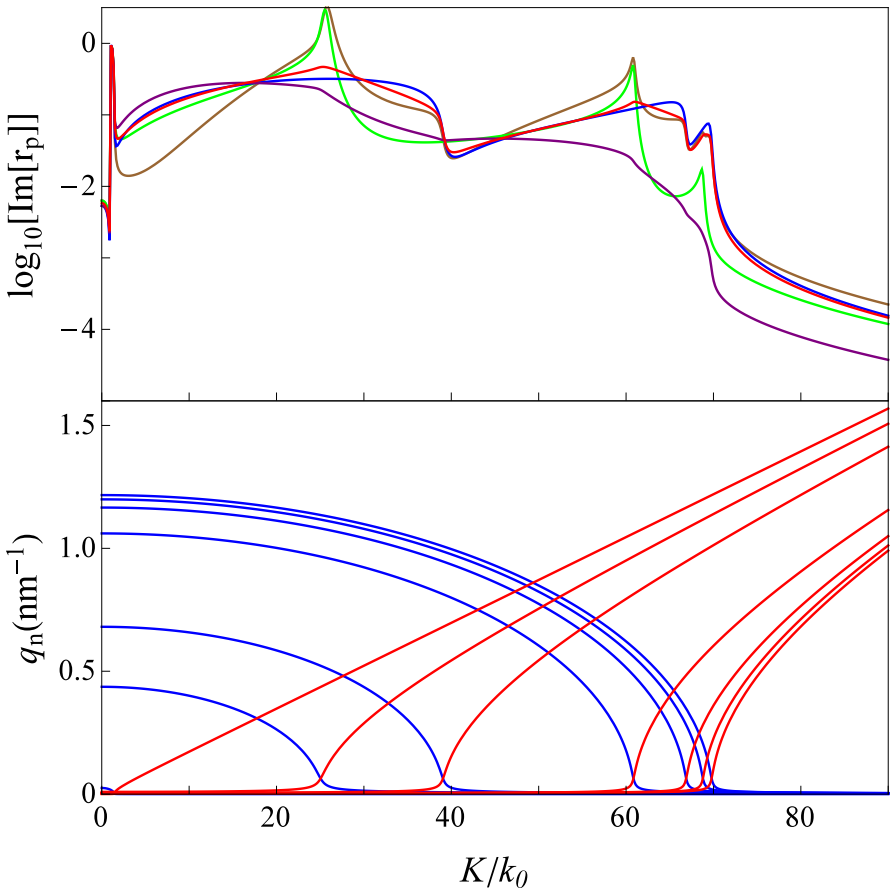

Figure 6.6: Top: Logarithmic plot of $\mathbb{I}\mathrm{m}[r_p]$ as a function of K for the three-resonance ZnO model at $\hbar\omega = 3.44\mathrm{eV}$. Includes Agarwal *et al.* (red), Ting *et al.* (brown), Fuchs-Kliewer (green), Rimbey-Mahan (blue) and Pekar (purple) ABC's. Bottom: Comparison between the real (blue) and imaginary (red) components of the seven q_n values used in the $\boldsymbol{E}$ ansatz (6.9). The peaks in $\mathbb{I}\mathrm{m}[r_p]$ roughly coincide with the values of K where q_n changes from describing a transmitted wave (dominated by $\mathbb{R}\mathrm{e}[q_n]$) to an evanescent wave (dominated by $\mathbb{I}\mathrm{m}[q_n]$), similar to Fig. 5.7.

Figure 6.7 displays $u_{\mathrm{tot}}(\omega)$ at a fixed distance of $8\mathrm{nm}$ from the surface of ZnO. The results depend strongly on the choice of ABC, with the Ting *et al.* ABC giving the largest peaks, followed by Fuchs-Kleiwer, Agarwal *et al.*, Rimbey-Mahan and finally Pekar. This behaviour agrees with the results for the single-resonance model in section 5.5.3. Separating the results into s- and p-polarization contributions, as in Fig.6.8 for the Agarwal ABC, reveals six separate peaks at each of the ω_{Tm} and ω_{Lm} values. The p-polarization peaks were found to be much larger than their s-polarization counterparts in the $z \to 0$ limit of the single-resonance model. However, the u_{tot} peak at ω_{L1} has been suppressed by the proximity of the $m = 2$ resonance and is now comparable in size to the s-polarization peaks.

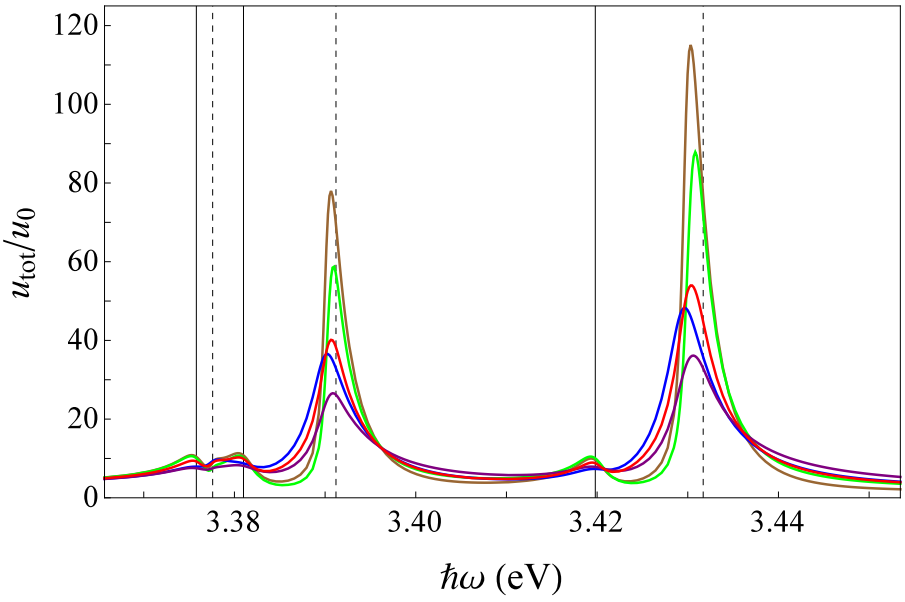

Figure 6.7: Rescaled spectral energy density $u_{\mathrm{tot}}(\omega)$ at a distance of $8\mathrm{nm}$ from the planar boundary of the nonlocal medium ZnO described by a three-resonance susceptibility. Vertical lines indicate ω_{Tm} (solid) and ω_{Lm} (dashed) values. The peak at ω_{T1} is suppressed by the presence of the $m = 2$ resonance. Plot styles follow the conventions in Fig. 6.3.

The origin of this behaviour can be traced back to Fig. 6.6. Recall that each nonlocal resonance in the susceptibility (6.1) leads to an additional transverse and longitudinal wave in the medium. The $\mathbb{I}\mathrm{m}[r_p]$ peak at the largest K value is associated with the waves introduced by the $m = 1$ resonance. This peak is very small due to the presence of a nearby peak in $\mathbb{I}\mathrm{m}[r_p]$ at a smaller K value, which is associated with the waves introduced by the $m = 2$ resonance. This leads to an overall suppression of the $m = 1$ peak in the

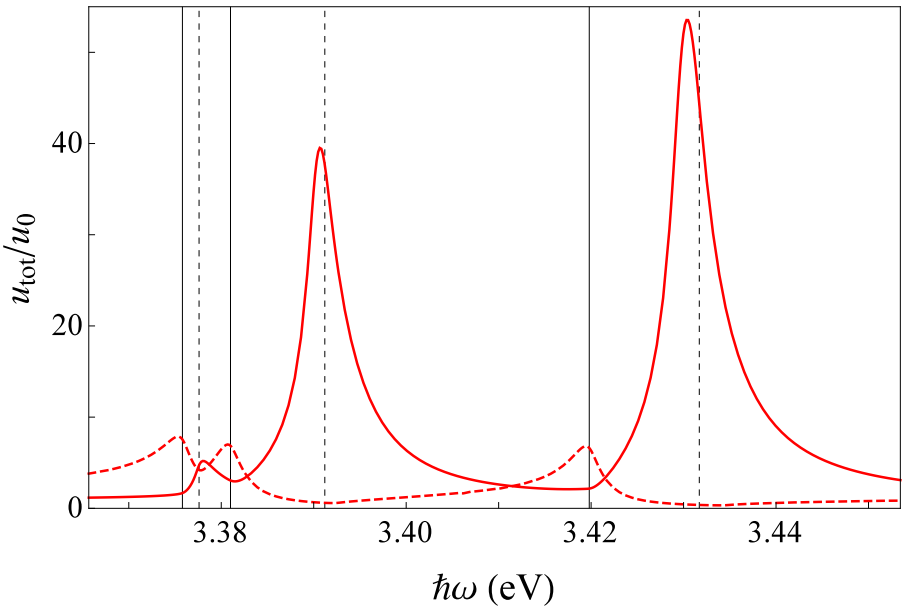

Figure 6.8: Comparison between s- (dashed) and p-polarization (solid) contributions to $u_{\mathrm{tot}}(\omega)$ at a distance of $8\mathrm{nm}$ from the surface of ZnO using the Agarwal ABC.

p-polarization, and is a feature that cannot be described by the single-resonance model. This behaviour is less pronounced in the s-polarization, which only contains transverse waves, and therefore fewer peaks in $\mathbb{I}\mathrm{m}[r_s]$.

6.6.2 Heavy/light exciton bands

The more complex heavy/light exciton model used for GaAs is now considered. The results for $\mathbb{I}\mathrm{m}[r_p]$ at $\hbar\omega = 1.517\mathrm{eV}$ in Fig. 6.9 display the same behaviour discussed in section 6.6.1 for the non-interacting exciton model, with each peak in $\mathbb{I}\mathrm{m}[r_p]$ corresponding to the value of K where each wave goes from propagating (dominated by $\mathbb{R}\mathrm{e}[q_n]$) to evanescent (dominated by $\mathbb{I}\mathrm{m}[q_n]$) behaviour. It is important to note that the two-resonance model contains more waves, and therefore more peaks in $\mathbb{I}\mathrm{m}[r_p]$, than the single-resonance approximations discussed in section 6.5.2.

Figure 6.10 displays the results for $u_{\mathrm{tot}}(\omega)$ a distance of $8\mathrm{nm}$ from the planar boundary of the heavy/light exciton model of GaAs. While the results initially appear similar to those of the single-resonance in section 5.5.3, Fig. 6.11 reveals that neither of the single-resonance approximations discussed in section 6.5.2 provide an accurate result for $u_{\mathrm{tot}}(\omega)$. This inaccuracy can be traced back to the behaviour of r_s and r_p for evanescent

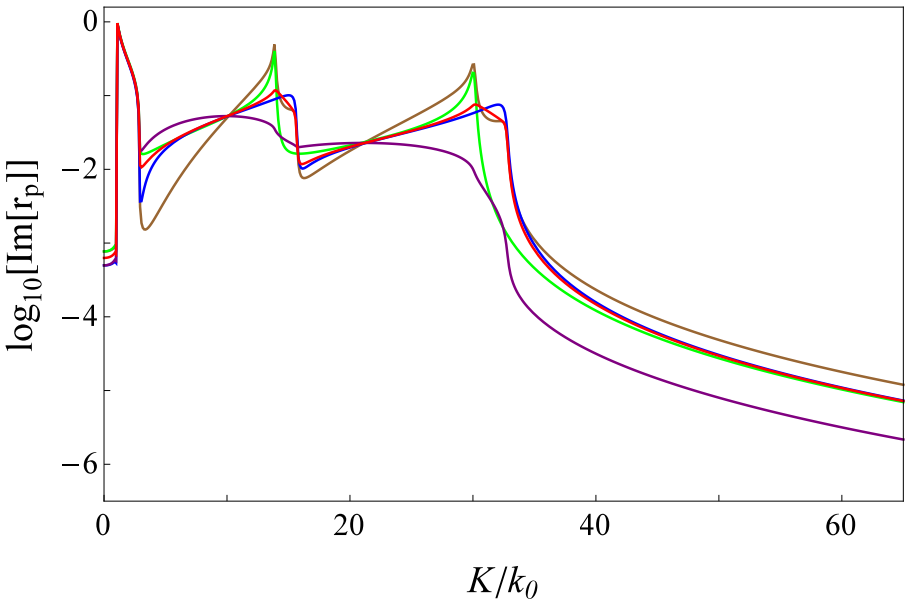

Figure 6.9: Logarithmic plot of $\mathbb{Im}[r_p]$ as a function of K for the GaAs heavy/light exciton model at $\hbar\omega = 1.517\text{eV}$. Plot styles follow the conventions in Fig. 6.3.

waves. While both approximations provide relatively accurate results for the reflection coefficient in the case of propagating waves, as seen in Fig. 6.5, the value of u_{tot} close to the boundary is dominated by the evanescent wave integral. Here, the key features of $\mathbb{Im}[r_s]$ and $\mathbb{Im}[r_p]$ are the peaks coinciding with the changeover values of the wave vectors q_n. The single-resonance model contains fewer waves and therefore fewer peaks in $\mathbb{Im}[r_{s/p}]$ compared to the two-resonance model, leading to the inaccuracies observed in Fig. 6.11.

It is clear from the results of sections 6.6.1 and 6.6.2 that multiple exciton bands, especially those that are closely spaced or exhibit degeneracy, cannot be considered separately when calculating the spectral energy density of thermal and zero-point radiation close to the surface of a nonlocal medium. Both sets of $u_{\text{tot}}(\omega)$ results in Fig. 6.7 and 6.10 display behaviour that is not found in the single resonance case described in chapter 5.5.3, such as the suppression of peaks in ZnO or the failures of the single-resonance approximations in GaAs.

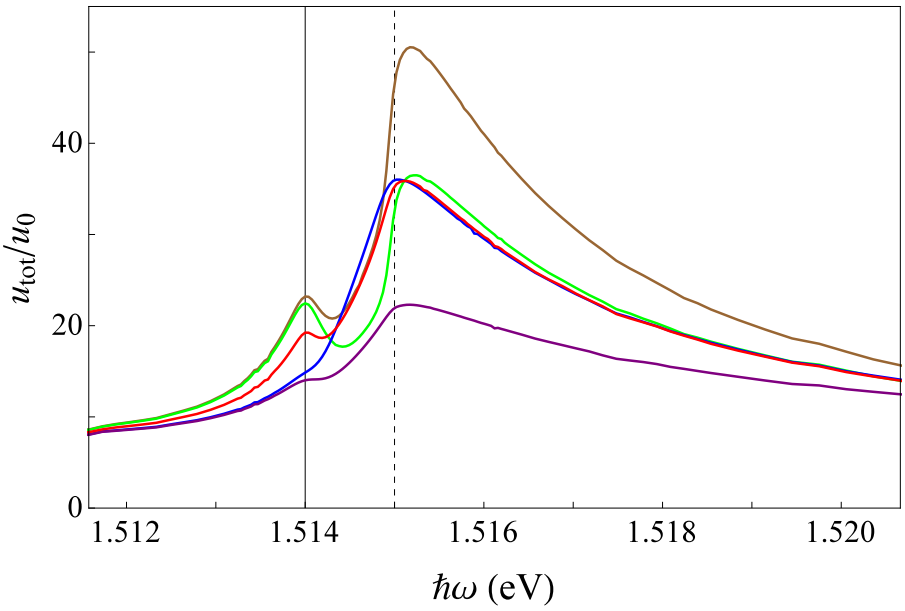

Figure 6.10: Rescaled spectral energy density $u_{\rm tot}(\omega)$ at a distance of 8nm from the planar boundary of the nonlocal medium GaAs described by a two-resonance susceptibility. Plot styles follow the conventions in Fig. 6.3.

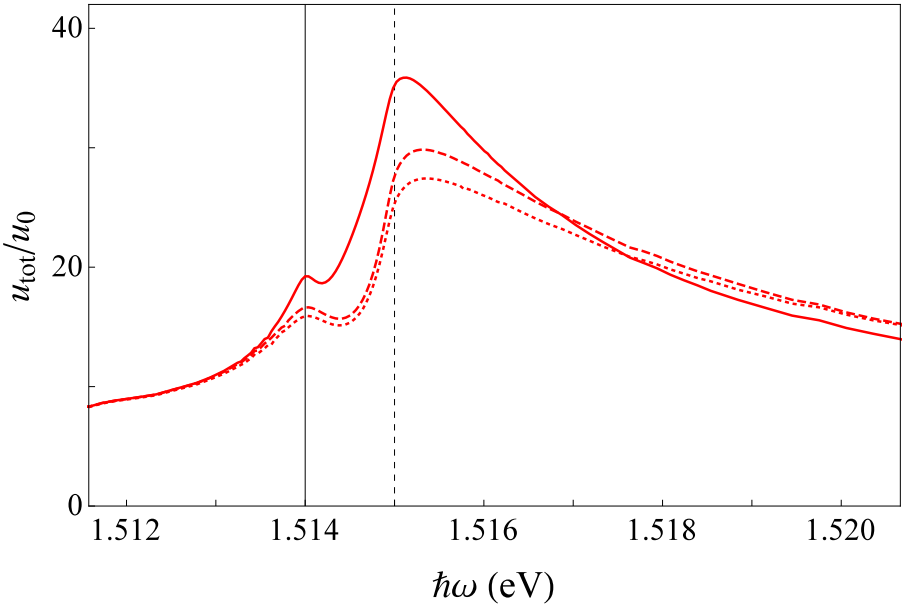

Figure 6.11: Detail of Fig. 6.10 comparing the heavy/light exciton model (solid line) and the single-resonance approximations using $D_{\rm eff}$ (dashed line) and D^* (dotted line) using the Agarwal ABC. Despite the success of the approximations in calculating r_p for propagating waves in Fig. 6.5, neither provides an accurate result for $u_{\rm tot}(\omega)$ near the resonant frequency.

6.7 Chapter summary

This chapter has extended the Halevi-Fuchs generalized ABC model to susceptibilities containing multiple resonances, each with the same Dk^2 wave vector dependence [62]. An ansatz for the electric field containing a sum of plane waves inside the medium was used in conjunction with the electromagnetic wave equations to derive a set of equations relating the amplitude of the various transmitted waves. These equations acted as the ABCs for the multi-resonance model and allowed exact expressions for the electromagnetic reflection and transmission coefficients to be derived. In practice, this amounted to finding solutions of the infinite medium dispersion relations and subsequently inverting a matrix equation, both of which were simple to perform numerically.

Results for the electromagnetic reflection coefficient were presented for a variety of models and ABCs and the differences to the single-resonance model in chapter 5 were discussed. In the particular case of degenerate heavy/light exciton bands, a new effective model parameter $\sqrt{D^*} = (\sqrt{D_h} + \sqrt{D_l})/2$ was found for the single-band approximation, providing an improved fit to r_s and r_p for propagating waves compared to the one currently used in literature.

The derived expressions for r_s and r_p were subsequently used to calculate the spectral energy density of zero-point and thermal radiation outside an isotropic nonlocal medium with multiple spatially-dispersive resonances in the susceptibility. While the results shared the same basic features found in the single-resonance case in chapter 5, such as the removal of the $1/|z|^3$ divergence and peaks in $u_{\mathrm{tot}}(\omega)$ at ω_T and ω_L, additional behaviour was found due to the presence of multiple resonances, such as the suppression of ω_T peaks in u_{tot}.

Chapter 7

Extending the Halevi-Fuchs model III. Uniaxial crystals and linear k terms

The extensions made to the Halevi-Fuchs model in chapters 5 and 6 were both limited to isotropic media with an exciton band structure that could be reduced to the simple Dk^2 term in the denominator of the electromagnetic susceptibility. This chapter further extends the Halevi-Fuchs generalized ABC model to include two new concepts: anisotropy and exciton bands with alternate k dependences [62]. Both of these features are found in crystals with certain symmetry groups [59,60] , including uniaxial crystals [64–66] which are the focus of this chapter.

Like the multi-resonance model featured in chapter 6, previous authors [71–73] have calculated the electromagnetic reflection coefficient of a nonlocal media containing these features, but only for a specific ABC and orientation of the medium. In particular, Mahan and Hopfield [71] considered the case of Cadmium Sulfide (CdS), a uniaxial medium with wurtzite crystal structure. The symmetry of this system allows for energy terms that are linear in wave vector to appear in the valence bands of CdS [60]. This in turn leads to the splitting of otherwise degenerate exciton bands by a linear $\pm k$ term in the dispersion relations.

This chapter extends the Halevi-Fuchs multi-resonance model described in chapter 6 to the case of uniaxial crystals, incorporating both anisotropy and exciton bands with a $\pm k$ term in the dispersion relation. The electromagnetic reflection and transmission coefficients are derived for a range of crystal orientations and subsequently used in the calculation of spectral energy density of thermal and zero-point radiation [62].

Section 7.1 considers the susceptibility and dispersion relations of the infinite medium, highlighting the difficulties introduced by anisotropy, such as the tensor susceptibility. The Halevi-Fuchs multi-resonance model is further modified in section 7.2 for the half-infinite uniaxial crystal and a set of equations relating the various transmitted wave amplitudes are derived. Exact expressions are subsequently derived for the electromagnetic reflection and transmission coefficients in section 7.3 for a number of different crystal orientations. Numerical results for the reflection coefficients and the resulting spectral energy density are presented in section 7.4, highlighting the key differences to the simpler nonlocal models featured in chapters 5 and 6.

7.1 The infinite medium

This chapter starts by considering the infinite uniaxial crystal. In general, the tensor susceptibility of a crystal can be brought to a diagonal form with the correct choice of co-ordinate axes [26]. The resulting expression is therefore determined by three independent functions describing the electromagnetic response in the direction of each axis. In uniaxial crystals, the functions in the directions parallel and perpendicular to the crystal axis $\boldsymbol{c}$ are not equal. The tensor susceptibility of uniaxial crystals can therefore be reduced to the form $\chi_{ij} = \chi_i \delta_{ij}$ when $\boldsymbol{c}$ is aligned with one of the co-ordinate axis, such as:

$$\boldsymbol{\chi}(\boldsymbol{k}, \omega) = \begin{pmatrix} \chi^{\perp}(\boldsymbol{k}, \omega) \\ \chi^{\perp}(\boldsymbol{k}, \omega) \\ \chi^{\parallel}(\boldsymbol{k}, \omega) \end{pmatrix} \tag{7.1}$$

for the $\boldsymbol{c} \parallel \hat{\boldsymbol{z}}$ case, where the $\parallel$ and $\perp$ superscripts denote components parallel and perpendicular to the crystal axis $\boldsymbol{c}$. The exact form of $\chi^{\perp}$ and $\chi^{\parallel}$ depend on the medium.

The symmetry of uniaxial crystals such as zincblende and wurtzite can lead to linear k terms in the exciton dispersion relations, which act to split otherwise degenerate bands [59, 60]:

$$\hbar\omega_{\pm}(\boldsymbol{k}) = \hbar\omega_T + \frac{\hbar^2 k_{\perp}^2}{2m_{\mathrm{ex}\perp}} + \frac{\hbar^2 k_{\parallel}^2}{2m_{\mathrm{ex}\parallel}} \pm \zeta k_{\perp}, \tag{7.2}$$

where $m_{\mathrm{ex}\perp}$ and $m_{\mathrm{ex}\parallel}$ are the exciton masses and $k_{\parallel}$ and $k_{\perp}$ are wave vector components parallel and perpendicular to $\boldsymbol{c}$ respectively. This behaviour is known as linear splitting and is shown in Fig. 7.1. Note that both exciton bands are required to preserve the overall symmetry of the system.

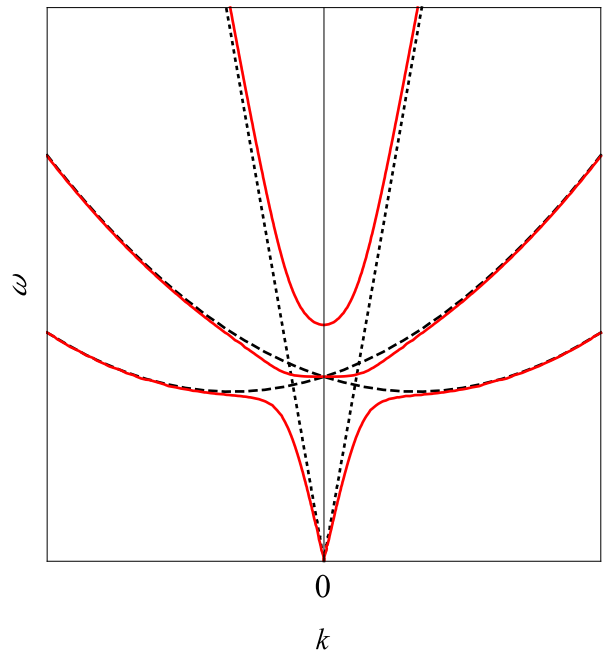

Figure 7.1: Exciton band behaviour (black dashed) in the presence of linear splitting compared to the light line (black dotted) and dispersion relations for transverse $\boldsymbol{E}$ waves in an infinite medium (solid red) when γ is set to zero (not to scale).

In the corresponding nonlocal susceptibility, equation (7.2) is approximated to [71] :

$$\omega_{\pm}^2(\boldsymbol{k}) = \omega_T^2 + D_{\perp}k_{\perp}^2 + D_{\parallel}k_{\parallel}^2 \pm \xi k_{\perp}, \tag{7.3}$$

where

$$D_{\perp/\parallel} = \frac{\hbar\omega_T}{m_{\mathrm{ex}\perp/\parallel}}, \qquad \xi = \frac{2\omega_T\zeta}{\hbar}. \tag{7.4}$$

The susceptibility of the uniaxial crystal therefore contains two resonances:

$$\begin{aligned}\chi_+(\boldsymbol{k}) + \chi_-(\boldsymbol{k}) =& \frac{\omega_p^2}{(\omega_T^2 + D_{\perp}k_{\perp}^2 + D_{\parallel}k_{\parallel}^2 + \xi k) - \omega^2 - i\gamma\omega} \\ &+ \frac{\omega_p^2}{(\omega_T^2 + D_{\perp}k_{\perp}^2 + D_{\parallel}k_{\parallel}^2 - \xi k) - \omega^2 - i\gamma\omega},\end{aligned} \tag{7.5}$$

that can be collected to a single fraction:

$$\chi_{\mathrm{lin}}^{\perp}(\boldsymbol{k}) = \frac{2\omega_p^2(\omega_T^2 + D_{\perp}k_{\perp}^2 + D_{\parallel}k_{\parallel}^2 - \omega^2 - i\gamma\omega)}{(\omega_T^2 + D_{\perp}k_{\perp}^2 + D_{\parallel}k_{\parallel}^2 - \omega^2 - i\gamma\omega)^2 - \xi^2 k_{\perp}^2}. \tag{7.6}$$

Previous work on the subject [71] has found that linear splitting is only present in the susceptibility for components of the electric field that are perpendicular to the crystal axis $\boldsymbol{c}$. When $\boldsymbol{E} \parallel \boldsymbol{c}$, the exciton bands were found to be degenerate with $\zeta = 0$, leading to the resonance:

$$\chi^{\parallel}_{\text{lin}}(\boldsymbol{k}) = \frac{2\omega_p^2}{(\omega_T^2 + D_\perp k_\perp^2 + D_\parallel k_\parallel^2) - \omega^2 - i\gamma\omega}. \tag{7.7}$$

The expressions for $\chi^{\perp}_{\text{lin}}$ and $\chi^{\parallel}_{\text{lin}}$ in (7.6) and (7.7) are used in the tensor susceptibility of the uniaxial crystal, denoted $\boldsymbol{\chi}_{\text{lin}}$, which reduces to a simple vector form such as (7.1) when $\boldsymbol{c}$ is aligned with a co-ordinate axis.

The differences between the components of the susceptibility can have a significant effect on the $\boldsymbol{E}$ dispersion relations. In the simplest case, the crystal axis is aligned with one of the co-ordinate axes and the susceptibility $\boldsymbol{\chi}_{\text{lin}}$ takes a vector form, such as (7.1) for $\boldsymbol{c} \parallel \hat{\boldsymbol{z}}$. Using the co-ordinate system of chapters 5 and 6, with $\boldsymbol{k} = (K, 0, q)$, the electromagnetic wave equation takes the form:

$$\begin{pmatrix} K \\ 0 \\ q \end{pmatrix} \times \begin{pmatrix} K \\ 0 \\ q \end{pmatrix} \times \begin{pmatrix} E_x \\ E_y \\ E_z \end{pmatrix} + \left(\frac{\omega}{c}\right)^2 \begin{pmatrix} [1 + \chi_{\text{lin}x}(K,0,q)]E_x \\ [1 + \chi_{\text{lin}y}(K,0,q)]E_y \\ [1 + \chi_{\text{lin}z}(K,0,q)]E_z \end{pmatrix} = 0, \tag{7.8}$$

where $\boldsymbol{k}$ and ω dependence has been omitted from E_i. Equation (7.8) can be decoupled into a lone equation for E_y (s-polarization) and pair of coupled equations for E_x and E_z (p-polarization). The corresponding dispersion relations are therefore strongly dependent upon the orientation of the crystal axis.

While the choice of co-ordinate system is arbitrary for an infinite medium and can be selected to simplify calculations, the same is not true in the half-infinite case. The definition of the $z = 0$ plane as the boundary of the half-infinite medium and $y = 0$ as the plane of incidence in the calculation of the electromagnetic reflection and transmission coefficients means that the wave equation will not always take the simplified form in (7.8). Sections 7.1.1-7.1.3 consider various orientations of the crystal axis and the associated solutions to the electromagnetic wave equation.

7.1.1 The $\boldsymbol{c} \parallel \hat{\boldsymbol{y}}$ orientation

The simplest case is found when $\boldsymbol{c}$ is aligned with $\hat{\boldsymbol{y}}$, perpendicular to the plane of incidence. Table 7.1 displays the various components of $\boldsymbol{\chi}_{\text{lin}}$ for this orientation. This case had previously been studied by Mahan and Hopfield [71] using the Pekar ABC. Linear splitting is not present in $\chi_{\text{lin}y}$, which means the reflection and transmission coefficients for the s-polarization can therefore be calculated using the derivations presented in previous chapters.

The expressions for $\chi_{\text{lin}x}$ and $\chi_{\text{lin}z}$ are identical and both contain linear splitting. The dispersion relation can once again be split into

$$k_0^2 \left[1 + \chi_{\text{lin}x}(q)\right] - \left(K^2 + q^2\right) = 0 \tag{7.9}$$

for transverse waves, and

$$\left[1 + \chi_{\text{lin}x}(q)\right] = 0 \tag{7.10}$$

for longitudinal waves. The susceptibility $\chi_{\text{lin}x}(q)$ contains two poles with $\mathbb{I}\text{m}[q] > 0$, leading to three $\mathbb{I}\text{m}[q] > 0$ solutions for (7.9) and two for (7.10). The p-polarization therefore contains a total of five waves.

Table 7.1: Components of $\boldsymbol{\chi}_{\text{lin}}$ in the $\boldsymbol{c} \parallel \hat{\boldsymbol{y}}$ crystal orientation.

	$\boldsymbol{c} \parallel \hat{\boldsymbol{y}}$
$\chi_{\text{lin}x}$	$\frac{2\omega_p^2[\omega_T^2+D_\perp(K^2+q^2)-\omega^2-i\gamma\omega]}{[\omega_T^2+D_\perp(K^2+q^2)-\omega^2-i\gamma\omega]^2-\xi^2(K^2+q^2)}$
$\chi_{\text{lin}y}$	$\frac{2\omega_p^2}{[\omega_T^2+D_\perp(K^2+q^2)]-\omega^2-i\gamma\omega}$
$\chi_{\text{lin}z}$	$\frac{2\omega_p^2[\omega_T^2+D_\perp(K^2+q^2)-\omega^2-i\gamma\omega]}{[\omega_T^2+D_\perp(K^2+q^2)-\omega^2-i\gamma\omega]^2-\xi^2(K^2+q^2)}$

7.1.2 The $\boldsymbol{c} \parallel \hat{\boldsymbol{x}}$ and $\boldsymbol{c} \parallel \hat{\boldsymbol{z}}$ orientations

The electric field dispersion relations take a different form when $\boldsymbol{c}$ lies in the plane of incidence and is aligned with either $\hat{\boldsymbol{x}}$ or $\hat{\boldsymbol{z}}$. Table 7.2 displays the various components of $\boldsymbol{\chi}_{\text{lin}}$ for these orientations. The dispersion relation for the s-polarization is given by:

$$k_0^2 \left[1 + \chi_{\text{lin}y}(q)\right] - \left(K^2 + q^2\right) = 0. \tag{7.11}$$

The susceptibility component $\chi_{\text{lin}y}$ contains a linear splitting term for both orientations and gives a total of three $\mathbb{Im}[q] > 0$ solutions, corresponding to three transverse waves in the s-polarization.

The p-polarization is far more complex. The inequality $\chi_{\text{lin}x} \neq \chi_{\text{lin}z}$ means the dispersion relation cannot be split into separate transverse and longitudinal equations. The dispersion relation instead takes the form:

$$k_0^2 \left[1 + \chi_{\text{lin}x}(q)\right] \left[1 + \chi_{\text{lin}z}(q)\right] - K^2 \left[1 + \chi_{\text{lin}x}(q)\right] - q^2 \left[1 + \chi_{\text{lin}z}(q)\right] = 0, \qquad (7.12)$$

which has a total of four $\mathbb{Im}[q] > 0$ solutions. It is important to note that the four corresponding waves are no longer purely transverse or longitudinal. Care must be taken later in the derivation when rewriting E_z components in terms of E_x.

Table 7.2: Components of $\boldsymbol{\chi}_{\text{lin}}$ in the $\boldsymbol{c} \parallel \hat{\boldsymbol{x}}$ and $\boldsymbol{c} \parallel \hat{\boldsymbol{z}}$ crystal orientations.

	$\boldsymbol{c} \parallel \hat{\boldsymbol{x}}$	$\boldsymbol{c} \parallel \hat{\boldsymbol{z}}$
$\chi_{\text{lin}x}$	$\frac{2\omega_p^2}{\omega_T^2+D_\perp q^2+D_\parallel K^2-\omega^2-i\gamma\omega}$	$\frac{2\omega_p^2[\omega_T^2+D_\perp K^2+D_\parallel q^2-\omega^2-i\gamma\omega]}{[\omega_T^2+D_\perp K^2+D_\parallel q^2-\omega^2-i\gamma\omega]^2-\xi^2K^2}$
$\chi_{\text{lin}y}$	$\frac{2\omega_p^2[\omega_T^2+D_\perp q^2+D_\parallel K^2-\omega^2-i\gamma\omega]}{[\omega_T^2+D_\perp q^2+D_\parallel K^2-\omega^2-i\gamma\omega]^2-\xi^2q^2}$	$\frac{2\omega_p^2[\omega_T^2+D_\perp K^2+D_\parallel q^2-\omega^2-i\gamma\omega]}{[\omega_T^2+D_\perp K^2+D_\parallel q^2-\omega^2-i\gamma\omega]^2-\xi^2K^2}$
$\chi_{\text{lin}z}$	$\frac{2\omega_p^2[\omega_T^2+D_\perp q^2+D_\parallel K^2-\omega^2-i\gamma\omega]}{[\omega_T^2+D_\perp q^2+D_\parallel K^2-\omega^2-i\gamma\omega]^2-\xi^2q^2}$	$\frac{2\omega_p^2}{\omega_T^2+D_\perp K^2+D_\parallel q^2-\omega^2-i\gamma\omega}$

7.1.3 Other c orientations

Section 7.1.1 and 7.1.2 have considered the simplest orientations of the uniaxial crystal, where $\boldsymbol{c}$ aligned with one of the co-ordinate axis. Each of these cases allow the multi-resonance derivation in chapter 6 to be used with only minor alterations. When the crystal axis $\boldsymbol{c}$ is neither perpendicular or parallel to both the $z = 0$ boundary and the $y = 0$ plane of incidence, the susceptibility must be expressed as a full tensor, rather than the simplified vector form $\chi_{ij} = \chi_i \delta_{ij}$ used in (7.8). If the crystal axis lies within the xz-plane of incidence, but is not aligned with $\hat{\boldsymbol{x}}$ or $\hat{\boldsymbol{z}}$, the χ_{xz} and χ_{zx} susceptibility components will be nonzero. In this case, the method used for the tensor susceptibility in chapter 5, which has the same set of nonzero χ_{ij} components, could potentially be applied. Other orientations would lead to coupling between E_y and $E_{x/z}$. This would require a different derivation as the s- and p-polarizations cannot be considered separately in such a case.

7.2 The half-infinite medium

The susceptibility of the half-infinite medium is once again defined by rewriting the Halevi-Fuchs model to give:

$$\chi_i'(x-x',y-y',z,z') = \begin{cases} \chi_0\delta(x-x')\delta(y-y')\delta(z-z') \\ \quad + \chi_{\text{lin}i}'(x-x',y-y',z,z') & \text{if } z,z'>0, \\ 0 & \text{otherwise,} \end{cases} \tag{7.13}$$

$$\chi_{\text{lin}i}'(x-x',y-y',z,z') = \chi_{\text{lin}i}(x-x',y-y',z-z') + U_{mi}\chi_{\text{lin}i}(x-x',y-y',z+z'). \tag{7.14}$$

While this chapter assumes $\chi_{\text{lin}i}$ is an isolated resonance with the background susceptibility χ, additional nonlocal resonances could also be included explicitly in (7.13).

The expressions in (7.13) and (7.14) can be substituted into the $\boldsymbol{P}$ definition in (2.3) using the relevant expressions for $\chi_{\text{lin}i}$ found in Table 7.1 and 7.2. After performing a Fourier transform in the xy-plane, the ansatz (6.9) is also substituted for the electric field, using the $\mathbb{I}\text{m}[q] > 0$ solutions to the dispersion relations (7.9-7.12) for the given crystal axis orientation. The polarization field is once again expressed with an integration over q:

$$P_i(z) = \chi_0 E_i(z) + \frac{i}{2\pi}\int_{-\infty}^{\infty} dq e^{iqz} \sum_{n=1}^{N} \left[\frac{1}{q_n - q} + \frac{U_{\text{lin}i}}{q_n + q}\right] \chi_{\text{lin}i}(q) E_i^{(n)}, \quad z > 0, \tag{7.15}$$

which can be evaluated by performing a contour integration in the upper half-plane of complex q. The number of poles enclosed by this contour depends on the exact form of $\chi_{\text{lin}i}$.

If linear splitting is not present (such as $\chi_{\text{lin}x}$ in the $\boldsymbol{c} \parallel \hat{\boldsymbol{x}}$ case), $\chi_{\text{lin}i}$ describes the simple parabolic exciton bands covered in previous chapters and contains a single $\mathbb{I}\text{m}[q] > 0$ pole, denoted Γ_i. The resulting expression for P_i is identical to (6.11) in the single-resonance case. This leads to the single equation:

$$\sum_{n=1}^{N} \left(\frac{1}{q_n - \Gamma_i} + \frac{U_{\text{lin}i}}{q_n + \Gamma_i}\right) E_i^{(n)} = 0, \tag{7.16}$$

that must be satisfied for the wave equation to be valid at all z. If linear splitting is present $\chi_{\text{lin}i}$ contains two $\mathbb{I}\text{m}[q] > 0$ poles, which are labelled $\Gamma_i^{(+)}$ and $\Gamma_i^{(-)}$. Evaluating the q

integral in (7.15) leads to the result:

$$\begin{aligned} P_i(z) = &\sum_{n=1}^{N} \chi_{\mathrm{lin}i}(q_n) E_i^{(n)} e^{iq_n z} \\ &- F_i^{(+)} \sum_{n=1}^{N} \left(\frac{1}{q_n - \Gamma_i^{(+)}} + \frac{U_{\mathrm{lin}i}}{q_n + \Gamma_i^{(+)}} \right) E_i^{(n)} e^{i\Gamma_i^{(+)} z} \\ &- F_i^{(-)} \sum_{n=1}^{N} \left(\frac{1}{q_n - \Gamma_i^{(-)}} + \frac{U_{\mathrm{lin}i}}{q_n + \Gamma_i^{(-)}} \right) E_i^{(n)} e^{i\Gamma_i^{(-)} z}, \end{aligned} \tag{7.17}$$

where $F_i^{(\pm)}$ is a simple prefactor. The terms not proportional to $\exp(iq_n z)$ lead to a pair of equations identical to (7.16), but with different values of Γ:

$$\begin{aligned} \sum_{n=1}^{N} \left(\frac{1}{q_n - \Gamma_i^{(+)}} + \frac{U_{\mathrm{lin}i}}{q_n + \Gamma_i^{(+)}} \right) E_i^{(n)} &= 0, \\ \sum_{n=1}^{N} \left(\frac{1}{q_n - \Gamma_i^{(-)}} + \frac{U_{\mathrm{lin}i}}{q_n + \Gamma_i^{(-)}} \right) E_i^{(n)} &= 0. \end{aligned} \tag{7.18}$$

It is clear from (7.16) and (7.18) that the inclusion of linear k terms in the susceptibility does not significantly alter the derivation of the field amplitude ratios presented in section 6.3.2. The main differences are therefore due to the anisotropic nature of the nonlocal medium, which means that each orientation of the crystal axis requires a different treatment.

7.3 Electromagnetic reflection coefficients

As in the previous sections, the electromagnetic reflection coefficients r_s and r_p are defined in (2.34) and (2.35) in terms of the surface impedance of the nonlocal medium. The corresponding definitions for $Z_s(0^+)$ and $Z_p(0^+)$ in (2.36) and (2.37) also apply to the case of the uniaxial crystal. Once again, the field amplitude ratios of the various transmitted waves in the nonlocal medium must be found. This section considers this calculation for the crystal axis orientations discussed in section 7.1.

7.3.1 The $\boldsymbol{c} \parallel \hat{\boldsymbol{y}}$ orientation

The $\boldsymbol{c} \parallel \hat{\boldsymbol{y}}$ case is first considered. This specific orientation of the crystal axis was previously studied by Mahan and Hopfield [71], and is the simplest of the cases described

in section 7.1. The $\chi_{\mathrm{lin}y}$ component in Table 7.1 does not contain linear splitting. The derivation of electromagnetic reflection and transmission coefficients in the s-polarization is therefore identical to the Halevi-Fuchs model. However, linear splitting is present in both $\chi_{\mathrm{lin}x}$ and $\chi_{\mathrm{lin}z}$, which apply to the p-polarization. The dispersion relations (7.9-7.10) lead to three transverse and two longitudinal waves in the nonlocal medium. Substituting $\chi_{\mathrm{lin}x}$ and $\chi_{\mathrm{lin}z}$ into the polarization field integral (7.15) also leads to the pair of equations (7.18) for both E_x and E_z. The E_z equations can be written in terms of E_x using (5.29) to give a total of four equations relating the amplitude of the five waves in the medium, which is sufficient to calculate the field amplitude ratios $E_x^{(n)}/E_x^{(1)}$ required for the surface impedance.

7.3.2 The $\boldsymbol{c} \parallel \hat{\boldsymbol{x}}$ and $\boldsymbol{c} \parallel \hat{\boldsymbol{z}}$ orientations

The other two orientations present additional challenges. Linear splitting is present in $\chi_{\mathrm{lin}y}$ for both the $\boldsymbol{c} \parallel \hat{\boldsymbol{x}}$ and $\boldsymbol{c} \parallel \hat{\boldsymbol{z}}$ orientations in Table 7.2. The s-polarization therefore contains three transverse waves from the dispersion relation (7.11) and two equations of the form (7.18) for E_y. There is sufficient information to calculate the field amplitude ratios $E_y^{(n)}/E_y^{(1)}$ used in the surface impedance $Z_s(0^+)$ and the reflection coefficient r_s.

The p-polarization is far more complex, as linear splitting is only present in one of the relevant susceptibility components $\chi_{\mathrm{lin}x}$ and $\chi_{\mathrm{lin}z}$, as seen in Table 7.2. The dispersion relation (7.12) leads to four waves inside the medium. The polarization field integral (7.15) leads to the pair of equations (7.18) when linear splitting is present in $\chi_{\mathrm{lin}i}$ and a the single equation (7.16) when it is absent, for a total of three equations relating the four wave amplitudes. There is sufficient information to calculate the field amplitude ratios required for the surface impedance $Z_p(0^+)$ and the reflection coefficient r_p. However, care must be taken when rewriting the E_z equations in terms of E_x as the waves are no longer purely transverse or longitudinal. The relationship between the two components of the field is instead found by looking at the $\hat{\boldsymbol{x}}$ component of the wave equation (7.8), which gives:

$$\eta^{(n)} = \frac{E_z^{(n)}}{E_x^{(n)}} = -\frac{1}{Kq_n}\left\{k_0^2\left[1+\chi_{\mathrm{lin}x}(q_n)\right] - q_n^2\right\}. \tag{7.19}$$

The relationship between the magnetic and electric fields must be similarly modified to

give:

$$\tau^{(n)} = \frac{B_y^{(n)}}{E_x^{(n)}} = \left[\frac{q_n - K\eta^{(n)}}{k_0}\right] = \frac{k_0}{q_n}\left[1 + \chi_{\text{lin}x}(q_n)\right], \tag{7.20}$$

which is used in the calculation of the surface impedance in (2.37).

In each of the cases in this section, there are $N-1$ equations relating the N waves in each polarization. There is therefore sufficient information to calculate the field amplitude ratios, followed by the surface impedances and the electromagnetic reflection coefficients. The electromagnetic transmission coefficients can subsequently be derived in the same manner as in section 6.3.3 by applying the Maxwell boundary conditions at the surface of the medium, but these are not covered in this chapter.

7.4 Results

This section presents numerical results for the uniaxial crystal CdS using the model parameters [60] in Table 7.3. The nonlocal parameters $D_{\perp/\parallel}$ and ξ have been calculated from the measured values of $m_{\text{ex}\perp/\parallel}$ and ζ using the definitions in (7.4).

Table 7.3: List of CdS [60] model parameters, where $m_{\text{e}0}$ is the rest electron mass and c is the speed of light in the vacuum.

	CdS
χ_0	6.5
$\hbar\omega_T$ (eV)	2.5674
$\hbar\omega_L$ (eV)	2.5688
$\hbar\gamma$ (meV)	0.075
$m_{\text{ex}\perp}$ ($m_{\text{e}0}$)	1.3
$m_{\text{ex}\parallel}$ ($m_{\text{e}0}$)	1.02
ζ ($\times 10^{-12}$ eV m)	5.6
$\hbar\omega_p$ (eV)	0.164
$D_\perp c^2$ ($\times 10^{-6}$)	3.86
$D_\parallel c^2$ ($\times 10^{-6}$)	4.93
ξ ($\times 10^{19}\text{ms}^{-2}$)	6.637

7.4.1 Electromagnetic reflection coefficients

Figure 7.2 presents $|r_s(\omega)|$ and $|r_p(\omega)|$ at a fixed incident angle for CdS for a range of ABCs, using the model parameters in Table 7.3. Figure 7.3 considers only the Agarwal *et al.* ABC and instead presents the results near the resonant frequency ω_T for a range of incident angles. Results are compared for the crystal axis $\boldsymbol{c}$ aligned with $\hat{\boldsymbol{x}}$, $\hat{\boldsymbol{y}}$ and $\hat{\boldsymbol{z}}$.

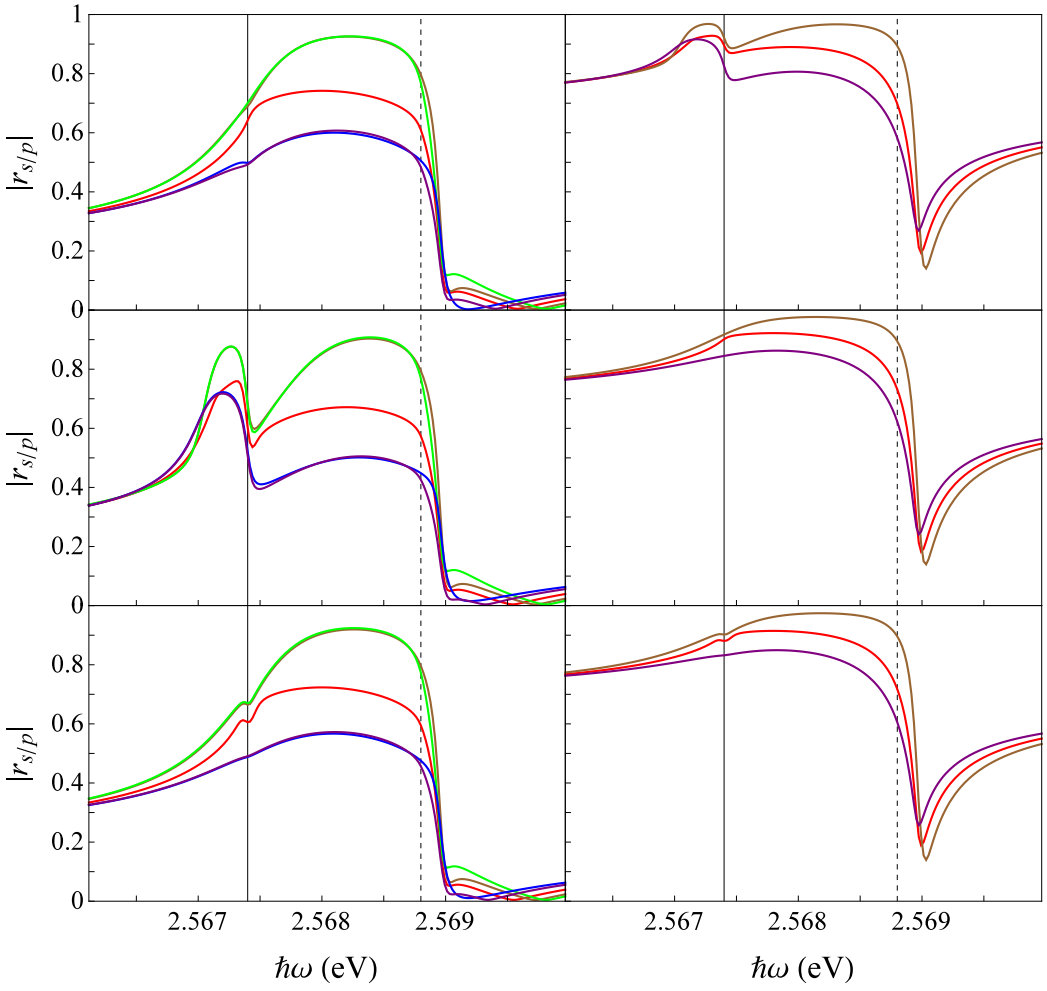

Figure 7.2: Absolute value of r_p (left) and r_s (right) for the CdS model at a fixed incident angle of 60° with the crystal axis $\boldsymbol{c}$ aligned with $\hat{\boldsymbol{x}}$ (top), $\hat{\boldsymbol{y}}$ (middle) and $\hat{\boldsymbol{z}}$ (bottom). Vertical lines indicate ω_T (solid) and ω_L (dashed) values. Includes Agarwal *et al.* (red), Ting *et al.* (brown), Fuchs-Kliewer (green), Rimbey-Mahan (blue) and Pekar (purple) ABCs. The effects of linear splitting are most pronounced in r_p for $\boldsymbol{c} \parallel \hat{\boldsymbol{y}}$ and r_s for $\boldsymbol{c} \parallel \hat{\boldsymbol{x}}$.

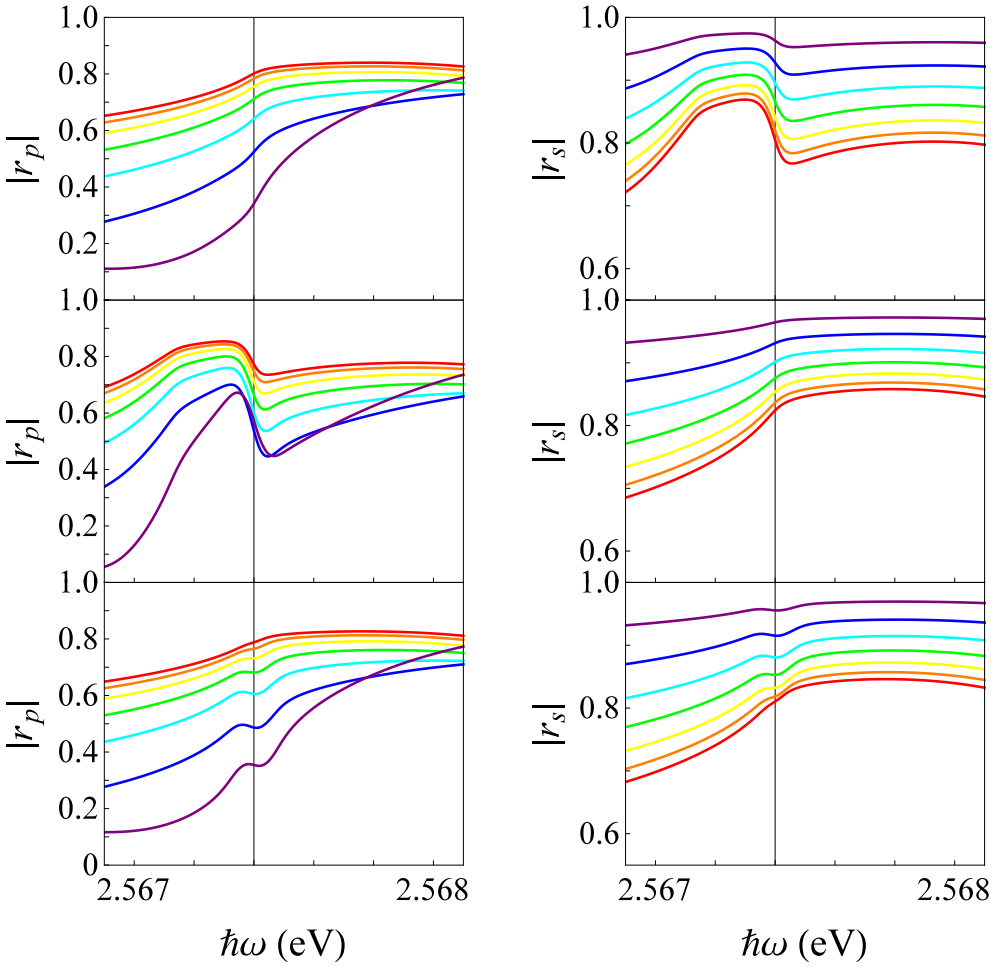

Figure 7.3: Absolute value of r_p (left) and r_s (right) near the resonant frequency of the anisotropic CdS model with the crystal axis $\boldsymbol{c}$ aligned with $\hat{\boldsymbol{x}}$ (top), $\hat{\boldsymbol{y}}$ (middle) and $\hat{\boldsymbol{z}}$ (bottom) using the Agarwal *et al*. ABC. The vertical line indicates the position of $\hbar\omega_T$. Contains the results for the incident angles $\theta_i = 20°$ (red), $30°$ (orange), $40°$ (yellow), $50°$ (green), $60°$ (cyan), $70°$ (blue) and $80°$ (pruple). The effects of linear splitting are the strongest in the r_p ($\boldsymbol{c} \parallel \hat{\boldsymbol{y}}$) and r_s ($\boldsymbol{c} \parallel \hat{\boldsymbol{x}}$) cases. The effects of linear splitting increase with θ_i in the $\boldsymbol{c} \parallel \hat{\boldsymbol{z}}$ cases, as K is the sole wave vector in the linear splitting term of the susceptibility, as seen in Table 7.2. The r_s result in the $\boldsymbol{c} \parallel \hat{\boldsymbol{y}}$ case is identical to that of the Halevi-Fuchs model, as linear splitting is not present in the corresponding susceptibility component $\chi_{\mathrm{lin}y}$.

The s-polarization is first considered. As discussed in section 7.3.1, the $\boldsymbol{c} \parallel \hat{\boldsymbol{y}}$ orientation result is identical to that of the Halevi-Fuchs model, as linear splitting is not present in $\chi_{\mathrm{lin}y}$. The $\boldsymbol{c} \parallel \hat{\boldsymbol{z}}$ orientation displays only minor differences to the $\xi = 0$ result, with a small additional peak in $|r_s|$ just below the resonant frequency ω_T that depends on the choice of ABC, with $U_y = 1$ giving the largest peak and $U_y = -1$ the smallest. The peak is also dependent on the incident angle and grows as θ_i (and K), is increased. This is because the linear splitting term in $\chi_{\mathrm{lin}y}$ in Table 7.2 only contains the wave vector K.

The $\boldsymbol{c} \parallel \hat{\boldsymbol{x}}$ orientation displays the greatest difference to the $\xi = 0$ result, with an additional peak in $|r_s|$ below ω_T that is significantly larger than the one found in the $\boldsymbol{c} \parallel \hat{\boldsymbol{z}}$ orientation. While the behaviour of this new peak is determined by the choice of ABC, the U_y dependence is slightly different to the original peak, with $U_y = 0$ and $U_y = -1$ both giving similar maximum values. The angular dependence is also different to the $\boldsymbol{c} \parallel \hat{\boldsymbol{z}}$ case, with the differences to the $\xi = 0$ result decreasing as θ_i increases.

The p-polarization results are somewhat similar to those of the s-polarization, with an additional peak in $|r_p|$ just below the resonant frequency ω_T. The $\boldsymbol{c} \parallel \hat{\boldsymbol{x}}$ and $\boldsymbol{c} \parallel \hat{\boldsymbol{z}}$ orientations, which both contain linear splitting in only one of the relevant susceptibility components $\chi_{\mathrm{lin}x}$ and $\chi_{\mathrm{lin}z}$, display only minor differences to the $\xi = 0$ result. In the $\boldsymbol{c} \parallel \hat{\boldsymbol{z}}$ orientation, the new peak shares the ABC dependence of the original peak, with $U_x = 1$ giving the largest result and U_z having little effect. Just as in the s-polarization, the differences to the $\xi = 0$ result are found to increase with θ (and K), as the linear splitting terms in the susceptibility contain only the wave vector K. The results are therefore identical to the $\xi = 0$ at normal incidence. The $\boldsymbol{c} \parallel \hat{\boldsymbol{x}}$ orientation shares many of the features of the $\boldsymbol{c} \parallel \hat{\boldsymbol{z}}$ case, but is generally much closer to the $\xi = 0$ result. The main difference is found in the U_i-dependence, with $U_x = -1$ giving the largest peak and U_z also affecting results.

The largest difference to the $\xi = 0$ result is found in the $\boldsymbol{c} \parallel \hat{\boldsymbol{y}}$ orientation, where linear splitting is present in both $\chi_{\mathrm{lin}x}$ and $\chi_{\mathrm{lin}z}$. As in the $\xi = 0$ case, the result is mostly determined by the value of U_x, with U_z only affecting the result near the original reflection minima at ω_L and the new minima just above ω_T. However, the U_x dependence is different for each of the peaks, with $U_x = 0$ and $U_x = -1$ giving similar maximum values for the new peak.

In all cases, the difference between $m_{\mathrm{ex}\perp}$ and $m_{\mathrm{ex}\parallel}$ has little effect on the reflection coefficient for propagating waves compared to the choice of ABC. This agrees with the results of chapter 5, which considered a tensor susceptibility and found that the difference

in the nonlocal parameters for transverse and longitudinal waves only gave minor changes in r_p for propagating waves.

7.4.2 Spectral energy density

The final part of this section takes the derived expressions for the electromagnetic reflection coefficients and applies them to the calculation of the spectral energy density of thermal and zero-point radiation using (2.63). Chapter 5 found that the inclusion of spatial dispersion removed the unphysical $1/|z|^3$ divergence present in the local model and chapter 6 highlighted the differences between the single- and multi-resonance susceptibility models. This chapter considers the anisotropic medium CdS for a specific orientation of the crystal axis $\boldsymbol{c}$, aligned perpendicular to the planar boundary in the $\hat{\boldsymbol{z}}$ direction. Only this orientation retains the rotational invariance about the z-axis used in the derivation [102] of (2.63).

As in sections 5.5 and 6.6, the evanescent wave integral dominates the results for u_{tot} close to the boundary of the nonlocal medium. The overall behaviour of $\mathbb{Im}[r_s]$ and $\mathbb{Im}[r_p]$ remains unchanged from the previous sections, with peaks occurring at the K values when each wave vector q_n goes from being dominated by the real part (indicating propagating waves) to the imaginary part (evanescent waves), before obeying a $1/K^6$ and $1/K^4$ power law in the $K \to \infty$ limit, respectively.

Figure 7.4 shows the rescaled spectral energy density at a distance of $8\mathrm{nm}$ from the planar boundary of CdS for a variety of ABCs. The results display a three-peak structure that is unlike any of the parabolic exciton band models considered in section 5.5 and 6.6. While the peaks at the largest and smallest frequency both display the same U_i dependence found in the previous chapters, the behaviour of the new intermediate peak in u_{tot} between ω_T and ω_L is far more complex, but appears to be most pronounced when $U_x = U_y = 1$.

Figure 7.5 compares the s- and p-polarization contributions to the total result for the Ting *et al.* ABC, revealing two peaks in u_{tot} for each of the polarizations. The large peak in the p-polarization contribution near ω_L is still present and displays the ABC dependence as the parabolic exciton band cases in Fig. 5.11 and 6.10, however a smaller additional peak is also present just above ω_T. The largest difference is found in the s-polarization contribution. The peak previously found near ω_T is now a minimum, with peaks in u_{tot} either side that only depend on the value of U_y. The smaller of the two above the resonant frequency coincides with the smaller peak in the p-polarization contribution, leading to the overall three-peak structure in u_{tot} shown in Fig. 7.4.

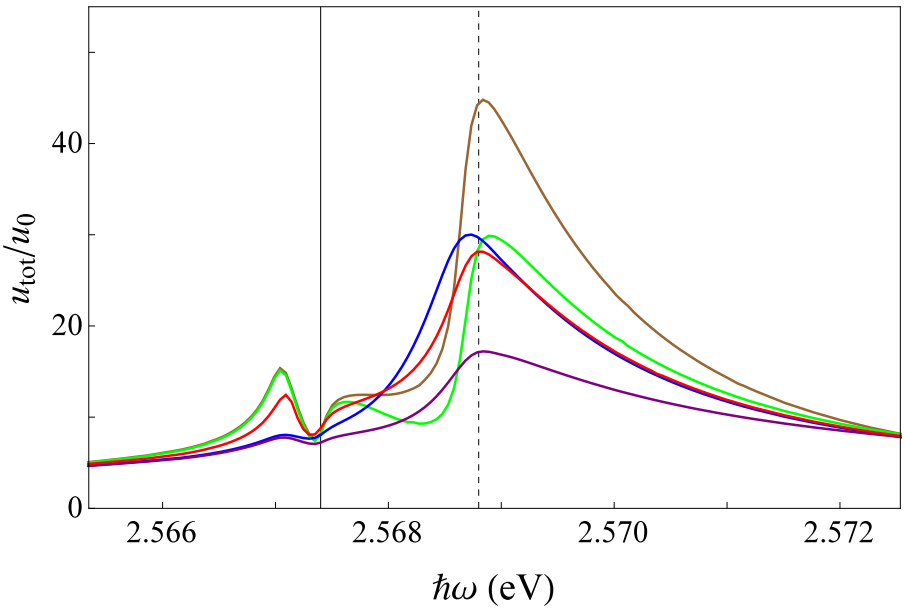

Figure 7.4: Rescaled spectral energy density $u_{\mathrm{tot}}(\omega)$ at a distance of $8\mathrm{nm}$ from the planar boundary of CdS with the crystal axis oriented perpendicular to the planar boundary $\boldsymbol{c} \parallel \hat{\boldsymbol{z}}$. Includes Agarwal *et al.* (red), Ting *et al.* (brown), Fuchs-Kliewer (green), Rimbey-Mahan (blue) and Pekar (purple) ABCs.

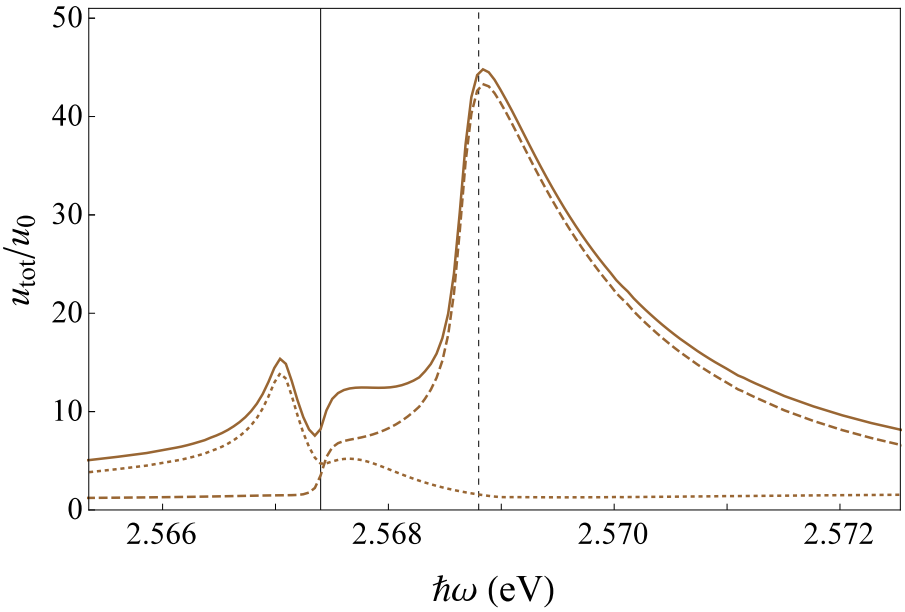

Figure 7.5: Detail of Fig. 7.4 comparing the total $u_{\mathrm{tot}}(\omega)$ (solid line) to the s-polarization (dotted line) and p-polarization (dashed line) contributions using the Ting *et al.* ABC. Each contribution contains two peaks in $u_{\mathrm{tot}}(\omega)$, leading to a three-peak structure in the final result.

The new behaviour found in the CdS $u_{\mathrm{tot}}(\omega)$ results in Fig. 7.4 contrasts strongly with the reflection coefficients for propagating waves in Fig. 7.2, where r_s and r_p exhibit only minor differences to the $\xi = 0$ results . Comparisons can again be drawn to the tensor susceptibility model in chapter 5, where the difference in transverse and longitudinal nonlocal parameters had little effect on r_p in Fig. 5.3, but a significant impact on u_{tot} in Fig. 5.11.

Once again, it is clear that many of the features found in real nonlocal materials that were not covered by the original Halevi-Fuchs model cannot be ignored in the calculation of the electromagnetic reflection coefficients. This chapter has shown that the introduction of anisotropy and linear splitting in exciton dispersion relations can lead to significant changes in the reflection spectra, in the form of additional peaks that strongly depend on both the choice of ABC and the orientation of the crystal axis. Further differences are found in the spectral energy density of thermal and zero-point radiation, where each of the peaks resulting from the original Halevi-Fuchs model have been split in two, giving an overall three-peak structure that would not be predicted by the simple parabolic exciton band models of previous chapters.

7.5 Chapter summary

This chapter continued the work of chapters 5 and 6 by extending the Halevi-Fuchs generalized ABC model to the case of uniaxial crystals, which are both anisotropic and can contain linear $\pm k$ wave vector terms in the susceptibility [62]. The anisotropic nature of the medium had the greatest impact on the derivation of the electromagnetic reflection coefficients. The tensor nature of the susceptibility meant every orientation of the uniaxial crystal led to a different expression for electromagnetic wave equation. However, the need to separate the s- and p-polarization components of the electric field in the Halevi-Fuchs derivation limited the possible orientations of the medium to those where the crystal axis was aligned with one of the co-ordinate axes. Further considerations were required for the type of wave in the nonlocal medium, as inequalities between susceptibility components led to solutions for waves that were neither purely transverse or longitudinal. Despite the additional complications introduced by the anisotropic susceptibility, it was found that the derivation of the field amplitude ratios presented in chapter 6 for the multi-resonance model could be applied to the uniaxial medium without any significant changes other than the initial calculation of the wave vectors used in the electric field ansatz.

Numerical results were presented for the uniaxial crystal CdS for a variety of ABCs and orientations of the crystal axis $\boldsymbol{c}$. The linear wave vector term $\pm k$ in the exciton dispersion relation was found to introduce an additional peak in the reflection spectrum near the resonant frequency. The size and shape of this new peak was mostly determined by the orientation of the crystal axis, with the greatest effects seen in the $\boldsymbol{c} \parallel \hat{\boldsymbol{x}}$ orientation for the s-polarization and $\boldsymbol{c} \parallel \hat{\boldsymbol{y}}$ orientation for the p-polarization. The orientation of $\boldsymbol{c}$ was also found to affect the dependence on both the incident angle θ_i and the choice of ABCs. For example, the changes introduced by linear splitting in the $\boldsymbol{c} \parallel \hat{\boldsymbol{z}}$ orientation were found to increase with the incident angle , but not in the $\boldsymbol{c} \parallel \hat{\boldsymbol{x}}$ orientation.

Finally, the results for r_s and r_p were applied to the calculation of the spectral energy density of thermal and zero-point radiation outside the half-infinite uniaxial crystal. Symmetry requirements limited this calculation to a single orientation of the crystal axis, perpendicular to the planar boundary. The linear $\pm k$ terms on the susceptibility were found to split the peaks in both the s- and p-polarization contributions to u_{tot}, leading to an overall three-peak structure unlike anything found in the tensor or multi-susceptibility models of chapters 5 and 6.

Chapter 8

Conclusions

8.1 Thesis summary

This thesis covered a variety of topics relating to the electromagnetic susceptibility that could be divided into two main groups. The first was an investigation into the microscopic origin of absorption in dielectrics, providing a detailed calculation for a long-held assumption that has formed the basis of many key works on the subject. The second was a series of improvements to a macroscopic model of a half-infinite medium with spatial dispersion, incorporating many more of the features that are found in real materials.

The work presented in chapter 3 [25] verified a proposal made by Hopfield [2], who found that a simple model of a dielectric with linear coupling to the electromagnetic field only absorbed light at the resonant frequencies of the medium and lacked the broadband absorption found in real materials. In his paper, he argued that the inclusion of nonlinear interactions would solve this problem, but did not provide any calculations to support his statement. While previous work [9–13] investigating this claim has focused on the quantum regime, where a full analysis remains challenging, or used phenomenological methods such as the reservoir [3, 14–22], which lack a clear relationship to the underlying physics, chapter 3 presented a classical calculation for a microscopic medium with nonlinear interactions that naturally emerged from the r^{-3} dipole-dipole interaction.

The effective linear susceptibility of an infinite chain of particles, each with an electric dipole moment and displacement from the lattice sites, was extracted by rearranging the nonlinear equations of motion to find the electromagnetic wave equation for the system. This was performed by treating the nonlinear coupling between the particle dipoles and displacements as a perturbation of the system and using a complex iteration method to

process higher-order interaction terms. Elements of quantum field theory [110], including the Dyson equation and Feynman diagrams, were modified and used to simplify the notationally cumbersome calculation of the effective linear susceptibility. Exact expressions were derived for one of the leading-order and one of the higher-order terms in the perturbation series, with imaginary components relating to absorption found when the intermediate fields in the iteration process satisfied their corresponding dispersion relations. While the model used was one-dimensional, the results were also applicable to a three-dimensional cubic lattice under certain restrictions.

Chapter 3 also performed a series of numerical calculations to investigate the frequency and wave vector dependence of the derived effective linear susceptibility. While the limitations of perturbation theory led to unrealistically large results, the inclusion of nonlinear interactions not only led to the broadband absorption predicted by Hopfield, but also provided an excellent fit to the widely used Lorentz model of susceptibility. This contrasts strongly with the phenomenological approach [3], where a specific frequency-dependent coupling term is required for the same results, rather than the nonlinear interaction that naturally emerges from the r^{-3} dipole-dipole interaction. The wave vector dependence was found to be far more complicated, with the various imaginary contributions to the lower-order terms cancelling each other out as the wave vector is increased, leaving a higher-order term to dominate the result. The full wave vector dependence would therefore require the calculation of a large number of higher-order terms.

The second half of the thesis dealt with a different light-matter interaction on a macroscopic scale: the calculation of electromagnetic reflection and transmission coefficients for a half-infinite nonlocal medium. A key consequence of spatial dispersion is the presence of multiple waves in the medium [27], which mean the Maxwell boundary conditions are insufficient to solve for the unknown wave amplitudes. Additional information has historically been provided in terms of additional boundary conditions (ABCs) on the polarization field of the medium, each derived under a specific set of assumptions regarding the behaviour of the medium [33–56]. In 1984, Halevi and Fuchs [4] presented a generalized ABC model for the susceptibility of a half-infinite nonlocal medium that incorporated the ABCs derived by previous authors.

The majority of the second half of this thesis extended the Halevi-Fuchs model to include many more of the features found in real materials [61, 62]. Before this was done, chapter 4 took a closer look at the derivations behind the widely-used Pekar ABC [55] and the Halevi-Fuchs generalized ABC model [4]. In both cases, certain assumptions had

been made that initially appear straightforward, but actually require careful consideration that was not provided in the original derivations.

In the case of the Pekar ABC [55], based on a microscopic model with nearest-neighbour coupling, an oversight was made in the choice of boundary position in the transition between the microscopic and macroscopic regimes. Closer examination revealed that Pekar had derived a condition for the polarization field just outside, rather than inside, the half-infinite medium. Chapter 4 provided an independent derivation for the nonlocal susceptibility of Pekar's half-infinite model with nearest-neighbour coupling. The resulting expression was similar the Halevi-Fuchs model [4], containing both a bulk response term and a term describing the polarization waves reflecting on a point outside the medium, the location of which coincides with the choice of boundary in Pekar's paper. A new set of complex ABCs were found, that reduced to Pekar's result under certain approximations. This model was subsequently extended to include j^{th}-nearest neighbour coupling determined by a $1/r^N$ power law. Increasing j and decreasing N (to a lesser extent) were both found to increase the effective distance travelled by the reflected wave, further changing the result from Pekar ABC. Despite this, the Pekar ABC was still found to be a good approximation near the resonant frequency, but failed to hold far from the resonant frequency or for wavelengths comparable to the lattice spacing.

The second half of chapter 4 took a closer look at an assumption made by Halevi and Fuchs in the derivation of the electromagnetic reflection coefficients for their generalized ABC model [4]. Halevi and Fuchs found that specifying a specific form of the nonlocal susceptibility was insufficient to solve the electromagnetic wave equation. An ansatz for the electric field inside the medium (a sum of plane waves using wave vector solutions of the infinite medium dispersion relation) was introduced and subsequently used to find a set of relations for the transmitted wave amplitudes. While this was a safe assumption far from the boundary, where the effects of the surface are negligible, the calculation of the electromagnetic reflection and transmission coefficients depends on the field behaviour at the boundary, where there are significant differences to the bulk medium. Halevi and Fuchs provided no justification for the choice of ansatz in this critical region.

Chapter 4 performed an independent check for the validity of the Halevi-Fuchs ansatz inside the half-infinite medium while making no prior assumptions regarding the electric field. An iteration process was applied to the nonlocal wave equation to derive a series expression for the electric field that perfectly agreed with the perturbative expansion of the Halevi-Fuchs ansatz throughout the entire nonlocal medium, including the critical region

just inside the boundary, justifying their assumption.

With the underlying assumptions behind the Halevi-Fuchs model checked independently, chapters 5-7 presented various extensions to the generalized ABC model [61, 62]. The original Halevi-Fuchs derivation considered a single-resonance scalar susceptibility with a specific k^2 wave vector dependence in the denominator, describing the electromagnetic response of isolated, parabolic exciton bands in isotropic materials. The Halevi-Fuchs model was therefore limited in applications to real materials, which can display a significantly broader range of exciton band behaviour determined by the structure, symmetry and degeneracies of the valence and conduction bands of a crystal.

Chapter 5 started by replacing the scalar single-resonance susceptibility used as the basis of the Halevi-Fuchs model with the more general (and often overlooked) tensor expression for the susceptibility of a homogeneous, isotropic, non-gyroscopic, nonlocal medium with different nonlocal parameters for transverse and longitudinal field components [26]. Exact expressions were derived for the electromagnetic reflection and transmission coefficients [61]. The difference between transverse and longitudinal nonlocal parameters was found to have little effect on the numerical results for propagating incident waves, with the exception of the transmitted longitudinal wave for certain ABCs.

Chapter 6 took a different approach to extending the Halevi-Fuchs model by considering a scalar bulk susceptibility containing multiple resonances, each with the same basic k^2 wave vector dependence in the denominator [62]. The increase in resonances led to a corresponding increase in the number of waves in the nonlocal medium, and the Halevi-Fuchs derivation was modified to find exact expressions for the electromagnetic reflection and transmission coefficients in a system with an arbitrary number of susceptibility resonances. Comparisons to the single-resonance results were made for a number of systems, noting the differences in ABC dependence in the case of closely spaced resonances. An improved single-resonance approximation was found for a medium with degenerate heavy/light exciton bands, providing a closer fit to the two-resonance system than the one currently used in the literature [70].

Finally, chapter 7 further extended the multi-resonance model in chapter 6 to incorporate two new features: anisotropy and linear splitting k terms in otherwise degenerate exciton bands [62], both of which are found in uniaxial crystals [59,60,64–66]. The multi-resonance derivation of the electromagnetic reflection and transmission coefficients was found to need only minor alterations for such a medium, however the need to separate the s- and p-polarization components of the electric field imposed certain restrictions upon

the orientation of the crystal. The tensor nature of the susceptibility had the greatest impact on the results, modifying the electromagnetic wave equation and leading to solutions for waves that were no longer purely transverse or longitudinal for certain orientations. The presence of linear k splitting led to completely new behaviour, with an additional peak in the reflection spectrum depending upon the orientation of the crystal.

The key result of this research was found in the application of the electromagnetic reflection and transmission coefficients derived in chapters 5-7 to the calculation of the spectral energy density of thermal and zero-point radiation outside the medium. In each case, the inclusion of spatial dispersion was found to naturally remove an unphysical divergence at the boundary of the medium, caused by evanescent waves with arbitrarily large wave vectors parallel to the surface [5, 81, 101]. Numerical calculations of the spectral energy density revealed additional features in results based upon the model being studied. In chapter 5, the difference in transverse and longitudinal nonlocal parameters, which lead to minor differences in reflection coefficients for propagating waves, was found to have a significant effect on results, even at a distance of $10\mathrm{nm}$ from the surface. While the results for the multi-resonance model in chapter 6 shared the same basic features as the single-resonance model, additional behaviour was found only when all resonances were considered together, such as the suppression of peaks in the spectral energy density and the failure of the single-resonance approximation. Finally, the linear k term in the uniaxial crystal studied in chapter 7 lead to a splitting of peaks in the spectral energy density that was not present in the previous chapters, giving an overall three-peak spectrum.

8.2 Future work

This section discusses the various possibilities for future research based upon the work presented in this thesis. The work of chapter 3 is somewhat limited in this regard, as the iteration process and subsequent derivation was primarily intended as a method to verify the assumptions made by Hopfield, but there are still a number of potential areas for further work. The first would be to consider other forms of nonlinear interaction — either higher order terms in the expansion of the r^{-3} dipole-dipole interaction or different form of coupling function. This could also be extended to the calculation of higher order F_n terms. Another, more intriguing, possibility is to focus on the nonlinear field terms that were previously discarded in section 3.3 and derive an effective nonlocal susceptibility for the dipole model. This could subsequently be used to study the re-emission of light from the medium once the lattice is excited.

The second half of this thesis is a much richer source of future work. The expressions for the electromagnetic reflection and transmission coefficients derived in chapters 5-7 can be applied to a wide range of further calculations relating to light-matter interactions near a half-infinite nonlocal medium. This thesis has already considered the specific case of the spectral energy density, resolving some of the issues present with a local model. Other potential applications include the radiative heat transfer coefficient [5], the local density of states [123] and components of the stress-energy tensor [124].

While the extensions in chapters 5-7 have increased the range of behaviour covered by the Halevi-Fuchs model, there remains additional scope for improvement. In particular, the multi-resonance derivation in chapter 6 could be extended to arbitrary k-dependences in the denominator of the susceptibility, in the same manner that chapter 7 modified the derivation for linear k terms. As long as the polarization field integral over q in (6.10) contains simple poles and can be evaluated using Cauchy's residue theorem [114], there should be sufficient information to derive the electromagnetic reflection and transmission coefficients, as each additional q_n solution to the infinite medium dispersion relation (2.15) will be accompanied by an equation of the form (6.12) relating the various wave amplitudes of the transmitted waves. One interesting proposal would be to investigate the effect of retaining the previously omitted k^4 terms in the expression for $\omega_T^2(k)$ in the susceptibility (2.24) of the original Halevi-Fuchs model [4]. Such an inclusion would likely have an effect on the calculation of the spectral energy density u_{tot} due to the additional peaks present in $\mathbb{I}\mathrm{m}[r_{s/p}]$ for evanescent waves.

Another potential improvement has already been mentioned in section 5.2. The derivations presented in this thesis assumes that the surface of the nonlocal medium is perfectly smooth. Boundary roughness has already been in the case of the local medium [118, 119] and could potentially be incorporated in a similar manner.

Finally, the concepts used for the half-infinite medium both in the original Halevi-Fuchs derivation and chapters 5-7 could be applied to a curved surface. The particular cases of the dielectric ball [98] and the conducting sperical shell [99] are of some interest. Previous calculations have found that the use of a local medium leads not only to unphysical divergences in the energy density at the spherical surfaces, but also in other components of the stress-energy tensor. Of particular interest is the radial electromagnetic stress, which gives rise to a force on the surface of the ball. The underlying reason behind these divergences bears some similarities to the half-infinite medium, as they are caused by waves with arbitrarily large *angular* momentum moving along the surface of the ball. The greatest changes to the derivation will be in the choice of ansatz for the system, which must be expressed in terms of Bessel functions rather than simple plane waves.

Bibliography

[1] *Classical Electrodynamics,* 3rd ed.
J. D. Jackson (Wiley, New York, 1999).

[2] *Theory of the Contribution of Excitons to the Complex Dielectric Constant of Crystals*
J. Hopfield, Phys. Rev. **112**, 1555 (1958).

[3] *Quantisation of the electromagnetic field in dielectrics*
B. Huttner and S. M. Barnett, Phys. Rev. A **46**, 4306 (1992).

[4] *Generalised additional boundary condition for non-local dielectrics. I. Reflectivity*
P. Halevi and R. Fuchs, Journal of Physics C: Solid State Physics **17**, 21 (1984).

[5] *Surface electromagnetic waves thermally excited - Radiative heat transfer, coherence properties and Casimir forces revisited in the near field*
K. Joulain, J. P. Mulet, F. Marquier, R. Carminati and J. J. Greffet, Surf. Sci. Rep. **57**, 59 (2005).

[6] *On the Theory of Dispersion of X-Rays*
R. de L. Kronig, J. Opt. Soc. Am. **12**, 547 (1926).

[7] *La diffusion de la lumire par les atomes*
H. A. Kramers, Atti Cong. Intern. Fisici, **2**, 545 (1927).

[8] *Quantum Mechanics: Non-relativistic theory* 3rd ed.
L. D. Landau and E. M. Lifshitz (Pergamon Press, Oxford, 1977).

[9] *Contribution of Scattering of Polaritons by Phonons to Absorption of Light Waves in II-VI Crystals*
Contributions of Scattering of Polaritons by Phonons to Emission of Radiation by Solids
W. C. Tait and R. I. Weiner, Phys. Rev. **166**, 769 (1968); **178**, 1404 (1969).

[10] *Effect of the Polariton-Phonon Coupling on the Spatial Dispersion*
V. V. Hizhnyakov, Phys. Stat. Sol. **34**, 421 (1969).

[11] *Polariton-Phonon Interaction in Molecular Crystals*
C. Mavroyannis, J. Math. Phys. **11**, 491 (1970).

[12] *Theory of damping and fluctuations of the polariton due to its interaction with lattice vibrations*
W. Egler and H. Haken, Z. Physik B **28**, 51 (1977).

[13] *On the Damping of the Excitonic Polaritons*
H. N. Cam, N. V. Hieu and N. A. Viet, Phys. Stat. Sol. (B) **126**, 247 (1984).

[14] *Hamiltonian treatment of the electromagnetic field in dispersive and absorptive structured media*
N. A. R. Bhat and J. E. Sipe, Phys. Rev. A **73**, 063808 (2006).

[15] *Field quantization in inhomogeneous absorptive dielectrics*
L. G. Suttorp and M. Wubs, Phys. Re. A **70**, 013816 (2004).

[16] *Field quantization in inhomogeneous anisotropic dielectrics with spatio-temporal dispersion*
L. G. Suttorp, J. Phys. A **40**, 3697 (2007).

[17] *Casimir force in the presence of a medium*
F. Kheirandish and M. Amooshahi, Phys. Rev. A **74**, 042102 (2006).

[18] *Electromagnetic field quantization in an anisotropic magnetodielectric medium with spatialtemporal dispersion*
M. Amooshahi and F. Kheirandish, J. Phys. A **41**, 275402 (2008).

[19] *Canonical quantization of electromagnetic field in an anisotropic polarizable and magnetizable medium*
M. Amooshahi, J. Math. Phys. **50**, 062301 (2009).

[20] *Casimir force in the presence of a medium*
F. Kheirandish, M. Soltani and J. Sarabadani, Phys. Rev. A **81**, 052110 (2010).

[21] *Canonical quantization of macroscopic electromagnetism*
Casimir effect from macroscopic quantum electrodynamics
T. G. Philbin, New J. Phys. **12**, 123008 (2010); **13**, 063026 (2011).

[22] *Canonical quantization of electromagnetism in spatially dispersive media*
S. A. R. Horsley and T. G. Philbin, New J. Phys. **16**, 013030 (2014).

[23] *Quantum dynamics of the damped harmonic oscillator*
T. G. Philbin, New J. Phys. **14**, 083043 (2012).

[24] *Example of the description of dissipative processes in terms of reversible dynamic equations and some comments on the fluctuation-dissipation theorem*
V. I. Tatarskiĭ, Sov. Phys.-Usp. **30**, 134 (1987).

[25] *Absorption in dipole-lattice models of dielectrics*
R. J. Churchill and T. G. Philbin, Phys. Rev. A, **93**, 053809 (2016).

[26] *Electrodynamics of Continuous Media* 2nd ed.
L. D. Landau, E. M. Lifshitz and L. P. Pitaevskii (Butterworth-Heinemann, Oxford, 1984).

[27] *Electrodynamics of Media with Spatial Dispersion*
A. A. Rukhadze and V. P. Silin, Sov. Phys. Usp. **4**, 459 (1961).

[28] *Unusual resonances in nanoplasmonic structures due to nonlocal response*
S. Raza, G. Toscano, A. P. Jauho, M. Wubs and N. Asger Mortensen, Phys. Rev. B **84**, 121412(R) (2011).

[29] *Nonlocal Effects in the Nanofocusing Performance of Plasmonic Tips*
A. Wiener, A. I. Fernández–Domiínguez, A. P. Horsfield, J. B. Pendry and S. A. Maier, Nano Lett. **12**, 3308 (2012).

[30] *Transformation-Optics Description of Nonlocal Effects in Plasmonic Nanostructures*
A. I. Fernández–Domiínguez, A. Wiener, F. J. García–VIdal, S. A. Maier S A and J. B. Pendry, Phys. Rev. Lett. **108** 106802 (2012).

[31] *Resonance shifts and spill-out effects in self-consistent hydrodynamic nanoplasmonics*
G. Toscano, J. Straubel, A. Kwiatkowski, C. Rockstuhl, F. Evers, H. Xu, N. Asger Mortensenand, and M. Wubs, Nat. Comm. **6**, 7132 (2015).

[32] *Asymptotics of surface-plasmon redshift saturation at subnanometric separations*
O. Schnitzer, V. Giannini, R. V. Craster, and S. A. Maier, Phys. Rev. B **93**, 041409 (2016).

[33] *Structure of the Electromagnetic Field in a Spatially Dispersive Medium*
G. S. Agarwal and D. N. Pattanayak, and E. Wolf, Phys. Rev. Lett. **27**, 1022 (1971).

[34] *Refraction and reflection on a spatially dispersive medium*
G. S. Agarwal, D. N. Pattanayak, and E. Wolf, Opt. Commun. **4**, 255 (1971).

[35] *Surface polaritons in a spatially dispersive medium*
G. S. Agarwal, Opt. Commun. **4**, 221 (1972).

[36] *Optics of Polaritons in Bounded Media*
J. L. Birman and J. J. Sein, Phys. Rev. B **6**, 2482 (1972).

[37] *New Method in the Theory of Surface Polaritons*
G. S. Agarwal, Phys. Rev. B **8**, 4768 (1973).

[38] *Effect of Spatial Dispersion on the Properties of a Semi-Infinite Dielectric*
A. A. Maradudin and D. L. Mills, Phys. Rev. B **7**, 2787 (1973).

[39] *Polaritons*
Birman J, Zeyher R. In: Burstein E, DeMartini F, editors. (Pergamon, New York, 1974).

[40] *Polaritons*
Mills D. In: Burstein E, DeMartini F, editors. (Pergamon, New York, 1974).

[41] *Electrodynamics of nonlocal media*
J. T. Foley and A. J. Devaney, Phys. Rev. B **12**, 3104 (1975).

[42] *Attenuated total reflection spectra of surface exciton polaritons*
M. F. Bishop, A. A. Maradudin, and D. L. Mills, Phys Rev B **14**, 4744 (1976).

[43] *Electrodynamics of bounded spatially dispersive media: The additional boundary conditions*
C. S. Ting, M. J. Frankel, J. L. Birman Solid State Commun. **17**, 1285 (1975).

[44] *Anomalous Skin Effect for Specular Electron Scattering and Optical Experiments at Non-Normal Angles of Incidence*
K. L. Kliewer, R. R. Fuchs, Phys. Rev. **172**, 607 (1968).

[45] *Surface Plasmon in a Semi-Infinite Free-Electron Gas*
K. L. Kliewer, R. R. Fuchs, Phys. Rev. B **3**, 2270 (1971).

[46] *Calculated dispersion of surface excitons*
B. Fischer, H. J. Queisser, Solid State Commun. **16**, 1125 (1975).

[47] *Optical properties of spatially dispersive dielectric spheres*
R. Ruppin, J Opt. Soc. Am. **71**, 755 (1981).

[48] *Surface impedance of a spatially dispersive medium*
P. R. Rimbey and G. D. Mahan, Solid State Commun **15**, 35 (1974).

[49] *Dispersion relation for surface wannier excitons*
P. R. Rimbey, Phys Status Solidi **68**, 617 (1975).

[50] *Aspects of spatial dispersion in the optical properties of a vacuum-dielectric interface*
D. Johnson and P. R. Rimbey, Phys. Rev. B **14**, 2398 (1976).

[51] *Additional boundary conditions and surface exciton dispersion relations*
P. R. Rimbey, Phys. Rev. B **15**, 1215 (1977).

[52] *Erratum: Additional boundary conditions and surface exciton dispersion relations*
P. R. Rimbey, Phys. Rev. B **18**, 971 (1978).

[53] *The theory of electromagnetic waves in a crystal in which excitons are produced*
S. I. Pekar, Sov. Phys. JETP **6**, 785 (1958).

[54] *Dispersion of light in the exciton absorption region of crystals*
S. I. Pekar, Sov. Phys. JETP **7**, 813 (1958).

[55] *Theory of electromagnetic waves in a crystal with excitons*
S. I. Pekar, J Phys. Chem. Solids **5**, 11 (1958).

[56] *On the theory of absorption and dispersion of light in crystals*
S. I. Pekar, Sov. Phys. JETP **9**, 314 (1959).

[57] *On the transformation of light into heat in solids. I*
J. Frenkel, Phys. Rev. **37** (1), 17 (1931).

[58] *On the transformation of light into heat in solids. II*
J. Frenkel, Phys. Rev. **37** (19), 1276 (1931).

[59] *Exciton dispersion in degenerate bands*
E. O. Kane, Phys. Rev. B **11**, 3850 (1975).

[60] *The dispersion of excitons, polaritons and biexcitons in direct-gap semiconductors*
B. Hönerlage, R. Lévy, J. B. Grun, C. Klingshirn and K. Bohnert, Physics Reports, **124**(3), 161 (1984).

[61] *Electromagnetic reflection, transmission, and energy density at boundaries of nonlocal media*
R. J. Churchill and T. G. Philbin, Phys. Rev. B, **94**, 235422 (2016).

[62] *Reflection and transmission in nonlocal susceptibility models with multiple resonances*
R. J. Churchill and T. G. Philbin, Phys. Rev. B, **95**, 205406 (2017).

[63] *Exciton dispersion in semiconductors with degenerate bands*
M. Altarelli and N. O. Lipari, Phys. Rev. B **15**, 4898 (1977).

[64] *Evidence for nonparabolic dispersion of the B exciton in CdS*
E. S. Koteles and G. Winterling, Journal of Luminescence **18**, 267 (1979).

[65] *Direct Measurement of Three-Branch Exciton-Polariton Dispersion in CdS*
E. S. Koteles and G. Winterling, Phys. Rev. Lett. **44**, 948 (1980).

[66] *Polaritons associated with nearly degenerate excitons: Their dispersion and the resulting reflectivity for the* $1s$ *exciton in CuBr*
P. Fiorini, J. C. Merle and M. Simon, Phys. Rev. B **22**, 4941 (1980).

[67] *Dielectric theory of interacting excitonic resonances*
J. Lagois, Phys. Rev. B **16**, 1699 (1977).

[68] *Depth-dependent eigenenergies and damping of excitonic polaritons near a semiconductor surface*
J. Lagois, Phys. Rev. B **23**, 5511 (1981).

[69] *Valence-band parameters and g factors of cubic zinc selenide derived from free-exciton magnetoreflectance*
H. Venghaus, Phys. Rev. B **19**, 3071 (1979).

[70] *Polariton Reflectance and Photoluminescence in High-Purity GaAs*
D. D. Sell, S. E. Stokowski, R. Dingle and J. V. DiLorenzo, Phys. Rev. B **7**, 4568 (1973).

[71] *Optical Effects of Energy Terms Linear in Wave Vector*
G. D. Mahan and J. J. Hopfield, Phys. Rev. **135**, A428 (1964).

[72] *New surface polariton in spatially dispersive semiconductors*
P. Halevi, Oliver B. M. Hardouin Duparc, A. A. Maradudin, and R. F. Wallis, Phys. Rev. B **32**, 6986(R) (1985).

[73] *Attenuated total reflectivity of semiconductors with wave-vector-linear band splitting*
P. Halevi, Oliver B. M. Hardouin Duparc, A. A. Maradudin, and R. F. Wallis, Phys. Rev. B **36**, 2783 (1987).

[74] *Resonance Absorption by Nuclear Magnetic Moments in a Solid*
E. M. Purcell, H. C. Torrey, and R. V. Pound, Phys. Rev. **69**, 681 (1946).

[75] *Variation of the Fluorescence Decay Time of a Molecule in Front of a Mirror*
K. H. Drexhage, H. Kuhn and F. P. Schäfer, Ber. Bunsenges. Phys. Chem. **72**, 329 (1968).

[76] *Fluorescence near interfaces: The role of photonic mode density*
W. L. Barnes, J. Mod. Opt. **45**, 661 (1998).

[77] *Principles of Nano-Optics*
L. Novotny and B. Hecht (Cambridge University Press, Cambridge, 2006).

[78] *Near field radiative heat transfer between two nonlocal dielectrics*
F. Singer, Y. Ezzahri, and K. Joulain, J. Quant. Spec. Rad. Trans. **154**, 55 (2015).

[79] *Nonlocal study of the near field radiative heat transfer between two n-doped semiconductors*
F. Singer, Y. Ezzahri, and K. Joulain, Int. J. Heat Mass Transfer **90**, 34 (2015).

[80] *Spatial dispersion in Casimir forces - a brief review*
R. Esquivel-Sirvent, C. Villarreal, W. L. Mochan, A. M. Contreras-Reyes and V. B. Svetovoy, J. Phys. A. **39** (21), 6323 (2006).

[81] *Vacuum energy in the presence of dielectric and conducting surfaces*
P. Candelas, Annals of Physics **143**, 2 (1982).

[82] *Electromagnetic field correlations near a surface with a nonlocal optical response*
C. Henkel and K. Joulain, Appl, Phys. B **84**, 61 (2006).

[83] *Optimizing the Drude-Lorentz model for material permittivity: Method, program, and examples for gold, silver, and copper*
H. S. Sehmi, W. Langbein, and E. A. Muljarov, Phys. Rev. B **95**, 115444 (2017)

[84] *Optimizing the Drude-Lorentz model for material permittivity: Examples for semiconductors*
H. S. Sehmi, W. Langbein, and E. A. Muljarov, arXiv:1705.05218

[85] *Handbook of optical constants of solids*
E. D. Palik, editor (Academic press, Oxford, 1998).

[86] *Theoretical and Experimental Effects of Spatial Dispersion on the Optical Properties of Crystals*
J. J. Hopfield and D. G. Thomas, Phys. Rev. **132**, 563 (1963).

[87] *The Structure of Electronic Excitation Levels in Insulating Crystals*
G. H. Wannier, Phys. Rev. **52**, 191 (1937).

[88] *On the Theory of Absorption and Dispersion of Light in Crystals*
S. I. Pekar, Sov. Phys. JETP **36**, (9), 451 (1959).

[89] *Real-space Hopfield diagonalization of inhomogeneous dispersive media*
C. R. Gubbin, S. A. Maier and S. De Liberato, Phys. Rev. B **94**, 205301 (2016).

[90] *Atomic Theory of Electromagnetic Interactions in Dense Materials*
U. Fano, Phys. Rev. **103**, 1202 (1956).

[91] *Additional boundary conditions: An historical mistake*
K. Henneberger, Phys. Rev. Lett. **80**, 2889 (1998); **83**, 1265 (1999).

[92] *Comment on "Additional Boundary Conditions: An Historical Mistake"*
D. F. Nelson and B. Chen, Phys. Rev. Lett. **83**, 1263 (1999).

[93] *Comment on "Additional Boundary Conditions: An Historical Mistake"*
R. Zeyher, Phys. Rev. Lett. **83**, 1264 (1999).

[94] *Additional Boundary Conditions - Critical Comparison between Theory and Experiment*
P. Halevi and G. Hernndez-Cocoletzi, Phys. Rev. Lett. **48**, 1500 (1982).

[95] *Classical electrodynamics of non-specular dielectric surfaces*
F. Garcia-Moliner and F. Flores, J. Phys. France **38**, 851-862 (1977).

[96] *New Green-function formalism for surface optics*
J. E. Sipe, J. Opt. Soc. Am. B **4** (4), 481 (1987).

[97] *Effect of temperature on the molecular attracting forces between condensed bodies The Theory of Molecular Attractive Forces between Solids*
E. M. Lifshitz Zh. Eksp. Teor. Fiz. **29** 94 (1955), Sov. Phys. JETP **2**, 73 (1956).

[98] *Semiclassical electron models: Casimir self-stress in dielectric and conducting balls*
K. A. Milton, Annals of Physics, **127** (1), 49 (1980).

[99] *Quantum Electromagnetic Zero-Point Energy of a Conducting Spherical Shell and the Casimir Model for a Charged Particle*
T. H. Boyer, Phys. Rev. **174**, 1764 (1968).

[100] *Thermal radiation scanning tunnelling microscopy*
Y. De Wilde, F. Formanek, R. Carminati, B. Gralak, P. A. Lemoine, K. Joulain, J. P. Mulet, Y. Chen and J. J. Greffet, Nature (London) **444**, 740 (2006).

[101] *Spatial coherence of thermal near fields*
C. Henkel, K. Joulain, R. Carminati, J.J. Greffet, Opt. Comm. **186**, 57 (2000).

[102] *Near-field heat transfer in a scanning thermal microscope*
A. Kittel, W. Müller-Hirsch, J. Parisi, S. A. Biehs, D. Reddig and M. Holthaus, Phys. Rev. Lett. **95**, 224301 (2005).

[103] *Mie resonance-based dielectric metamaterials*
Q. Zhao, J. Zhou, F. Zhang and D. Lippens, Mater. Today **12**, 60 (2009).

[104] *Past achievements and future challenges in the development of three-dimensional photonic metamaterials*
C. M. Soukoulis and M. Wegener, Nat. Photonics **5**, 523 (2011).

[105] *Dielectric metamaterials based on electric and magnetic resonances of silicon carbide particles*
J. A. Schuller, R. Zia, T. Taubner and M. L. Brongersma, Phys. Rev. Lett. **99**, 107401 (2007).

[106] *Broadband optical scattering in coupled silicon nanocylinders*
C. Wang, Z. Y. Jia, K. Zhang, Y. Zhou, R. H. Fan, X. Xiong and R. W. Peng, J. Appl. Phys. **115**, 244312 (2014).

[107] *Dipole coupling and dual Fano resonances in a silicon nanodimer*
Z. Y. Jia, J. N. Li, H. W. Wu, C. Wang, T. Y. Chen, R. W. Peng and M. Wang, J. Appl. Phys. **119**, 074302 (2016).

[108] *Statistical Physics: Part 1* 3rd ed.
L. D. Landau, E. M. Lifshitz (Pergamon Press, Oxford, 1980).

[109] *The Quantum Theory of Light* 3rd ed.
R. Loudon (Oxford university Press, Oxford, 2000).

[110] *An Introduction to Quantum Field Theory*
M. E. Peskin and D. V. Schroeder (Addison-Wesley, 1995)

[111] *Quantum field theory and the standard model*
M. D. Schwartz (Cambridge University Press, Cambridge, 2013).

[112] *Table of Integrals, Series, and Products* 7th ed.
I. S. Gradshteyn, I. M. Ryzhik - Zwillinger (Academic Press, London, 2007).

[113] *Statistical mechanics of assemblies of coupled oscillators*
G. W. Ford, M. Kac, and P. Mazur, J. Math. Phys. **6** (4), 504 (1965).

[114] *Mathematical methods for physicists* 5th ed.
G. B. Arfken and H. J. Weber (Harcourt/Academic Press, London, 2001).

[115] *Phonon dispersions of silicon and germanium from first-principles calculations*
S. Wei and M. Chou, Phys. Rev. B **50**, 2221 (1994).

[116] *Measurement of the damping dispersion of exciton polaritons in CdS*
M. Dagenais and W. F. Sharfin, Phys. Rev. Lett. **58**, 1776 (1987).

[117] *An angular spectrum representation approach to the Goos-Hänchen shift*
M. McGuirk, C. K. Carniglia, J. Opt. Soc. Am. **67**, 103 (1977).

[118] *Optical response of a thin film with arbitrary deterministic roughness of the interfaces*
S. Wang, P. Halevi, Phys. Rev. B **47**, 10815 (1993).

[119] *Statistical properties of spontaneous emission from atoms near a rough surface*
S. A. Biehs and J. J. Greffet, Phys. Rev. A **84**, 052902 (2011).

[120] *Nonperiodic metallic gratings transparent for broadband terahertz waves*
X. P. Ren, R. H. Fan, R. W. Peng, X. R. Huang, D. H. Xu, Y. Zhou and M. Wang, Phys. Rev. B **91**, 045111 (2015).

[121] *Structured Metal Film as a Perfect Absorber*
X. Xiong, S. C. Jiang, Y. H. Hu, R. W. Peng and M. Wang, Advanced Materials, **25**(29), 3994 (2013).

[122] *Excitons and the Absorption Edge in ZnSe*
G. E. Hite, D. T. F. Marple, M. Aven, and B. Segall, Phys. Rev. **156**, 850 (1967).

[123] *Definition and measurement of the local density of electromagnetic states close to an interface*
K. Joulain, R. Carminati, J. P. Mulet, J. J. Greffet, Phys. Rev. B **68**, 245405 (2003).

[124] *The Energy Density in the Casimir Effect*
The Electromagnetic Field Stress Tensor between Dielectric Half-Spaces

V. Sopova and L. H. Ford, Phys. Rev. D **66**, 045026 (2002); Phys. Rev. D **72**, 033001 (2005).